SISSA  ISAS

SCUOLA INTERNAZIONALE SUPERIORE DI STUDI AVANZATI
INTERNATIONAL SCHOOL FOR ADVANCED STUDIES

High-frequency properties of extragalactic radio sources

Thesis submitted for the degree of
"Doctor Philosophiæ"

Candidate:

Roberto Ricci

Supervisors:

Prof. Luigi Danese
Prof. Gianfranco De Zotti
Prof. Ronald D. Ekers

October 2004

Contents

Chapter 1

Introduction

1.1 High-frequency radio source populations

Determining the statistical properties of extragalactic sources at high frequency is of great interest in its own and is also crucial in view of the scientific exploitation of the high sensitivity and high resolution maps of the Cosmic Microwave Background (CMB) provided by the currently flying WMAP satellite and by forthcoming space missions, such as the Planck satellite, as discrete radio sources act as a CMB foreground that has not been well constrained yet.

What kind of sources may be expected to show up in the millimetre spectral region? We know that most sources that dominate the source counts at lower frequencies ($\nu \lesssim 8.4$ GHz) fade away at higher frequencies. Steep-spectrum ($\alpha < -0.5; S \propto \nu^{\alpha}$) radio sources tend to further steepen their spectra because of electron ageing effects, but also it has long been known (Owen & Mufson 1978; Witzel et al. 1978) that only a fraction of sources with flat or rising spectra up to 5 GHz keeps that trend up to much higher frequencies, while others become optically thin. This already illustrates some of the very interesting astrophysical phenomena that can be studied at high frequencies: mechanisms for electron energy losses, transition from optically thick to optically thin regimes of radio emitting magneto-ionic blobs, intrinsic polarization, magnetic field orientation, etc.

We will now survey the basic properties of a number of rare classes of extragalactic radio sources characterized by radio spectra keeping flat or inverted up to high frequencies.

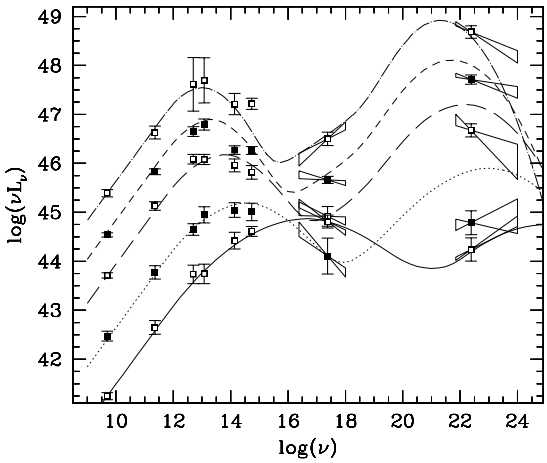

Figure 1.1: Averaged Spectral Energy Distributions for the sample selected by Fossati et al. (1998), binned according to radio luminosity. The overlaid curves are analytic approximations obtained according to the one-parameter model described in Fossati et al. (1998).

1.1.1 Blazars

Millimetre-wavelength surveys will have a great impact on the study of the classes of sources with "non-standard" radio spectra, keeping flat or inverted up to very high (100 GHz) frequencies. The best known population of this kind are blazars.

Blazars, which are phenomenologically divided into flat-spectrum radio quasars (FSRQs) and BL Lacertae objects, represent a composite population, with Spectral Energy Distributions (SEDs) characterized by two broad peaks: the synchrotron and the inverse Compton peak occurring at widely separated frequencies (Fig. 1.1). They also have a sort of bimodal distribution of polarization properties. An inverse correlation between luminosity and synchrotron peak frequency hints at a continuity or an evolutionary link between the various sub-populations (Ghisellini et al. 1998; Fossati et al. 1998).

According to the current theoretical paradigm, the phenomenology of bright blazars can be explained by a sequence in the source power and intensity of the diffuse radiation field, surrounding the relativistic jet, which determines the distributions of synchrotron and inverse Compton peak frequencies.

The two main discovery techniques, radio and X-ray selection, have individuated two sub-classes of BL Lac objects with different distributions of radio to X-ray luminosity ratios. The X-ray selected objects appear to be substantially weaker in the radio, although no evidence has been found of a significant population of radio-silent BL Lacs. There are therefore two possibilities: either the X-ray and radio selection techniques are sampling the extremes of the BL Lac population distribution, or they are discovering populations with intrinsically different properties.

There are also hints that the radio to mm spectral indices of faint flat-spectrum sources tend to be steeper than those found in bright samples (Tornikoski et al. 2000, 2001).

The characterization of variability and polarization in blazars is still an important open issue. Very compact objects are variable, with typical timescales limited by the causality argument to $\delta t > d/c$, where d is the source size and c is the light speed. In some cases the spectral shape was also found out to be variable, possibly suggesting evolutionary relationships between different classes of sources. In flat-spectrum sources another important and very debated variability feature appears on short timescales: Intra Day Variability (IDV) (Wagner & Witzel 1995; Krichbaum et al. 2002); for recent developments on the role played by interstellar scintillation to explain this phenomenon see Kedziora-Chudczer et al. (2003), Jauncey et al. (2003a), and Lovell et al. (2003).

The dominant emission process for powerful radio sources is known to be synchrotron radiation that is intrinsically highly polarized. Yet the observed polarization degree of most sources observed at MHz or GHz frequencies is not higher than a few percent. The depolarization may be due either to random alignment of the magnetic field or to the differential Faraday rotation of the emergent radiation along the line of sight. As the latter effect scales as ν^{-2}, it is thought to provide only a minor contribution to the source depolarization at millimetre wavelengths. Thus the Faraday depth could be determined through measurements of (intrinsic) polarization at high frequency, together with low-frequency polarization measurements.

It is also important to point out that, because of Doppler boosting, very high redshift blazars can show up at relatively bright radio fluxes. This will permit to investigate the abundance of supermassive black holes and their host galaxies at cosmic ages of about 1 Gyr, thus allowing us to explore the early phases of structure formation and the origin of the radio phenomenon. Several $z > 4$ blazars have already been detected at flux density

levels $S \gtrsim 50 - 100$ mJy (Snellen et al. 2001; Romani et al. 2004).

1.1.2 Extreme GPS sources

A class of sources that is expected to show up in millimeter surveys is that of extreme GHz Peaked Spectrum (GPS) sources or High Frequency Peakers (HFPs). GPS sources are powerful ($P_{1.4\mathrm{GHz}} \gtrsim 10^{25}$ W Hz^{-1}), compact ($\lesssim 1$ kpc) radio sources with a convex spectrum peaking at GHz frequencies. They are identified with both quasars and galaxies. The properties of the two sub-populations are very different: they have different redshift, rest-frame frequency, linear size and radio morphology distributions (Stanghellini et al. 1998, 1999, 2001; Snellen et al. 1999). It thus seems that the AGN unification schemes, according to which the differences between the two populations are due to orientation effects, are not valid for the GPS class.

In low-frequency ($\nu \leq 5$ GHz) surveys, GPS sources peaking at $\nu \gtrsim 10$ GHz are strongly under-represented because they are still in the self-absorbed spectral region, and have thus faint fluxes. Anyhow small (some tens of objects) samples of this kind of sources are available (Edge et al. 1996, 1998; Crawford et al. 1996; Grainge & Edge 1998; Tornikoski et al. 2000; Tornikoski et al. 2001; Guerra et al. 2002; Partridge et al. 2003). In Grainge & Edge (1998) a GPS having a rest-frame peak frequency of 190 GHz is reported.

There is now wide consensus on the nature of GPS sources: they would correspond to the early stages of the evolution of powerful radio sources, when the radio emitting region grows and expands within the interstellar medium of the host galaxy, before emerging out in the intergalactic medium and becoming an extended radio source (Fanti et al. 1995; Readhead et al. 1996; Begelman 1996; Snellen et al. 2000). A conclusive evidence in favour of the *youth* scenario came from measurements of hot-spot propagation velocity. Velocities of up to $v \simeq 0.4c$ were measured implying dynamical ages of $\sim 10^3$ years (Owsianik & Conway 1998; Owsianik et al. 1998; Polatidis et al. 1999; Taylor et al. 2000; Tschager et al. 2000). Estimates of radiative ages of a sample of Compact Steep Spectrum (CSS) sources by Murgia et al. (1999) are also consistent with young ages.

A clear anti-correlation (Fig. 1.2) between the peak (turnover) frequency and the projected linear size of GPS (and CSS) sources has been reported by Fanti et al. (1990) and O'Dea & Baum (1997), suggesting that the process (probably synchrotron self-absorption or alternatively free-free absorption , cf. Bicknell et al. 1997) responsible for the turnover

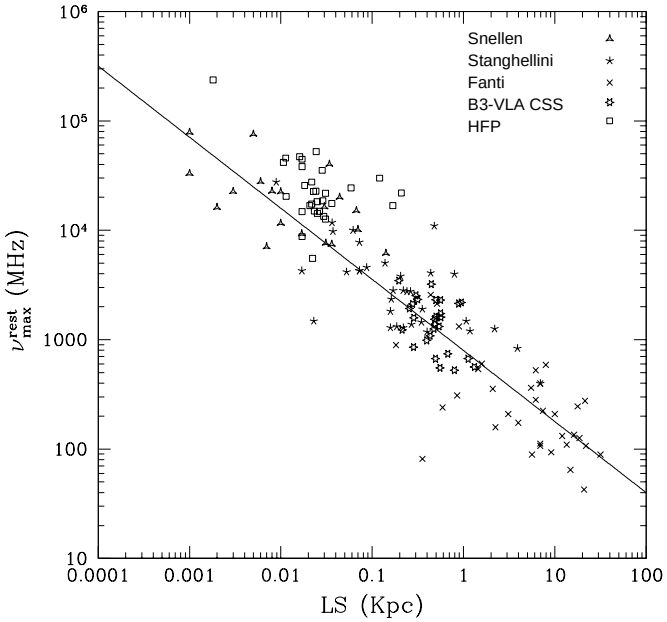

Figure 1.2: Rest frame turnover frequency vs. linear size for CSS/GPS samples and for the HFP sample studied by Dallacasa et al. (2000). (After Tinti et al. 2003)

depends on the source size in a simple manner. Although this anti-correlation does not necessarily translate into an evolutionary sequence, there are indications of a decrease of the peak frequency as the emitting blob expands.

An important issue connected to the GPS source evolution scenario is the source luminosity behaviour as a function of source age. According to self-similar evolution models (Fanti et al. 1995; Begelman 1996) the radio power drops as the source expands, so that GPS sources evolve into lower luminosity radio sources. De Zotti et al. (2000), using this model, were able to reproduce the observed counts, redshift and peak frequency distributions of available samples (Stanghellini et al. 1998; Snellen et al. 1998; Marecki et al. 1999). An alternative luminosity evolution model was proposed by Snellen et al. (2000), whereby GPS source luminosity *increases* with time (while the peak frequency decreases) until a linear size $l \simeq 1$ kpc is reached, and decreases subsequently. This scenario is consistent with the positive correlation between peak flux and linear size, but this property only refers to the source population and does not necessarily reflect the evolution of individual sources. The two scenarios offer widely different predictions for counts of GPS sources at millimetre wavelengths. In the former a significant fraction of bright ($S > 1$ Jy) radio sources at $\nu > 30$ GHz are GPS sources, whereas in the latter very

few GPS sources are expected to show up at high frequencies. Bright large-area millimetre surveys will be able to clearly discriminate among them.

There are indications in literature that GPS sources hardly show any variability (O'Dea 1998; Marecki et al. 1999), even if extensive systematic studies are still lacking. Flux density monitoring data at 2.3 and 8.4GHz for a sample of 33 southern hemisphere GPS sources, drawn from the 2.7 GHz Parkes survey, shows that only a small fraction of these sources ($\simeq 10\%$) varies (Jauncey et al. 2003b). From a preliminary study of a complete sample of GPS sources (Stanghellini et al. 1999; Tinti et al. 2003) it is apparent that GPS galaxies present low variability, while GPS quasars are found to vary as strongly as compact flat-spectrum quasars.

Another interesting issue is GPS source polarization. Even if synchrotron emission is intrinsically polarized up to a very high level ($\sim 75\%$), very low polarization has been detected in GPS sources at cm wavelengths ($\sim 0.2\%$ at 6 cm; O'Dea et al. 1990; Aller et al. 1992; Stanghellini et al. 1998). Faraday depolarization is supposed to be responsible for the low polarization (O'Dea 1998), at least in some cases, in particular for GPS quasars. Very large Rotation Measures (RM $\gtrsim$ 1000 rad m^{-2}) have been indeed detected (Kato et al. 1987; Aizu et al. 1990; Taylor et al. 1992; Inoue et al. 1995). In order to depolarize the synchrotron emission to the observed level, Faraday RMs must reach really extreme values (RM $\gtrsim 5 \times 10^5$ rad m^{-2}) or alternatively, the magnetic fields need to be entangled on very small angular scales ($\theta \lesssim 1$ mas). Similar values are also associated to radio galaxies in cluster centres subject to cooling flows (Perley 1990; Taylor et al. 1992; Ge & Owen 1994). It is not clear whether GPS sources with high RMs are in cooling flow clusters or the high RMs are produced in some other way.

1.1.3 Advection Dominated Systems

There are indications that the latest phases of AGN evolution also produce radio spectra peaking at high frequencies.

There is growing evidence that all massive ellipticals harbour, in their nuclei, black holes having masses of 10^8-10^{10} M$_\odot$ (Kormendy & Gebhardt 2001). The black-hole masses are correlated with the galaxy bulge luminosity (Magorrian et al. 1998), with the central velocity dispersion (Ferrarese & Merritt 2000; Gebhardt et al. 2000) and the central light concentration (Graham et al. 2001). However, these galaxies do not generally show

significant AGN activity. Although a few faint AGNs have been detected in X-rays (e.g, in the $L_X/L_E \sim 10^{-(6-7)}$ range, where L_E is the Eddington luminosity of the SMBH; Fabbiano & Juda 1997; Ho et al. 2001; Pellegrini et al. 2003; Fabbiano et al. 2003), the absence of a luminous AGN is puzzling, given that elliptical galaxies tend to host large quantities of centrally concentrated hot interstellar medium (ISM; see Fabbiano 1989 for an early review), so that lack of fuel does not seem to be an option.

For example, the circum-nuclear regions studied so far with the *Chandra* ACIS show the presence of hot gas close to the accretion radius; this implies, when applying the spherical Bondi accretion theory, accretion luminosities comparable to those of luminous AGN, in the case of a standard radiative efficiency of ~ 0.1 (e.g., Di Matteo et al. 1999; Loewenstein et al. 2001; Fabbiano et al. 2003; Baganoff et al. 2003).

Rees et al. (1982) proposed that at least the final stages of accretion in elliptical galaxies may be explained by rotating accretion flows (Advection Dominated Accretion Flows, ADAFs), characterized by very low radiative efficiency (Fabian & Rees 1995). The ADAF mechanism implies strongly self-absorbed thermal cyclo-synchrotron emission due to a near-equipartition magnetic field in the inner parts of the accretion flows, that can be easily detected at cm to mm wavelengths (Fig. 1.3). VLA observations at high radio frequencies (up to 43 GHz) have shown, albeit for a limited sample of objects, that all the observed compact cores of elliptical and S0 galaxies indeed have radio spectra rising up to $\simeq$ 20-30 GHz (Di Matteo et al. 1999).

There are however evidences that ADAF models overpredict the high-frequency nuclear radio emission in a number of nearby early-type galaxies (Di Matteo et al. 1999; Di Matteo et al. 2001). An alternative mechanism to ADAF is offered by ADIOS (Advection-Dominated Input Output Solution), whereby, when radiative efficiency is very low, a large fraction of plasma in the accretion flow may be unbound, leading to significant winds (Blandford & Begelman 1999; Narayan & Yi 1994). The radio emission in the inner regions of the accretion disk turns out to be suppressed because of the large amount of energy dumped into the surrounding medium by outflows or jets, resulting in a reduction of the accretion rate. Both the intensity and the peak of the radio emission are mass loss rate dependent.

There is still not a large consensus on the prevailing mechanism responsible for low-radiative efficiency advection systems and high-frequency source count predictions based

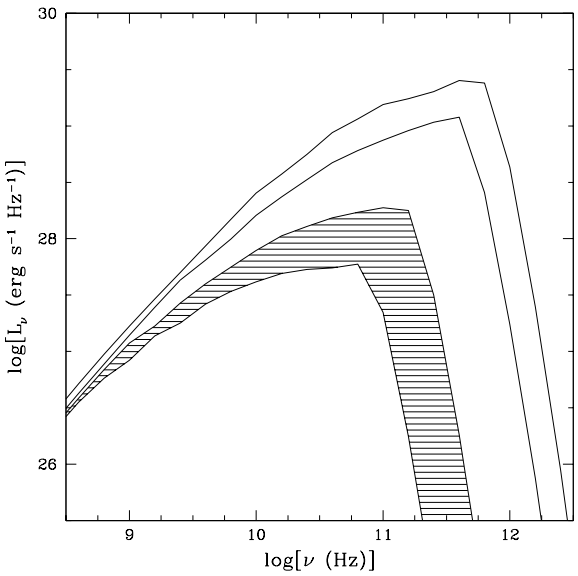

Figure 1.3: Synchrotron emission from low radiative efficiency accretion flows. The lines correspond to different amounts of mass loss in the flows. The uppermost curve shows the standard ADAF model with no outflows. The shaded region indicates the range of luminosities that best fit the data in the cores of ellipticals observed so far (Di Matteo et al. 2000). (After Perna & Di Matteo 2000)

on these models still cover a wide spread. Perna & Di Matteo (2000), for instance, seem to strongly overestimate the high-frequency source counts. New calculations based on the same model provide much lower values (see Chapter 2 for further details).

As radio emission and AGN central BH mass appear to be correlated (Franceschini et al. 1998; Salucci et al. 1999), millimetre source counts could also provide information on the supermassive black hole mass function. A considerable improvement could be obtained if radio and X-ray measurements are combined (Yi & Boughn 1998).

1.1.4 Radio afterglow of Gamma-Ray Bursts (GRBs)

The afterglow emission of GRBs can be modelled as synchrotron emission from a decelerating shock-wave in an ambient medium, plausibly the interstellar medium of the host galaxy (Waxman 1997; Wijers & Galama 1999; Mészáros 1999). The radio flux, above the self-absorption break, occurring at $\lesssim$ 5 GHz, is proportional to $\nu^{1/3}$ up to the peak frequency that decreases with time. The counts of GRB radio afterglows at various frequencies have been estimated by Ciardi & Loeb (2000). As can be seen in Chapter 2

the number of GRB afterglows predicted to be seen at 18 and 30 GHz is very low: a large area ($> 10^3$ sq. deg.) survey would detect some of them down to a limiting flux density of 1 mJy.

1.1.5 Dusty and starburst galaxies

When deep mm surveys are performed, a different population emerges in the source counts, i.e. galaxies with an extreme star formation activity, up to 10^3 $M_\odot$/year. In this type of objects the dominant emitting mechanism is dust re-radiation of starlight. A large fraction, or even most, of star formation is heavily obscured by dust, thus surveys in the mm/sub-mm regions, where dust mainly radiates, are best suited to study the early evolution of galaxies.

The physical and evolutionary properties of these sources are still not well understood. The semi-analytic models (Coles et al. 2000; Devriendt & Guiderdoni 2000), that work so well in predicting the galaxy structure formation in the framework of hierarchical clustering paradigm when matched with detailed numerical simulations, fail completely to reproduce the (sub)-mm source counts provided, for instance by SCUBA or MAMBO (Blain et al. 1999; Chapman et al. 2002). In fact, according to the hierarchical clustering scenario, most star formation is predicted to occur in small proto-galaxies having typical star formation rates of 10 $M_\odot$/year, that later merge to form larger galaxies. In the traditional "monolithic" approach, instead, giant elliptical galaxies are allowed to form even at high redshift ($z \gtrsim 2$), generating most of their star component in a single gigantic starburst, followed by passive stellar evolution. This evolutionary scenario seems to provide predictions in better agreement with experimental (sub)-mm counts. The pure monolithic approach, however, is unable to provide a consistent description of structure formation starting from primordial density fluctuations.

One way to overcome this problem is provided by a scheme (Granato et al. 2001, 2004) whereby the merging history of dark matter haloes was hierarchical but the baryon component anti-hierarchically filled the larger potential wells first, the collapse of baryons in smaller clumps being hindered by feedback effects (e.g. supernova winds from early star formation and central engine ignition in active nuclei). The (sub)-mm counts predicted by this scheme are in good agreement with observations.

As the SCUBA galaxies are expected to be highly biased tracers of the dark matter

distribution and therefore strongly clustered, they appear to be a good benchmark for the clustering predictions of Granato et al. anti-hierarchical structure formation model. Recent results (Magliocchetti et al. 2001; Perrotta et al. 2003) show that SCUBA data are consistent with model predictions (Granato et al. 2001, 2004).

Another important effect acting on the sub-mm/mm emitting proto-spheroids is gravitational lensing. It was estimated that the lensing effect on (sub)-mm counts is so strong, that almost all spheroids detected at 850 μm with flux densities larger than $\sim$ 60 mJy are strongly amplified by gravitational lensing (Perrotta et al. 2003).

1.1.6 Cluster and galaxy-scale Sunyaev-Zel'dovich effect

An important astrophysical foreground for CMB observations are clusters of galaxies. As predicted by Sunyaev & Zel'dovich (1970), the inverse Compton scattering of the CMB photons against the hot and diffuse electron gas trapped in the potential wells of clusters of galaxies, and responsible for their X-ray emission, yields a systematic shift of photons from the Rayleigh-Jeans to the Wien side of the spectrum. This thermal effect, arising from the thermal motion of the electrons, is described by the Kompaneets equation (Kompaneets 1957). The spectral form of this thermal effect is given by a function $g(x) = x^4 e^x [x \cdot \coth(x/2) - 4]/(e^x - 1)^2$, where $x = h\nu/kT_{\rm CMB}$, which is negative (positive) at values of x smaller (larger) than $x_0 = 3.83$, corresponding to a critical frequency $\nu_0 = 217$ GHz.

The main emphasis so far has been on the measurement of the SZ effect in individual clusters (see Birkinshaw 1999 for a review). On the other hand, the SZ effect carries important information on the intergalactic medium in clusters of galaxies and on its cosmological evolution. Also, SZ surveys can detect massive clusters with low electron densities, which are weak in X-rays (because the X-ray emission is proportional to n_e^2), while the amplitude of the SZ effect is linear in n_e.

SZ effects on galactic scales can also be associated to the formation of spheroidal galaxies (De Zotti et al. 2004a; Rosa-Gonzales et al. 2004). In fact, when the proto-galaxy collapses with the gas shock-heated to virial temperature, (Rees & Ostriker 1977; White & Rees 1978) the proto-galactic gas is expected to have a large thermal energy content, leading to a detectable SZ signal. In a later phase, feedback from the active nucleus at the centre of the spheroid, in the form of energetic outflows or blast-waves,

could ionize the IGM electrons and energize them enough to produce a detectable SZ signal (Ikeuchi 1981; Natarajan et al. 1998; Natarajan & Sigurdsson 1999; Aghanim et al. 2000; Platania et al. 2002; Lapi et al. 2003). Experimental evidence of these effects is still to be found, but an excess in the CMB primordial anisotropies, that is unlikely to be attributable to extragalactic radio sources, seen by CBI (Mason et al. 2003) and BIMA (Dawson et al. 2002), could be more easily explained by the aforesaid galactic-scale SZ effects.

Further details on the physics and the counts of galaxy clusters through the SZ effect are provided in Chapter 2.

1.2 CMB anisotropies in total intensity and polarization

A very active research area at this time is the study of Cosmic Microwave Background (CMB) radiation, the remnant blackbody radiation from the photon-baryon plasma that pervaded the early universe. The CMB temperature is highly isotropic, but does contain anisotropies at the level of $\Delta T/T \sim 10^{-5}$, caused by variation in the density of the photon-baryon plasma in different regions at the time of decoupling between matter and radiation. As such, the CMB anisotropies are a direct probe of conditions in the early universe and allow for precise measurements of fundamental cosmological parameters such as the vacuum energy density (Ω_Λ), the dark matter density ($\Omega_{\rm DM}$), the baryon density ($\Omega_{\rm b}$), the Hubble constant (h), the age of the universe and so on.

1.2.1 CMB temperature fluctuations

Since the CMB spectrum is an extremely accurate blackbody (Fixen et al. 1996) with a nearly constant temperature across the sky T, its anisotropies are generally described in terms of a temperature fluctuation $\Theta(\hat{\mathbf{n}}) \equiv \Delta T/T$.

If these fluctuations are Gaussian, then the multipole moments of the temperature field

$$\Theta_{lm} = \int d\hat{\mathbf{n}} Y^*_{lm}(\hat{\mathbf{n}})\Theta(\hat{\mathbf{n}}) \tag{1.1}$$

are fully characterized by their power spectrum

$$< \Theta^*_{lm}\Theta_{l'm'} >= \delta_{ll'}\delta_{mm'}C_l \tag{1.2}$$

whose values as a function of l are independent in a given realization. This is the reason why the spherical harmonic analysis is preferred in studying CMB anisotropies. Since the angular scale $\theta = 2\pi/l$, large multipole moments correspond to small angular scales. Likewise, since in this limit the variance of the field is $\int d^2 l C_l/(2\pi)^2$, the power spectrum is usually presented as

$$\Delta_T^2 \equiv \frac{l(l+1)}{2\pi} C_l T^2 \tag{1.3}$$

the power per logarithmic interval in wavenumber for $l \gg 1$.

While COBE (Smoot et al. 1992) first detected anisotropy on the largest angular scales ($\theta \geq 7^\circ$), CMB anisotropy experiments in the last decade have pushed the goal to smaller and smaller scales. For example TOCO (Miller et al. 1999), Boomerang (de Bernardis et al. 2000) and Maxima1 (Lee et al. 2001) were able to detect the first acoustic peak, WMAP (Bennett et al. 2003a) reached the multipole $l \sim 1000$ and the Planck satellite (Tauber 2001), scheduled for launch in 2007 will go a factor of two higher.

The angular power spectra of all experiments begin at $l = 2$ and exhibit relatively large errors at low multipoles. The reason is that the predicted power is the average power in the multipole moments l an observer would see in an ensemble of universes. However, a real observer is limited to one Universe and one sky with its own set of Θ_{lm}'s, $2l+1$ numbers for each l. The fact that there are only $2l+1$ m-samples of the power in each multipole moment sets the accuracy with which we can measure CMB angular power spectra. The inevitable uncertainty (*cosmic variance*) is

$$\Delta C_l = \sqrt{\frac{2}{2l+1}} C_l \tag{1.4}$$

When the temperature of the Universe was ~ 3000K at the redshift $z_* \simeq 10^3$, electrons and protons combined to form neutral hydrogen, an event known as recombination (Peebles 1968; Zel'dovich et al. 1969). Before this epoch, free electrons kept photons and baryons together through Thomson and Coulomb scattering, so the cosmological primordial plasma was a tightly coupled *photon-baryon fluid* (Peebles & Yu 1970).

The most striking features in the CMB angular power spectrum produced by high-resolution and high-sensitivity CMB experiments are peaks and troughs (Fig. 1.4). Their existence, the spacing between adjacent peaks and the location of the first peak are properties that depend on the initial conditions (primordial density power spectrum) and on the energy contents of the Universe (for an extensive review on CMB anisotropies see

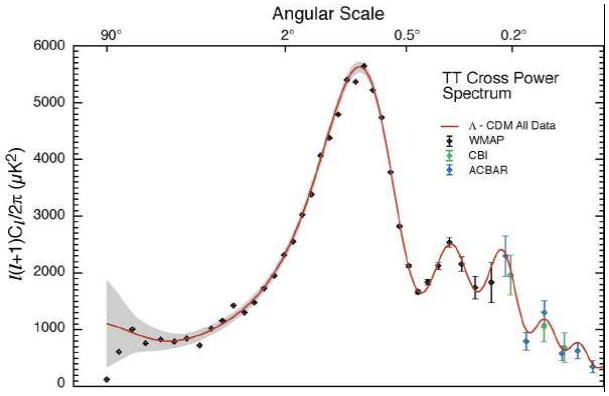

Figure 1.4: The WMAP angular power spectrum of CMB temperature fluctuations (dots), compared with CBI (Mason et al. 2003) and ACBAR (Runyan et al. 2003; Goldstein et al. 2003) data. The best fit ΛCDM model (solid line) is shown together with the cosmic variance expected for that model (grey band). (After Bennett et al. 2003a)

Hu & Dodelson 2002).

After recombination the photons basically travel freely to us, so translating the inhomogeneities in the photon distribution at recombination into the anisotropy spectrum today is simply a problem of projection. This projection depends almost completely on the angular diameter distance between us and the surface of last scattering. That distance also depends on the energy contents of the Universe after recombination through the expansion rate.

In describing the physical theory of acoustic peaks, for simplicity reasons we will use the idealization of a perfect photon-baryon fluid neglecting the dynamical effects of gravity and the baryons. Perturbations in this perfect fluid can be described by a simple continuity equation and an Euler equation that incorporate the basic properties of acoustic oscillations.

The discussion of acoustic oscillations exclusively takes place in the Fourier domain. This because perturbations are small and so the evolution equations are linear, and different Fourier modes evolve independently. For example the monopole of the temperature field is decomposed into:

$$\Theta_{l=0,m=0}(\mathbf{x}) = \int \frac{d^3k}{(2\pi)^3} e^{i\mathbf{k}\cdot\mathbf{x}} \Theta(\mathbf{k}) \tag{1.5}$$

Temperature perturbations in Fourier space follow the equation

$$\dot{\Theta} = -\frac{1}{3} k v_\gamma \tag{1.6}$$

that is the continuity equation for the photon temperature in Fourier space and v_γ is the scalar photon velocity. The time derivative is with respect to *conformal time* $\eta \equiv \int dt/a(t)$, $a(t)$ being the expansion scale factor.

The second equation, the Euler equation for a fluid, is an expression of momentum conservation. In Fourier space it simply reads:

$$\dot{v_\gamma} = k\Theta \tag{1.7}$$

Differentiating the continuity equation and inserting the Euler equation yields the most basic form of the oscillator equation

$$\ddot{\Theta} + c_s^2 k^2 \Theta = 0 \tag{1.8}$$

where $c_s \equiv \sqrt{\dot{p}/\dot{\rho}} = 1/\sqrt{3}$ is the sound speed in the fluid. This equation basically states that pressure gradients act as a restoring force to any initial perturbation in the system which thereafter oscillates at the speed of sound.

In the limit of large scales, compared to the sound horizon, the perturbation is frozen into its initial conditions. On small scales, instead, the amplitude of the Fourier modes will show temporal oscillations. Thus, modes that are caught at maxima *or* minima of their oscillation on the last scattering surface correspond to peaks in the power spectrum.

Moreover, a spatial inhomogeneity in the CMB temperature of wavelength λ appears as an angular anisotropy of scale $\theta \simeq \lambda/D$ where $D(z)$ is the comoving angular diameter distance from the observer to redshift z.

In a spatially curved universe, the angular diameter distance no longer equals the coordinate distance making the peak locations sensitive to the spatial curvature of the Universe (Doroshkevich et al. 1978; Kamionkowski et al. 1994). The result is that objects in an open (closed) universe are closer (further) than they appear, and this translates into the fact that a given comoving scale at a fixed distance subtends a larger (smaller) angle in a closed (open) universe than in a flat universe. This is the reason why the first peak position is tightly related to the curvature of the universe. In particular the fact that the first acoustic peak has been observed at $l \simeq 200$ means that the geometry of the Universe is *flat* at a good confidence level.

1.2.2 CMB polarization fluctuations

General considerations of Thomson scattering suggest that the primordial anisotropies are up to 10% polarized. The first detection of CMB polarization is due to the DASI experiment (Kovac et al. 2002) and was confirmed by the analysis of first-year WMAP data (Kogut et al. 2003).

The polarization field can be analyzed in a way very similar to the temperature field, save for one complication. In addition to its strength polarization has also an orientation, depending on the relative strength of the two linear polarization states. When studying CMB polarization, cosmologists (Seljak 1997; Kamionkowski et al. 1997; Zaldarriaga & Seljak 1997) found that the scalar E and pseudo-scalar B modes provide a more useful description than the more commonly used Q and U Stokes parameters. E and B modes are linear but non-local combinations of the Stokes Q and U and possess interesting and useful properties: being parity invariant, the cross correlation between the pseudo-scalar B and the scalar Θ or E vanishes. Moreover, the amplitude of the EE spectrum (C_l^{EE}) is below the temperature spectrum by a factor of ten. Second, the oscillatory structure is very similar to the temperature oscillations: they are out of phase but correlated with each other. The final feature of the polarization spectrum is the comparative smallness of the BB spectrum. The reason for this is that scalar density perturbations do not produce B modes to first order. A detection of substantial B polarization would be indicative of the presence of vectorial or tensorial perturbations (strictly linked to the gravitational wave background).

The physical mechanism generating CMB polarization is sketched below. The dissipation of acoustic oscillations leaves a signature in the CMB polarization (see Hu & White 1997 for a more complete treatment). Thomson scattering induces a linear polarization in the scattered radiation. Incoming radiation makes an electron oscillate in the direction of its electric field vector or polarization $\hat{\epsilon}'$ causing it to radiate with an outgoing polarization parallel to that direction. However, since the outgoing polarization $\hat{\epsilon}$ must be orthogonal to the outgoing direction, incoming radiation that is polarized parallel to the outgoing direction cannot scatter, leaving only one polarization state. Equivalently, it can be said that the Thomson differential cross section is $d\sigma_T/d\Omega \propto |\hat{\epsilon}' \cdot \hat{\epsilon}|^2$.

Now, as the incoming radiation comes from all angles, if it were completely isotropic, radiation coming along an orthogonal direction $\hat{\mathbf{y}}$ (see Fig. 1.5) would provide the

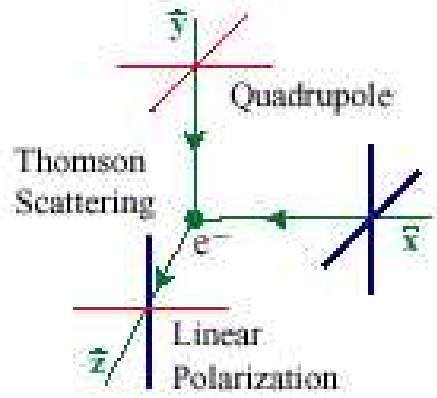

Figure 1.5: Thomson scattering of quadrupole temperature anisotropies (depicted here in the $x - y$ plane) that generates the linear polarization.

polarization state that is missing from that coming along the $\hat{\mathbf{x}}$ direction, leaving the net outgoing radiation unpolarized. Thus, only quadrupole temperature anisotropy in the radiation field generates a net linear polarization via Thomson scattering.

1.3 CMB foreground contamination

A major problem for anisotropy measurements is the presence of confusing microwave foregrounds. Compact sources in the relatively nearby universe also emit radiation in the high-frequency (30-100 GHz) range used for CMB experiments, thus they naturally interpose between us and the primordial microwave background creating different degrees of contaminations on different angular scales. In particular, at the resolution ($\sim 0.1 - 1$ degrees) of current and forthcoming CMB experiments (VSA, WMAP, Planck) the compact objects appear as point sources and so the contamination from these sources is called point source confusion.

With their poor angular resolution, the CMB experiments cannot identify any but the strongest point sources. It is necessary to measure the location and strength of the foreground sources with another instrument to enable source subtraction.

1.3.1 Basic formalism

The study of the background radiation provides unique information not only on diffuse emission but also on discrete sources which are beyond the detection limit. The basic formalism used to describe small scale fluctuations of extragalactic source foreground is

briefly summarized below (De Zotti et al. 1996).

The mean differential number counts *per steradian* dN/dS at a given flux density S can be written as:

$$\frac{dN}{dS} = \int_{z_l}^{z_h} dz \frac{dV}{dz} \frac{dL(S,z)}{dS} \psi[L(S,z),z] \tag{1.9}$$

where $\psi[L(S,z),z]$ is the epoch-dependent luminosity function and dV/dz is the volume element *per unit solid angle*, which in a Friedmann universe without cosmological constant is given by:

$$\frac{dV}{dz} = \frac{c}{H_0} \frac{d_L^2}{(1+z)^3(1+\Omega z)^{1/2}} \tag{1.10}$$

and d_L is the luminosity distance:

$$d_L = \frac{c}{H_0} z \left\{ 1 + z \frac{2-\Omega}{2+\Omega z + 2(1+\Omega z)^{1/2}} \right\} \tag{1.11}$$

The flux density S is related to the rest-frame luminosity L in the same frequency interval $\Delta\nu$ by

$$S_{\Delta\nu} = \frac{L_{\Delta\nu} K(L,z)}{4\pi d_L^2} \tag{1.12}$$

where $K(L,z)$ is the K-correction. If flux densities and luminosities are per unit frequency interval, at a frequency ν, the K-correction reads:

$$K = (1+z) \frac{L[\nu(1+z)]}{L(\nu)} \tag{1.13}$$

If a radio source has a power-law spectrum with spectral index α where $L_\nu \propto \nu^{-\alpha}$ then the K-correction formula becomes very simple and Eq. (1.12) reads:

$$S_{\Delta\nu} = \frac{L_{\Delta\nu}(1+z)^{1-\alpha}}{4\pi d_L^2} \tag{1.14}$$

In the case of a frequency interval $\nu_1 - \nu_2$, the K-correction becomes:

$$K(L,z) = \frac{\int_{\nu_1(1+z)}^{\nu_2(1+z)} L(\nu) d\nu}{\int_{\nu_1}^{\nu_2} L(\nu) d\nu} \tag{1.15}$$

If S is monotonically decreasing with increasing z, $z_h = \min[z_{\max}, z(S, L_{\max})]$ and $z_l = z(S, L_{\min})$, $z_{\max}$ being the redshift at which the sources started to emit radiation and $z(S,L)$ the redshift of a source having a flux density S and a luminosity L.

After Eq. (1.12) we obtain:

$$\frac{dL(S,z)}{dS} = \frac{L}{S} \left(1 + \frac{d \ln K(L,z)}{d \ln L} \right)^{-1} \tag{1.16}$$

Since the K-correction is usually supposed to be a function of redshift only, the last term in Eq. (1.16) is generally ignored. However, in some cases as X-ray emission from rich clusters of galaxies, a dependence of the K-correction on the cluster luminosity has been observed (Edge & Stewart 1991). Another interesting case are rising spectrum (synchrotron self-absorbed, SSA) radio sources which according to Fossati et al. (1998) and Ghisellini et al. (1998) present a different peak frequency at different luminosities.

The contribution of unresolved sources (i.e. sources fainter than the detection limit S_d) to the background intensity *per steradian* is:

$$\begin{aligned} I &= \int_0^{S_d} \frac{dN}{dS} S dS \\ &= \frac{1}{4\pi}\frac{c}{H_0}\int_{z(S_d,L_{\min})}^{z_{\max}} \frac{dz}{(1+z)^3(1+\Omega z)^{1/2}} \int_{L_m(z)}^{L_M} d\log L\ n(L,z)\ L\ K(L,z) \\ &= \frac{1}{4\pi}\frac{c}{H_0}\int_{L_{\min}}^{L_{\max}} d\log L\ L \int_{z(S_d,L)}^{z_{\max}} dz\ n(L,z)\frac{K(L,z)}{(1+z)^3(1+\Omega z)^{1/2}} \end{aligned} \tag{1.17}$$

where $L_{\min}$ and $L_{\max}$ are the minimum and maximum local source luminosities, $L_m(z)$ is the minimum source luminosity at the redshift z, $L_M = \min[L_{\max}, L(S_d, z)]$; $n(L,z) = \ln 10 L\psi(L,z)$ is the number density of sources of luminosity L, at redshift z, per unit $d\log L$.

The first formula can be used when the number counts of a source population is observationally determined.

The intensity fluctuations due to inhomogeneities in the space distribution of unresolved sources observed within the effective solid angle $\omega_{\rm eff,I}$ are given by:

$$\delta I = \frac{c}{H_0}\frac{\omega_{\rm eff,I}}{4\pi}\int_{L_{\min}}^{L_{\max}} d\log L L \int_{z(S_d,L)}^{z_{\max}} dz \frac{K(L,z)}{(1+z)^3(1+\Omega z)^{1/2}}\delta n(L,z) \tag{1.18}$$

where $\delta n(L,z)$ is the fluctuation around the mean, $n(L,z)$, of the number density of sources having luminosity L. This formula is valid if we assume that sources are point-like. As shown by Rowan-Robinson & Fabian (1974) this is a good approximation as far as angular sizes of sources do not exceed the beamwidth, as is usually the case in CMB anisotropy experiments where angular scales are $\theta \gtrsim 5 - 10$ arcmin.

Given the spatial response function of the detector, $f(\theta,\phi)$, the effective solid angle is:

$$\omega_{\rm eff,I} = \int d\omega f(\theta,\phi) \tag{1.19}$$

The angular correlation of the intensity fluctuations, as a function of beam displacement, θ_*, is

$$C(\theta_*) =< \delta I(\theta,\phi)\delta I'(\theta',\phi') > \tag{1.20}$$

where $\delta I(\theta,\phi)$ and $\delta I'(\theta',\phi')$, are intensity fluctuations seen along the directions (θ,ϕ) and (θ',ϕ') forming an angle θ_*. The average is performed on all the possible couples of intensity fluctuations separated by an angle θ_* on the sky.

There are two contributions to the angular correlation function $C(\theta_*)$: the Poissonian term, which represents the cell-to-cell fluctuations in the counts of *randomly* distributed objects, given by:

$$C_P(\theta_*) = \omega_{\rm eff,P}(\theta_*)\int_{L_{\rm min}}^{L_{\rm max}} d\log L \int_{z(S_d,L)}^{z_{\rm max}} dz \left(\frac{LK(L,z)}{4\pi d_L^2}\right)^2 \frac{dV}{dz} n(L,z) \tag{1.21}$$

where the effective solid angle

$$\omega_{\rm eff,P}(\theta_*) = \int_{\omega\bigcap\overline{\omega}} d\omega' f(\theta,\phi) f(\overline{\theta},\overline{\phi}) \tag{1.22}$$

subject to the condition that the pairs of angles (θ,ϕ) and $(\overline{\theta},\overline{\phi})$ define the same physical direction in the sky. The intersection of the beam patterns $\omega\bigcap\overline{\omega}$ obviously means that the $C_P(\theta_*)$ vanishes if the two fields of view do not overlap.

The second contribution to the angular correlation function is given by the term due to source clustering which, under the approximations that the maximum scale of appreciable clustering is much smaller than the Hubble radius $r_H \equiv c/H_0$ and the angular separation θ is much less than one radian, can be written as:

$$\begin{aligned} C_c(\theta_*) &= \left(\frac{c}{4\pi H_0}\right)^2 \int d\omega f(\theta,\phi)\int d\overline{\omega} f(\overline{\theta},\overline{\phi}) \int_{z_m(L_{\rm min},S_d)}^{z_{\rm max}} dz \frac{j_{\rm eff}^2}{(1+z)^6(1+\Omega z)} \cdot \\ &\cdot \int_{\max[z_m - z, -\Delta(r_{\rm max})]}^{\min[z_{\rm max}-z,\Delta(r_{\rm max})]} d(\delta z)\xi(r,z) \end{aligned} \tag{1.23}$$

where $\Delta(r_{\rm max})$ is the value of δz corresponding to the maximum scale of clustering, and

$$j_{\rm eff}(z) = \int_{L_{\rm min}}^{\min[L_{\rm max},L(S_d,z)]} d\log L L n_c(L,z) K(L,z) \tag{1.24}$$

$n_c(L,z)$ being the comoving number density of sources.

In Eq. (1.23) the term $\xi(r,z)$ is the redshift-dependent spatial correlation function, that, following Peebles (1980) can be parametrized as:

$$\xi(r,z) = h(z)\xi_0(r) \tag{1.25}$$

$$\xi_0(r) = (r_0/r)^\gamma \tag{1.26}$$

with $\gamma \simeq 1.8$.

The factor $h(z)$ allows for clustering evolution and after Peebles (1980) is frequently parametrized as:

$$h(z) = (1+z)^{-(3+\epsilon)} \tag{1.27}$$

If a power-law representation of $\xi_0(r)$ holds up to very large distances ($r_{\max} \to \infty$) and the beam displacement θ_* is much larger than the instrumental beamwidth a much simpler expression of $C_c(\theta_*)$ can be analytically worked out (Totsuji & Kihara 1969; Peebles 1980, §52).

Furthermore, in case of non-evolving objects and $\epsilon \simeq 0$, the dominant contribution to the integral over dz in Eq. (1.23) comes from $z \ll 1$ and the result is only weakly dependent on the exact redshift distribution:

$$\Gamma(\theta_*) \propto \theta_*^{(1-\gamma)/2} r_0^{\gamma/2} (j_{\rm sources}/j_{\rm background})_{z=0} \tag{1.28}$$

where the term $\Gamma(\theta_*)$ is the dimensionless autovariance function which is defined as:

$$\Gamma(\theta) = |W(\theta)|^{1/2} \tag{1.29}$$

$$W(\theta) = \frac{C(\theta)}{< I >^2} \tag{1.30}$$

being $< I >$ the *residual* background intensity (after the removal of bright sources). Finally, the small scale fluctuations are obtained by Eqs. (1.21) and (1.23) by setting $\theta_* = 0$.

In the Poissonian case, they are simply given by the formula:

$$(\delta I)^2 \equiv C(0) = \frac{\omega_{\rm eff,P}(0)}{4\pi} \int_0^{S_d} S^2 \frac{dN}{dS} dS \tag{1.31}$$

An interesting consideration is that the different dependence of Poisson and non-Poisson fluctuations on the flux distribution of the undetected sources has this remarkable implication: higher resolution surveys allowing for the identification and subtraction of sources down to much fainter limits may lead to a significant decrease in the residual Poisson fluctuations but will not appreciably decrease the amplitude of non-Poisson fluctuations as the latter are dominated by the faintest sources that are clustered on the relevant scales.

1.3.2 Diffuse and point-like foregrounds

At high Galactic latitudes and in the frequency range $40 - 200$ GHz, CMB intensity fluctuations stand out well above any other astrophysical signals, but moving closer to the Galactic plane there are three types of diffuse Galactic emissions (synchrotron, free-free and dust), which provide a confusing foreground to CMB anisotropies.

Galactic synchrotron emission

Synchrotron emission is produced by cosmic-ray electrons accelerated in magnetic fields. The acceleration occurs in Type Ib and Type II supernova remnants.

Galactic synchrotron radiation depends on the energy spectrum of the electrons and the intensity of the magnetic field (Ribicki & Lightman 1979; Longair 1994).

Since the relativistic electron energy distribution varies across the Galaxy, as does the magnetic field $\mathbf{B}$, the resulting synchrotron emission can be characterized by a wide range of spectral behaviours, and hence the observed morphology of synchrotron sky maps changes substantially with frequency. The synchrotron spectral index, α, is related to the electron power law index p, by $\alpha = -(p-1)/2$ at frequencies greater than a few GHz, where self-absorption is negligible.

The synchrotron emission spectrum is further affected by cosmic ray propagation, energy loss (via synchrotron ageing, inverse Compton scattering, adiabatic expansion and free-free) and degree of confinement (highly confined electrons lose their energy before they escape from the halo of the Galaxy). A steep spectral index (e.g. $\alpha < -0.9$, $\beta < -2.9$, where $\beta = \alpha - 2$ is the temperature spectral index) indicates a high rate of energy loss and a low escape rate, whereas a flatter spectral index indicates that electrons can escape the Galaxy before losing a significant fraction of their energy.

Synchrotron emission arises from two types of sources: electrons trapped in the magnetic fields of discrete supernova remnants and diffuse emission from cosmic ray electrons spread throughout the Galaxy. More than 90% of the observed synchrotron emission arises from a diffuse component having a direction-dependent spectral index that generally lies in the range $-0.5 > \alpha > -1.1$ corresponding to $-2.5 > \beta > -3.1$ and $2.0 < p < 3.2$. The nonthermal spectral index is seen to steepen off the disk in our Galaxy and the same effect is also seen in external galaxies. The observed steepening implies that the energy loss is important (Lisenfeld & Völk 2000).

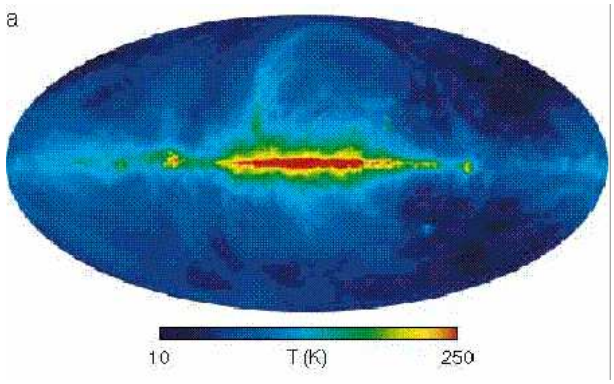

Figure 1.6: The Haslam 408 MHz sky map largely dominated by synchrotron emission. (After Bennett et al. 2003b)

In Fig. 1.6 the full sky radio emission mapped with moderate sensitivity at 408 MHz by Haslam et al. (1981) is shown. The map is dominated by synchrotron emission. Low-frequency (< 10 GHz) spectral studies of the synchrotron emission indicate that $\beta \simeq -2.7$, although substantial variations from this mean value occur across the sky (Reich & Reich 1988; Lawson et al. 1987). Voelk (1989) predicts a break in the synchrotron spectrum of the Milky Way at 22 GHz, arising from a break in the relativistic electron energy spectrum at 20 GeV. The steepening at frequencies above the break, due to synchrotron losses, is estimated to be $\beta = -0.5$. Synchrotron steepening with values higher than this has been observed in a few discrete sources (Green & Scheuer 1992; Morsi & Reich 1987), indicating additional processes beyond synchrotron losses.

Physical steepening effects compete against an observational measurement bias towards flat spectrum components. Steep spectral index synchrotron components seen at low frequency become weak relative to flat-spectrum components when observed at higher microwave frequencies. Thus, it results that flatter spectrum components will increasingly dominate in observations at higher microwave frequencies.

The steepening effects in high-frequency synchrotron maps are described in Fig. 1.7, where first-year WMAP (Bennett et al. 2003b) spectral index histograms are shown. The steep spectral index $\beta \sim -2.75$ between the Haslam 408-MHz and the WMAP MEM (Maximum Entropy Method) solution at K-band (22.5 GHz) is seen to further steepen in going from K-band to higher frequency bands (Ka and Q, 33 and 41 GHz, respectively).

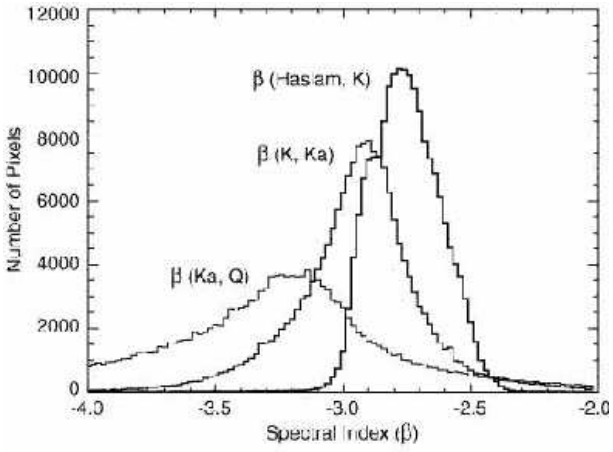

Figure 1.7: Spectral index histogram obtained from different WMAP frequency bands: K (23 GHz), Ka (33 GHz) and Q (41 GHz), also compared with Haslam et al. (1981) radio continuum map. (After Bennett et al. 2003b)

Free-free emission

A diffuse foreground is also produced by Galactic free-free emission. Galactic free-free emission is due to thermal bremsstrahlung from hot ($T_e \gtrsim 10^4 K$) electrons produced in the interstellar gas by the UV radiation (for reviews see Smoot 1998 and Bartlett & Amram 1998).

Free-free thermal emission has a $T_A \sim \nu^\beta$ high-frequency ($\nu > 10$ GHz) spectrum, with $\beta = -2.15$, and a low-frequency rising spectrum ($T_A \sim \nu^2$) due to optically thick self-absorption.

No sky map of free-free emission is available because free-free is not the dominant emission at any radio frequency: at low frequencies synchrotron emission is dominant, whereas at high frequencies dust gives the main contribution.

For this reason, high-resolution large-scale maps of Hα (hydrogen transition $n = 3 \rightarrow 2$) emission (Dennison et al. 1998; Gaustad et al. 2001; Haffner et al. 2002; Reynolds et al. 2002) are used as an approximate template for the free-free emission, except in regions of high interstellar dust optical depth, $\tau > 1$, at the Hα wavelength (about 16% of the sky).

Diffuse Galactic Hα emission is considered as a good tracer of diffuse free-free emission, because the ionizing medium is the same and the intensity is proportional to the emission measure, $EM \equiv \int N_e^2 dl$ where N_e is the electron number density and the integral is performed along the line of sight.

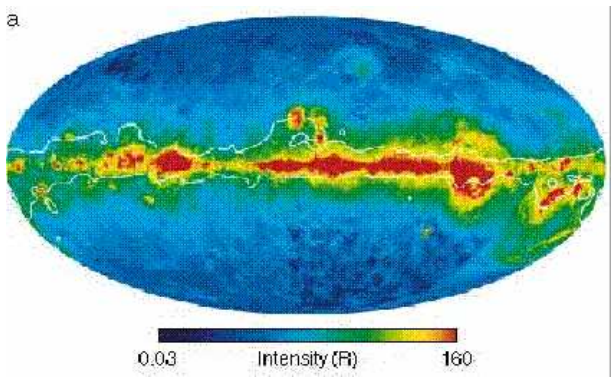

Figure 1.8: Extinction corrected Hα map of the sky. The high opacity $\tau > 1$ regions, where extinction correction is unreliable, are roughly demarcated by the contour lines. (After Bennett et al. 2003b)

Using the definition of the emission measure and the formula for the free-free volume emissivity (Oster 1961), Bennett et al. (2003b) obtained an expression for the free-free antenna temperature in the WMAP frequency range ($23 - 94$ GHz):

$$T_A(\mu K) = 1.44 EM_{cm^{-6}pc} \times \frac{[1 + 0.22\ \ln(T_e/8000K) - 0.14\ \ln(\nu/41\mathrm{GHz})]}{(\nu/41\mathrm{GHz})^2(\mathrm{T_e}/8000\mathrm{K})^{1/2}} \tag{1.32}$$

The free-free spectral index in the WMAP frequency range:

$$\beta_{ff} = -2 - \frac{1}{10.48 + 1.5\ \ln(T_e/8000K) - \ln \nu_{\mathrm{GHz}}} \tag{1.33}$$

does not extend to arbitrary low frequencies, but $T_A \simeq \tau_\nu T_e$, thus the antenna temperature measurement can be used to infer the optical depth τ_ν and extend the antenna temperature to low frequencies, where $\tau_\nu \geq 1$.

Finkbeiner (2003a) assembled a full sky Hα map using data from several surveys: the Wisconsin H-Alpha Mapper (WHAM), the Virginia Tech Spectral-Line Survey (VTSS), and the Southern H-Alpha Sky Survey (SHASSA). This map, together with the Schlegel et al. (1998) extinction sky map, are used to compute a best-guess map (Fig. 1.8) of free-free emission in regions where $\tau < 1$, under the assumption that ionized gas and dust are extended in the same regions.

There are several sources of uncertainty and error in this approximate template: (a) Hα light and free-free scatter dust grains in a different way; (b) uncertainty in the Hα measurement calibration; (c) errors in separating geocoronal emission from Hα emission; (d) possible inaccuracies in Balmer atomic rates; (e) T_e variations across the Galaxy

not precisely known; (f) uncertainties in the ionization state of helium; (g) extinction correction assumes that Hα emission is co-extensive to dust along the line of sight. It could be difficult to assess and propagate all these sources of error.

A full-sky template map of the Galactic free-free foreground emission component was also provided by Dickinson et al. (2003). They corrected the Hα maps for dust absorption using the 100-μm dust maps of Schlegel et al. (1998), showing that, for a range of longitudes, the Galactic latitude distribution of absorption suggests that it is 33% of the full extragalactic absorption. A reliable absorption corrected Hα map was produced for the 95% of the sky (the Galactic plane area and some isolated dense dust clouds at intermediate latitude were not recovered). The dust-corrected Hα data were then converted into radio surface brightness. The full-sky free-free template map, was then compared to the Haslam et al. (1981) 408-MHz sky map, and they found that, to provide a pure synchrotron all-sky map, the correction for the free-free component amounts to $\simeq 6\%$ at intermediate and high latitudes.

Dust emission

Galactic dust is heated by the interstellar radiation field (ISRF), absorbing optical and UV photons and emitting energy in the far-IR. The equilibrium temperature in the limit of large dust grains is $T_{\rm eq} \simeq 18 - 20$K. The emission spectrum from a greybody at that temperature has a peak at $\lambda \sim 140\mu$m and extends out to microwave wavelengths. The Berkeley-Durham dust map (Schlegel et al. 1998) is based on IR radiation from dust observed by IRAS and DIRBE and is extended in frequency by Finkbeiner et al. (1999).

Measurements of the thermal dust spectral index generally lie in the range $1.5 \leq \beta_d \leq 2$. For WMAP wavelenghts, the Finkbeiner et al. (1999) extrapolation predicts $\beta_d \simeq 1.6$. More recently, Dupac et al. (2001, 2002) have observed the inversion relation between dust temperature and spectral index, predicted by Schwartz (1982), in sources observed with the PRONAOS (PROgramme NAtional d'Observation Submillimetriques) 2-m balloon telescope in the wavelength range $200 - 580\mu$m.

Draine & Lazarian (1998) proposed spinning dust emission as another possible contaminant producing a significant signal at a few tens of GHz. Magneto-dipole emissivity was also suggested by Draine & Lazarian (1999). Bennett et al. (2003b) interpret the substantial dust-correlated emission, far exceding the expected thermal dust emission,

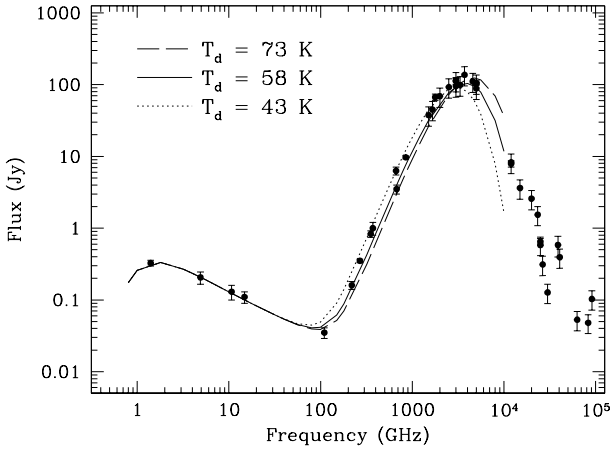

Figure 1.9: Radio-to-IR Spectral Energy Distribution for the radio galaxy Arp 220 is shown along with the model starburst SEDs for three different dust temperature. (After Yun et al. 2002)

observed at all WMAP frequencies, as dust-correlated synchrotron radiation, attributing the correlation to the natural association of relativistic electrons produced by supernovae with massive star formation in dusty clouds, and deriving an upper limit of 5% to the contribution of spinning dust at 23 GHz. Finkbeiner (2003b) suggests an alternative interpretation: much, perhaps, most of the dust-correlated emission at these frequencies is indeed spinning dust and explores the spectral dependence on environment and finds that models similar to Drain & Lazarian (1998) spinning dust provide a good fit to the full-sky data.

Extragalactic sources

The main classes of extragalactic sources acting as CMB foregrounds have been described in Section 1.1. The minimum in the Spectral Energy Distribution (SED) for most classes of these sources occurs at a few millimetre wavelengths (i.e. close to the CMB peak frequency), as shown in Fig. 1.9.

A steep increase with frequency of dust emission in the mm/sub-mm region (typically $S_\nu \propto \nu^{3.5}$) is also evident and the cross-over between radio and dust components is only weakly dependent on the their relative intensity. The dust temperature is higher for distant high-luminosity sources, thus partially compensating for the redshift effect. As a consequence, an abrupt change in the population of bright sources observed above ~ 1 mm occurs: radio sources dominate at longer wavelengths (cf. Toffolatti et al. 1998),

whereas the sub-mm region is most populated by dusty galaxies (Smail et al. 1997)

As radio sources follow predominantly a Poisson distribution on the sky, they produce white noise in the CMB angular power spectrum (i.e. $C_l \propto$ const.). Thus we get that the temperatute fluctuations follow this scaling with respect to multipole moments l:

$$(< (\Delta T/T)^2 >)^{1/2} \equiv l(l+1)C_l/2\pi \propto l^2 \tag{1.34}$$

for $l \gg 1$.

This means that the smaller the angular scale the higher the discrete extragalactic radio source contamination is.

Various methods have been devised to recover point sources from CMB high-resolution maps. Optimal Filtering in Fourier domain was explored by Tegmark & De Oliveira-Costa (1998), while Hobson et al. (1999) tested the Maximum Entropy Method (MEM), whereby information on the power spectrum of point sources in each frequency channel is introduced and correlations between frequencies are assumed. The Mexican Hat wavelet technique combined with MEM was also experimented by Vielva et al. (2001). The results of these tests confirmed that the discrete extragalactic radio source foreground is one of the most diffucult to separate from the CMB anisotropy maps, because of the poor knowledge of the frequency scaling of the various high-frequency emitting radio source populations and the variety of individual spectra.

For this reasons, direct methods such as the actual detection of radio source populations in high-frequency selected blind surveys using ground-based instruments are very important to better assess their degree of contamination in CMB maps.

Power spectrum of foreground fluctuations

The Galactic synchrotron angular power spectrum dependence on the multipole moment l from 408 and 1420 MHz radio maps was estimated to be $C_l \propto l^{-2}$ for $l \leq 300$ by Lasenby (1996). At high Galactic latitude a steeper mean power spectrum was obtained by Tegmark & Efstathiou (1996): $C_l \propto l^{-3}$.

The same dependence on l was also found for dust and free-free emission. Kogut et al. (1996) compared COBE DMR with DIRBE maps finding a correlation between free-free and dust emission. The spatial power index -3.0 is a well-determined value for dust and HI on degree angular scale. Hα images of Northern Celestial Pole (NCP) by Gaustad et al. (1996), analysed by Veeraraghavan et al. (1997) give $C_{ff} \propto l^{-2.27\pm0.07}$ on angular

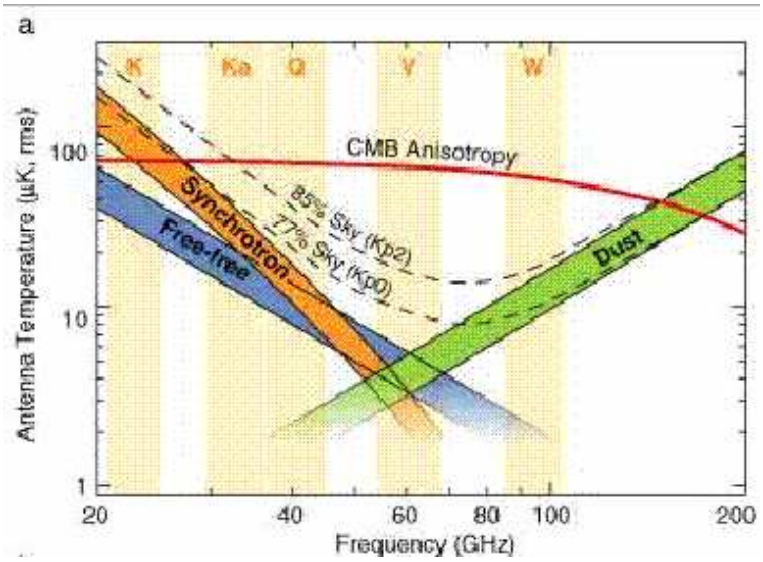

Figure 1.10: CMB anisotropy intensity as a function of frequency is compared with Galactic synchrotron, free-free and dust foregrounds. The dotted lines represent the WMAP masks Kp0 and Kp2 cutting out different amounts of sky across the Galactic plane. The shaded areas show the frequency ranges of WMAP bands.

scales from $10'$ to a few degrees (significantly flatter than that inferred by the COBE data, Kogut et al. 1996). However the rms amplitude is considerably lower. The angular power spectrum of dust emission fluctuations determined by Gautier et al. (1992) based on IRAS data gives $C_{\rm dust} \propto l^{-3}$ in the range $4'$ to 8 degrees.

For $l < 300$ (angular scales $> 30'$) diffuse Galactic emission dominates foreground fluctuations even at high Galactic latitudes. The minimum contamination is reported by Kogut et al. (1996) at 70 GHz. Recent estimates, obtained by Bennett et al. (2003b) are shown in Fig. 1.10.

For larger l values the dominant contribution comes from discrete extragalactic radio sources having a minimum contamination at $150 - 200$ GHz (Toffolatti et al. 1998). An overview of the angular power spectra of the foregrounds contributing to fluctuations at radio frequencies $\nu \leq 100$ GHz is shown in Fig. 1.11.

It is apparent that source removal is more effective in reducing the fluctuation level at the lowest than at the highest frequencies. At $\lambda \gtrsim 1$ mm, fluctuations are dominated by the brightest galaxies below the detection limit, whereas at shorter wavelengths the dominant population is constituted by evolving dusty galaxies having counts so steep that a major contribution to fluctuations comes from much fainter fluxes.

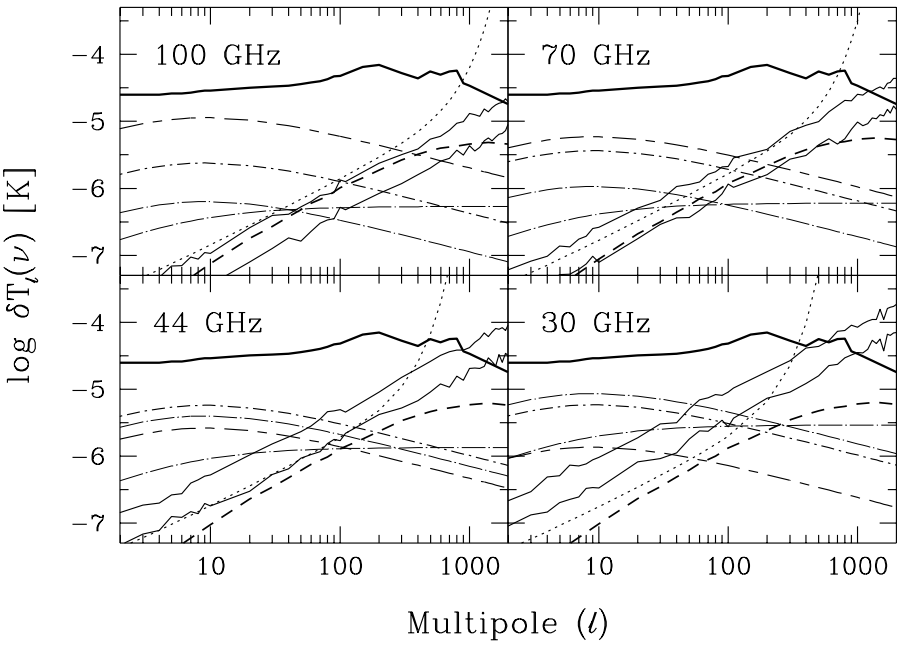

Figure 1.11: Angular power spectra of the foreground components contributing to fluctuations in the four frequency channels of the Planck Low Frequency Instrument (LFI). Fluctuations in the Galactic emission at $|b| > 30°$ are represented by long+short dashes (dust), dots+short dashes (free-free), and dots+long dashes (synchrotron). The roughly diagonal solid lines show the contributions of extragalactic sources, neglecting the clustering effect and assuming that sources brighter than 1 Jy (upper line) or 0.1 Jy can be identified and removed. Heavy dashes show the power spectrum of anisotropies due to the SZ effect on clusters. The dotted line shows the unsmoothed noise contribution of the instrument (after De Zotti et al. 1999a).

Polarization

Polarized foreground power spectra have not been studied as extensively as intensity power spectra, yet.

For a power-law electron energy spectrum $dN/dE = N_0 E^{-p}$ the polarization level Π, assuming uniform magnetic fields, is given by (Le Roux 1961; Ginzburg & Sirovatskii 1964):

$$\Pi = \frac{3(p+1)}{3p+7} \tag{1.35}$$

Thus, for $p \sim 3$, $\Pi \sim 75\%$, but non-uniformities in magnetic fields on beam width angular scales or/and differential Faraday rotation significantly decrease the linear

polarization level. However, the Faraday rotation optical depth $\propto \nu^{-2}$, therefore Faraday depolarization is almost suppressed at the high frequencies where CMB anisotropy experiments are usually carried out.

Free-free emission is known to be unpolarized, whereas 5% polarization of Galactic dust has been measured by the ARCHEOPS experiment (Benoît et al. 2003) in Galactic plane regions.

Recent results by De Zotti et al. (1999b), Mesa et al. (2002) and Tucci et al. (2003) are adding new hints on the high-frequency radio source polarization contamination.

The dependence on frequency of the contamination of polarized foregrounds to the polarized CMB angular power spectrum is shown in Fig. 1.12. At lower frequencies ($\nu = 30$ GHz), the polarized synchrotron contamination is dominant at multipoles $l \lesssim 100$. For higher l discrete radio sources give the main contribution. At 100 GHz synchrotron fades away and the dominant foreground is dust and the radio sources are responsible for the upward bending at $l \gtrsim 1000$. At 217 GHz dust is by far the dominant contaminant to polarized CMB. The separate contribution of synchrotron, discrete radio sources and dust to the polarized foreground contamination at 70 GHz is shown in Fig. 1.13.

New results on the polarization properties of extragalactic radio sources at 18.5 GHz are also presented in Chapter 4 of this Thesis.

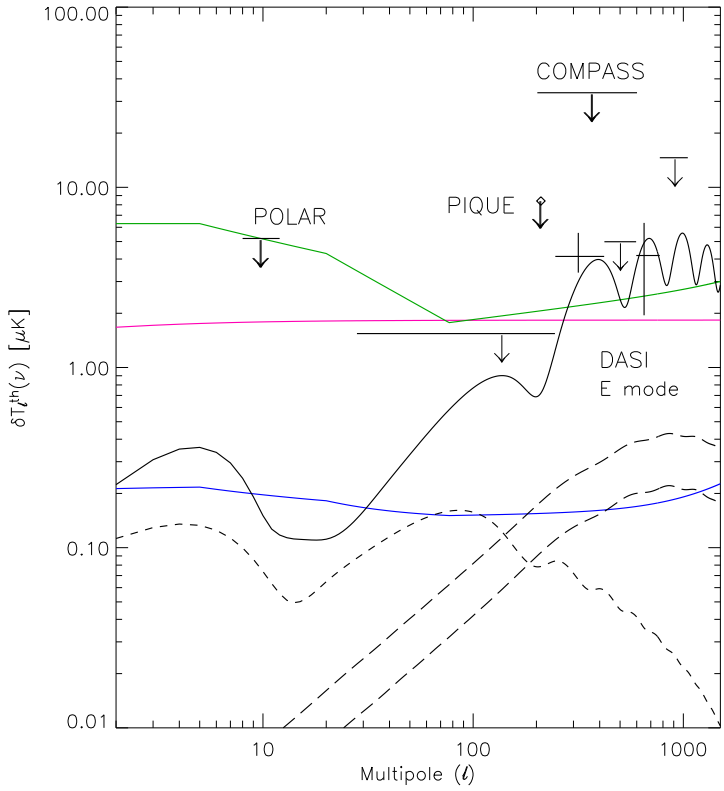

Figure 1.12: The effect of contamination of polarized synchrotron, discrete source and dust foreground to polarized CMB angular power spectrum (APS). Solid line: E-mode CMB APS; short-dashed line: B-mode CMB APS; long-dashed lines: B-modes enhanced by gravitational lensing; green line: foregrounds at 30 GHz; blue line: foregrounds at 100 GHz; red line: foregrounds at 217 GHz. Polarization detections and upper limits of four CMB experiments are also shown. Radio sources are detected/removed from foregrounds down to $S = 200$ mJy. (Courtesy of C. Burigana)

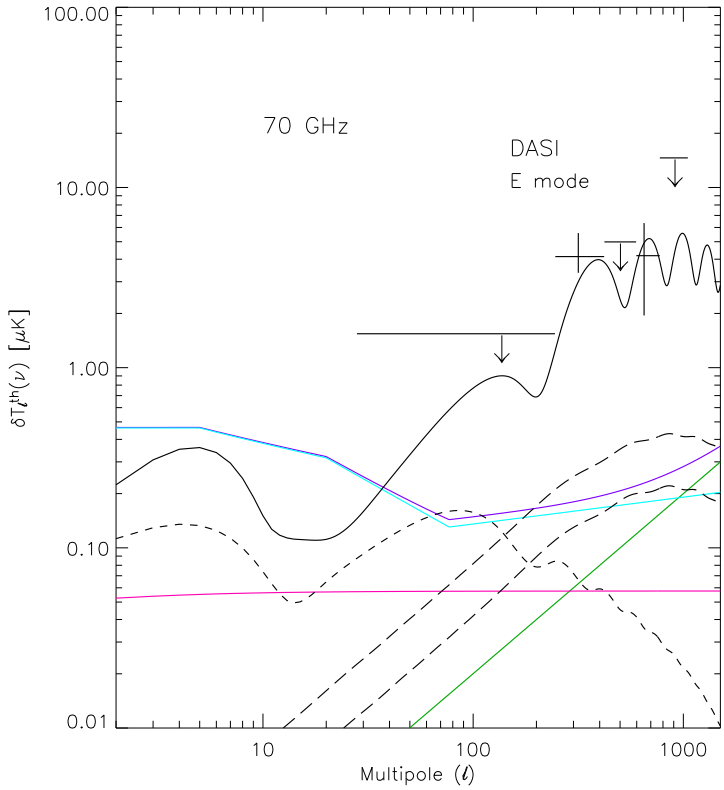

Figure 1.13: The effect of contamination of polarized synchrotron, discrete source and dust foreground to polarized CMB APS at 70 GHz. CMB lines as above; green line: discrete radio sources; blue line: synchrotron; red line: dust. Polarization detections and upper limits for the DASI experiment are also shown. Radio sources are detected/removed from foregrounds down to $S = 200$ mJy. (Courtesy of C. Burigana)

Chapter 2

Predictions for high-frequency radio surveys

2.1 Introduction

The new broad-band correlators for compact interferometric arrays and multi-beam receivers are beginning to enable large area surveys at high radio frequencies (≥ 15 GHz), hitherto impossible because the beam solid angle scales as ν^{-2} (assuming diffraction limited performance) so that surveying large areas of the sky becomes quickly impractical at high frequencies with conventional techniques. As described in Chapter 1, the high-frequency surveys will have a major impact on astrophysics.

As a new observational window opens up, it is useful to utilize models exploiting the available information to foretell which source populations the planned surveys will be able to detect as a function of their depth, which redshift range will these surveys explore, which information on formation and evolution of each source population will they be able to provide. Answering these questions is a key step towards an optimal planning of the surveys.

In this Chapter we will present a new model for canonical radio source populations, allowing for different evolutionary behaviours for two classes of flat-spectrum sources (flat-spectrum radio quasars and BL Lac objects) and two classes of steep-spectrum sources (FR I and FR II). The structure of the models is described in Section 2.2, while in Section 2.3 we present the data sets used to determine the parameters. In Section 2.4 we work out predictions of counts for several special source populations, including star-forming galaxies, extreme GPS sources, ADAF/ADIOS sources, Sunyaev-Zeldovich effects on scales from

clusters of galaxies to large galaxies, radio afterglows of γ-ray bursts. Our main conclusions are summarized and discussed in Section 2.5.

We have adopted a flat ΛCDM cosmology with $\Omega_\Lambda = 0.7$ and $H_0 = 65\,\mathrm{km\,s^{-1}\,Mpc^{-1}}$.

2.2 The evolutionary model for canonical radio source populations

We have considered different epoch-dependent luminosity functions (LFs) for two flat-spectrum [flat-spectrum radio quasars (FSRQs) and BL Lacertae type objects (BL Lacs)], and two steep-spectrum (FRI and FRII; Fanaroff & Riley 1974) radio source populations. In general, we have adopted LFs (in units of $\mathrm{Mpc}^{-3}\,(d\log L)^{-1}$) of the form

$$\Phi(L,z) = \frac{n_0}{(L/L_*)^a + (L/L_*)^b}\ . \tag{2.1}$$

The exception are FRI sources for which we have adopted the analytic expression given by Dunlop & Peacock (1990) for low-power steep-spectrum sources (their Eq. (9)).

Luminosity evolution was assumed for all sub-populations, except for FRIs which, following Dunlop & Peacock (1990), were assumed not to evolve. Only in the case of FSRQs enough information is available to look (although in a simplified manner) for evidences of a decline of the space density at high redshifts. For these sources, we have assumed:

$$L_{*,\mathrm{FSRQ}}(z) = L_*(0)\ 10^{[k_\mathrm{ev}\,z(2z_\mathrm{top}-z)]}\ . \tag{2.2}$$

For the other evolving populations we have used the simpler expression:

$$L_*(z) = L_*(0)\exp[k_\mathrm{ev}\tau(z)]\ , \tag{2.3}$$

where $\tau(z)$ is the look-back time in H_0^{-1} units.

We have allowed for the high-frequency spectral steepenings of steep-spectrum radio sources exploiting the quadratic fits by FR-type and radio power derived by Jackson & Wall (2001; their Table 2). Simple power-law spectra with index $\alpha_\mathrm{flat} = -0.1$ ($S_\nu \propto \nu^\alpha$) have been adopted for flat-spectrum sources.

The best fit values of the parameters were derived using the routine "amoeba" (Press et al. 1992) exploiting the downhill simplex method in multidimensions. The fitted data sets are described below and the parameter values are listed in Table 2.1.

Table 2.1: Best fit values of the parameters of the evolutionary models for canonical radio sources. Luminosities $L_\star$ are in units of erg s^{-1} Hz^{-1}.

Source type	luminosity function				evolution	
	$\log n_0(\mathrm{Mpc}^{-3})$	a	b	$\log L_\star$	$k_{\rm ev}$	$z_{\rm top}$
FSRQ	-8.990	0.691	3.245	34.033	0.224	2.248
BL Lac	-7.814	0.929	1.302	32.715	0.765	
FR II	-8.387	1.163	4.394	33.480	5.181	

2.3 Data sets

2.3.1 The first year WMAP catalog of extragalactic sources

As illustrated by Fig. 2.1, the first-year WMAP catalog of extragalactic sources appears to be complete to $S_K \simeq 1.25$ Jy in the K-band (centered at 22.8 GHz). Their distribution as a function of Galactic latitude (Fig. 2.2) shows a clear deficit at $b < 10°$. Removing the 4 sources in this region, we are left with 155 sources above the completeness limit, over an area of 10.4 sr. For all these sources we have determined the 4.85–22.8 GHz spectral index, using the 4.85 flux densities from the GB6 (Gregory et al. 1996) or PMN (available at http://www.parkes.atnf.csiro.au/) catalogs. We have searched the NED and VizieR on-line databases for optical identifications and redshifts. The search yielded 91 flat-spectrum radio quasars (FSRQs), 28 BL Lacs, 17 unclassified flat-spectrum sources and 19 steep-spectrum sources (we define as flat-spectrum sources those with spectral index $\alpha > -0.5$, $S_\nu \propto \nu^\alpha$). The K-band counts of the complete WMAP sub-sample of 155 sources and the counts of sources identified as FSRQs and BL Lacs, are given, with their errors, in Table 2.2.

Redshift measurements were found for 86 FSRQs, 27 BL Lacs, 9 unclassified flat-spectrum sources and for 18 steep-spectrum sources. The redshift distribution of FSRQs and BL Lacs are given in Tables 2.3 and 2.4.

The redshift distributions and the counts of FSRQs (Figs. 2.3 and 2.4) and of BL Lacs (Fig. 2.5) have been corrected by a factor of $(1 + 17/119)$ to include the 17 unclassified flat-spectrum sources, partitioned among the two populations in proportion to the number of classified sources in each population. In computing the model redshift distributions, the surveyed area has been decreased by a factor of 0.94 in the case of FSRQs and of 0.96 in the case of BL Lacs, to allow for the incompleteness of redshift measurements. Poisson

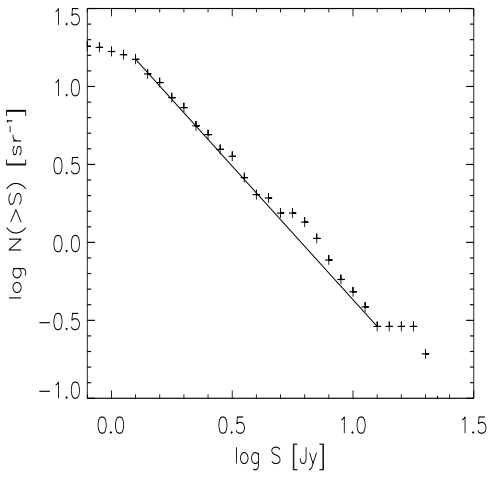

Figure 2.1: Integral counts of extragalactic sources in the WMAP K-band (centred at 22.8 GHz).

errors (Gehrels 1986) have been adopted both for the counts and the redshift distributions.

2.3.2 The Parkes quarter-Jansky flat-spectrum sample

The sample (Jackson et al. 2002) comprises 878 sources with spectral index $\alpha^{5\mathrm{GHz}}_{2.7\mathrm{GHz}} \geq -0.4$ ($S_\nu \propto \nu^\alpha$), selected from several surveys to different depths at 2.7 GHz. The catalog compiled by Jackson et al. (2002) includes optical identifications and redshifts for most of the sources; 827 are compact extragalactic radio sources, 38 have either extended radio structure or are Galactic objects, 13 are unidentified (4 of which because of obscuration by Galactic stars). Of the 827 compact extragalactic radio sources, 624 are FSRQs, 54 are BL Lacs and 149 flat-spectrum radio sources. As in the case of WMAP data, we have subdivided the latter plus the unidentified sources among the FSRQs and the BL Lacs, in proportion to the fraction of classified sources belonging to each population, i.e. we increase the counts of both populations by a factor $1 + (149 + 13)/(624 + 54)$.

While the full sample has been used to derive the differential source counts (shown in Fig. 2.6 and Table 2.5 for FSRQs and Fig. 2.7 and Table 2.6 for BL Lacs), for the analysis of the redshift distribution we have defined a complete sub-sample aiming at maximizing the fraction of sources with measured redshift. To this end, we have first focussed on areas surveyed to at least 0.25 mJy, keeping only sources brighter than this limit, for a total of 618 sources. Of these, 437 are FSRQs, 360 of which (82%) have measured redshift, 47

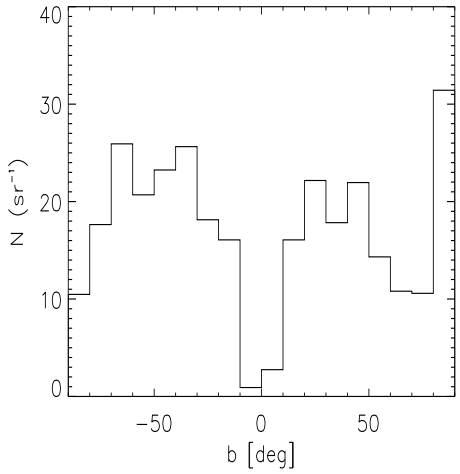

Figure 2.2: Surface density of WMAP extragalactic sources as a function of Galactic latitude.

Table 2.2: Total K-band counts of the complete WMAP sub-sample (Col. 4), and the counts of FSRQ sub-sample (Col. 7) and BL Lac sub-sample (Col. 10) in logarithmic flux density bins (Cols. 1 and 2). The number of objects per bin in the complete sub-sample are given in Col. 3. $\sigma-$ and $\sigma+$ are the lower and upper error bars of the counts, respectively. The source count units are $\mathrm{sr}^{-1}(\log S)^{-1}$.

(1) $\log\ S_{\min}$	(2) $\log\ S_{\max}$	(3) N	(4) n(S)	(5) $\sigma-$	(6) $\sigma+$	(7) n(S)	(8) $\sigma-$	(9) $\sigma+$	(10) n(S)	(11) $\sigma-$	(12) $\sigma+$
0.10	0.15	30	57.7	10.5	12.6	38.9	9.1	11.5	8.8	4.2	7.0
0.15	0.20	15	28.8	7.4	9.5	23.8	7.1	9.6	4.4	2.8	5.8
0.20	0.25	22	42.3	8.9	11.1	28.1	7.7	10.2	6.6	3.6	6.4
0.25	0.30	12	23.1	6.6	8.8	8.7	4.1	6.8	2.2	1.8	5.1
0.30	0.35	18	34.6	8.1	10.2	21.6	6.7	9.2	4.4	2.8	5.8
0.35	0.40	7	13.5	5.0	7.3	8.7	4.1	6.8	6.6	3.6	6.4
0.40	0.50	14	13.5	3.6	4.6	8.7	3.0	4.3	5.5	2.4	3.7
0.50	0.60	16	15.4	3.8	4.9	13.0	3.7	4.9	2.2	1.4	2.9
0.60	0.70	5	4.9	2.1	3.3	5.4	2.3	3.7	0.0	0.0	2.0
0.70	0.90	8	3.8	1.3	1.9	1.1	0.7	1.4	2.7	1.2	1.9

Table 2.3: Redshift distribution of FSRQs in the WMAP sample. N_z is the source number in the redshift bin [log $z_{\rm min}$, log $z_{\rm max}$]. $\sigma-$ and $\sigma+$ are the lower and upper error bars, respectively.

log $z_{\rm min}$	log $z_{\rm max}$	N_z	$\sigma-$	$\sigma+$
-0.900	-0.800	1.143	0.945	2.629
-0.800	-0.700	1.143	0.945	2.629
-0.700	-0.600	1.143	0.945	2.629
-0.600	-0.500	1.143	0.945	2.629
-0.500	-0.400	3.429	1.866	3.335
-0.400	-0.300	4.571	2.187	3.615
-0.300	-0.200	8.000	2.950	4.309
-0.200	-0.100	16.000	4.229	5.520
-0.100	0.000	13.714	3.903	5.223
0.000	0.100	13.714	3.903	5.223
0.100	0.200	11.429	3.553	4.880
0.200	0.300	13.714	3.903	5.223
0.300	0.400	3.429	1.866	3.335
0.400	0.500	4.571	2.187	3.615
0.500	0.600	1.143	0.945	2.629

Table 2.4: Redshift distribution of BL Lacs in the WMAP sample. N_z is the source number in the redshift bin [log $z_{\rm min}$, log $z_{\rm max}$]. $\sigma-$ and $\sigma+$ are the lower and upper error bars, respectively.

log $z_{\rm min}$	log $z_{\rm max}$	N_z	$\sigma-$	$\sigma+$
-1.200	-1.100	1.143	0.945	2.629
-1.100	-1.000	0.000	0.000	2.104
-1.000	-0.900	0.000	0.000	2.104
-0.900	-0.800	0.000	0.000	2.104
-0.800	-0.700	0.000	0.000	2.104
-0.700	-0.600	0.000	0.000	2.104
-0.600	-0.500	3.429	1.866	3.335
-0.500	-0.400	1.143	0.945	2.629
-0.400	-0.300	1.143	0.945	2.629
-0.300	-0.200	5.714	2.469	3.865
-0.200	-0.100	2.286	1.477	3.015
-0.100	0.000	5.714	2.469	3.865
0.000	0.100	2.286	1.477	3.015
0.100	0.200	4.571	2.187	3.615

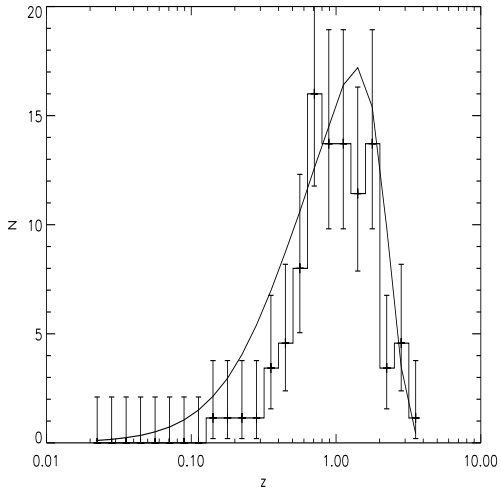

Figure 2.3: Redshift distribution of WMAP FSRQs (histogram) compared with the best-fit model (solid line).

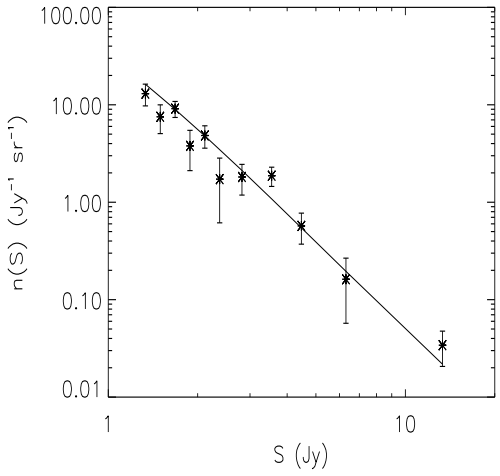

Figure 2.4: Differential counts of WMAP FSRQs compared with the best-fit model (solid line).

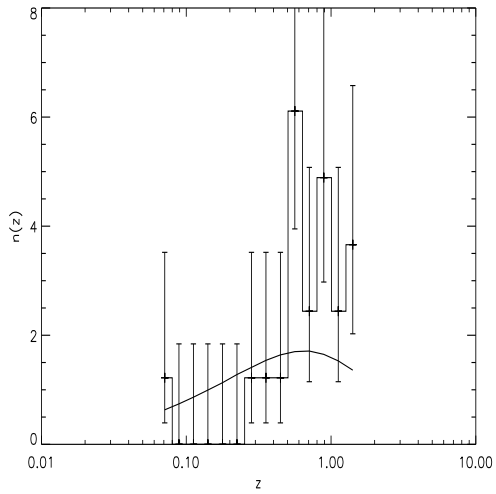

Figure 2.5: Redshift distribution of WMAP BL Lacs (histogram) compared with the best-fit model (solid line).

are BL Lacs, only 10 of which (21%) have measured redshift, and 111 are flat-spectrum galaxies (32, i.e. 29%, with redshift). Clearly, only in the case of FSRQs the fraction of sources with measured redshifts is large enough for a meaningful redshift distribution to be derived. Further restricting the sample to $\delta > -50^\circ$ (Fig. 2.8), we are left with 370 FSRQs, 345 of which (93%) with measured redshift, 95 sources classified as galaxies, and 2 unidentified sources. The redshift distribution of FSRQs for this sub-sample is thus well defined (Fig. 2.9 and Table 2.7). As in the case of the counts, we have corrected the redshift distribution by a factor of $1 + (95 + 2)/(370 + 47)$ to allow for a fraction of flat-spectrum galaxies and unidentified sources proportional to the ratio FSRQ/(FSRQ+BL Lacs).

2.3.3 The Kühr 1 Jy sample

The sample (Kühr et al. 1981) comprises 518 sources to a 5 GHz flux density limit of 1 Jy, over an area of 9.811 sr. Based on the catalogued spectral indices, 299 sources are flat-spectrum ($\alpha > -0.5$, $S_\nu \propto \nu^\alpha$) and 219 are steep-spectrum. The former population includes 212 FSRQs, 200 of which (94%) have measured redshift, 26 BL Lacs (20 of which, 77%, with measured redshift, and 61 either classified as galaxies or missing a morphological classification. As before, we have distributed the latter sources among FSRQs and BL Lacs, thus increasing the counts of both types by a factor of $1 + 61/(212 + 26)$. The fits to the

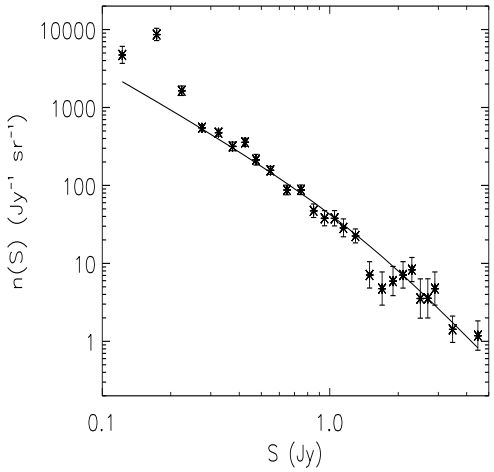

Figure 2.6: Counts of FSRQs in the Parkes quarter-Jy sample compared with the best-fit model (solid line).

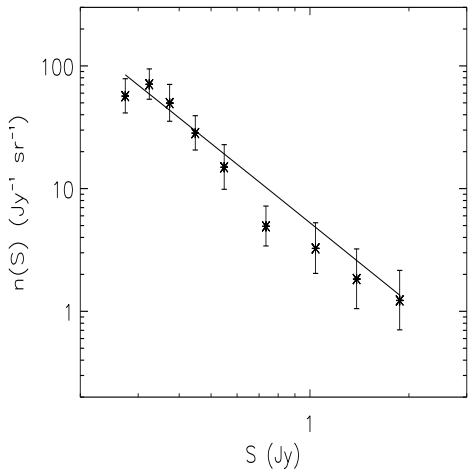

Figure 2.7: Counts of BL Lac objects in the Parkes quarter-Jy sample compared with the best-fit model (solid line).

Table 2.5: Differential source counts for the FSRQs of the quarter-Jy Parkes sample. In Cols. (1) and (2) are flux density bin extrema; in Col. (3) the survey effective area in that flux density bin; in Col. (4) the source number per flux density; in Col. (5) the counts per steradian and in Cols. (6) and (7) the lower and upper error bars in the counts.

(1) log $S_{\rm min}$ (Jy)	(2) log $S_{\rm max}$ (Jy)	(3) $A_{\rm eff}$ (sr)	(4) N	(5) dN/sr^{-1}	(6) $\sigma-$	(7) $\sigma+$
-1.000	-0.824	0.0687	13	189.229	51.805	68.413
-0.824	-0.699	0.0687	24	349.345	70.742	86.900
-0.699	-0.602	0.5784	38	65.698	10.615	12.483
-0.602	-0.523	3.6013	80	22.214	2.480	2.771
-0.523	-0.456	3.6013	69	19.160	2.301	2.596
-0.456	-0.398	3.6013	46	12.773	1.877	2.174
-0.398	-0.347	3.6013	52	14.439	1.995	2.292
-0.347	-0.301	3.6013	31	8.608	1.538	1.841
-0.301	-0.222	4.2794	54	12.619	1.710	1.960
-0.222	-0.155	5.2329	37	7.071	1.158	1.364
-0.155	-0.097	5.2329	37	7.071	1.158	1.364
-0.097	-0.046	5.2329	20	3.822	0.847	1.061
-0.046	0.000	5.2329	16	3.058	0.757	0.971
0.000	0.041	5.2329	16	3.058	0.757	0.971
0.041	0.079	5.2329	12	2.293	0.653	0.871
0.079	0.146	5.2329	19	3.631	0.826	1.040
0.146	0.204	5.2329	6	1.147	0.455	0.685
0.204	0.255	5.2329	4	0.764	0.366	0.604
0.255	0.301	5.2329	5	0.955	0.413	0.646
0.301	0.342	5.2329	6	1.147	0.455	0.685
0.342	0.380	5.2329	7	1.338	0.493	0.720
0.380	0.415	5.2329	3	0.573	0.312	0.558
0.415	0.448	5.2329	3	0.573	0.312	0.558
0.448	0.477	5.2329	4	0.764	0.366	0.604
0.477	0.602	5.2329	6	1.146	0.455	0.685
0.602	0.699	5.2329	5	0.955	0.413	0.646
0.699	1.653	5.2329	7	1.338	0.493	0.720

Table 2.6: Differential source counts for the BL Lacs of the quarter-Jy Parkes sample. In Cols. (1) and (2) are flux density bin extrema; in Col. (3) the survey effective area in that flux density bin; in Col. (4) the source number per flux density; in Col. (5) the counts per steradian and in Cols. (6) and (7) the lower and upper error bars in the counts.

(1) log $S_{\rm min}$ (Jy)	(2) log $S_{\rm max}$ (Jy)	(3) $A_{\rm eff}$ (sr)	(4) N	(5) dN/sr^{-1}	(6) $\sigma-$	(7) $\sigma+$
-0.602	-0.523	3.6013	8	2.221	0.769	1.097
-0.523	-0.456	3.6013	10	2.777	0.863	1.186
-0.456	-0.398	3.6013	7	1.944	0.717	1.047
-0.398	-0.301	3.6013	8	2.221	0.769	1.097
-0.301	-0.222	4.2794	5	1.168	0.505	0.790
-0.222	-0.046	5.2329	6	1.147	0.455	0.685
-0.046	0.079	5.2329	4	0.764	0.366	0.604
0.079	0.204	5.2329	3	0.573	0.312	0.558
0.204	0.342	5.2329	3	0.573	0.312	0.558

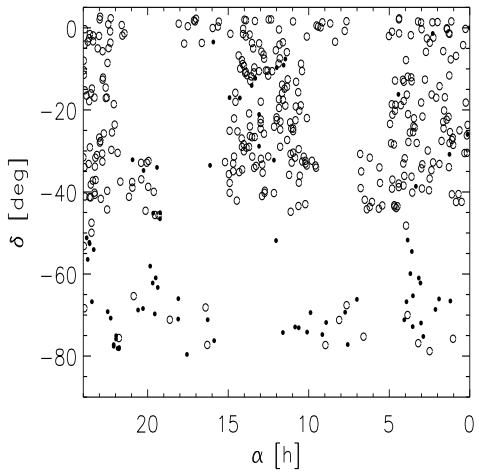

Figure 2.8: Sky map of the FSRQs in the quarter-Jy sample. Open circles represent sources with measured redshift, the bullets are sources without redshift measurements.

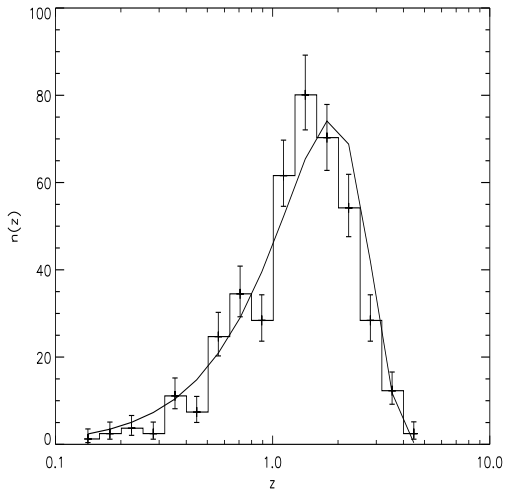

Figure 2.9: Redshift distribution of FSRQs in the Parkes quarter-Jy sample (histogram) compared with the best-fit model (solid line).

Table 2.7: Redshift distribution of FSRQs in the quarter-Jy Parkes sample. N_z is the source number in the redshift bin $[\log\ z_{\rm min}, \log\ z_{\rm max}]$. $\sigma-$ and $\sigma+$ are the lower and upper error bars, respectively.

$\log\ z_{\rm min}$	$\log\ z_{\rm max}$	N_z	$\sigma-$	$\sigma+$
-0.90	-0.80	1	0.827	2.300
-0.80	-0.70	2	1.292	2.638
-0.70	-0.60	3	1.633	2.918
-0.60	-0.50	2	1.292	2.638
-0.50	-0.40	9	2.943	4.110
-0.40	-0.30	6	2.380	3.584
-0.30	-0.20	20	4.430	5.550
-0.20	-0.10	28	5.260	6.350
-0.10	0.00	23	4.760	5.870
0.00	0.10	50	7.050	8.120
0.10	0.20	65	8.035	9.100
0.20	0.30	57	7.519	7.589
0.30	0.40	44	6.610	7.680
0.40	0.50	23	4.760	5.870
0.50	0.60	10	3.109	4.270
0.60	0.70	2	1.292	2.638

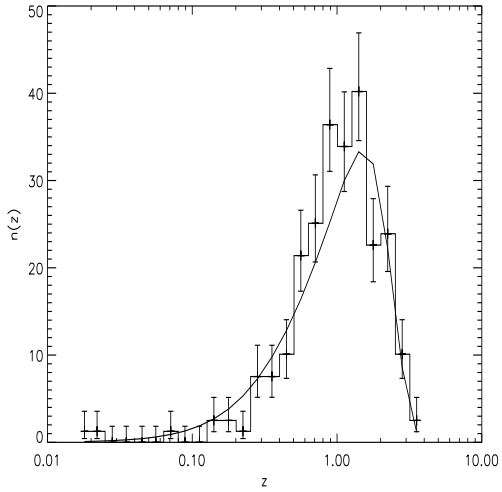

Figure 2.10: Redshift distribution of FSRQs in the Kühr et al. (1981) sample (histogram) compared with the best-fit model (solid line).

redshift distribution are shown in Fig. 2.10 and Table 2.8 for FSRQs and Fig. 2.11 and Table 2.9 for BL Lacs. The steep-spectrum sources, 178 of which (81%) have measured redshift (Fig. 2.12 and Table 2.10), have all been taken as FRII.

2.3.4 Other data sets

Furthermore, we have fitted the 5 GHz counts (Fig. 2.13) by Gregory & Condon (1991) and Pauliny-Toth et al. (1978a,b), the 15 GHz 9C counts plus the 18 GHz ATCA counts (Fig. 2.14) by Waldram et al. (2003) and Ricci et al. (2004b), respectively, and the ATCA 18 GHz counts (Fig. 2.15) of flat-spectrum sources (Ricci et al. 2004b).

In our scheme, blazars (FSRQs plus BL Lacs) account for the entire population of flat-spectrum radio sources. We thus require that the sum of their local luminosity functions matches the estimates of the local luminosity functions of flat-spectrum sources by Peacock (1985) and Toffolatti et al. (1987). The fit is shown in Fig. 2.16.

2.4 Special source populations

2.4.1 Star-forming galaxies

The radio emission of galaxies correlates with their star-formation rate, as demonstrated by the well established tight correlation with far-IR emission (Helou et al. 1985; Gavazzi et

Table 2.8: Redshift distribution of FSRQs in the Kühr sample. N_z is the source number in each redshift bin [log $z_{\rm min}$, log $z_{\rm max}$]. $\sigma-$ and $\sigma+$ are the lower and upper error bars, respectively. Effective counts are multiplied by a factor 1.26 to take incompleteness in account.

z	log $z_{\rm min}$	log $z_{\rm max}$	N_z	$\sigma-$	$\sigma+$
0.018	-1.70	-1.60	1	0.827	2.300
0.022	-1.60	-1.50	1	0.827	2.300
0.028	-1.50	-1.40	0	0.000	1.841
0.035	-1.40	-1.30	0	0.000	1.841
0.045	-1.30	-1.20	0	0.000	1.841
0.056	-1.20	-1.10	0	0.000	1.841
0.071	-1.10	-1.00	1	0.827	2.300
0.089	-1.00	-0.90	0	0.000	1.841
0.112	-0.90	-0.80	0	0.000	1.841
0.141	-0.80	-0.70	2	1.292	2.638
0.178	-0.70	-0.60	2	1.292	2.638
0.224	-0.60	-0.50	1	0.827	2.300
0.282	-0.50	-0.40	6	2.380	3.584
0.355	-0.40	-0.30	6	2.380	3.584
0.447	-0.30	-0.20	8	2.768	3.950
0.562	-0.20	-0.10	17	4.080	5.200
0.708	-0.10	0.00	20	4.430	5.550
0.891	0.00	0.10	29	5.350	6.450
1.122	0.10	0.20	27	5.160	6.260
1.413	0.20	0.30	32	5.630	6.720
1.778	0.30	0.40	18	4.200	5.320
2.239	0.40	0.50	19	4.320	5.440
2.818	0.50	0.60	8	2.768	3.950
3.548	0.60	0.70	2	1.292	2.638

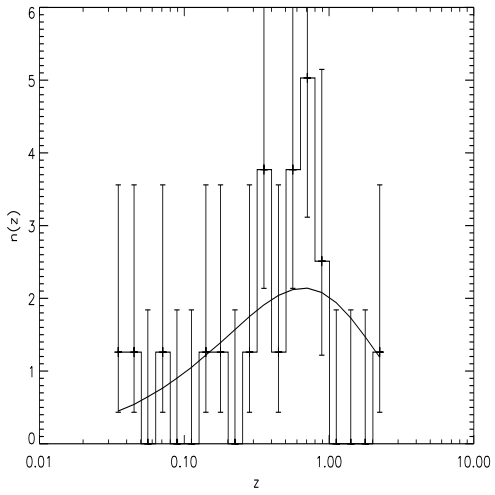

Figure 2.11: Redshift distribution of BL Lacs in the Kühr et al. (1981) sample (histogram) compared with the best-fit model (solid line).

Table 2.9: Redshift distribution of BL Lacs in the Kühr sample. N_z is the source number in each redshift bin [log $z_{\rm min}$, log $z_{\rm max}$]. $\sigma-$ and $\sigma+$ are the lower and upper error bars, respectively. Effective counts are multiplied by a factor 1.26 to take incompleteness in account.

z	log $z_{\rm min}$	log $z_{\rm max}$	N_z	$\sigma-$	$\sigma+$
0.035	-1.50	-1.40	1	0.827	2.300
0.045	-1.40	-1.30	1	0.827	2.300
0.056	-1.30	-1.20	0	0.000	1.841
0.071	-1.20	-1.10	1	0.827	2.300
0.089	-1.10	-1.00	0	0.000	1.841
0.112	-1.00	-0.90	0	0.000	1.841
0.141	-0.90	-0.80	1	0.827	2.300
0.178	-0.80	-0.70	1	0.827	2.300
0.224	-0.70	-0.60	0	0.000	1.841
0.282	-0.60	-0.50	1	0.827	2.300
0.355	-0.50	-0.40	3	1.633	2.918
0.447	-0.40	-0.30	1	0.827	2.300
0.562	-0.30	-0.20	3	1.633	2.918
0.708	-0.20	-0.10	4	1.914	3.163
0.891	-0.10	0.00	2	1.292	2.638
1.122	0.00	0.10	0	0.000	1.841
1.413	0.10	0.20	0	0.000	1.841
1.778	0.20	0.30	0	0.000	1.841
2.239	0.30	0.40	1	0.827	2.300

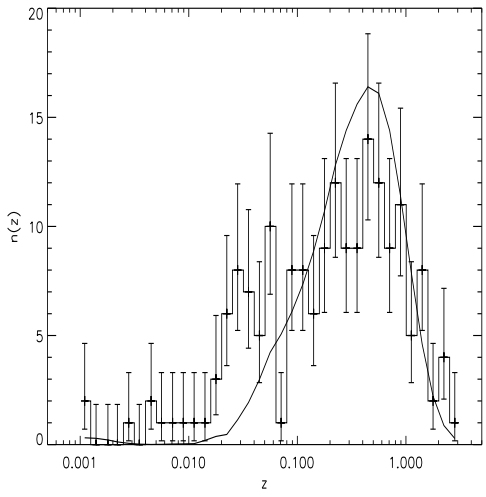

Figure 2.12: Redshift distribution of steep-spectrum sources in the Kühr et al. (1981) sample (histogram) compared with the best-fit model (solid line).

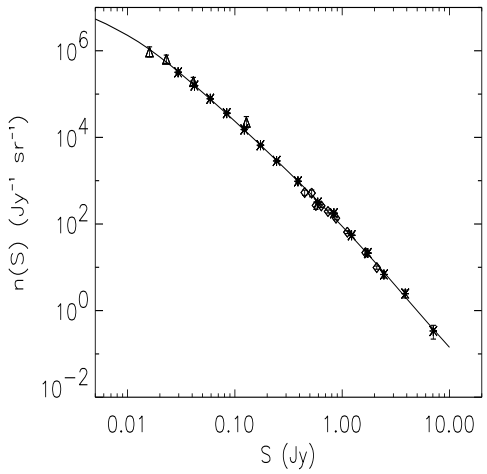

Figure 2.13: Differential counts at 5 GHz compared with the best-fit model (solid line). Data from Gregory & Condon (1991, asterisks) and Pauliny-Toth et al. (1978a, diamonds; 1978b, triangles).

Table 2.10: Redshift distribution of steep-spectrum sources in Kühr sample. N_z is the source number in each redshift bin [log $z_{\rm min}$, log $z_{\rm max}$]. $\sigma-$ and $\sigma+$ are the lower and upper error bars, respectively.

z	log $z_{\rm min}$	log $z_{\rm max}$	N_z	$\sigma-$	$\sigma+$
0.0011	-3.00	-2.90	2	1.2920	2.6380
0.0014	-2.90	-2.80	0	0.0000	1.8410
0.0018	-2.80	-2.70	0	0.0000	1.8410
0.0022	-2.70	-2.60	0	0.0000	1.8410
0.0028	-2.60	-2.50	1	0.8270	2.3000
0.0035	-2.50	-2.40	0	0.0000	1.8410
0.0045	-2.40	-2.30	2	1.2920	2.6380
0.0056	-2.30	-2.20	1	0.8270	2.3000
0.0071	-2.20	-2.10	1	0.8270	2.3000
0.0089	-2.10	-2.00	1	0.8270	2.3000
0.0112	-2.00	-1.90	1	0.8270	2.3000
0.0141	-1.90	-1.80	1	0.8270	2.3000
0.0178	-1.80	-1.70	3	1.6330	2.9180
0.0224	-1.70	-1.60	6	2.3800	3.5840
0.0282	-1.60	-1.50	8	2.7680	3.9500
0.0355	-1.50	-1.40	7	2.5810	3.7700
0.0447	-1.40	-1.30	5	2.1600	3.3820
0.0562	-1.30	-1.20	10	3.1090	4.2700
0.0709	-1.20	-1.10	1	0.8270	2.3000
0.0891	-1.10	-1.00	8	2.7680	3.9500
0.1122	-1.00	-0.90	8	2.7680	3.9500
0.1413	-0.90	-0.80	6	2.3800	3.5840
0.1778	-0.80	-0.70	9	2.9430	4.1100
0.2239	-0.70	-0.60	12	3.4150	4.5700
0.2818	-0.60	-0.50	9	2.9430	4.1100
0.3548	-0.50	-0.40	9	2.9430	4.1100
0.4467	-0.40	-0.30	14	3.7000	4.8300
0.5623	-0.30	-0.20	12	3.4150	4.5700
0.7079	-0.20	-0.10	9	2.9430	4.1100
0.8913	-0.10	0.00	11	3.2660	4.4200
1.1220	0.00	0.10	5	2.1600	3.3820
1.4125	0.10	0.20	8	2.7680	3.9500
1.7783	0.20	0.30	2	1.2920	2.6380
2.2387	0.30	0.40	4	1.9140	3.1630
2.8184	0.40	0.50	1	0.8270	2.3000

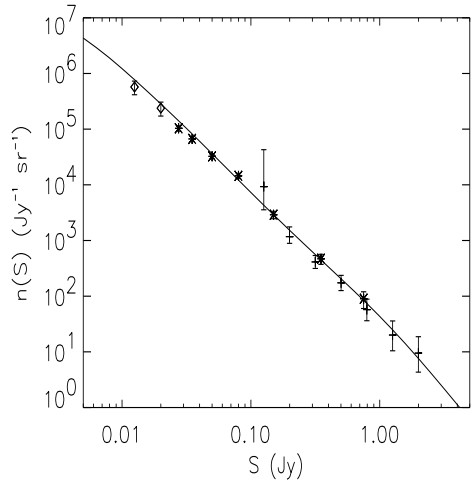

Figure 2.14: Comparison of the model (solid line) with the differential 15 GHz counts from the main survey (asterisks) and the deeper survey (diamonds) by Waldram et al. (2003) and with total differential counts (crosses) at 18 GHz by Ricci et al. (2004b).

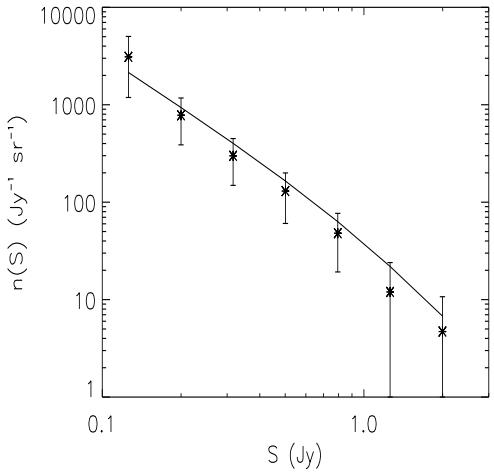

Figure 2.15: Differential counts (asterisks) at 18 GHz of flat-spectrum sources by Ricci et al. (2004b) compared with the best-fit model (solid line).

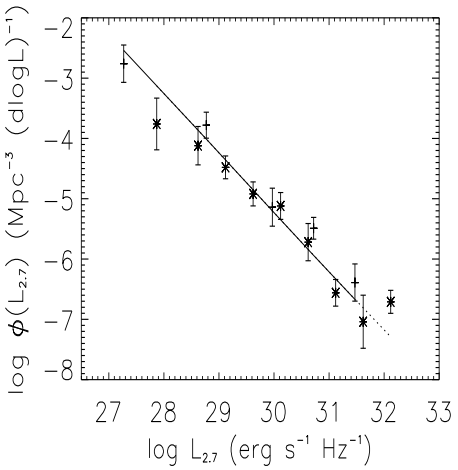

Figure 2.16: Local luminosity functions at 2.7 GHz by Peacock (1985) (crosses) and Toffolatti et al. (1987) (asterisks) compared with the best-fit model (solid line).

al. 1986; Condon 1992; Garrett 2002; Morganti et al. 2004). The cross-over between synchrotron plus free-free emission, prevailing at cm wavelengths, and thermal dust emission generally occurs at $\lambda \simeq 2$–3 mm, so that at frequencies of tens of GHz there are contributions from both components, the former being associated to normal late-type and starburst galaxies at low to moderate redshifts, the latter to the high-redshift population detected by sub-mm surveys ("SCUBA galaxies").

Following Granato et al. (2001, 2004) we interpret "SCUBA galaxies" as proto-spheroidal galaxies in the process of forming most of their stars. Their epoch-dependent luminosity function is computed using the physical model by Granato et al. (2004), which describes the star-formation and chemical enrichment histories and, interfaced with the code GRASIL (Silva et al. 1998), yields the spectrophotometric evolution from radio to X-ray wavelengths. The values of GRASIL parameters were determined by Silva et al. (2004) comparing the model predictions with a broad variety of observational data.

Normal late-type and starburst galaxies are dealt with in a more phenomenological manner, following Silva et al. (2004). Briefly, we adopted the 60 μm local luminosity functions of "warm" and "cold" galaxies (based on IRAS colors), determined by Saunders et al. (1990), for starburst and late-type galaxies, respectively. The local luminosity functions were cut off at $L_{60\mu\mathrm{m}} = 2 \times 10^{32}$ erg s^{-1} Hz^{-1}. Extrapolations to other wavelengths were made using GRASIL spectral energy distributions fitting the data on

NGC 6090 (for starburst galaxies) and NGC 6946 (for late-type galaxies).

A density and luminosity evolution model ($LF[L(z), z] = LF[L(z)/(1+z)^{2.5}, z = 0] \times (1+z)^{3.5}$) was adopted for starburst galaxies, while a mild pure luminosity evolution ($L(z) = L(0)\,(1+z)^{1.5}$) was assumed for normal late-type galaxies. These evolutionary laws were applied up to $z = 1$. The luminosity functions were then kept to the (comoving) values they have at $z = 1$ up to a redshift cut-off $z_{\rm cut} = 1.5$.

2.4.2 Extreme GHz peaked spectrum (GPS) sources

A class of sources that is expected to come out in high-frequency surveys is that of extreme GHz Peaked Spectrum (GPS) or very high frequency peakers. GPS sources are extensively described in Section 1.1.2.

The models by De Zotti et al. (2000) imply that extreme GPS quasars, peaking at $\nu > 20\,$GHz, comprise a quite substantial fraction of bright ($S > 1\,$Jy) radio sources in the WMAP survey at $\nu \simeq 20\,$GHz, while GPS galaxies with similar $\nu_{\rm peak}$ should be about 10 times less numerous. Although the number of *candidate* GPS quasars in the WMAP survey is consistent with that expected from the models, when data at additional frequencies (Trushkin 2003) are taken into account such candidates look more blazars caught during a flare optically thick up to high frequencies. Furthermore, Tinti et al. (2004) have shown that most, perhaps two thirds, of the quasars in the sample of High Frequency Peaker candidates selected by Dallacasa et al. (2000) are likely blazars, while 9 out of 10 candidates classified as galaxies are consistent with being truly young sources.

In Figs. 2.17 and 2.18 we have provisionally plotted (dashed line in the upper right-hand panel) the predictions of the models by De Zotti et al. (2000) with a maximum intrinsic peak frequency $\nu_{p,i} = 200\,$GHz, decreasing by a factor of 3 the contribution of GPS quasars.

Large-area high-frequency surveys, coupled with follow-up simultaneous multi-frequency observations of GPS candidates, would be essential to assess the evolutionary properties of this population.

2.4.3 Late stages of AGN evolution

High radio frequency observations are also crucial to investigate late stages of the AGN evolution, characterized by low radiation/accretion efficiency. A review on the

characteristics of Advection Dominated Accretion Flows (ADAFs) and ADIOS (Advection Dominated Input Output Solutions) is provided in Section 1.1.3.

We have estimated the counts yielded by these low radiative efficiency flows (LREF) following Perna & Di Matteo (2000), i.e. we have taken the number density of such sources to be given, as a function of redshift, by their Eq. (5), with a cut-off at $z = 1$, and have used the emission spectrum corresponding to $p = 0.2$ in their Fig. 1, which corresponds to the upper end of the range of observed luminosities. The counts we obtain, shown by the dotted line in the upper right-hand panel of Figs. 2.17 and 2.18, are about a factor of ten below the estimates by Perna & Di Matteo (2000). We do not understand the reason for this strong discrepancy. We note however, that the conclusion of these Authors that the 30 GHz LREF counts can be comparable or even higher than those of sources known from low-frequency surveys is ruled out by the results of the Ryle telescope, ATCA and WMAP surveys.

2.4.4 Sunyaev-Zeldovich effects in galaxy clusters

The Sunyaev-Zel'dovich effect (Sunyaev & Zeldovich 1972) is caused by the inverse Compton scatter of CMB photons off the hot and diffuse electron gas trapped in the potential well of a galaxy cluster, and responsible for their X-ray emission. The intensity change across a cluster is give by:

$$\Delta I_\nu = 2\frac{(kT_{\rm CMB})^3}{(hc)^2} y g(x) \tag{2.4}$$

where $T_{\rm CMB}$ is the CMB temperature and $x = h\nu/kT_{\rm CMB}$. The spectral form of this "thermal effect" is described by the function $g(x) = x^4 \mathrm{e}^x [x \cdot \coth(x/2) - 4]/(\mathrm{e}^x - 1)^2$, which is negative (positive) at values of x smaller (larger) than $x_0 = 3.83$, corresponding to a critical frequency $\nu_0 = 217$ GHz. The Comptonization parameter is

$$y = \int \frac{kT_e}{mc^2} n_e \sigma_T dl, \tag{2.5}$$

where n_e and T_e are the electron density and temperature, respectively, σ_T is the Thomson cross section, and the integral is over a line of sight through the cluster. With respect to the incident radiation field, the change of the CMB intensity across a cluster can be viewed as a net flux emanating from the cluster which is given by the integral of intensity change over the solid angle subtended by the cluster:

$$\Delta F_\nu = \int \Delta I_\nu d\Omega \propto Y \equiv \int y d\Omega \tag{2.6}$$

The parameter Y in Eq. (2.6), called integrated Y-flux, is proportional to the gas-mass-weighted electron temperature $\langle T_e \rangle$ and to the gas mass $M_g = f_g M$, being M the cluster mass:

$$Y \propto f_g \langle T_e \rangle M \ . \tag{2.7}$$

Recent X-ray *Chandra* observations show that for massive clusters $f_g = 0.113 \pm 0.005$, independently of the cluster redshift (Allen et al. 2002). Simple scaling laws are used to derive, under the hydrostatic equilibrium hypothesis, the relation between the mass and the temperature of a cluster (see, e.g., Barbosa et al. 1996; Colafrancesco et al. 1997; Bryan & Norman 1998, and references therein):

$$T(M,z) = T_{15} h^{2/3} \left[\frac{\Omega_0 \Delta_c(\Omega_0, z)}{180} \right]^{1/3} \left(\frac{M}{M_{15}} \right)^{2/3} (1+z), \tag{2.8}$$

where Δ_c is the non-linear density contrast of a cluster that collapsed at redshift z and T_{15} is the temperature of a cluster of mass $M_{15} = 10^{15} h^{-1} M_\odot$ which collapses today. We calculate Δ_c using the equations reported in the appendix of Colafrancesco et al. (1997): the $M - T$ relation calculated in this way is perfectly consistent with Eq. (9) of Bryan & Norman (1998). Both simulations and observations indicate that temperatures of massive clusters follow quite well the relationship with mass and redshift expressed by Eq. (2.8) (see, e.g., Ettori et al. 2004 and references therein). Nevertheless, there is still some discussion on the exact value of T_{15}, whose values range from 6.6 keV to 8.8 keV (see, e.g., Pierpaoli et al. 2001, and references therein). This represents, at the moment, the largest source of uncertainty for the normalization of the power spectrum of the matter density fluctuations $P(k) \equiv |\delta_k|^2$ inferred from the observed cluster X-ray temperature function (XTF). Such normalization is usually given in term of the value of σ_8, i.e. the variance of the density perturbation $\sigma^2(R,z) \propto \int_o^\infty k^3 P(k,z) W^2(kR) dk/k$, where $W(kR)$ is the window function corresponding to the smoothing of the density field (see, e.g., Peebles 1993), on the scale of $R = 8h^{-1}$Mpc. Lower values of T_{15} result in higher values of σ_8 and viceversa (see, e.g., Ikebe et al. 2002; Pierpaoli et al. 2003). Here we choose $T_{15} = 7.75\,$keV, consistent with the simulations of Eke et al. (1998), and $\sigma_8 = 0.85$ yielding an XTF consistent with the observed one (see, e.g., Pierpaoli et al. 2003). The number counts for SZ clusters are then given by:

$$N(> \overline{\Delta F_\nu}) = \int \frac{dV}{dz} dz \int_{\overline{M(\Delta F_\nu, z)}} dM N(M,z), \tag{2.9}$$

where $N(M,z)$ is the cluster mass function and the lower bound of the mass integral is determined by requiring that clusters of mass $M > \overline{M}$ at redshift z have SZ fluxes greater than $\overline{\Delta F_\nu}$ (for details see, e.g., Colafrancesco et al. 1997). Here we adopt the mass function of Sheth et al. (2001):

$$N(M,z)dM = \sqrt{\frac{2\,a\,A^2}{\pi}}\rho_0\frac{1}{M^2}\left[1+\left(\frac{\sigma(M,z)}{\sqrt{a}\delta_c}\right)^{2p}\right]\cdot \\ \cdot \frac{d\ln\sigma}{d\ln M}\frac{\delta_c}{\sigma(M,z)}\exp\left[-\frac{1}{2}\frac{a\delta_c^2}{\sigma^2(M,z)}\right], \quad (2.10)$$

where ρ_0 is the present-day mass density of the Universe, $\delta_c = 1.68$, $a = 0.707$, $A = 0.3222$, $p = 0.3$.

2.4.5 Galaxy-scale Sunyaev-Zeldovich effects

Evidences of statistically significant detections at 30 GHz of arcminute scale fluctuations well in excess of predictions for primordial anisotropies of the cosmic microwave background (CMB) have recently been obtained by the CBI (Mason et al. 2003) and BIMA (Dawson et al. 2002) experiments. The interpretation of these results is still debated. Extragalactic sources are potentially the dominant contributor to fluctuations on these scales and must be carefully subtracted out. And indeed both groups devoted a considerable effort for this purpose. However a quite substantial residual contribution to the CBI signal is difficult to rule out (De Zotti et al. 2004a; Holder 2002), while the residual radio source contamination of the BIMA results is likely to be very small.

If indeed the detected signal cannot be attributed to extragalactic radio sources, its most likely source is the thermal Sunyaev-Zeldovich (SZ) effect (Gnedin & Jaffe 2001). The small-scale fluctuations due to the SZ effect within rich clusters of galaxies has been extensively investigated (Komatsu & Kitayama 1999; Bond et al. 2002). The estimated power spectrum was found to be very sensitive to the normalization (σ_8) of the density perturbation spectrum. A $\sigma_8 \gtrsim 1$, somewhat higher than indicated by other data sets, is apparently required to account for the CBI data.

On the other hand, significant SZ signals may be associated to the formation of spheroidal galaxies (De Zotti et al. 2004a; Rosa-Gonzalez et al. 2004). The proto-galactic gas is expected to have a large thermal energy content, leading to a detectable SZ signal, both when the proto-galaxy collapses with the gas shock-heated to the virial temperature (Rees & Ostriker 1977; White & Rees 1978), and in a later phase as the result of strong

feedback from a flaring active nucleus (Ikeuchi 1981; Natarajan et al. 1998; Natarajan & Sigurdsson 1999; Aghanim et al. 2000; Platania et al. 2002; Lapi et al. 2003).

These SZ signals, showing up on sub-arcmin scales, are potentially able to account for the BIMA results. Proto-galactic gas heated at the virial temperature and with a cooling time comparable with the expansion time may provide the dominant contribution. It must be stressed, however, that estimates are plagued by large uncertainties reflecting our poor understanding of the complex physics governing the thermal history of the proto-galactic gas, and, as stressed by the authors themselves, the counts of galactic-scale SZ effects computed by De Zotti et al. (2004a) may be more conservatively viewed as upper limits. On the other hand, the SZ effect turns out to be an effective probe of the thermal state of the gas and of its evolution, so that its detection, that may be within reach of future high-frequency surveys (cf. the bottom right-hand panel of Figs. 2.17 and 2.18) would provide unique information on early phases of galaxy evolution, essentially unaccessible by other means.

2.4.6 Radio afterglows of γ-ray bursts

In the upper right-hand panel of Figs. 2.17 and 2.18 we show (dot-dashed line) the estimates of the counts of GRB radio afterglows (kindly provided by B. Ciardi) yielded by the Ciardi & Loeb (2000) model. According to these estimates, a large area survey at $\simeq 1\,$cm to a flux limit $\simeq 1\,$mJy should discover some GRBs (see also Seaton & Partridge 2001).

2.5 Discussion and conclusions

A synoptic view of the contributions of the above source populations to the 20 and 30 GHz differential counts is presented in Figs. 2.17 and 2.18. As expected, and directly demonstrated by the high frequency 9C (Taylor et al. 2001; Waldram et al. 2003) and ATCA (Ricci et al. 2004b) surveys, the dominant population at bright flux densities are blazars. These are, however, a composite population, including the rapidly evolving Flat Spectrum Radio Quasars and the slowly evolving BL Lac objects. The former sub-population is prominent above $\simeq 100\,$mJy, but its counts converge rapidly at fainter flux densities, eventually falling below those of steep-spectrum FR II sources and approaching those of BL Lacs.

It is well known from very deep surveys at 1.4 – 8.4 GHz that a large fraction of micro-Jy radio sources are moderate redshift active star forming galaxies (Gruppioni et al. 2001; Fomalont et al. 2002; Chapman et al. 2003). Our models are consistent with these results, and indicate that below a few tens of μJy (at 20–30 GHz), there is a further change in the composition of the radio-source population as proto-spheroidal galaxies come into play, suddenly increasing the ratio of star forming to classical radio sources. Since these objects are predicted to be at typical redshifts of 2–3 and to be highly obscured by dust, their emergence will also increase the fraction of optically very faint sources and strongly shift the redshift distribution to higher redshifts.

The emission of star forming galaxies in the spectral region of interest here is dominated by synchrotron and free-free processes at rest-frame wavelengths longer than a few mm, and by thermal dust radiation at shorter wavelengths. The latter emission is characterized by a steeply inverted spectrum, $S_\nu \propto \nu^\alpha$, with $\alpha \sim 4$, causing a strongly negative K-correction and a sharp steepening of the counts. Counts of proto-spheroidal galaxies could be significantly higher than shown in Figs. 2.17 and 2.18 if the mm excess detected in our own Galaxy, combining Archeops with WMAP and DIRBE data (Bernard et al. 2003; Dupac et al. 2003), and in NGC1569 is a general property of the SED of dusty galaxies.

Below $\simeq 100\,\mu$Jy a significant contribution to the 20–30 GHz counts may come from Sunyaev-Zeldovich (1972) signals (De Zotti et al. 2004a; Rosa-Gonzalez et al. 2004) or free-free emission (Oh 1999) produced by proto-galactic plasma. While no attempts to estimate the counts of proto-galactic free-free sources have been produced yet, we show in Figs. 2.17 and 2.18 the tentative estimates of the counts of SZ effects by De Zotti et al. (2004a), that, as pointed out by the authors, should be more conservatively interpreted as (possibly generous) upper limits.

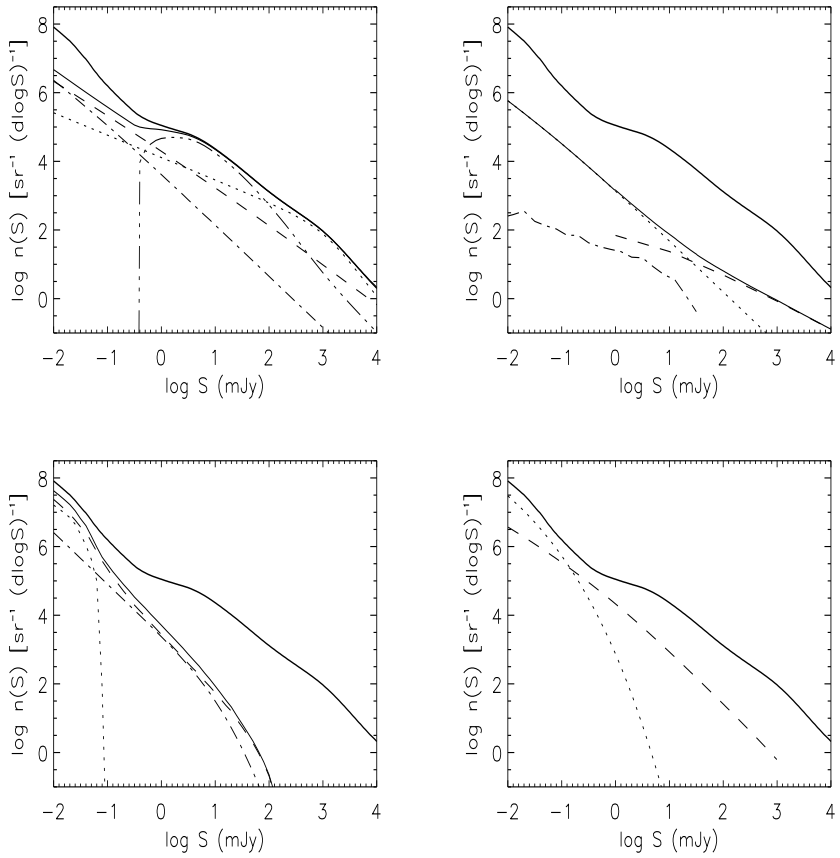

Figure 2.17: Predicted differential counts at 20 GHz for various extragalactic source populations. Upper left-hand panel (classical radio sources): FSRQs (dotted line); BL Lacs (dashed line); FRI (dot-dashed line); FRII (triple dot-dashed line). Upper right-hand panel (special sources): ADAFs (dotted line); extreme GPS quasars and galaxies (dashed line); GRB afterglows (dot-dashed line). Lower left-hand panel (star-forming galaxies): proto-spheroids (dotted line); spirals (dashed line); starburst galaxies (dot-dashed line). Bottom right panel: SZ effects on galactic scales (dotted line) and on cluster scales (dashed line). The sum of contributions shown in each panel and the overall total counts are indicated by a thin and thick solid line, respectively.

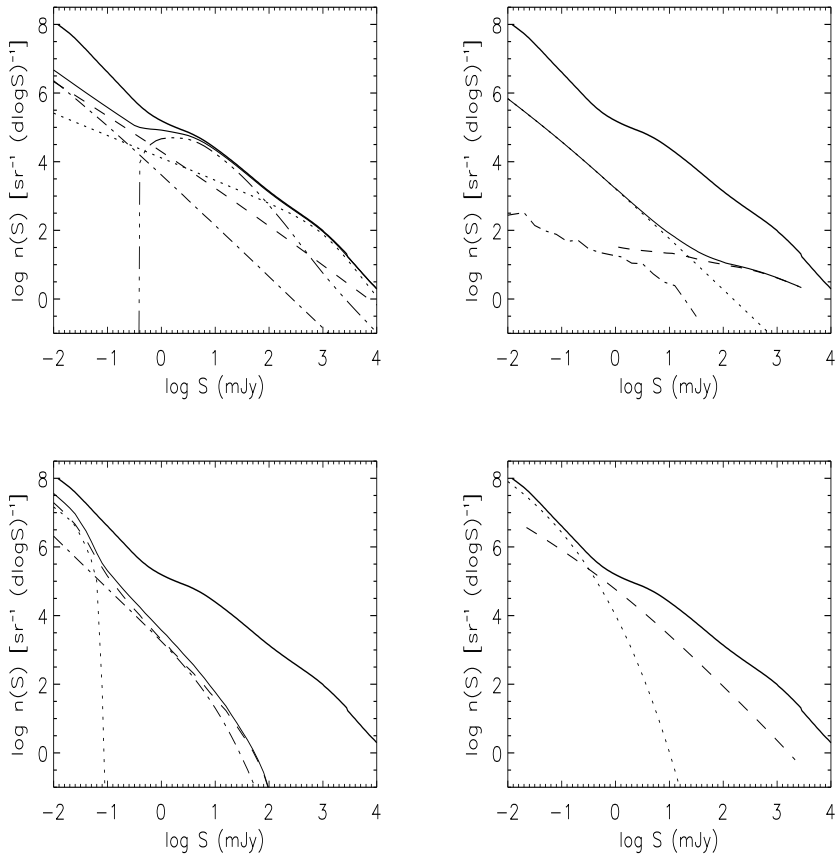

Figure 2.18: Same as in Fig. 2.17, but at 30 GHz.

Chapter 3

High-frequency radio surveys

3.1 Introduction

The radio–source population above 5 GHz has not been well studied yet. This is mainly because large radio telescopes typically have fields of view of a few arcmin at high frequencies, making it extremely time–consuming to carry out large–area surveys. Measuring the high–frequency properties of extragalactic radio sources is also crucial for interpreting the high–sensitivity and high–resolution maps of the Cosmic Microwave Background (CMB) provided by WMAP (Bennett et al. 2003a) and forthcoming missions like ESA's Planck satellite (Tauber 2001). Current analyses (De Zotti et al. 1999a) indicate that the best regions for high–resolution CMB mapping lie near 100 GHz, and that the fluctuations due to individual foreground radio sources are likely to be the main contaminant.

The brightest high–frequency radio sources are expected to be blazars (high and low-polarization flat-spectrum quasars and BL Lac objects) and galaxies with highly–inverted radio spectra such as the GHz Peaked Spectrum (GPS) sources (O'Dea 1998). The Michigan 8 GHz (λ3.8 cm) survey covered $\sim 2600\,\mathrm{deg}^2$ of sky and detected 55 sources down to a limiting flux density of 0.6 Jy. These sources were found to be different from those detected in low–frequency surveys, with 70% having flat or inverted spectra. More than 80% had optical counterparts on the Palomar Sky Survey, most of them QSOs (Brandie & Bridle 1974; Brandie, Bridle & Kesteven 1974).

The first blind radio survey above 8 GHz was carried out by Taylor et al. (2001) with the Ryle Telescope. They observed $63\,\mathrm{deg}^2$ of sky and detected 66 sources to a limiting flux density of 20 mJy at 15.2 GHz. A significant fraction (20%) of the sources they detected

would not have been predicted by a simple extrapolation from lower–frequency surveys. Two–thirds of their sources had flat or inverted spectra. The source density observed by Taylor et al. was also a factor of 1.3–2 lower than predicted by theoretical models based on low-frequency radio luminosity functions (Dunlop & Peacock 1990; Toffolatti et al. 1998).

The 15 GHz survey was extended by Waldram et al. (2003) to 520 $\deg^2$ in three regions of sky targeted by the Very Small Array (Watson et al. 2003). They found 465 sources above a completeness limit of $\sim$25 mJy in their main survey, although a total of $\sim$760 sources were detected down to a limiting flux density of 10 mJy.

A radio/optical follow-up of 176 sources from the 15 GHz 9C survey was performed by Bolton et al. (2004). Optical identifications were found for 155 of the radio sources. The continuum radio spectrum of the sources was sampled through simultaneous multi-frequency radio observations in the frequency range $1.4 - 43$ GHz. They defined two flux-limited samples, one containing 124 sources complete to 25 mJy and one of 70 sources complete to 60 mJy. Between $20 - 25\%$ of the objects in these flux-limited samples display convex radio spectra, rising between 1.4 and 4.8 GHz.

Preliminary radio source counts at 30 GHz have been measured by the DASI (Leitch et al. 2002), VSA (Grainge et al. 2003) and CBI (Mason et al. 2003) groups, and a catalogue of 208 point source candidates stronger than about 1 Jy from the first year of WMAP data (five frequency bands from 23–94 GHz) has recently been published by Bennett et al. (2003b). This discrete source catalogue was used in Chapter 2 to derive the predicted high-frequency source counts of FSRQs and BL Lacs.

3.2 ATCA 18 GHz Pilot Survey

In this Chapter, we present the results of a 18 GHz Pilot Survey performed at the Australia Telescope Compact Array (ATCA)[1] located in Narrabri (NSW, Australia).

3.2.1 Design and operation of the ATCA

The Australia Telescope Compact Array is an earth-rotation aperture synthesis radiointerferometer. Earth-rotation aperture synthesis was first used in the 1950s for radio observations of the sun. The technique was devised by Christiansen and Warburton

[1]For details see Journal of Electrical and Electronics Engineering, Australia, Special Issue, Vol. 12, No. 2, June 1992

(1955) and Ryle (1962) and is well explained in Thompson et al. (1986) and Chapter 1 of Perley et al. (1989). Chapter 1 of Thompson et al. (1986) includes a historical review. Essentially, the antennas are used in pairs to form interferometers. The visibility (i.e. the fraction of signal common to both antennas of a pair) is derived by multiplying the signals together. By combining the correlated signals obtained over a long period of time and with a large range of spacings between antennas, the Compact Array measures the spatial coherence function:

$$V = \int \mathbf{I}_{\nu(s)} e^{2\pi i \mathbf{s}\cdot(\mathbf{r_1}-\mathbf{r_2})} d\mathbf{\Omega}$$

where $\mathbf{I}_{\nu(s)}$ is the two dimensional intensity distribution on the sky, $\mathbf{s}$ is the unit vector in the direction of the celestial source, $(\mathbf{r_1} - \mathbf{r_2})$ is the separation vector between antennas 1 and 2 and $d\mathbf{\Omega}$ indicates integration over the sphere.

By Fourier transformation of the results obtained, an image of a radio source is produced. The image is formed with the same angular resolution as for observations with a single antenna of diameter equal to the largest spacing.

The ATCA consists of six 22-m radio antennas. Five of the six antennas lie along a three kilometre east-west oriented railway track. Since Sept 2001, a 214-m north-south track has been in operation, allowing the five movable antennas to be configured in compact configurations superior to previous arrays, as full-synthesis observations can be obtained in less than 12 hours. The sixth antenna lies on a 75-m rail-track three kilometres further west, thus allowing a maximum ATCA baseline of six kilometres. The antennas can be moved along the railway tracks and set up at any of 37 fixed stations. The stations contain ports that allow the antenna data to be transferred to the correlator in the control building. Owing to the location of stations and other physical constraints, the smallest baseline increment available is approximately 15m, and the shortest baseline is approximately 30m.

The antennas have a Cassegrain design, i.e. the receivers are located in a turret that protrudes through a hole in the main reflector surface. The antennas have an altitude-azimuth mount with wrap limits. The shaped (i.e. non-parabolic) dish and subreflector surfaces are designed to maximise the gain-to-antenna-noise ratio. The outer reflecting surfaces are perforated and are accurate enough to permit observations at frequencies up to 50 GHz. The inner 15.3-m of the dish is solid and can operate at up to 116 GHz.

A major feature of the ATCA is its wide bandwidth operation. The feedhorns and

BAND WAVELENGTH	20 cm	13 cm	6 cm	3 cm
(NAME)	(L)	(S)	(C)	(X)
Nominal frequency range (GHz)	1.25 – 1.78	2.20 – 2.50	4.40 – 6.86	8.00 – 9.20
Fractional frequency range	35%	13%	44%	14%
Number of antennas	6	6	6	6
Number of baselines	15	15	15	15
Primary beam (arcmin)	33'	22'	10'	5'
Synthesised beam (arcsec)	6"	4"	2"	1"
System sensitivity T_{sys}/G (Jy)	350	440	420	390

Table 3.1: Observing parameters of the 6km Compact Array.

front-end electronics operate over a very large range of frequencies, thus allowing (u,v) coverage to be increased by multi-frequency synthesis and dual frequency observations. The feedhorns are compact, with a corrugated interior surface and are designed for maximum frequency coverage, low noise, low spillover, low reflection and low cross-polarisation sidelobe levels. The feedhorns allow two simultaneous orthogonal linear polarisations to be measured (at frequencies almost an octave apart), and have a main lobe with near-constant, symmetrical beamwidth.

The frequencies at which the Australia Telescope operates are given in Table 3.1. The telescope is currently being upgraded for observations at millimetre wavelengths. The 12mm LNA receivers (Fig. 3.1) have already been installed on all the six ATCA antennas. They are tunable between 16 and 26 GHz and in the standard correlator configuration two spectral windows can be selected (at most 2.7 GHz apart).

Three prototypes of the 3mm systems are operational on three antennas. The final upgrade is scheduled to be completed in September 2004.

There are presently two feedhorns mounted on each antenna: a large feed-horn that operates at both the 20-cm/13-cm bands, and a smaller, 6-cm/3-cm band feedhorn.

The feedhorns and the receivers are mounted on a rotating turret. The rotating turret design ensures that the feedhorns are aligned with the optic axis of the antenna, allowing a wide field of view and dual-polarisation observations. The turrets are rotated automatically in accordance with the frequencies selected by the observing file. Rotating the turret orients the desired feed-horn and also ensures that the subsequent electronics suit the observing frequency. The 6-cm/3-cm band feed-horn is fitted with separate 6-

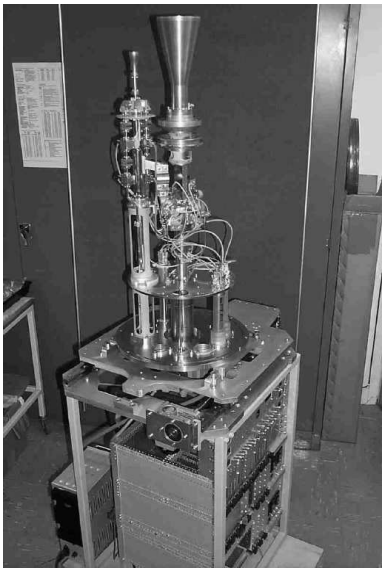

Figure 3.1: Low Noise Amplifier 12mm and 3mm receivers.

cm and 3-cm receivers, while the 20-cm/13-cm band feedhorns have 20-cm and 13-cm receivers. All receivers run continuously and use cooled FET and HEMT amplifiers that provide wide bandwidths and total system temperatures between 30K to 65K, depending on frequency.

The signals collected by the feedhorns are fed to the receiver systems for amplification and conversion to lower, more manageable frequencies. During observations each antenna provides four independent intermediate frequency (IF) outputs (two frequency bands, two polarisations). These channels allow simultaneous observations of both polarizations at the two available frequencies in either dual-receiver system. The frequencies can be anywhere in the range covered by the selected feed-horn. Note that narrow-band filters (for spectral-line observing) are only available for the first IF of each dual-receiver system.

In order to convert the received radio signals to lower frequencies, the radio signals are mixed with signals produced by a part of the CA known as the local oscillator. Four local oscillator signals provide four IF outputs to enable the dual-frequency, dual-polarisation operation. You can also switch frequencies at the end of each integration cycle (typically ten seconds). To change to a pair of frequencies covered by a different feed-horn requires a rotation of the turret and takes about twenty seconds.

3.2.2 Survey strategy and observations

An analogue wide–band prototype correlator originally developed for the Taiwanese CMB instrument AMiBA (Lo et al. 2001) was linked to two ATCA antennas to produce a two–element interferometer with 3.4 GHz bandwidth. The two 22m antennas were placed on the shortest ATCA baseline (30 m), giving a fringe spacing of ~ 90 arcsec at the centreband frequency of 18 GHz. The correlator produced 16 lag channels corresponding (after the Fourier inversion) to 8 frequency channels, each with a bandwidth of 425 MHz. This large total bandwidth allowed us to obtain high signal-to-noise measurements in the very short integration time used (0.2 sec/beam). Such rapid scanning was a design feature of the ATCA implemented to perform mosaic observation over large areas. This combination of wide bandwidth and fast scanning has made it possible to observe a large fraction of the sky despite the small ATCA primary beam at 18 GHz (HPBW = 2.3 arcmin). Only a single linear polarization was implemented in this correlator configuration.

No delay tracking had been built for this analogue correlator (AMiBA antennas are on a common tracking mount) so we designed an observing mode in which all observations are taken on the meridian where the delay for an east–west interferometer is zero.

The scanning strategy was as follows: the two ATCA antennas point in the same direction and scan the sky synchronously up and down between $\delta = -70^\circ$ and -60° in elevation along the meridian with a scan rate of 10° per minute (the maximum speed the antennas can slew in a closed loop in elevation). The Earth's rotation then allows us to cover a strip of the sky in raster scan mode. Antenna coordinates were sampled at 10 Hz. With an integration time of 80 ms, the antenna pointing was recorded every 0.8 arcmin.

The pilot survey run took place on 2002 September 13–17 during one observing period of 96 hours.

3.2.3 Survey data reduction

The antenna positions (obtained from the telescope encoders) and fringe visibilities (produced by the analogue correlator) were stored in data files. Custom MIRIAD (Sault, Teuben & Wright 1995) tasks were written to flag out bad data (e.g. antenna pointings more than 30 arcsec from one another) and to calibrate the visibilities in absolute flux and bandpass.

The next stage involved searching for peaks in the fringe visibility amplitudes above a

given signal-to-noise ratio in the time-ordered raster scans, to produce a candidate source list. This was done using the following steps:

1. We calculated the weighted complex mean of the 8 separate frequency channels to form a single 3.4 GHz wide band. The bandwidth smearing (Thompson 1999) in the worst case (a source at half power point of the primary beam) is 1/6 of the fringe spacing and can be ignored. Expressed in a different way our 15% bandwidth corresponds to a 5.6m variation in the 30m spacing used, which is a small fraction of the 22m dish diameter.

2. We applied a beam shape Gaussian (FWHM = 2.3 arcmin) filter acting as a weighted running mean for this short baseline to smooth out fluctuations (generated by receiver noise) on spatial scales less than the antenna primary beam.

3. In the plane defined by the real and imaginary parts of the fringe visibility we determined the dispersion along each axis. Points lying at $> n\sqrt{\sigma_x^2 + \sigma_y^2}$ are selected as candidate sources at $n\sigma$ level. In general a source generates up to 4 contiguous points along the time series corresponding to the sampling by different parts of the beam in steps of 0.8 arcmin. The candidate source position corresponds to the maximum visibility amplitude in this sequence.

4. We created a list of candidate point–source detections at a range of signal-to-noise ratios (3, 3.5, 4 and $5\,\sigma$) to explore the optimum detection strategy.

The raw candidate source lists were then merged into a single list. The number of 4σ candidate sources for the entire survey was 574. The measured rms noise in the scans was $\sigma_{\rm rms} = 15\,$mJy.

We performed a Monte Carlo simulation to estimate the number of spurious peaks generated by Gaussian noise at a given signal–to–noise ratio (see Table 3.2). The same number of real and imaginary parts of the fringe visibilities for each frequency channel was generated 30 times by sampling a Gaussian distribution with the same mean and standard deviation as the actual distributions. A cut-off value of S/N = 4 was chosen as a good trade-off, since lower values yield too many spurious peaks while for S/N = 5 we reject too many sources which are genuine detections. Since the S/N in the follow-up is very high compared with the 0.2 sec survey integration time, we could afford to explore the detection statistics by going well into the region of spurious detections due to noise.

S/N	N_{exp}	N_{sim}
3	542	529±21
3.5	111	104±10
4	24	16±4
5	5	0.13±0.35

Table 3.2: Comparison between the actual number of peaks in a raster scan during one test run (N_{exp}), and the number of spurious peaks predicted by a Monte Carlo simulation of the same scan (N_{sim}) as described in the text.

3.2.4 Follow-up observations

Follow-up synthesis–imaging observations of the S/N $\geq$ 4 candidate sources were carried out on 2002 October 8–12 with the ATCA in its hybrid H168B configuration, which has antennas along the new 214 m Northern Spur as well as the existing east–west railway track. At the time of this run, only three antennas had been equipped with low–noise 12 mm receivers, so only three baselines were available for imaging. We therefore observed each object over a wide range in hour angle to maximize (u, v) coverage. The angular resolution depends on the source declination. The median major and minor axis values are 30 and 13 arcsec respectively. The average rms noise in synthetized maps was $\sigma \simeq 1.5$ mJy.

We used the standard ATCA correlator, allowing us to observe in two spectral windows centred at 17.2 and 18.7 GHz each with a bandwidth of 128 MHz. At 18 GHz, the standard ATCA primary calibrator 1934 − 638 is too faint to provide a good absolute flux density scale, and we used the planet Mars as our primary calibrator. The fringe–visibility amplitude dependence on spatial frequency has been accurately modelled for the ATCA. The Mars model we used is described in Ulich (1981) and Rudy et al. (1987). As in Ulich (1981), the seasonal variation of Mars brightness temperature is also taken in account by the model.

3.2.5 Follow-up data reduction

Follow–up 18 GHz images

Reduction of the follow–up 18 GHz images was done in the standard way using the MIRIAD software package (Sault, Teuben & Wright 1995). The target sources and

calibrators were imaged in total intensity (Stokes I) and circular polarization (Stokes V). The sources were assumed to have zero circular polarization, and the Stokes V maps were used to estimate the rms noise. We used the MIRIAD Multi–Frequency Synthesis (MFS) algorithm at the Fourier inversion stage, since this improves (u, v) coverage by simultaneously Fourier–transforming the visibility data from both observing frequencies. After the Fourier inversion the maps were CLEANed, and the resulting clean components were restored using an elliptical Gaussian beam.

We used the maximum pixel value in the restored Stokes I maps together with the Stokes V rms noise to calculate the map S/N ratios. A source was considered to be detected when its S/N value was above 5.

The number of sources above this detection threshold was 282 out of 574 candidates. However, many candidate objects ($\sim$ 20%) were multiple detections of the same source, so that the actual number of spurious sources in the survey was smaller. These multiple observations were used to estimate data quality.

Flux density and position measurements

We reimaged the detected sources in all four Stokes parameters, applying the primary beam correction to restored maps and a natural weighting to the fringe visibilities before the Fourier inversion. The primary beam correction was only applied at this last stage, because the increase in noise near the map border complicates the detection statistics.

All but five of the confirmed (S/N$>$ 5) sources were well–fitted by a single elliptical Gaussian.

We created a final source list by removing all sources which had the same position (within the errors) as a previously–listed one. This decreased the final number of detected sources from 282 to 221, and most of the subsequent analysis was done on this list of objects. Source parameters determined by the MIRIAD IMFIT algorithm[2] for the confirmed sources are presented in Table 3.5. Any source having an angular size larger than 10 arcsec was dubbed (R) meaning "significantly resolved". Because of angular size measurement errors, point-like sources at the resolution of follow-up images could appear resolved.

[2]Described in wwwatnf.csiro.au/computing/software/miriad/taskindex.html

Source	b (deg)	$S_{\rm peak}$ (mJy)	Frac. pol.	ID
1147-6753	−5.9	1150	2.0%	QSO
1236-6150	+1.0	422	0.7%	Galactic
1243-6254	−0.06	787	2.8%	Galactic
1310-6245	+0.03	379	5.0%	Galactic?
1311-6246	−0.01	1264	0.5%	Galactic?
1337-6508	−2.7	765	5.1%	Extragalactic
1346-6021	+1.8	1503	7.9%	Radio galaxy
1400-6209	−0.4	231	15.1%	Galactic
1647-6438	−12.5	534	6.9%	Radio galaxy
1803-6507	−19.6	945	2.0%	Radio galaxy
1824-6717	−22.4	105	16.2%	Radio galaxy?
2303-6806	−46.0	848	3.7%	QSO
2312-6607	−48.1	102	2.0%	QSO?

Table 3.3: Linear polarization detections at 3 σ.

3.2.6 Polarization

Determining the level of polarization in foreground radio sources is critically important for the study of polarization anisotropies in the cosmic microwave background (e.g. Hu, Hedman & Zaldarriaga 2003). De Zotti et al. (1999b) and Mesa et al. (2002) estimate that extragalactic sources will not be a strong limiting factor in measurements of E-mode CMB polarization, but there are few existing measurements of the polarization of radio galaxies and quasars at frequencies above 5 GHz (Ricci et al. 2004a).

For all the sources and calibrators we produced polarized intensity p, fractional polarization m and position angle PA maps and the relative error maps after clipping (i.e. blanking) pixels with S/N ratios below 3. The peak flux in the Q, U and I maps was then measured at the I map peak position using the MIRIAD MAXFIT task (see the MIRIAD web page in the previous footnote), and the fractional linear polarization estimated through the relation:

$$m = \frac{\sqrt{Q^2 + U^2}}{I} \tag{3.1}$$

Only 13 of the 221 follow-up confirmed sources were found to have a linear polarization intensity $p = \sqrt{Q^2 + U^2}$ above $3\sigma_p$, where σ_p is typically 6 mJy (Table 3.3). Six of these have $|b| > 5^\circ$ and appear to be extragalactic. Two extra-galactic objects in the $|b| < 5^\circ$ Galactic strip were also detected in polarization.

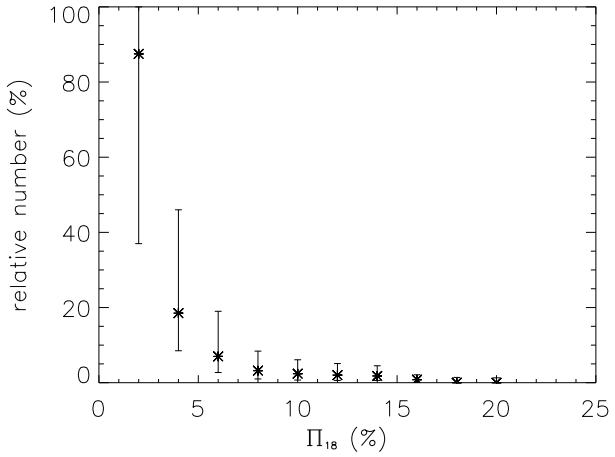

Figure 3.2: Fractional polarization distribution at 18 GHz given by the ratio between the number of polarization detected sources and the number of sources that could be detected at this level. Error bars provide the maximum range permitted by Poissonian errors in source sample size per bin.

In Fig. 3.2 we show the fraction of 18 GHz polarized sources that were actually detected below a certain polarization level inside the sample of sources that could be detected below that polarization level. This statistical method, similar to the one used by Auriemma et al. (1977) to study radio luminosity functions, gives an estimate of the fractional polarization distribution. Error bars indicate the maximum range inside each polarization sub-sample. The first polarization level is strongly affected by small number statistical Poissonian errors, having 7 polarization detections out of 8 sources in which polarization could be detected. If we take only the extragalactic sources into account we have a median polarization of $\sim 2.1\%$. The average flux density of all extragalactic sources contributing to the median is 1.0 Jy.

We also focused on the extragalactic source 1824−6717 (=PKS 1819−67), which has the highest fractional polarization (16.2%) so far measured in our sample. Since PKS 1819−67 is a widely–spaced (47 arcsec) double, with extended radio emission seen at lower frequencies (Fig. 3.3), it is unlikely to be a distant gravitationally–lensed radio galaxy. We are probably seeing a pair of radio hotspots in a powerful FRII radio galaxy. Since such sources are identified with intrinsically bright elliptical galaxies and no optical counterpart is seen on the DSS, the galaxy redshift should be $z > 1$.

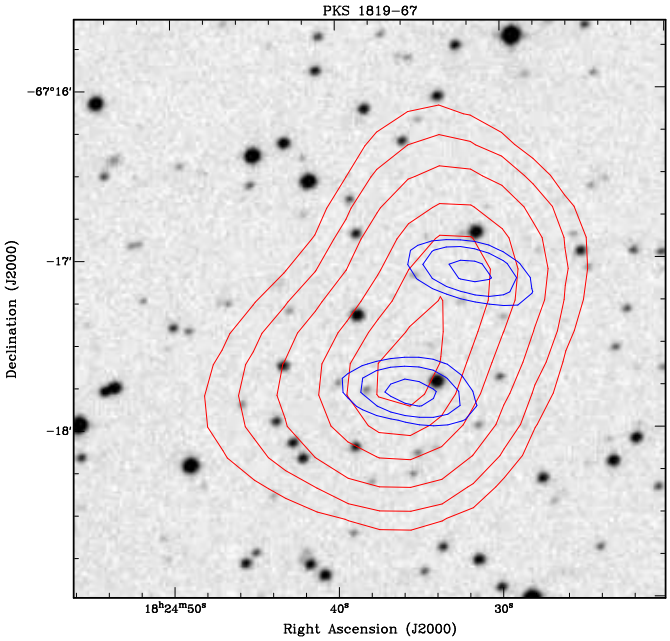

Figure 3.3: Radio contours for PKS 1819−67 at 843 MHz (larger scale) and 18 GHz (smaller scale) overlaid on a blue SuperCOSMOS image. This source has the highest linear polarization (16.2%) measured in our pilot study.

3.2.7 Distribution of sources

Distribution of the detected sources on the sky

As can be seen from Figs. 3.4 and 3.5, many of the confirmed 18 GHz sources lie in or near the Galactic plane.

Using the source density histogram in Fig. 3.4, we estimated the number of galactic objects that are expected to be found in the extragalactic surveyed region. The galactic plane shape in the source density histogram was fitted with a single Gaussian profile. The best fit parameters resulted to be $n_{\rm peak}$=2.3 deg^{-2}, b_0=0 and σ=0°.8, where $n_{\rm peak}$ is the source density peak, b_0 is the galactic latitude value at the source density peak and σ is the Gaussian profile width.

In the discussion which follows we assume that the 123 sources which have $|b| > 5°$, and which lie more than 5.5 degrees from the LMC centre ($\alpha = 5^{\rm h}\,23^{\rm m}\,34^{\rm s}.7$, $\delta = -69°\,45'\,22''$, J2000; $l = 280.47°$, $b = -32.89°$) are extragalactic. When split in this way, the final sample of confirmed sources in Table 3.5 contains 84 Galactic, 14 LMC and 123 extragalactic sources.

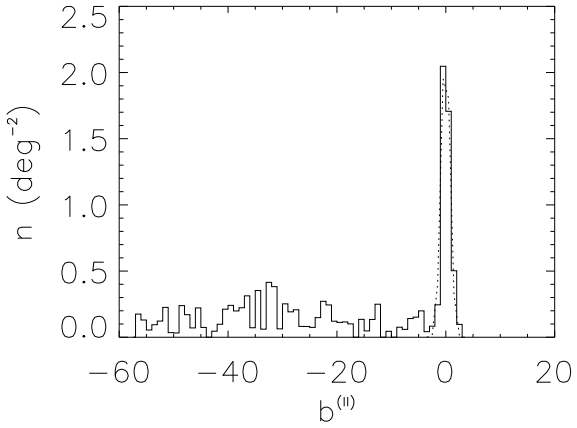

Figure 3.4: Histogram of source density in 1-degree bins of Galactic latitude b (corrected for the area surveyed). The peak near b=0° corresponds to Galactic disk sources such as HII regions. The surveyed area (see Fig. 3.5) only extends to $b = +3°$ so the apparent cut-off in sources at $b > +3°$ is not real.

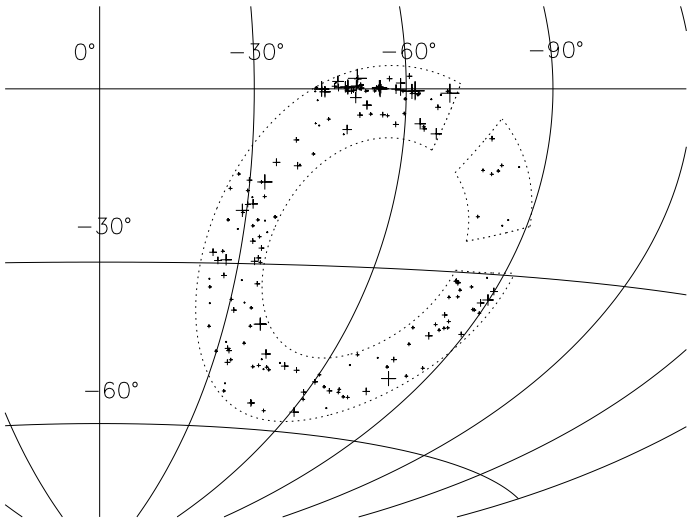

Figure 3.5: Equal area Aitoff projection sky map in galactic coordinates of the confirmed 18 GHz sources. Larger crosses correspond to brighter sources.

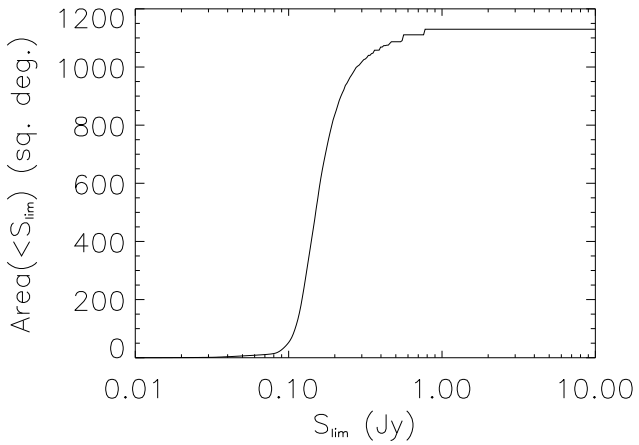

Figure 3.6: Effective area $A_{\rm eff}$ surveyed in the extragalactic region of the pilot survey scans as a function of the limiting flux density ($S_{\rm lim} = 4 \times \Delta S_{rms}$). The maximum surveyed area outside the Galactic latitude range ($|b^{\rm II}| > 5°$), excluding the LMC region, is $A_{\rm tot} = 1130\,{\rm deg}^2$.

Survey sensitivity

Because this pilot survey did not achieve uniform coverage, we made a quantitative assessment of the survey sky coverage through a survey sensitivity map, i.e. a sky map representing the limiting flux density value at every point of the sky covered by the survey. To create this map, the survey sky strip ($-71° < \delta < -59°$) was gridded into 30 arcsec×30 arcsec pixels, and the ∼ 2736890 survey sample pointings were projected onto this 1800×24000-pixel grid. To account for the antenna primary-beam pattern, this image was convolved with a 7×7-pixel discretized Gaussian function (HPBW = 2.3 arcmin). The convolved pointing number per pixel was then multiplied by the time $t_{\rm cross}$ taken by a single beam to sweep across a pixel ($t_{\rm cross} = 0.28\,{\rm sec}$) to get the pixel observing time. The antenna system temperature ($T_{\rm sys} = 78\,{\rm K}$), the antenna gain at 12mm ($G = 0.10\,{\rm K\,Jy}^{-1}$), the observing time per pixel τ and the correlator band-width ($\Delta\nu = 3.4\,{\rm GHz}$) were used to compute the pixel rms sensitivity $\Delta S_{\rm rms}$. A quantitative representation of the sensitivity map is offered by the effective area $A_{\rm eff}$ as a function of the limiting flux density (Fig. 3.6), which is simply given by the cumulative number of pixels for which $4 \times \Delta S_{\rm rms} \leq S_{\rm lim}$ multiplied by the single pixel area.

Differential counts of extragalactic sources

Here, we determine source counts for the extragalactic population at 18 GHz. We exclude Galactic sources, since many have large angular size and their integrated flux densities are underestimated in the follow–up snapshot images.

The counts were logarithmically binned in flux density starting from $S_{\rm lim}$=100 mJy with a common binsize of 0.2 dex. A limiting flux density of 100 mJy was chosen because only a handful of objects were detected below this flux density.

As the effective surveyed area $A_{\rm eff}$ drops with decreasing limiting flux density $S_{\rm lim}$ below $S_{\rm lim} \simeq 1$ Jy, the surface density of sources in the (small) flux density interval $\Delta S = S_2 - S_1$, $n(S)\Delta S$, is given by:

$$n(S)\Delta S = N_{\rm obs}(> S_1)\frac{1}{A_{\rm eff}(> S_1)} - N_{\rm obs}(> S_2)\frac{1}{A_{\rm eff}(> S_2)} \ , \qquad (3.2)$$

where $N_{\rm obs}(> S)$ is the number of counted sources brighter than S. This procedure is equivalent to the more commonly used method of calculating the effective area over which each source could have been observed and summing the inverse area in the flux density bin of interest (Katgert et al. 1973).

The computed source counts need to be corrected for incompleteness. The fraction of sources with true flux $S > 4\sigma$, that should be in our sample but are missed because their observed flux $S_{\rm obs} < 4\sigma$ is given by:

$$F_{\rm missed} = \frac{\int_{\sigma_{\rm min}}^{S/4} d\sigma \ A(\sigma) \ \int_0^{4\sigma} dS_{\rm obs} \ e^{-\frac{1}{2}\left(\frac{S-S_{\rm obs}}{\sigma}\right)^2} / \sqrt{2\pi}\sigma}{\int_{\sigma_{\rm min}}^{S/4} d\sigma \ A(\sigma)} \ . \qquad (3.3)$$

The values of $F_{\rm missed}$ as a function of S are shown in Table 3.4 together with their negative and positive errors.

We have used the lowest possible angular resolution in the survey to minimize the selection against extended sources, but any sources extended more than a few minutes of arc could be missed at the survey limit. This will have a very small effect on the estimate of the total source counts.

The uncertainties on differential counts were estimated by summing in quadrature the Poisson errors (Gehrels 1986) and the uncertainties in the effective area. The results are

Table 3.4: Differential counts of extragalactic sources, corrected for incompleteness.

S (Jy)	$F_{\rm missed}$ (%)	$n(S)$ (Jy^{-1} sr^{-1})	neg. err.	pos. err.
0.126	31.4	9298	5735	33452
0.200	14.3	1175	286	580
0.316	4.4	412	97	125
0.501	2.0	174	48	63
0.794	3.3	57	21	31
1.259	0.0	20	9.6	16
1.995	0.0	9.5	5.2	9.2
3.162	0.0	2.0	1.6	4.6

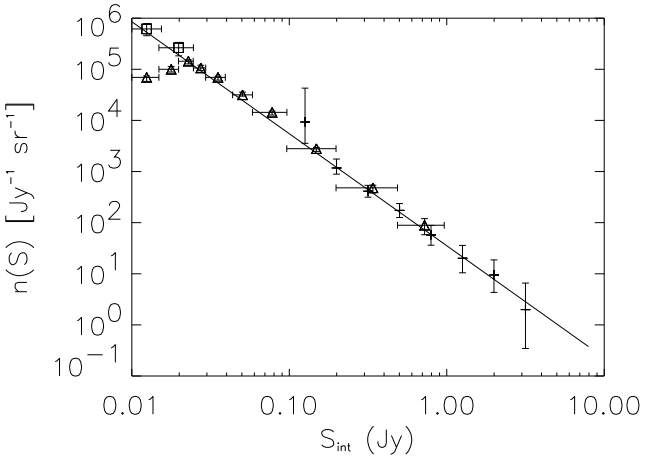

Figure 3.7: Effective area–corrected and completeness-corrected differential source counts of the extragalactic population at 18 GHz are presented together with 9C main survey (triangles) and deeper survey (squares) counts by Waldram et al. (2003). The solid line shows the least-squares linear fit to our counts. The two lowest flux density bins (triangles) of the 9C main survey are underestimated due to incompleteness.

plotted in Fig. 3.7, where we also show the least square linear fit given by:

$$n(S) = 57 \left(\frac{S}{\rm Jy}\right)^{-2.2\pm0.2} {\rm Jy}^{-1}{\rm sr}^{-1} \tag{3.4}$$

Our counts are in good agreement with those by Waldram et al. (2003) (9C survey) at 15 GHz (Fig. 3.8), as well as with the preliminary VSA (Grainge et al. 2003), DASI (Leitch et al. 2002), and WMAP counts (Bennett et al. 2003b) if we assume a radio spectral index $\alpha = 0$.

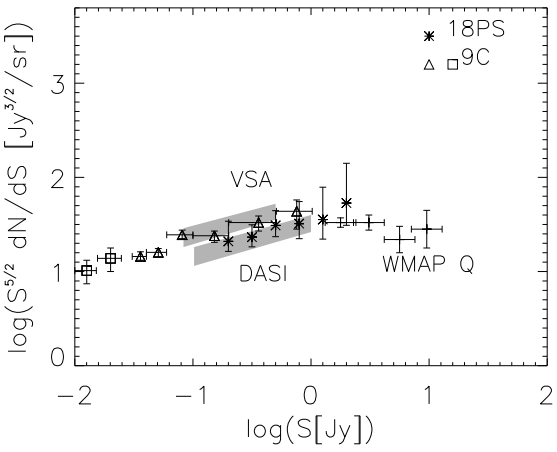

Figure 3.8: Euclidean normalized differential source counts from our pilot survey (18PS) compared with VSA, DASI, WMAP band Q (41 GHz) and 9C main (triangles) and deeper (squares) surveys. Modified version of Fig. 13 from Bennett et al. (2003b).

3.2.8 Comparison with data at lower radio frequencies

Position comparison

Twenty of the objects detected in the 18 GHz pilot survey are strong compact radio sources which have previously been observed by Ma et al. (1998) with Mark III VLBI at 2.3 and 8.4 GHz as part of a program to tie down the International Celestial Reference Frame. The mean offset is +0.5 arcsec in RA and −0.2 arcsec in Dec, with standard deviations of 3.0 and 1.4 arcsec respectively. These standard deviations are larger than the formal uncertainties (2.0 arcsec in RA and 1.1 arcsec in Dec) measured in the MIRIAD source–fitting, and reflect the true external errors in our position measurements.

We also cross-matched our extragalactic sub-sample with the 0.843 GHz SUMSS (Mauch et al. 2003) and 4.85 GHz PMN (Gregory et al. 1994) catalogues. All the 123 18 GHz extragalactic sources have a PMN counterpart, and all 102 sources lying in the region of overlap with SUMSS have a SUMSS counterpart.

Spectral index distribution

Fig. 3.9 shows that the low-frequency ($S_{0.843}$) and high-frequency (S_{18}) flux densities are uncorrelated. It is important to stress this point because in many CMB experiments the extragalactic radio source foreground is computed starting from low-frequency source

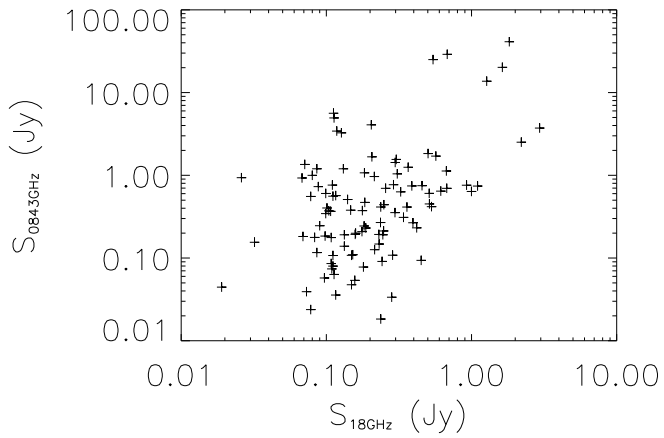

Figure 3.9: $S_{0.843}$ vs. S_{18} scatter plot. No evidence of a significant correlation between low- and high-frequency fluxes is present.

catalogues and assuming a distribution of spectral indices around a mean value to model the source population at high frequency (>30 GHz), but in doing this, a correlation between low- and high-frequency flux density is implicitly assumed.

In Fig. 3.10 we show the spectral index distribution (α where $S_\nu \propto \nu^\alpha$) for the extragalactic population. Most spectral indices are in the range $-1.5 \leq \alpha \leq 0.5$. Over 70 % of the extragalactic sources have a flat radio spectrum ($\alpha^{18}_{0.843} > -0.5$) and 29% have an inverted spectral index ($\alpha^{18}_{0.843} > 0$).

The $\alpha^{18}_{0.843}$ spectral index distribution we obtained is in good agreement with the Michigan 8 GHz survey (70% flat or inverted sources) and Taylor et al. (2001)'s distributions (2/3 of the sources flat or inverted). However, the 9C (Waldram et al. 2003) spectral index distribution between 1.4 GHz NVSS and 15 GHz flux densities, which goes about 4 times fainter, contains almost equal numbers of flat- and steep-spectrum sources (55% flat or inverted), suggesting that the ratio of flat- to steep-spectrum sources decreases at lower flux density. The same behaviour is found for the spectral index statistics of a lower frequency survey such as the 5 GHz selected 1 Jy sample (54% of flat or inverted spectrum sources, Stickel et al. 1994). Theoretical predictions based on low-frequency selected radio luminosity functions (e.g. Dunlop & Peacock 1990) and simple spectral scaling laws (flat spectrum $\alpha = 0$ and steep spectrum $\alpha = -0.7$) tend to overestimate the source density at high frequency and fail to reproduce the observed proportionality between flat and steep spectrum populations. High-frequency turn-over in radio source

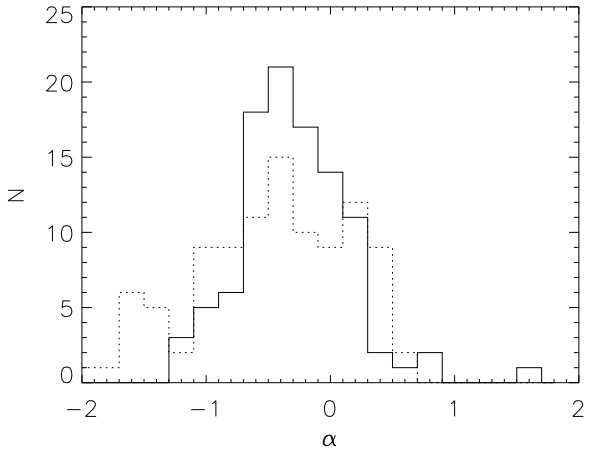

Figure 3.10: Spectral index distributions of the extragalactic sample. The solid line shows a histogram of the spectral indices $\alpha^5_{0.843}$ calculated from SUMSS at 843 MHz (median value=−0.22), and the dashed line α^{18}_5 calculated from PMN at 5 GHz (median value=−0.29).

spectra due to synchrotron electron ageing needs to be modelled as we are at reasonably high observing frequency and some sources lie at high redshift.

To better characterize the spectral behaviour of the extra-galactic population we also present an α^{18}_5 vs. $\alpha^5_{0.8}$ scatter plot in Fig. 3.11 for the 101 extragalactic objects having a flux density measurement at 0.8, 5 and 18 GHz.

We found that 15 sources classified as inverted at low frequency ($0 < \alpha^5_{0.8} < 0.5$) are also inverted at high frequency ($\alpha^{18}_5 > 0$). No sources out of the 6 High Frequency Peaker candidates having $\alpha^5_{0.8} > 0.5$ show a rising spectrum between 5 and 18 GHz. 14 sources being flat between 0.8 and 5 GHz ($-0.5 < \alpha^5_{0.8} < 0$) become inverted at higher frequency. Most of the steep spectrum ($\alpha^5_{0.8} < -0.5$) sources (except 2 objects) stay steep even in the high frequency range.

In the α^{18}_5 histogram in Fig. 3.10 there are 9 sources in the 0.4–0.6 bin but only 2 are present in the same spectral range in the $\alpha^5_{0.8}$ histogram. The radio spectra of these objects, shown in Fig. 3.12, are turning up at higher frequency. It is worth noticing that the PMN flux densities could be overestimated as the PMN survey beam was so large (3 arcmin) that it is possible that more than one source is included inside the beam area. This would flatten the 0.843–5 GHz spectral indices and steepen the 5–18 GHz ones.

Within the boundaries in Fig. 3.5 there are 12 WMAP sources. We found that six

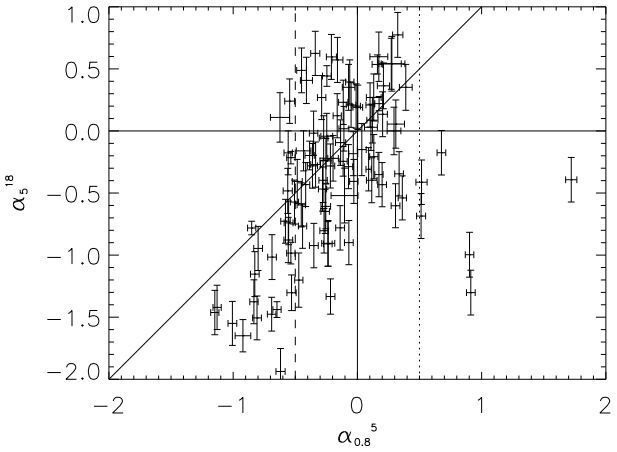

Figure 3.11: α_5^{18} vs. $\alpha_{0.8}^{5}$ scatter plot: the dashed line represents the separation between flat ($\alpha_{0.8}^{5} > -0.5$) and steep spectrum sources and while the dotted line is the threshold for selecting High Frequency Peaker ($\alpha_{0.8}^{5} > 0.5$) candidates at low frequency.

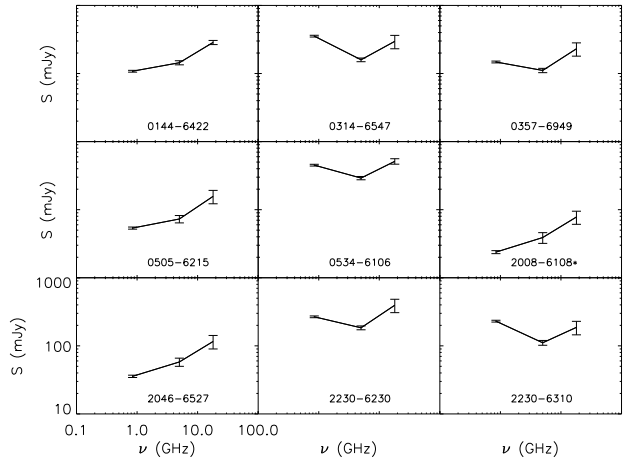

Figure 3.12: Radio spectra of the 9 objects in the $0.4 - 0.6$ bin of the α_5^{18} spectral index histogram (Fig. 3.10).

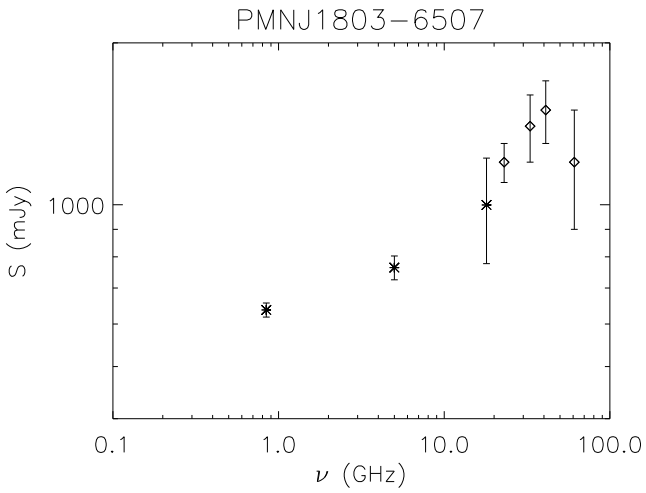

Figure 3.13: Radio spectrum spanning between 0.843 and 61 GHz of one of the 6 sources in the 18 GHz pilot survey present also into the WMAP discrete source catalogue. The WMAP points are represented by diamonds.

of them fall in small survey "holes" where the survey sensitivity was too poor or array antennas were unable to sample sky positions and amplitudes. The effect of these regions with poor or null sensitivity on the survey effective area and completeness is quantitatively taken in account in Fig. 3.6. For the six sources having a S/N $>$ 4 in the survey we were able to produce wide range (0.8–61 GHz) radio spectra which in four cases turned out to be steeply rising spectra. One source (PMNJ1803–6507) could be a HFP candidate possibly peaking at about 40 GHz (Fig. 3.13). Note that WMAP and 18 GHz pilot survey flux densities were measured within a few months of each other (i.e. they are near-simultaneous), the PMN (5 GHz) and SUMSS (0.843 GHz) measurements date from 10 and 4 years earlier respectively.

3.2.9 Optical identifications of extragalactic sources

Optical identifications from SuperCosmos

We used the SuperCOSMOS online database (Hambly et al. 2001) to search for optical counterparts to the 18 GHz sources detected in the pilot study. Our radio position errors are typically 3.0 arcsec in RA and 1.4 arcsec in Dec. The optical positions listed in the SuperCOSMOS catalogue also have an associated uncertainty of up to 1 arcsec, so we chose a cutoff radius of 8 arcsec around the radio position to search for an optical counterpart. Table 3.6 lists the results of this search for the 123 extragalactic sources in our sample. Of

these, 74 (60%) are identified with stellar objects (candidate QSOs), 30 (25%) with galaxies and 19 (15%) are blank fields, i.e. they have no optical counterpart in SuperCOSMOS. Some notes on individual sources are given in § 3.2.10.

The table columns are as follows:
(1) 18 GHz source name, as in Table 3.5.
(2,3) 18 GHz radio position (J2000.0) measured from the follow-up images as described in §5.1.
(4,5) The position (J2000.0) of the closest optical counterpart identified in the SuperCOSMOS catalogue. Where these columns are blank, there is no catalogued optical object within 8 arcsec of the 18 GHz radio position.
(6) Blue (B_J) apparent magnitude of the optical ID.
(7) SuperCOSMOS T parameter, where T=1 corresponds to a spatially–resolved galaxy and T=2 to a stellar object.
(8) Offset (in arcsec) between the radio and optical positions.
(9,10) Total (integrated) 18 GHz flux density and estimated error. Note that these are generally higher than the peak flux densities listed in Table 3.5.
(11,12) 5 GHz flux density (in mJy) from the PMN catalogue (Gregory 1994), and estimated error.
(13,14) 843 MHz flux density (in mJy) from the SUMSS catalogue (Mauch et al. 2003), and estimated error. Where no flux density is listed, the source lies in an area of sky where SUMSS observations had not been completed by mid–2003, and which was therefore not included in the Jul–1–2003 version of the SUMSS catalogue.
(15,16) Radio spectral index between 843 MHz and 18 GHz, and estimated error.
(17) Source name in the NASA Extragalactic Database (NED) and notes on NED sources, when available.

Sixteen of the objects in Table 3.6 have published redshifts, and these range from z=0.014 to 0.183 for the galaxies and z=0.54 to 3.15 for the QSOs.

Fig. 3.14 shows the relation between 18 GHz flux density and spectral index for sources identified with QSOs, galaxies and blank fields. There appears to be a clear similarity between QSO and galaxy spectral index distributions, while in low-frequency surveys these populations have a very different behaviour. We suggest that our sample is dominated by

AGN in galaxy nuclei rather than radio galaxy lobes. This then points to a close similarity between radio-loud QSO and galaxy nuclei populations.

Reliability of the optical IDs

We used a series of Monte Carlo tests to estimate the number of spurious SuperCOSMOS radio–source IDs which arise from the chance superposition of a radio source and a foreground star or galaxy. To do this, we offset the position of each radio source by an amount (typically 10–30 arcmin) which is significantly larger than our 8 arcsec matching radius, but small enough that the surface density of SuperCOSMOS stars and galaxies should be similar. We then cross–matched the offset radio positions with the SuperCOSMOS catalogue in the same way as was done for the genuine radio positions. This was done four times, with offsets to the north, south, east and west of the original positions, to measure the average number of spurious matches.

We found that for a cut-off radius of 8 arcsec and an optical magnitude $B_J < 22$ mag, roughly 17% of the optical IDs in Table 3.6 are likely to be spurious, giving an overall reliability of ∼83%. This could be improved by measuring more accurate radio positions for the 18 GHz sources, so that the cut-off radius for matching could be reduced. The small number of very faint optical IDs ($B_J = 22 - 23$ mag) in Table 3.6 is close to the number expected by chance, suggesting that almost all of these very faint objects are chance associations rather than genuine IDs.

Optical identification rate

Restricting the sample to a limiting magnitude of $B_J = 22.0$ where the SuperCOSMOS catalogue is complete and the reliability of the radio–optical matching high, we find an overall optical ID rate of 80±8% (98/122 extragalactic sources). When corrected statistically for chance coincidences with foreground objects, this drops to 73% with an optical ID brighter than $B_J = 22.0$, where 51% are stellar objects (candidate QSOs), 22% galaxies and 27% faint objects or blank fields. This rate is comparable with the 83% ID rate reported by Snellen et al. (2002) for a sample of flat–spectrum radio sources selected at 6 cm and with flux densities above 200 mJy. It is however much higher than that found for weak low-frequency samples (Windhorst, Kron & Koo 1984; McMahon et al. 2002).

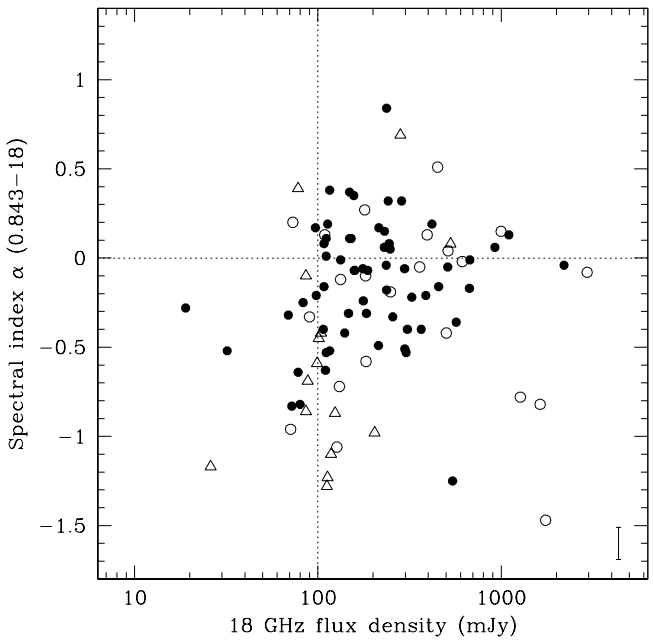

Figure 3.14: Plot of 0.843–18 GHz spectral index versus 18 GHz flux density for sources identified as QSOs (filled circles) and galaxies (open circles), and for sources which are blank fields ($B_J > 22$ mag, triangles). The error bar in the bottom right-hand corner is representative of the typical uncertainty in the spectral indices which is dominated by the typically 20% errors of 18 GHz flux densities.

3.2.10 Notes on individual sources

PKS 0021−686: We adopt the SuperCOSMOS classification as a stellar object, but note that the 2MASS Extended Objects catalogue (Jarrett et al. 2000) classified this as a galaxy with K_s(total)=13.65 mag. Detected as an X-ray source in the RASS Bright Source Catalogue (Voges et al. 1999).

PKS 0022−60: Compact double source shown in Fig. 3.15(a). The catalogued MRC flux density of 3.83 (±0.17) Jy at 408 MHz implies a radio spectral index $\alpha^{18}_{0.408} = -0.78 \pm 0.02$.

PKS 0101−649: The 843 MHz flux density is from Jones & McAdam (1992). Listed in the 2MASS Extended Objects catalogue as a galaxy with K_s(total)=13.41 mag.

PKS 0235−618: Detected as an X-ray source in the RASS Bright Source Catalogue. Jones & McAdam (1992) note that the original Parkes detection is resolved into a pair of unrelated sources at 843 MHz. The source detected at 18 GHz is associated with the western (brighter) member of the pair.

PMNJ 0422−6507: The optical ID is offset 7.9 arcsec in RA from the 18 GHz radio position, but is within 0.5 arcsec of the SUMSS position. We accept this as the correct ID because of the close agreement with the SUMSS position, and because the 18 GHz source is close to the edge of the observed field.

PKS 0516−621: The optical ID is within 0.1 arcsec of the VLBI position measured by Ma et al. (1998).

PKS 0522−611: Noted as a ROSAT X-ray source by Brinkmann, Siebert & Boller (1994).

PKS 1105−680: The optical ID found in SuperCOSMOS was first identified by Jauncey et al. (1989), and is within 0.1 arcsec of the Ma et al. (1998) VLBI position. The foreground Galactic extinction in this field ($b = -7.4°$) is $A_B = 0.99$ mag.

PKS 1133−681: There is no optical object within 5 arcsec of the 18 GHz radio position in the SuperCOSMOS catalogue. White et al. (1987) identify this source with a faint (B=22.2 mag.) galaxy which is just visible on the SuperCOSMOS B image. The foreground Galactic extinction in this field ($b = -6.6°$) is $A_B = 2.0$ mag.

PKS 1420−679: The SuperCOSMOS image shows no optical object within 5 arcsec of the radio position. White et al. (1987) identify this source with a faint (B=22.2 mag.) stellar object, but this should be regarded as uncertain without spectroscopic confirmation because of the high surface density of foreground stars at this low Galactic latitude. The Galactic extinction in this field ($b = -6.8°$) is $A_B = 2.4$ mag.

PKS 1448−648: The SuperCOSMOS image shows no optical object within 5 arcsec of the radio position. White et al. (1987) identify this source with a faint (B=22.0 mag.) galaxy which is 7.5 arcsec from the 18 GHz position, but this object is classified as stellar by SuperCOSMOS and may be a foreground star. The extinction in this low-latitude region ($b = -5.1°$) is $A_B = 3.2$ mag.

WKK 5585: Detected as an X-ray source in the RASS Bright Source Catalogue (Voges et al. 1999).

NGC 6328: This nearby (z=0.014) galaxy is the optical counterpart of the radio galaxy PKS 1718−649, which is the closest-known GPS radio source (Tingay et al. 1997).

PKS 1801−702: A bright elliptical galaxy without a catalogued redshift, K_s(total)=13.65 mag in the 2MASS Extended Objects catalogue.

PKS 1814−63: A nearby (z=0.0627) active galaxy, with K_s(total)=13.65 mag in the 2MASS Extended Objects catalogue.

PKS 1819−67: Highly-polarized double source with no optical ID, discussed in §3.2.6.

PKS 1922−62: This source is 4.5 arcmin from the strong radio source PKS 1922−62. Large pointing errors in PMN (Parkes telescope beam width is about 5 arcmin) are likely to be the cause of the offset.

PKS 1934−638: This strong and well–studied radio galaxy was the prototype GPS source (O'Dea et al. 1991).

PMNJ 2008−6110: Compact source with a highly–inverted radio spectrum and no optical ID.

MRC 2041−617: Detected as an X-ray source in the RASS Bright Source Catalogue (Voges et al. 1999) and shown in Fig. 3.15(c).

ESO 075−G41: The two components detected here (Fig. 3.15d) are the core and southern hotspot of this nearby (z=0.028) radio galaxy.

PKS 2210−637: Detected as an X-ray source in the RASS Bright Source Catalogue (Voges et al. 1999).

PKS 2300−683: Noted as a ROSAT X-ray source by Brinkmann, Siebert & Boller (1994).

PKS 2303−656: There is no optical counterpart in the SuperCOSMOS catalogue, but Jackson et al. (2002) report that a faint red galaxy is visible on CCD images of this field, with a tentative redshift of z=0.470 from an optical spectrum.

IRAS 23074−5957: Noted by Roy & Norris (1997) as a member of the rare class of 'radio–excess infrared galaxies'. Listed in the 2MASS Extended Objects catalogue with K_s(total)=14.00 mag.

PKS 2356−61: Well known FRII radio galaxy (Koekemoer & Bicknell 1998)– both hotspots are detected at 18 GHz. The host galaxy has K_s(total)=12.86 mag in the 2MASS Extended Objects catalogue.

3.3 Conclusions

The wide-band interferometer (total bandwidth spanning from 16 to 20 GHz) produced by linking a wide–band correlator to two ATCA antennas equipped with low–noise receivers allowed us to survey the sky at a rate of more than 12 deg^2 per hour to a detection limit

of $\sim 100\,\mathrm{mJy}$ despite the small primary beam area (FWHM = 2.3 arcmin). A total of 221 sources have been confirmed by follow-up observations and had flux densities and positions measured.

The distribution with Galactic latitude shows a sharp peak with FWHM in $|b|$ of 1.9° due to Galactic sources.

We exclude the galactic plane and use only the 123 sources with $|b| > 5°$. Although this pilot survey is not extremely uniform we know the sensitivity map and can estimate the 18 GHz counts of extragalactic sources down to $\simeq 100\,\mathrm{mJy}$. The results are in good agreement with the 15 GHz counts by Taylor et al. (2001), with the preliminary VSA (Grainge et al. 2003) and DASI (Leitch et al. 2002) counts, with the WMAP counts at 41 GHz (Bennett et al. 2003) and with the 9C survey at 15 GHz by Waldram et al. (2003). We determine the source counts particularly well in the crucial 200–800 mJy flux range, bridging the gap between the 9C and the WMAP surveys. With our estimate of the slope as $S^{-2.2}$ we can confirm that the Planck mission will only need to measure and correct for foreground sources down to the 100 mJy level in order to push the fluctuations due to extragalactic radio sources below the instrumental noise (cf. Fig. 6 of De Zotti et al. 1999a). At this flux level a blind survey of the entire sky at 20 GHz is feasible.

Although this survey has not revealed any new class of radio sources, we drew attention to the huge scatter in the flux - flux scatter plot (Fig. 3.9) which suggests that care is needed when using low-frequency surveys to correct high-frequency CMB observations.

The radio spectral index distribution of the extragalactic sources shows that over 70% of them are "flat"-spectrum ($\alpha^{18}_{0.843} > -0.5$, $S_\nu \propto \nu^\alpha$), including 30 (29%) sources with rising spectrum ($\alpha^{18}_{0.843} > 0$). We have a significant population of sources with minima in their spectrum in the 1-10 GHz range.

The optical identification rate of 73% is very high: 51% of the extragalactic sample sources are identified with stellar objects (candidate QSOs) and 22% with radio galaxies. This is almost a factor of 3 higher than the identification rate in surveys at comparable flux levels at 1.4 GHz. This indicates that the high-frequency source population has a luminosity function which does not extend to such high power as in lower frequency samples. We thus expect that high-frequency surveys will be more sensitive to clustering effects.

A statistical estimate of fractional polarization distribution yielded a median value

of 2.1% which is low compared with the steeper spectrum population. It agrees with the median polarization measured for the flat-spectrum population in the Kühr sample (Ricci et al. 2004a), again indicating that this high-frequency survey has not revealed any new population of sources at this flux level. With the median polarization below that expected for CMB E-mode, Planck will have no difficulty correcting for this foreground population. However B-mode CMB polarization is much harder to detect and correction for polarised sources will be necessary. Future targeted follow–up with much higher polarization sensitivity is possible.

In the near future we plan to cover 2×10^4 deg^2 in the southern sky by using an improved and more powerful version of the wide band correlator (3 baselines and 8 GHz bandwidth) being able to reach a 100% completeness for all sources with $S_{20\mathrm{GHz}} > 40$ mJy and we expect to detect $\simeq 2 \times 10^4$ extragalactic sources down to that limiting flux density.

This survey has confirmed a lower than expected density of sources at high frequency making the mm array calibration problem more difficult, however the full-sky ATCA 20 GHz (AT20G) survey will still be able to provide a superb calibration source network for ALMA with a density of about one source per square degree down to 40mJy.

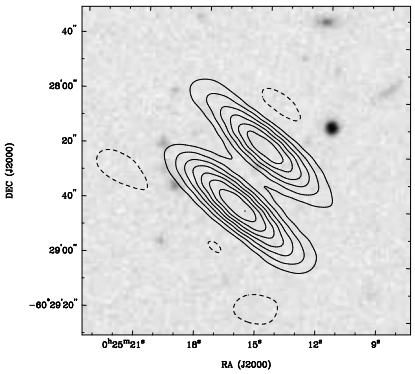

(a) PKS 0022−60

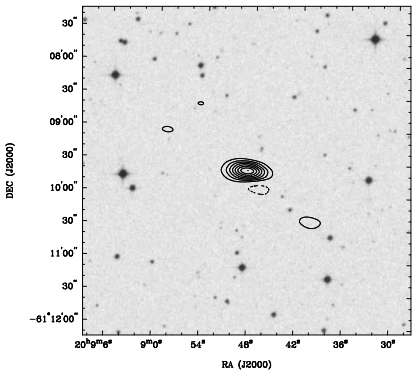

(b) PMNJ 2008−6110

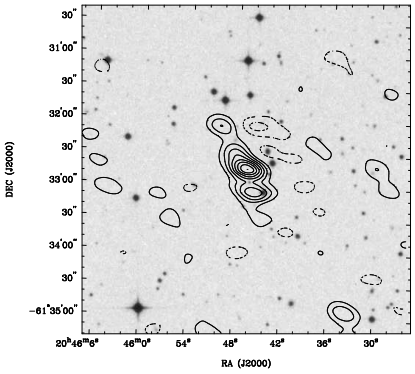

(c) MRC 2041−617

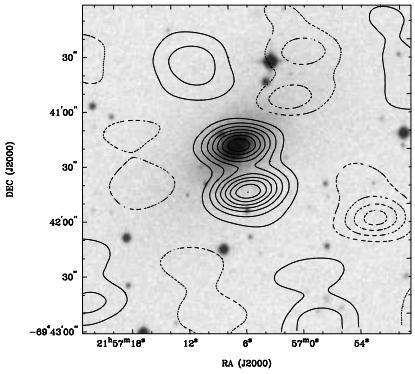

(d) ESO 075−41

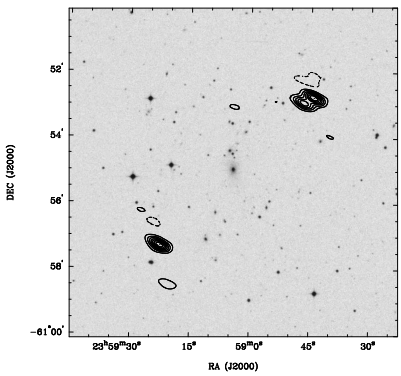

(e) PKS 2356−61

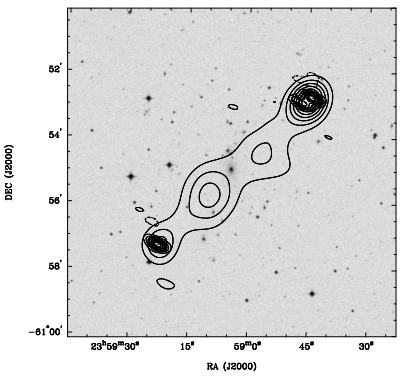

(f) PKS 2356−61 with 843 MHz contours

Figure 3.15: Radio contours overlaid on SuperCOSMOS optical images of sources detected at 18 GHz and discussed in the text.

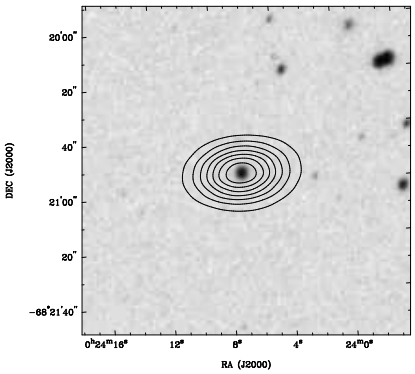

(a) PKS 0021−686

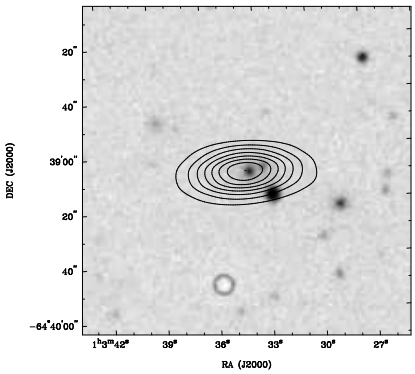

(b) PKS 0101−649

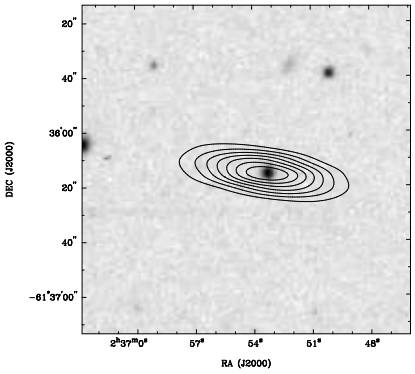

(c) PKS 0235−618

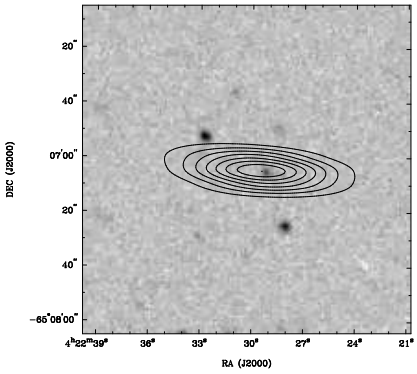

(d) PMNJ 0422−6507

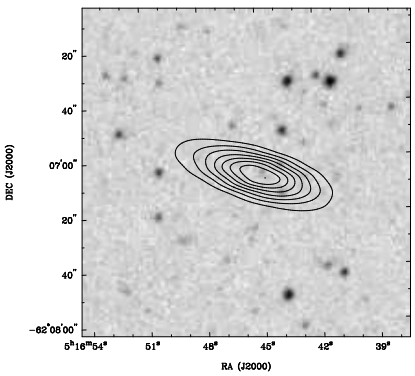

(e) PKS 0516−621

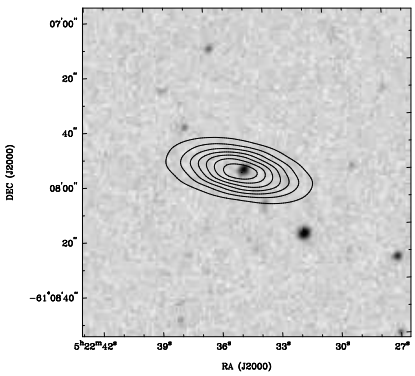

(f) PKS 0522−611

Figure 3.16: Radio contours overlaid on SuperCOSMOS optical images of sources detected at 18 GHz and discussed in the text.

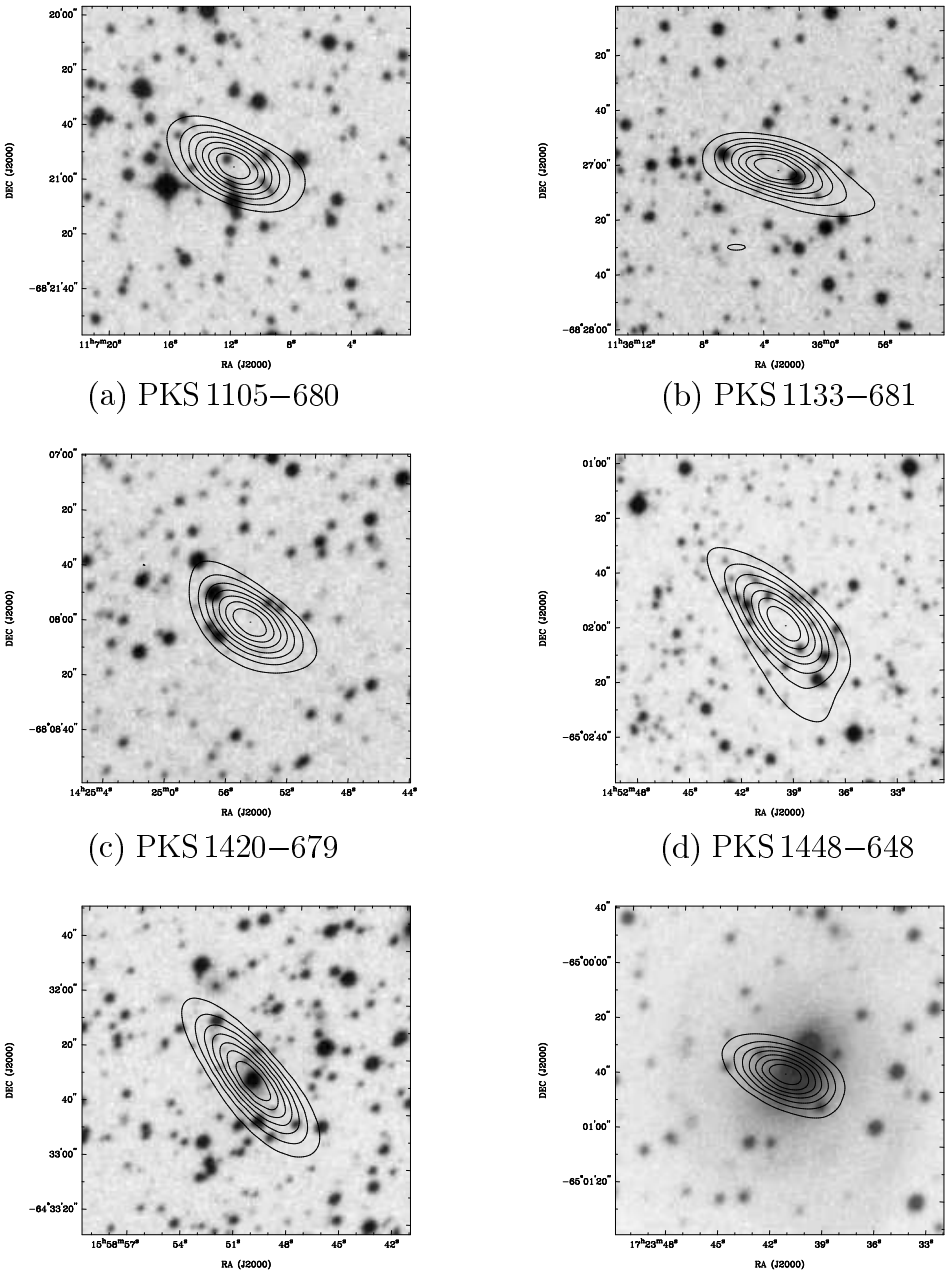

(a) PKS 1105−680 (b) PKS 1133−681

(c) PKS 1420−679 (d) PKS 1448−648

(e) WKK 5585 (f) NGC 6328

Figure 3.17: Radio contours overlaid on SuperCOSMOS optical images of sources detected at 18 GHz and discussed in the text.

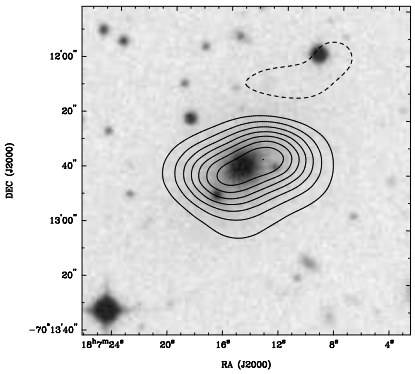

(a) PKS 1801−702

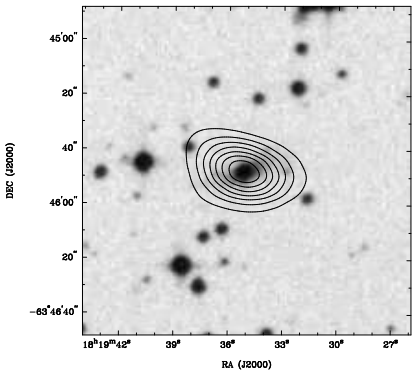

(b) PKS 1814−63

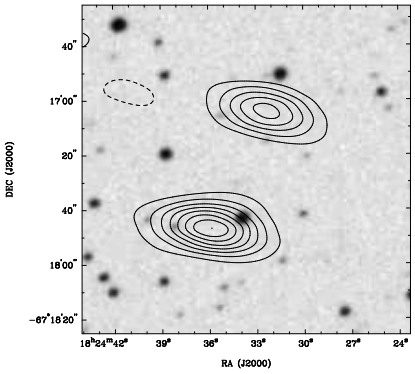

(c) PKS 1819−67

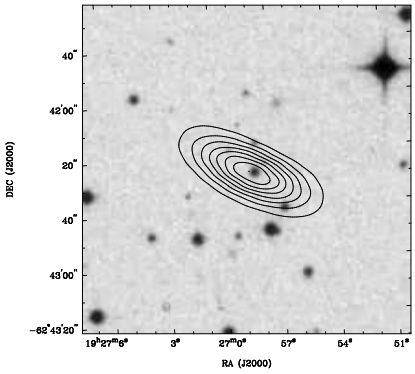

(d) SUMSSJ 192659−624225

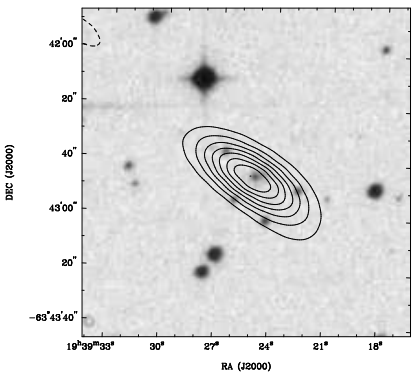

(e) PKS 1934−63

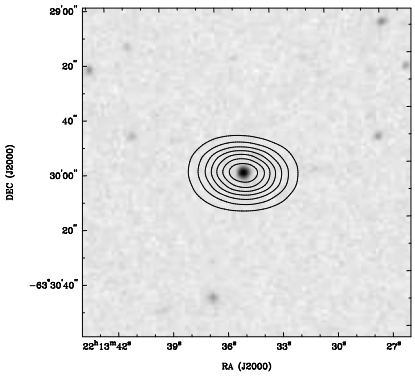

(f) PKS 2210−637

Figure 3.18: Radio contours overlaid on SuperCOSMOS optical images of sources detected at 18 GHz and discussed in the text.

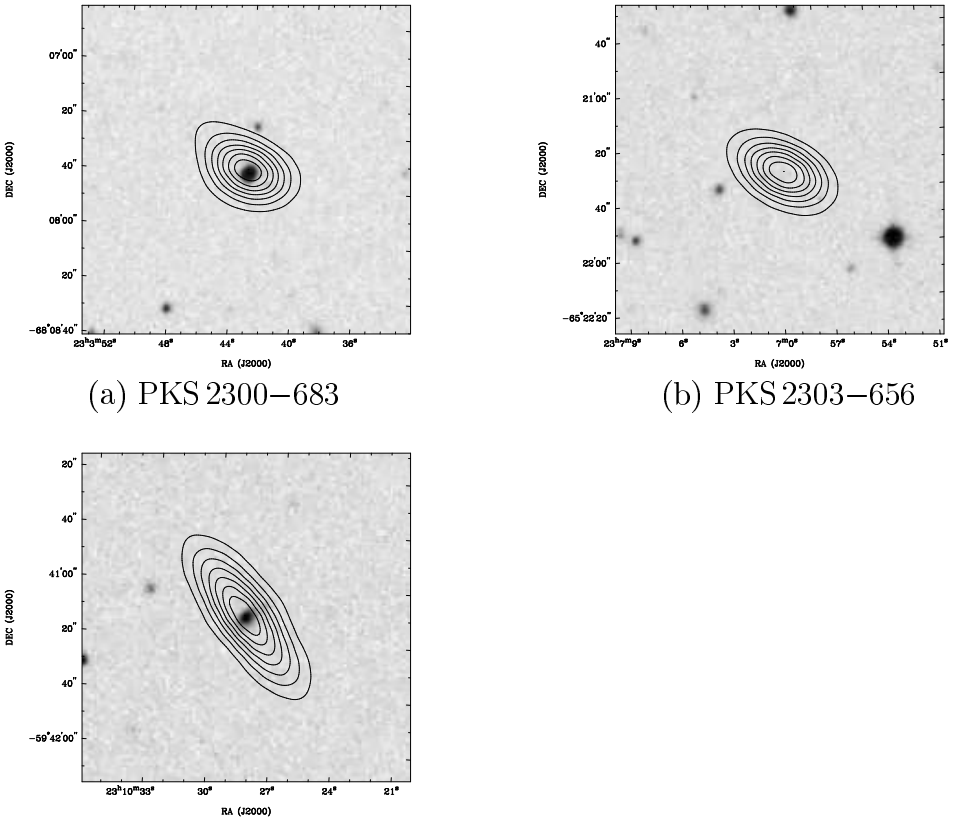

(a) PKS 2300−683

(b) PKS 2303−656

(c) IRAS 23074−5957

Figure 3.19: Radio contours overlaid on SuperCOSMOS optical images of sources detected at 18 GHz and discussed in the text.

Table 3.5: Measured positions and flux densities for confirmed 18 GHz detections. The listed parameters are as follows (1) Source name (L indicates a source within the boundaries of the LMC); (2,3) Source position (position errors are 2.0 sec and 1.1 arcsec in RA and dec respectively); (4,5) Galactic latitude and longitude; (6,7) Source offset from the pointing centre of the 18 GHz follow-up image; (8,9) 18 GHz peak flux density and its error; (10) Sources which are strongly resolved in the 18 GHz images (i.e. with angular sizes typically > 10 arcsec) are shown by an R.

(1) Name	(2) α (J2000)	(3) δ (J2000)	(4) l (deg)	(5) b (deg)	(6) ΔX (arcsec)	(7) ΔY (arcsec)	(8) S_{pk} (Jy)	(9) ΔS_{pk} (Jy)	(10) Extension
0024−6821	00 24 06.47	−68 20 54.3	306.7	−48.6	−63.7	16.6	0.333	0.067	–
0025−6028 (N)	00 25 15.36	−60 28 16.4	308.8	−56.4	47.1	41.6	0.046	0.009	R
0025−6028 (S)	00 25 16.46	−60 28 38.8	308.7	−56.4	55.2	19.2	0.056	0.012	R
0103−6438	01 03 33.93	−64 39 08.0	300.8	−52.4	−19.6	−16.9	0.260	0.052	–
0109−6048	01 09 15.35	−60 49 49.1	299.0	−56.2	−19.3	−77.1	0.830	0.166	–
0110−6315	01 10 17.05	−63 15 56.2	299.4	−53.7	54.3	−48.4	0.151	0.030	–
0112−6634	01 12 19.05	−66 34 45.1	299.7	−50.4	30.1	−28.0	0.377	0.075	–
0112−6752	01 13 11.81	−67 53 04.0	299.8	−49.1	83.6	−64.1	0.118	0.024	–
0132−6522	01 32 39.40	−65 23 35.3	296.1	−51.2	58.6	−55.2	0.102	0.020	–
0144−6422	01 44 16.82	−64 21 43.0	293.7	−51.8	−14.0	25.8	0.267	0.053	–
0150−6044	01 50 50.32	−60 44 07.6	290.3	−54.9	9.6	−0.6	0.066	0.013	–
0158−6333	01 58 55.42	−63 34 50.6	290.8	−51.9	69.5	−84.7	0.106	0.021	–
0158−6410	01 58 37.28	−64 11 28.5	291.3	−51.4	47.5	−40.4	0.132	0.026	–
0203−6846	02 03 53.41	−68 46 59.5	293.4	−47.0	−19.4	−48.5	0.070	0.014	–
0207−6217	02 08 01.25	−62 16 34.7	288.4	−52.6	22.7	29.3	0.150	0.030	–
0214−6149	02 14 15.90	−61 49 34.0	287.0	−52.7	−71.4	21.0	0.233	0.047	–
0214−7025	02 14 04.15	−70 27 07.1	293.3	−45.1	0.7	−104.9	0.147	0.029	–
0236−6135	02 36 54.39	−61 36 14.4	283.2	−51.3	131.2	−68.5	0.485	0.097	–
0251−6801	02 51 10.91	−68 02 08.5	287.5	−45.3	−34.0	−35.5	0.074	0.015	–
0303−6211	03 03 51.28	−62 11 24.9	280.2	−48.7	128.0	−6.9	1.519	0.304	–
0303−6458	03 03 50.90	−64 58 53.8	283.2	−46.8	−0.5	−10.8	0.140	0.028	–
0314−6547	03 14 22.47	−65 48 24.3	283.0	−45.4	−27.8	−50.2	0.288	0.058	–
0323−6027	03 23 08.55	−60 26 31.5	276.0	−48.0	41.1	49.5	0.151	0.030	–
0340−6702	03 40 28.23	−67 03 16.9	282.0	−42.6	36.4	−75.9	0.172	0.034	–
0341−5953	03 41 21.81	−59 54 08.6	273.5	−46.4	−1.3	−45.5	0.144	0.029	–
0357−6949	03 57 30.38	−69 48 44.2	283.9	−39.7	89.9	22.7	0.205	0.041	–
0408−6544	04 08 20.67	−65 45 09.1	278.6	−40.9	16.5	−49.9	0.513	0.103	–
0422−6506	04 22 30.42	−65 07 04.7	277.1	−39.8	91.0	−59.8	0.104	0.021	–
0424−6646	04 25 07.79	−66 46 49.7	278.9	−38.9	111.2	−48.7	0.221	0.044	–
0428−6437	04 28 11.05	−64 38 23.0	276.2	−39.4	0.3	−35.9	0.161	0.032	–
0431−6405 L	04 31 28.25	−64 06 31.6	275.4	−39.3	−24.5	−40.8	0.152	0.030	–
0433−6029	04 33 34.28	−60 30 14.7	270.9	−40.2	24.3	−64.8	0.340	0.068	–
0438−6502 L	04 38 40.25	−65 03 21.9	276.2	−38.2	8.0	−81.8	0.091	0.018	–
0443−6651 L	04 43 17.55	−66 52 05.1	278.2	−37.2	−79.2	−32.1	0.255	0.051	–
0503−6048	05 04 01.88	−60 49 52.5	270.2	−36.4	21.0	−99.4	0.112	0.022	–
0505−6215	05 05 46.83	−62 15 44.9	271.9	−36.0	−22.1	4.1	0.147	0.029	–
0505−6236	05 05 48.66	−62 36 11.0	272.3	−35.9	4.6	2.0	0.139	0.028	–
0509−6852 L	05 09 51.96	−68 53 03.6	279.7	−34.3	−5.6	−29.5	0.138	0.028	R
0515−6721 L	05 15 38.54	−67 21 26.8	277.8	−34.1	84.0	−4.6	0.201	0.040	–

Table 3.5: Confirmed 18 GHz detections. (*continued*)

(1) Name	(2) α (J2000)	(3) δ (J2000)	(4) l (deg)	(5) b (deg)	(6) ΔX (arcsec)	(7) ΔY (arcsec)	(8) S_{pk} (Jy)	(9) ΔS_{pk} (Jy)	(10) Extension
0516−6205	05 16 45.74	−62 07 05.3	271.5	−34.8	117.4	−77.3	0.465	0.093	–
0522−6106	05 22 34.34	−61 07 58.2	270.2	−34.2	−55.3	−60.0	1.018	0.204	–
0526−6749 *L*	05 26 36.23	−67 49 07.1	278.1	−32.9	80.5	31.6	0.143	0.029	–
0534−6106	05 34 35.86	−61 06 05.5	270.1	−32.7	−51.7	24.5	0.481	0.096	–
0535−6601 *L*	05 35 43.26	−66 02 00.8	275.9	−32.3	38.1	−47.9	0.100	0.020	R
0537−6908 *L*	05 37 45.32	−69 10 07.9	279.6	−31.7	49.8	−81.0	0.412	0.082	R
0538−6901 *L*	05 38 31.83	−69 02 05.6	279.4	−31.7	−38.4	−49.4	0.090	0.018	R
0538−6906 *L*	05 38 32.66	−69 06 56.9	279.5	−31.7	−28.4	−5.9	0.148	0.030	R
0540−6938 *L*	05 39 44.28	−69 38 42.7	280.1	−31.5	−81.9	3.4	0.449	0.090	R
0540−6941 *L*	05 40 25.32	−69 40 13.3	280.1	−31.5	58.9	81.6	0.050	0.010	R
0540−6944 *L*	05 40 05.90	−69 44 42.3	280.2	−31.5	30.6	−23.1	0.136	0.027	R
0552−6401 *L*	05 52 24.34	−64 02 10.4	273.5	−30.6	−24.0	−11.4	0.096	0.019	R
0713−6428	07 13 01.69	−64 29 06.7	275.4	−22.1	−47.1	−62.8	0.055	0.011	–
0719−6327	07 19 07.12	−63 26 59.3	274.5	−21.1	−32.7	31.6	0.089	0.018	–
0744−6919	07 44 20.74	−69 19 06.0	281.4	−20.8	−11.8	26.9	0.221	0.044	–
0827−6021	08 27 36.30	−60 21 43.8	275.4	−12.5	9.7	−34.8	0.065	0.013	–
0842−6408	08 42 41.70	−64 09 59.9	279.6	−13.3	30.8	−115.0	0.090	0.018	–
0845−6525	08 45 11.79	−65 27 22.7	280.8	−13.8	36.1	−89.7	0.257	0.051	–
0846−6313	08 46 35.97	−63 13 34.8	279.1	−12.4	−0.2	−21.7	0.097	0.019	–
0901−6636	09 01 16.23	−66 36 29.7	282.8	−13.2	96.7	−12.8	0.183	0.037	–
0931−6227	09 31 27.39	−62 29 34.4	282.0	−8.1	−45.7	−95.3	0.244	0.049	–
1107−6819	11 07 11.45	−68 20 54.9	293.5	−7.4	−97.1	−65.0	0.988	0.198	–
1111−6110	11 10 47.47	−61 11 07.3	291.1	−0.6	−97.7	−12.3	0.028	0.006	–
1111−6114	11 11 19.65	−61 17 23.5	291.2	−0.7	141.7	−150.5	2.939	0.588	–
1115−6113	11 15 30.68	−61 13 02.9	291.6	−0.5	−74.4	13.8	0.145	0.029	R
1116−6109	11 15 53.73	−61 09 22.5	291.7	−0.4	−81.4	18.4	0.185	0.037	R
1123−6416	11 23 19.26	−64 17 37.5	293.6	−3.0	−37.4	−44.4	0.369	0.074	–
1124−6212	11 24 51.68	−62 12 58.4	293.0	−1.0	−30.1	−2.3	0.083	0.017	R
1136−6826	11 36 02.21	−68 27 06.7	296.1	−6.6	6.6	−28.6	0.414	0.083	–
1138−6329	11 38 58.38	−63 28 30.3	294.9	−1.7	49.3	33.7	0.051	0.010	R
1138−6809	11 38 22.16	−68 10 33.9	296.2	−6.3	−4.6	−40.9	0.184	0.037	R
1147−6753	11 47 32.98	−67 53 42.9	297.0	−5.8	−73.5	15.0	1.155	0.231	–
1200−6304	12 00 57.08	−63 04 14.9	297.3	−0.8	34.6	4.9	0.092	0.018	R
1203−6308	12 03 09.95	−63 08 16.7	297.5	−0.8	−13.9	1.1	0.162	0.032	R
1203−6311	12 03 16.44	−63 11 16.7	297.5	−0.8	29.9	14.4	0.118	0.024	–
1204−6320	12 04 06.84	−63 21 41.5	297.7	−1.0	39.3	−64.6	0.074	0.015	–
1208−6314	12 09 00.99	−63 15 58.3	298.2	−0.8	87.6	−90.4	0.770	0.154	–
1209−6243	12 09 55.72	−62 44 23.1	298.2	−0.3	80.5	−47.0	0.088	0.018	R
1210−6250	12 10 00.66	−62 49 56.6	298.2	−0.3	−98.1	3.3	3.936	0.787	–
1214−6259	12 15 00.71	−62 59 25.4	298.8	−0.4	32.1	17.3	0.029	0.006	–
1214−6300	12 14 56.79	−63 02 25.9	298.8	−0.5	19.0	−127.8	0.080	0.016	–
1215−6254	12 15 23.70	−62 55 14.2	298.8	−0.3	−111.3	−56.1	0.545	0.109	R

Table 3.5: Confirmed 18 GHz detections. (*continued*)

(1) Name	(2) α (J2000)	(3) δ (J2000)	(4) l (deg)	(5) b (deg)	(6) ΔX (arcsec)	(7) ΔY (arcsec)	(8) S_{pk} (Jy)	(9) ΔS_{pk} (Jy)	(10) Extension
1215−6300	12 15 24.38	−63 01 26.1	298.9	−0.4	104.7	−47.1	2.780	0.556	R
1215−6301	12 15 48.75	−63 02 55.1	298.9	−0.5	5.1	−72.0	0.233	0.047	R
1222−6036	12 22 06.09	−60 35 32.9	299.3	2.1	−36.0	27.1	0.258	0.052	–
1224−6649	12 24 30.42	−66 50 21.8	300.3	−4.1	−15.1	−35.7	0.198	0.040	–
1225−6424	12 25 55.95	−64 25 58.1	300.2	−1.7	32.0	−75.1	0.108	0.022	–
1231−6311	12 31 11.24	−63 11 41.9	300.7	−0.4	−38.8	0.1	0.174	0.035	–
1235−6302	12 35 35.46	−63 02 29.4	301.1	−0.2	71.0	10.5	0.991	0.198	–
1236−6150	12 36 02.62	−61 51 13.5	301.1	1.0	−16.7	−26.3	0.982	0.196	R
1239−6845	12 39 46.91	−68 45 27.8	301.9	−5.9	81.1	11.2	0.220	0.044	–
1243−6254	12 43 32.40	−62 55 04.9	302.0	−0.1	139.4	−48.9	0.810	0.162	–
1254−6111	12 54 46.16	−61 11 36.3	303.3	1.7	−42.2	−36.3	0.247	0.049	–
1258−6719	12 58 28.69	−67 19 43.6	303.6	−4.5	38.6	13.1	0.122	0.024	–
1308−6707	13 08 17.26	−67 07 04.2	304.6	−4.3	−4.3	23.8	0.417	0.083	–
1310−6238	13 09 59.13	−62 37 57.5	305.1	0.2	−47.3	28.5	0.106	0.021	R
1310−6245	13 10 08.19	−62 46 07.7	305.1	0.0	−163.4	−58.7	0.572	0.114	–
1311−6229	13 11 45.73	−62 29 09.4	305.3	0.3	−43.4	−4.5	0.522	0.104	R
1311−6232	13 11 07.09	−62 34 44.2	305.2	0.2	7.5	−123.4	0.111	0.022	–
1311−6233	13 12 14.74	−62 34 34.1	305.3	0.2	157.1	−43.0	2.155	0.431	R
1311−6243	13 11 14.29	−62 45 03.5	305.2	0.0	2.0	−68.3	3.657	0.731	R
1311−6246	13 11 54.81	−62 47 08.8	305.3	−0.0	80.9	−20.9	2.062	0.412	R
1312−6234	13 12 30.78	−62 34 32.9	305.4	0.2	−153.4	−31.7	2.722	0.544	R
1314−6223	13 13 53.78	−62 23 25.2	305.5	0.4	−84.9	−16.4	0.224	0.045	R
1314−6244	13 14 19.68	−62 44 33.2	305.5	0.0	39.1	−22.2	0.451	0.090	R
1314−6247	13 14 09.49	−62 47 30.8	305.5	−0.0	37.6	3.1	0.097	0.019	R
1317−6227	13 17 03.38	−62 28 20.1	305.9	0.3	−11.1	−51.0	0.153	0.031	–
1321−6300	13 21 16.88	−63 01 13.4	306.3	−0.3	5.9	−28.4	0.119	0.024	R
1332−6249	13 32 49.20	−62 48 30.1	307.6	−0.3	−46.4	40.7	0.039	0.008	R
1332−6646	13 32 37.79	−66 46 49.2	307.0	−4.2	34.3	−17.1	0.220	0.044	–
1336−6249	13 36 32.40	−62 49 05.5	308.0	−0.4	71.2	25.5	0.185	0.037	–
1337−6508	13 37 52.35	−65 09 24.8	307.8	−2.7	8.5	−41.8	0.794	0.159	–
1339−6142	13 39 58.92	−61 42 44.9	308.6	0.6	56.3	−19.7	0.061	0.012	R
1340−6144	13 40 52.32	−61 45 33.2	308.7	0.6	−33.1	−60.3	0.027	0.005	–
1342−6208	13 43 01.97	−62 08 57.3	308.9	0.1	34.8	−34.4	0.339	0.068	–
1343−6131	13 43 20.00	−61 31 57.1	309.1	0.7	35.7	−56.0	0.137	0.027	–
1345−6213	13 45 28.18	−62 14 31.9	309.2	−0.0	71.2	−78.9	0.141	0.028	–
1346−6021	13 46 44.56	−60 23 18.4	309.7	1.8	152.5	−99.6	1.961	0.392	–
1346−6026	13 46 14.35	−60 29 25.3	309.6	1.7	69.2	−154.4	0.584	0.117	R
1347−6020	13 47 17.27	−60 21 13.3	309.8	1.8	31.6	−17.3	0.055	0.011	R

Table 3.5: Confirmed 18 GHz detections. (*continued*)

(1) Name	(2) α (J2000)	(3) δ (J2000)	(4) l (deg)	(5) b (deg)	(6) ΔX (arcsec)	(7) ΔY (arcsec)	(8) S_{pk} (Jy)	(9) ΔS_{pk} (Jy)	(10) Extension
1347−6021	13 47 29.86	−60 21 07.0	309.8	1.8	−38.0	33.9	0.078	0.016	R
1350−6134	13 50 41.20	−61 35 12.6	309.9	0.5	−112.7	−23.5	0.900	0.180	–
1350−6140	13 50 35.00	−61 40 20.0	309.9	0.4	85.5	39.0	0.153	0.031	–
1350−6147	13 50 14.96	−61 48 55.3	309.8	0.3	−21.5	−71.2	0.091	0.018	–
1353−6631	13 53 57.25	−66 30 50.1	309.1	−4.4	−4.5	34.8	0.347	0.069	–
1355−6326	13 55 46.22	−63 26 43.1	310.0	−1.5	8.1	−37.1	1.090	0.218	–
1356−6206	13 57 00.69	−62 07 11.9	310.5	−0.2	11.9	−70.8	0.371	0.074	R
1400−6209	14 00 34.36	−62 10 37.6	310.9	−0.4	114.6	−85.6	0.220	0.044	–
1404−6119	14 04 55.16	−61 20 04.9	311.6	0.3	15.6	−58.9	1.758	0.352	–
1406−6158	14 06 38.84	−61 58 22.3	311.6	−0.4	−36.2	9.5	0.282	0.056	–
1407−6119	14 07 22.67	−61 20 30.5	311.9	0.2	4.7	−61.5	0.128	0.026	R
1407−6126	14 07 26.09	−61 26 24.6	311.9	0.1	86.7	−7.7	0.044	0.009	R
1407−6127	14 07 35.87	−61 27 26.6	311.9	0.1	113.8	17.3	0.298	0.060	R
1408−6109	14 08 42.72	−61 10 41.1	312.1	0.3	55.9	−66.1	1.210	0.242	R
1408−6146	14 08 06.55	−61 46 18.0	311.9	−0.2	−3.1	17.8	0.142	0.028	R
1417−5950	14 17 41.71	−59 50 35.7	313.6	1.2	−47.3	−25.6	0.993	0.199	–
1419−6050	14 19 35.26	−60 51 52.5	313.5	0.2	31.1	−68.6	0.436	0.087	–
1421−5954	14 21 40.60	−59 53 56.2	314.0	1.0	−2.8	11.8	0.046	0.009	–
1424−6021	14 24 58.05	−60 22 52.9	314.2	0.4	44.8	−97.0	0.362	0.072	R
1424−6808	14 24 55.62	−68 07 54.6	311.5	−6.8	42.6	19.3	0.791	0.158	–
1434−6839	14 34 28.47	−68 39 51.6	312.1	−7.6	51.7	−50.7	0.018	0.004	–
1441−6030	14 42 02.07	−60 30 22.0	316.1	−0.5	37.4	7.9	1.019	0.204	R
1444−5946	14 45 16.62	−59 48 29.8	316.8	−0.0	163.1	−90.9	2.986	0.597	R
1444−5950	14 45 03.00	−59 49 07.5	316.8	−0.0	60.2	60.4	0.248	0.050	R
1444−5953	14 44 52.52	−59 53 25.4	316.7	−0.1	−11.1	−7.4	0.038	0.008	R
1445−5948	14 45 12.43	−59 48 39.0	316.8	−0.0	25.9	15.9	0.404	0.081	R
1445−5949	14 45 22.28	−59 49 31.4	316.8	−0.1	−163.6	23.6	2.245	0.449	R
1445−5952	14 45 11.73	−59 52 28.6	316.8	−0.1	20.5	24.2	0.025	0.005	–
1452−5910	14 52 05.23	−59 10 08.1	317.9	0.2	−5.8	−8.0	0.101	0.020	–
1452−6502	14 52 39.49	−65 01 59.2	315.3	−5.1	28.5	37.8	0.118	0.024	–
1455−5936	14 55 41.96	−59 37 09.6	318.1	−0.4	98.4	−23.6	0.059	0.012	R
1457−6108	14 57 48.91	−61 09 44.3	317.6	−1.9	57.3	−55.2	0.091	0.018	–
1512−6507	15 12 33.69	−65 06 52.7	317.1	−6.2	42.2	34.2	0.064	0.013	–
1516−6425	15 16 40.02	−64 25 24.1	317.8	−5.8	13.1	−11.2	0.073	0.015	–
1546−6835	15 46 43.04	−68 37 35.4	317.8	−11.0	−27.1	−97.4	0.219	0.044	–
1558−6433	15 58 50.77	−64 32 26.7	321.4	−8.6	50.1	49.2	0.401	0.080	–
1619−6820	16 19 37.26	−68 21 23.0	320.3	−12.8	62.3	−41.9	0.081	0.016	–
1624−6808	16 24 18.01	−68 09 11.5	320.7	−13.0	44.7	−56.5	0.568	0.114	–

Table 3.5: Confirmed 18 GHz detections. (*continued*)

(1) Name	(2) α (J2000)	(3) δ (J2000)	(4) l (deg)	(5) b (deg)	(6) ΔX (arcsec)	(7) ΔY (arcsec)	(8) S_{pk} (Jy)	(9) ΔS_{pk} (Jy)	(10) Extension
1647−6438	16 47 37.54	−64 38 01.0	325.0	−12.5	−73.5	8.9	0.549	0.110	–
1703−6509	17 03 50.55	−65 11 06.5	325.6	−14.2	72.8	−76.4	0.100	0.020	–
1721−6154	17 21 39.47	−61 54 42.1	329.6	−14.0	102.1	13.8	0.328	0.066	–
1723−6500	17 23 42.08	−65 00 36.3	327.0	−15.8	101.9	−0.3	2.816	0.563	–
1726−6426	17 26 57.92	−64 27 54.8	328.0	−15.9	−0.4	−57.0	0.192	0.038	–
1734−6214	17 35 08.24	−62 15 22.1	330.1	−15.6	113.4	−53.0	0.244	0.049	–
1736−5951	17 36 30.65	−59 51 59.2	332.3	−14.5	19.9	−4.4	0.205	0.041	–
1743−6627	17 43 49.08	−66 26 27.6	326.7	−18.3	18.5	39.1	0.148	0.030	–
1749−6258	17 49 25.80	−62 58 17.6	330.2	−17.3	32.7	21.5	0.168	0.034	–
1754−6424	17 54 41.82	−64 23 45.6	329.1	−18.5	−1.1	68.3	0.071	0.014	–
1759−5947	17 59 06.39	−59 46 59.1	333.8	−17.0	18.0	16.7	0.091	0.018	–
1803−6507	18 03 23.38	−65 07 36.8	328.8	−19.6	78.1	18.0	0.992	0.198	–
1807−6414	18 07 54.08	−64 13 50.9	329.9	−19.7	−12.4	14.0	0.428	0.086	–
1807−7012	18 07 14.76	−70 12 39.9	323.9	−21.8	19.1	−25.8	0.131	0.026	R
1819−6346	18 19 35.06	−63 45 47.8	330.9	−20.8	−39.3	27.0	1.444	0.289	–
1821−6840	18 21 16.13	−68 40 40.7	325.9	−22.5	60.6	−30.6	0.019	0.004	–
1822−6359	18 22 17.04	−63 59 12.4	330.7	−21.1	105.6	−11.4	0.085	0.017	–
1824−6717 (N)	18 24 31.84	−67 17 04.8	327.4	−22.4	−93.5	17.4	0.105	0.023	R
1824−6717 (S)	18 24 35.53	−67 17 47.1	327.4	−22.4	−72.2	−25.0	0.123	0.027	R
1836−6648	18 36 59.51	−66 49 06.8	328.3	−23.4	26.6	−15.7	0.127	0.025	R
1840−6151	18 40 15.05	−61 52 06.3	333.6	−22.4	−27.8	−30.2	0.241	0.048	–
1840−6957	18 40 48.37	−69 57 48.1	325.0	−24.5	27.6	−36.9	0.026	0.005	R
1848−6416	18 48 55.68	−64 15 38.8	331.3	−24.0	17.4	44.2	0.075	0.015	–
1852−6848	18 52 31.68	−68 48 16.2	326.5	−25.3	−61.3	29.8	0.098	0.020	–
1903−6748	19 03 00.80	−67 49 35.4	327.7	−26.1	−35.0	−60.4	0.411	0.082	–
1913−6950	19 13 31.69	−69 50 36.7	325.6	−27.2	−37.7	8.2	0.273	0.055	–
1926−6242	19 26 58.58	−62 42 26.2	333.8	−27.9	65.8	−0.2	0.126	0.025	–
1930−6056	19 30 06.01	−60 56 09.4	335.8	−28.1	−29.0	−8.3	0.601	0.120	–
1933−6942	19 33 31.89	−69 42 57.7	325.9	−28.9	56.6	−7.5	0.360	0.072	–
1939−6343	19 39 25.53	−63 42 44.7	332.7	−29.4	76.6	39.2	1.139	0.228	–
1940−6906	19 40 26.09	−69 07 55.1	326.5	−29.6	107.4	−70.0	0.561	0.112	–
1941−6211	19 41 21.90	−62 11 20.5	334.5	−29.5	76.3	3.5	0.454	0.091	–
1942−7016	19 42 46.03	−70 15 42.8	325.2	−29.7	35.5	31.0	0.107	0.021	–
2004−6347	20 04 29.68	−63 47 22.8	332.6	−32.2	31.0	7.9	0.412	0.082	–
2008−6108	20 08 48.59	−61 09 39.2	335.7	−32.8	11.5	−40.3	0.080	0.016	–
2014−6713	20 15 00.98	−67 12 59.1	328.5	−32.9	86.9	6.9	0.061	0.012	–
2021−6124	20 21 01.69	−61 24 49.3	335.3	−34.2	−9.2	−11.1	0.166	0.033	–
2027−7007	20 27 25.26	−70 07 17.7	324.8	−33.5	88.1	13.2	0.258	0.052	–
2045−6133 (N)	20 45 46.93	−61 32 42.1	334.6	−37.1	−7.6	43.8	0.054	0.012	R
2045−6133 (S)	20 45 45.81	−61 33 07.7	334.6	−37.1	−15.5	18.2	0.013	0.003	R
2046−6527	20 46 50.04	−65 27 27.1	329.8	−36.4	75.1	−17.2	0.108	0.022	–
2059−6744	20 59 09.69	−67 45 24.5	326.6	−36.9	−7.3	−32.6	0.084	0.017	–

Table 3.5: Confirmed 18 GHz detections. (*continued*)

(1) Name	(2) α (J2000)	(3) δ (J2000)	(4) l (deg)	(5) b (deg)	(6) ΔX (arcsec)	(7) ΔY (arcsec)	(8) S_{pk} (Jy)	(9) ΔS_{pk} (Jy)	(10) Extension
2107−6547	21 06 59.78	−65 47 44.2	328.6	−38.3	−7.5	−40.2	0.290	0.058	–
2114−6851	21 14 14.15	−68 50 59.0	324.7	−37.8	54.9	44.8	0.110	0.022	–
2120−6111	21 21 04.24	−61 11 24.0	333.6	−41.3	59.5	−6.9	0.201	0.040	–
2150−6801	21 50 13.43	−68 02 48.4	323.6	−41.1	53.0	−50.4	0.200	0.040	–
2156−6331	21 56 48.82	−63 31 05.4	328.3	−44.0	18.9	8.6	0.095	0.019	–
2157−6940 (N)	21 57 05.45	−69 41 22.6	321.3	−40.6	−49.8	−58.5	0.579	0.129	R
2157−6940 (S)	21 57 04.53	−69 41 49.7	321.3	−40.6	−54.6	−85.5	1.242	0.275	R
2204−6130	22 03 59.48	−61 30 21.9	330.1	−45.8	−3.6	10.0	0.245	0.049	–
2208−6325	22 08 47.75	−63 25 47.6	327.4	−45.2	125.9	−6.5	0.261	0.052	–
2213−6329	22 13 34.66	−63 30 01.7	326.9	−45.6	−49.1	−5.7	0.309	0.062	–
2215−6609	22 15 44.92	−66 09 14.3	323.7	−44.2	−6.5	1.5	0.097	0.019	–
2230−6230	22 31 08.11	−62 31 20.1	326.2	−47.8	76.9	−45.2	0.389	0.078	–
2230−6310	22 30 10.56	−63 10 43.3	325.5	−47.3	24.0	6.7	0.180	0.036	–
2300−6032	23 00 47.82	−60 32 29.6	324.5	−51.7	−15.9	24.2	0.030	0.006	–
2303−6806	23 03 43.77	−68 07 36.1	317.0	−46.0	37.8	−40.0	0.874	0.175	–
2306−6521	23 06 59.61	−65 21 31.0	319.0	−48.0	72.5	9.8	0.096	0.019	–
2306−6706	23 06 51.83	−67 06 42.4	317.5	−47.0	86.5	−12.3	0.083	0.017	–
2310−5940	23 10 28.55	−59 41 12.1	324.0	−53.1	49.5	−50.0	0.099	0.020	–
2312−6607	23 12 58.90	−66 07 30.7	317.6	−48.1	78.3	6.4	0.106	0.021	–
2326−6613	23 26 12.55	−66 12 32.9	315.8	−48.7	63.8	41.1	0.082	0.016	–
2327−6645	23 27 45.40	−66 44 42.3	315.2	−48.3	14.2	20.8	0.176	0.035	–
2335−6636	23 35 12.11	−66 37 10.4	314.3	−48.8	−23.0	−34.5	0.108	0.022	–
2342−6826	23 42 09.45	−68 25 29.8	312.2	−47.4	2.4	70.2	0.088	0.018	–
2356−6820	23 56 00.75	−68 20 04.6	310.5	−48.0	−67.7	16.3	0.589	0.118	–
2358−6053 (N)	23 58 44.35	−60 52 46.5	314.1	−55.1	−4.8	37.7	0.394	0.087	R
2358−6053 (S)	23 58 46.98	−60 52 56.1	314.1	−55.1	14.4	28.0	0.286	0.064	R
2359−6057	23 59 22.77	−60 57 17.5	313.9	−55.0	27.5	5.3	0.207	0.041	–

Table 3.6: Radio spectra and optical IDs for extragalactic 18 GHz sources ($|b| > 5°$, and excluding objects within 5.5 degrees of the LMC centre). Sources marked with a # in column 1 are resolved doubles in our 18 GHz images: for these objects, the position is that of the radio centroid and the 18 GHz flux density is the total for both components. Sources marked with a *G* in column 1 lie at low Galactic latitude ($5° < |b| < 10°$) – tentative optical identifications are given for these objects, but they are not included in the analysis of optical counterparts in § 3.2.9

(1)	(2)	(3)	(4)	(5)	(6)	(7)	(8)
Name	Radio position (J2000)		Optical position (J2000)		B_J (mag)	T	Δ ($''$)
0024−6821	00 24 06.47	−68 20 54.3	00 24 06.72	−68 20 54.5	17.62	2	1.4
0025−6028 #	00 25 15.91	−60 28 27.6	···	···	>22		
0103−6438	01 03 33.93	−64 39 08.0	01 03 33.75	−64 39 07.7	18.88	1	1.2
0109−6048	01 09 15.35	−60 49 49.1	01 09 15.56	−60 49 47.7	22.01	1	2.1
0110−6315	01 10 17.05	−63 15 56.2	01 10 16.71	−63 15 56.4	20.12	2	2.3
0112−6634	01 12 19.05	−66 34 45.1	01 12 18.90	−66 34 45.3	17.86	2	0.9
0112−6752	01 13 11.81	−67 53 04.0	01 13 11.27	−67 53 03.0	20.86	2	3.2
0132−6522	01 32 39.40	−65 23 35.4	01 32 38.89	−65 23 35.7	20.25	2	3.2
0144−6422	01 44 16.82	−64 21 43.0	01 44 16.77	−64 21 42.8	21.35	2	0.4
0150−6044	01 50 50.32	−60 44 07.7	01 50 50.20	−60 44 07.5	20.51	2	0.9
0158−6410	01 58 37.28	−64 11 28.5	01 58 36.89	−64 11 27.9	19.51	1	2.6
0158−6333	01 58 55.42	−63 34 50.6	01 58 54.99	−63 34 50.1	18.85	2	2.9
0203−6846	02 03 53.42	−68 46 59.6	···	···	>22		
0207−6217	02 08 01.25	−62 16 34.7	02 08 01.22	−62 16 35.5	18.85	2	0.8
0214−7025	02 14 04.15	−70 27 07.1	02 14 04.44	−70 27 06.3	19.35	2	1.7
0214−6149	02 14 15.90	−61 49 34.0	02 14 16.22	−61 49 33.7	20.56	2	2.3
0236−6135	02 36 54.40	−61 36 14.5	02 36 53.26	−61 36 15.2	18.18	2	8.2
0251−6801	02 51 10.92	−68 02 08.5	02 51 11.52	−68 02 07.5	19.09	2	3.5
0303−6211	03 03 50.06	−62 11 25.4	03 03 50.64	−62 11 25.5	19.48	2	4.1
0303−6458	03 03 50.91	−64 58 53.8	03 03 50.62	−64 58 54.9	23.32	2	2.2
0314−6547	03 14 21.91	−65 48 24.8	03 14 22.58	−65 48 25.1	19.03	2	4.1
0323−6027	03 23 08.55	−60 26 31.5	03 23 08.45	−60 26 31.8	20.69	2	0.8
0340−6702	03 40 28.24	−67 03 17.0	03 40 28.21	−67 03 16.4	19.24	2	0.6
0341−5953	03 41 21.82	−59 54 08.6	03 41 21.60	−59 54 08.9	18.21	2	1.7
0357−6949	03 57 30.38	−69 48 44.2	03 57 30.13	−69 48 44.9	22.59	2	1.5
0408−6544	04 08 20.67	−65 45 09.1	04 08 20.29	−65 45 08.5	22.49	2	2.4
0422−6506	04 22 30.42	−65 07 04.7	04 22 29.18	−65 07 05.6	20.42	2	7.9
0424−6646	04 25 07.79	−66 46 49.7	04 25 08.10	−66 46 50.6	16.79	2	2.0
0428−6437	04 28 11.05	−64 38 23.0	04 28 11.07	−64 38 23.6	21.63	1	0.6
0433−6029	04 33 34.29	−60 30 14.7	04 33 34.27	−60 30 12.7	19.10	1	2.0
0503−6048	05 04 01.89	−60 49 52.6	05 04 01.70	−60 49 52.6	19.42	2	1.4
0505−6215	05 05 46.84	−62 15 45.0	05 05 46.71	−62 15 44.5	19.42	2	1.0
0505−6236	05 05 48.66	−62 36 11.0	05 05 48.53	−62 36 11.0	20.80	2	0.9
0516−6205	05 16 45.74	−62 07 05.3	05 16 44.90	−62 07 05.3	21.20	2	5.9
0522−6106	05 22 34.35	−61 07 58.2	05 22 34.41	−61 07 57.0	18.46	2	1.3
0534−6106	05 34 35.87	−61 06 05.5	05 34 35.75	−61 06 06.5	19.29	1	1.3
0713−6428	07 13 01.70	−64 29 06.7	07 13 02.27	−64 29 10.1	20.34	1	5.0
0719−6327	07 19 07.12	−63 26 59.4	···	···	>22		
0744−6919	07 44 20.75	−69 19 06.0	07 44 20.40	−69 19 07.2	21.65	2	2.2

Table 3.6: Radio spectra and optical IDs for extragalactic 18 GHz sources (*contd*)

(1)	(2)	(3)	(4)	(5)	(6)	(7)	(8)
Name	Radio position (J2000)		Optical position (J2000)		B_J (mag)	T	Δ ($''$)
0827−6021	08 27 36.30	−60 21 43.8	08 27 35.92	−60 21 43.1	21.90	1	2.9
0842−6408	08 42 41.70	−64 09 59.9	08 42 40.99	−64 10 00.8	21.72	2	4.7
0845−6525	08 45 11.79	−65 27 22.7	08 45 11.33	−65 27 23.0	18.01	2	2.9
0846−6313	08 46 35.97	−63 13 34.8	08 46 35.80	−63 13 33.6	19.34	2	1.7
0901−6636	09 01 16.23	−66 36 29.7	09 01 15.58	−66 36 33.3	23.46	2	5.3
0931−6227 *G*	09 31 27.39	−62 29 34.4	09 31 27.54	−62 29 35.6	20.18	2	1.6
1107−6819 *G*	11 07 11.45	−68 20 54.9	11 07 12.68	−68 20 50.6	18.47	2	8.1
1136−6826 *G*	11 36 02.21	−68 27 06.7	···	···	>22		
1138−6809 *G*	11 38 22.16	−68 10 33.9	11 38 22.57	−68 10 32.0	21.51	2	3.0
1147−6753 *G*	11 47 32.98	−67 53 42.9	11 47 32.40	−67 53 42.7	20.69	2	3.3
1239−6845 *G*	12 39 46.91	−68 45 27.8	12 39 47.05	−68 45 29.4	16.82	2	1.8
1424−6808 *G*	14 24 55.62	−68 07 54.6	···	···	>22		
1434−6839 *G*	14 34 28.47	−68 39 51.6	14 34 28.60	−68 39 51.2	17.47	1	0.8
1452−6502 *G*	14 52 39.49	−65 01 59.2	···	···	>22		
1512−6507 *G*	15 12 33.69	−65 06 52.7	15 12 33.11	−65 06 52.6	21.25	1	3.6
1516−6425 *G*	15 16 40.02	−64 25 24.1	15 16 39.78	−64 25 21.6	18.23	2	2.9
1546−6835	15 46 43.04	−68 37 35.4	···	···	>22		
1558−6433	15 58 50.77	−64 32 26.7	15 58 50.31	−64 32 29.5	16.84	1	4.1
1619−6820	16 19 37.26	−68 21 23.0	16 19 37.55	−68 21 25.5	19.13	1	3.0
1624−6808	16 24 18.01	−68 09 11.5	16 24 18.42	−68 09 12.4	17.05	2	1.3
1647−6438	16 47 37.54	−64 38 01.0	16 47 37.78	−64 38 00.2	20.05	1	1.8
1703−6509	17 03 50.55	−65 11 06.4	17 03 50.46	−65 11 06.2	18.10	2	0.6
1721−6154	17 21 39.46	−61 54 42.1	17 21 39.00	−61 54 42.2	18.91	2	3.2
1723−6500	17 23 42.08	−65 00 36.3	17 23 41.03	−65 00 36.6	13.16	1	6.6
1726−6426	17 26 57.92	−64 27 54.8	···	···	>22		
1734−6214	17 35 08.24	−62 15 22.1	17 35 07.95	−62 15 21.3	19.59	2	2.2
1736−5951	17 36 30.65	−59 51 59.2	17 36 30.81	−59 51 58.7	21.52	2	1.3
1743−6627	17 43 49.08	−66 26 27.6	17 43 49.03	−66 26 28.4	20.76	2	0.9
1749−6258	17 49 25.80	−62 58 17.6	17 49 25.91	−62 58 16.9	19.08	1	1.0
1754−6424	17 54 41.82	−64 23 45.6	17 54 42.00	−64 23 45.7	19.15	2	1.2
1759−5947	17 59 06.39	−59 46 59.1	···	···	>22		
1803−6507	18 03 23.38	−65 07 36.8	18 03 23.24	−65 07 33.6	18.19	1	3.3
1807−6414	18 07 54.08	−64 13 50.9	18 07 54.56	−64 13 49.6	21.41	1	3.4
1807−7012	18 07 14.76	−70 12 39.9	18 07 14.59	−70 12 39.5	18.23	1	1.0
1819−6346	18 19 35.06	−63 45 47.8	18 19 35.07	−63 45 48.1	16.80	1	0.3
1821−6840	18 21 16.13	−68 40 40.7	18 21 16.18	−68 40 40.0	21.85	2	0.8
1822−6359	18 22 17.04	−63 59 12.4	···	···	>22		
1824−6717#	18 24 33.69	−67 17 26.0	···	···	>22		
1836−6648	18 36 59.51	−66 49 06.8	18 36 59.26	−66 49 08.1	19.54	1	2.0
1840−6151	18 40 15.05	−61 52 06.3	18 40 15.44	−61 52 05.8	21.96	2	2.8
1840−6957	18 40 48.37	−69 57 48.1	···	···	>22		
1848−6416	18 48 55.68	−64 15 38.8	18 48 55.50	−64 15 38.7	18.99	2	1.2

Table 3.6: Radio spectra and optical IDs for extragalactic 18 GHz sources (*contd*)

(1)	(2)	(3)	(4)	(5)	(6)	(7)	(8)
Name	Radio position (J2000)		Optical position (J2000)		B_J (mag)	T	Δ ($''$)
1852−6848	18 52 31.68	−68 48 16.2	···	···	>22		
1903−6748	19 03 00.80	−67 49 35.4	19 03 01.25	−67 49 36.0	18.90	2	2.6
1913−6950	19 13 31.69	−69 50 36.7	···	···	>22		
1926−6242	19 26 58.58	−62 42 26.2	19 26 58.12	−62 42 27.0	18.64	2	3.3
1930−6056	19 30 06.01	−60 56 09.4	19 30 06.15	−60 56 09.2	20.57	2	1.0
1933−6942	19 33 31.89	−69 42 57.7	19 33 31.15	−69 42 58.8	19.95	2	4.0
1939−6343	19 39 25.53	−63 42 44.7	19 39 24.85	−63 42 45.5	18.87	1	4.6
1940−6906	19 40 26.09	−69 07 55.1	19 40 25.52	−69 07 56.9	18.36	2	3.6
1941−6211	19 41 21.90	−62 11 20.5	19 41 22.04	−62 11 20.8	21.17	1	1.0
1942−7016	19 42 46.03	−70 15 42.8	19 42 45.42	−70 15 45.0	19.29	2	3.8
2004−6347	20 04 29.68	−63 47 22.8	20 04 29.46	−63 47 23.3	19.35	2	1.5
2008−6108	20 08 48.59	−61 09 39.2	···	···	>22		
2014−6713	20 15 00.98	−67 12 59.1	20 15 00.13	−67 12 59.0	19.02	1	4.9
2021−6124	20 21 01.69	−61 24 49.3	20 21 01.35	−61 24 49.1	20.46	1	2.4
2027−7007	20 27 25.26	−70 07 17.7	20 27 24.52	−70 07 17.5	19.19	2	3.8
2045−6133#	20 45 46.37	−61 32 54.8	20 45 46.27	−61 32 56.7	20.73	2	2.1
2046−6527	20 46 50.04	−65 27 27.1	20 46 49.66	−65 27 27.5	21.58	2	2.4
2059−6744	20 59 09.69	−67 45 24.5	20 59 09.72	−67 45 22.5	18.22	1	2.0
2107−6547	21 06 59.78	−65 47 44.2	21 06 59.73	−65 47 43.7	20.88	2	0.6
2114−6851	21 14 14.15	−68 50 59.0	21 14 13.42	−68 51 02.1	19.58	2	5.0
2120−6111	21 21 04.24	−61 11 24.0	21 21 04.07	−61 11 24.7	18.75	2	1.4
2150−6801	21 50 13.43	−68 02 48.4	21 50 13.42	−68 02 50.2	20.83	2	1.8
2156−6331	21 56 48.82	−63 31 05.4	21 56 49.15	−63 31 05.9	19.98	2	2.3
2157−6940#	21 57 05.45	−69 41 22.6	21 57 06.14	−69 41 24.0	13.85	1	3.9
2204−6130	22 03 59.48	−61 30 21.9	22 03 59.53	−61 30 23.4	19.86	1	1.6
2208−6325	22 08 47.75	−63 25 47.6	22 08 47.25	−63 25 47.3	18.41	2	3.4
2213−6329	22 13 34.66	−63 30 01.7	22 13 34.76	−63 30 01.6	18.52	2	0.7
2215−6609	22 15 44.92	−66 09 14.3	22 15 45.30	−66 09 13.7	21.19	2	2.4
2230−6230	22 31 08.11	−62 31 20.1	22 31 07.83	−62 31 19.5	20.25	1	2.0
2230−6310	22 30 10.56	−63 10 43.3	22 30 10.35	−63 10 43.4	19.85	2	1.4
2300−6032	23 00 47.82	−60 32 29.6	23 00 47.76	−60 32 29.1	19.75	2	0.7
2303−6806	23 03 43.77	−68 07 36.1	23 03 43.54	−68 07 37.3	16.26	2	1.8
2306−6521	23 06 59.61	−65 21 31.0	···	···	>22		
2306−6706	23 06 51.83	−67 06 42.4	···	···	>22		
2310−5940	23 10 28.55	−59 41 12.1	23 10 28.45	−59 41 11.9	18.35	1	0.7
2312−6607	23 12 58.90	−66 07 30.7	23 12 58.84	−66 07 31.7	18.77	2	1.1
2326−6613	23 26 12.55	−66 12 32.9	···	···	>22		
2327−6645	23 27 45.40	−66 44 42.3	23 27 45.26	−66 44 42.6	22.25	2	0.9
2335−6636	23 35 12.11	−66 37 10.4	···	···	>22		
2342−6826	23 42 09.45	−68 25 29.8	23 42 09.41	−68 25 30.0	20.53	2	0.3
2356−6820	23 56 00.75	−68 20 04.6	23 56 00.68	−68 20 03.4	17.61	2	1.3
2358−6053#	23 58 45.15	−60 52 49.7	23 59 04.34	−60 54 59.6	16.61	1	
2359−6057#	23 59 22.77	−60 57 17.5	(as above)				

Table 3.6: Radio spectra and optical IDs for extragalactic 18 GHz sources (*contd*)

(1) Name	(9) S_{18} (mJy)	(10) ±	(11) S_5 (mJy)	(12) ±	(13) S_{843} (mJy)	(14) ±	(15) $\alpha_{18}^{0.843}$	(16) ±	(17) NED name & notes
0024−6821	366	14	482	25	1250.2	37.5	−0.40	0.10	PKS 0021−686
0025−6028 #	198	44	416	22	···	···	···	···	PKS 0022−60
0103−6438	290	58	356	19	770.0	69.3	−0.32	0.10	PKS 0101−649
0109−6048	872	194	674	34	···	···	···	···	PKS 0107−610 (QSO)
0110−6315	154	34	187	12	···	···	···	···	PKS 0108−635 (QSO)
0112−6634	415	92	287	16	···	···	···	···	PKS 0110−668 (QSO)
0112−6752	127	28	123	9	···	···	···	···	PMN J0113−6753
0132−6522	107	24	233	13	366.5	14.8	−0.40	0.10	PKS 0131−656
0144−6422	286	20	144	10	108.1	3.3	+0.32	0.03	PMN J0144−6421
0150−6044	69	15	60	8	182.0	5.5	−0.32	0.09	PMN J0150−6044
0158−6410	133	30	150	10	190.8	5.8	−0.12	0.09	PMN J0158−6411
0158−6333	111	25	206	12	558.9	16.8	−0.53	0.09	PKS 0157−638
0203−6846	86	19	289	16	1198.8	36.0	−0.86	0.09	PKS 0202−690
0207−6217	158	35	275	15	193.0	5.9	−0.07	0.09	PMN J0207−6216
0214−7025	149	33	95	8	107.8	3.4	+0.11	0.09	PMN J0214−7027
0214−6149	248	55	386	21	212.4	6.5	+0.05	0.09	PKS 0212−620
0236−6135	511	113	362	19	604.1	18.2	−0.05	0.09	PKS 0235−618 (QSO)
0251−6801	78	17	198	12	555.0	16.7	−0.64	0.09	PKS 0250−682
0303−6211	1713	380	1882	85	2513.4	75.4	−0.13	0.09	PKS 0302−623 (QSO)
0303−6458	149	33	95	8	47.5	1.7	+0.37	0.09	PMN J0303−6458
0314−6547	297	66	159	10	353.9	10.7	−0.06	0.09	PKS 0313−660 (QSO z=0.636)
0323−6027	159	35	344	19	199.2	6.0	−0.07	0.04	PMN J0323−6026 (QSO)
0340−6702	177	39	254	14	374.0	11.3	−0.24	0.09	PMN J0340−6703
0341−5953	147	33	208	13	378.6	11.4	−0.31	0.08	PKS 0340−600
0357−6949	231	51	111	8	147.7	4.5	+0.15	0.09	PMN J0357−6948
0408−6544	543	121	3352	169	25028.8	750.9	−1.25	0.09	PKS 0408−65 (QSO)
0422−6506	108	24	114	9	176.8	5.5	−0.16	0.09	PMN J0422−6507
0424−6646	242	54	303	16	90.9	3.0	+0.32	0.09	PKS 0425−669
0428−6437	180	40	113	9	77.8	2.8	+0.27	0.09	PMN J0428−6438
0433−6029	359	80	563	29	413.5	12.5	−0.05	0.09	PKS 0432−606 (QSO)
0503−6048	116	26	372	20	568.4	17.1	−0.52	0.09	PKS 0503−608 (QSO)
0505−6215	157	35	73	9	53.7	1.9	+0.35	0.09	PMN J0505−6215
0505−6236	152	34	136	10	109.7	3.4	+0.11	0.09	PMN J0505−6236
0516−6205	530	118	410	22	417.8	12.6	+0.08	0.09	PKS 0516−621 (QSO)
0522−6106	1101	244	664	34	740.7	22.3	+0.13	0.08	PKS 0522−611 (QSO z=1.40)
0534−6106	513	47	291	16	450.7	13.6	+0.04	0.04	PKS 0534−611 (QSO)
0713−6428	71	16	311	17	1352.8	40.6	−0.96	0.09	MRC 0712−643
0719−6327	99	22	323	18	602.9	18.1	−0.59	0.09	PKS 0718−633
0744−6919	237	53	255	14	413.7	12.4	−0.18	0.09	PKS 0744−691 (QSO)
0827−6021	96	21	132	10	···	···	···	···	PMNJ 0827−6021

Table 3.6: Radio spectra and optical IDs for extragalactic 18 GHz sources (*contd*)

(1) Name	(9) S_{18} (mJy)	(10) ±	(11) S_5 (mJy)	(12) ±	(13) S_{843} (mJy)	(14) ±	(15) $\alpha_{18}^{0.843}$	(16) ±	(17) NED name & notes
0842−6408	113	25	80	8	63.3	2.2	+0.19	0.09	PMN J0842−6409
0845−6525	237	53	392	21	18.3	1.1	+0.84	0.10	PMN J0845−6527
0846−6313	108	24	104	9	85.7	2.7	+0.08	0.06	PMN J0846−6313
0901−6636	230	51	176	11	192.7	5.9	+0.06	0.09	PKS 0900−664
0931−6227 *G*	258	57	394	21	···	···	···	···	MRC 0930−622
1107−6819 *G*	1153	256	1183	60	···	···	···	···	PKS 1105−680 (QSO z=0.588)
1136−6826 *G*	479	106	704	36	···	···	···	···	PKS 1133−681
1138−6809 *G*	184	41	1131	57	···	···	···	···	PKS 1136−67
1147−6753 *G*	1378	216	2555	129	···	···	···	···	PKS 1145−676 (QSO)
1239−6845 *G*	258	57	669	34	···	···	···	···	PKS 1236−684 (QSO)
1424−6808 *G*	850	189	925	47	···	···	···	···	PKS 1420−679
1434−6839 *G*	20	4	65	7	···	···	···	···	WKK 3258 (Galaxy)
1452−6502 *G*	146	32	409	22	···	···	···	···	PKS 1448−648
1512−6507 *G*	71	16	238	14	···	···	···	···	PKS 1508−649
1516−6425 *G*	78	17	165	11	···	···	···	···	PMN J1516−6425
1546−6835	233	52	156	10	···	···	···	···	PMN J1546−6837
1558−6433	431	96	580	30	···	···	···	···	WKK 5585 (Galaxy)
1619−6820	84	19	275	15	···	···	···	···	PKS 1614−682
1624−6808	613	136	1969	99	···	···	···	···	PKS 1619−680 (QSO z=1.360)
1647−6438	614	136	1225	62	643.7	19.4	−0.02	0.09	MRC 1642−645
1703−6509	99	22	269	15	344.5	10.4	−0.41	0.09	PKS 1658−651
1721−6154	340	75	253	15	309.9	9.4	+0.03	0.09	PMN J1721−6154
1723−6500	2945	654	4275	216	3724.2	111.7	−0.08	0.09	NGC 6328 (AGN z=0.01421)
1726−6426	204	13	1288	65	4076.0	122.3	−0.98	0.03	PMN J1726−6427
1734−6214	256	57	426	22	696.3	20.9	−0.33	0.09	PMN J1735−6215
1736−5951	236	62	286	16	268.5	8.1	−0.04	0.11	PKS 1732−598 (QSO)
1743−6627	176	39	172	11	208.7	6.4	−0.06	0.09	PKS 1738−664
1749−6258	182	40	230	13	244.0	7.4	−0.10	0.09	PMN J1749−6258
1754−6424	83	18	113	9	177.4	5.4	−0.25	0.09	PMN J1754−6423
1759−5947	112	25	729	37	5625.5	168.8	−1.28	0.09	PKS 1754−59
1803−6507	999	222	764	39	637.3	19.2	+0.15	0.09	PKS 1758−651
1807−6414	450	100	167	11	93.7	3.1	+0.51	0.09	PMN J1807−6413
1807−7012	131	13	462	24	1198.8	36.0	−0.72	0.04	PKS 1801−702 (Galaxy)
1819−6346	1631	79	4439	224	20185.4	605.6	−0.82	0.03	PKS 1814−63 (Sy2 z=0.0627)
1821−6840	19	4	37	7	44.5	1.7	−0.28	0.09	PMN J1821−6840
1822−6359	113	25	823	42	4935.3	181.4	−1.23	0.09	PKS 1817−64
1824−6717#	206	36	1137	57	3440.0	133.8	−0.92	0.06	PKS 1819−67
1836−6648	127	28	740	38	3259.7	97.8	−1.06	0.09	PKS 1831−668
1840−6151	245	54	192	12	190.9	5.8	+0.08	0.10	PKS 1835−619
1840−6957	26	6	170	11	935.7	34.1	−1.17	0.10	PKS 1835−700
1848−6416	80	18	294	16	999.2	30.0	−0.83	0.09	PKS 1844−643

Table 3.6: Radio spectra and optical IDs for extragalactic 18 GHz sources (*contd*)

(1) Name	(9) S_{18} (mJy)	(10) ±	(11) S_5 (mJy)	(12) ±	(13) S_{843} (mJy)	(14) ±	(15) $\alpha_{18}^{0.843}$	(16) ±	(17) NED name
1852−6848	101	22	170	11	402.5	12.1	−0.45	0.09	PKS 1847−688
1903−6748	419	21	316	17	231.6	7.0	+0.19	0.03	PMN J1903−6749
1913−6950	282	63	···	···	33.6	1.3	+0.69	0.09	SUMSS J191330−695036
1926−6242	133	30	···	···	138.8	5.0	−0.01	0.10	SUMSS J192659−624225
1930−6056	675	150	880	45	695.6	20.9	−0.01	0.09	PKS 1925−610 (QSO)
1933−6942	388	86	397	21	743.8	22.3	−0.21	0.09	PKS 1928−698 (QSO)
1939−6343	1272	350	5926	299	13721.7	411.7	−0.78	0.11	PKS 1934−63 (Sy2 z=0.1830)
1940−6906	568	126	1034	52	1705.0	51.2	−0.36	0.09	PKS 1935−692 (QSO z=3.154)
1941−6211	502	111	873	44	1831.9	55.0	−0.42	0.09	PKS 1936−623 (QSO)
1942−7016	111	25	398	21	79.8	2.5	+0.11	0.09	PMN J1942−7015
2004−6347	456	13	659	34	748.6	22.5	−0.16	0.02	PMN J2004−6347
2008−6108	78	17	39	7	23.8	1.2	+0.39	0.10	PMN J2008−6110
2014−6713	73	16	68	8	39.2	1.5	+0.20	0.09	PMN J2014−6713
2021−6124	183	41	488	25	1070.8	32.2	−0.58	0.09	PKS 2016−615 (QSO)
2027−7007	308	68	386	20	1040.7	31.3	−0.40	0.09	PKS 2022−702 (QSO z=0.6970)
2045−6133#	68	12	361	19	927.7	37.1	−0.84	0.09	MRC 2041−617
2046−6527	116	26	58	8	35.7	1.4	+0.38	0.10	PMN J2046−6527
2059−6744	90	20	129	9	245.7	9.3	−0.33	0.09	PMN J2059−6745
2107−6547	303	67	631	32	1554.8	46.7	−0.53	0.09	PKS 2102−659
2114−6851	140	31	321	17	509.7	15.3	−0.42	0.09	PKS 2109−690 (QSO z=2.910)
2120−6111	214	48	599	31	966.0	29.0	−0.49	0.09	MRC 2117−614
2150−6801	215	48	181	11	126.1	3.9	+0.17	0.09	PMNJ 2150−6803
2156−6331	97	22	97	9	57.4	1.9	+0.17	0.09	PMNJ 2156−6331
2157−6940#	1821	304	12059	609	41200.2	1454.8	−1.02	0.06	ESO 075−G41 (AGN z=0.028273)
2204−6130	249	55	419	22	440.9	13.3	−0.19	0.09	PKS 2200−617
2208−6325	298	66	639	33	1428.8	42.9	−0.51	0.09	PKS 2204−63 (QSO z=0.6180)
2213−6329	325	72	239	14	630.8	25.3	−0.22	0.09	PKS 2210−637
2215−6609	110	24	284	16	761.2	22.9	−0.63	0.09	PKS 2212−664
2230−6230	395	88	184	12	267.0	8.1	+0.13	0.09	PKS 2227−627
2230−6310	187	42	111	9	230.5	7.0	−0.07	0.09	PMNJ 2230−6310
2300−6032	32	7	102	9	154.9	4.7	−0.52	0.09	PMNJ 2300−6032
2303−6806	924	205	415	22	759.0	28.6	+0.06	0.09	PKS 2300−683 (QSO z=0.5120)
2306−6521	104	23	329	18	371.9	11.2	−0.42	0.09	PKS 2303−656
2306−6706	88	20	271	15	729.6	21.9	−0.69	0.09	PKS 2303−673
2310−5940	109	24	185	12	73.8	3.5	+0.13	0.10	IRAS 23074−5957 (Gal. z=0.14148)
2312−6607	111	25	267	15	107.2	3.4	+0.01	0.09	PMNJ 2312−6607
2326−6613	86	19	143	10	116.4	3.6	−0.10	0.09	PMN J2326−6612
2327−6645	184	25	237	14	470.0	14.2	−0.31	0.06	PKS 2324−670 (QSO)
2335−6636	118	26	812	41	3421.9	127.3	−1.10	0.09	PKS 2332−66
2342−6826	98	22	130	9	184.2	5.6	−0.21	0.09	PMN J2342−6825
2356−6820	671	97	918	46	1126.4	33.8	−0.17	0.06	PKS 2353−68 (QSO z=1.7160)
2358−6053#	680	108	5624	284	29000.0	2900.0	−1.23	0.11	PKS 2356−61 (N) (AGN z=0.09631)
2359−6057#	275	61							PKS 2356−61 (S)

Chapter 4

High-frequency polarization study of Kühr sample

4.1 Introduction

Measurements of polarization properties of extragalactic radio sources provide unique information on magnetic field structure. The fractional polarization is a measure of the degree of order of the magnetic field in the emitting region. If synchrotron self-absorption and Faraday rotation can be neglected, the linear polarization position angle will be orthogonal to the magnetic field orientation. Given this, it is surprising that high radio frequency polarimetric surveys of *complete* samples of extragalactic radio sources are so rare.

The general high-frequency polarization properties of radio sources are poorly known. Multi-frequency observations by Jones et al. (1985) and Rudnick et al. (1985) of 20 flat-spectrum sources ($\alpha < 0.5$; $S \propto \nu^{-\alpha}$) showed that the median value of polarization is $\sim 2.5\%$ in the range 1.4–90 GHz, independent of frequency. This would suggest that the general polarization properties can be accounted for by largely random magnetic fields. Note, however, that Jones et al. and Rudnick et al. stressed that their sample is not complete and selection criteria may introduce unpredictable biases. On the other hand, the relatively constant polarization fraction suggests that differential Faraday rotation, or decreased contribution of relatively unpolarized opaque regions, or greater magnetic field ordering on the smaller scales dominating at millimeter wavelengths, may play minor roles (see also Saikia & Salter 1988). Okudaira et al. (1993) made linear polarization observations at 10 GHz for a complete sample of 93 flat-spectrum sources selected at 5

GHz ($S_{5\rm GHz} > 0.8$ Jy). Okudaira et al. do not provide an average value for the fractional polarization at 10 GHz. From their tabulated source values we could infer a median fractional polarization of 2.3%. On the other hand, Aller et al. (1999) find that the fractional linear polarization of an incomplete sample of 41 BL Lac objects is generally higher at 14.5 GHz (median value 5%) than at 4.8 GHz (median value 3.6%). Also, the millimeter/sub-millimeter polarization survey of 26 blazars by Nartallo et al. (1998) yielded a median fractional polarization at 0.8–1.1 mm of 7.1%, while the NVSS data indicate, for the same objects, a median fractional polarization of $\simeq 2\%$ at 1.4 GHz (Mesa et al. 2002). For a sample of steep-spectrum sources with multi-frequency polarimetric observations by Klein et al. (2003), Mesa et al. (2002) find a steady increase with frequency of the mean fractional polarization from $\simeq 3\%$ at 1.4 GHz to 8.65% at 10.6 GHz. It should be noted, however, that the sample is biased towards high polarizations as it only includes sources which have been detected in polarization at 10.6 GHz. The same effect may occur in the high redshift radio galaxy sample observed by Pentericci et al. (2000) at high resolution (0".2), where typical fractional polarization of 10–20% at 8.4 GHz were found.

A good understanding of the high-frequency polarization properties of extragalactic sources is crucial in analysing the polarization of the cosmic microwave background (CMB). This has been detected recently by the DASI experiment at 30 GHz (Kovac et al. 2002) and by the WMAP satellite (Kogut et al. 2003) in several bands in the range 23–94 GHz. The extraction of the very weak CMB polarization signal requires both high sensitivity and careful control of foregrounds. In the frequency range relevant to these experiments, the polarized emission of extragalactic radio sources is expected to be the main contaminant on small angular scales (Sazhin & Korolëv 1985; De Zotti et al. 1999b).

In this Chapter we describe the results of linear polarization measurements at 18.5 GHz of 250 of the 258 southern ($\delta < 0°$) extragalactic sources in the 5 GHz Kühr et al. (1981) all-sky sample. This sample is complete to $S_{5\rm GHz} \geq 1$ Jy, and contains 527 objects. This is, by far, the largest *complete* sample of radio sources for which high-frequency polarization measurements have been carried out. Observations and data reduction are described in Sect. 4.2 and 4.3, respectively. The results are analyzed and discussed in Sect. 4.4. In Sect. 4.5 we summarize our main conclusions.

4.2 Observations

Measurements were carried out with the Australia Telescope Compact Array (ATCA), which was extensively described in Chapter 3. We took snapshot observations of the southern sources in the EW367 array configuration using the prototype 12mm receivers in the commissioning phase, mounted on three CA antennas. The two frequency bands were centered at 18.5 and 18.65 GHz with each band having a bandwidth of 128 MHz. The array configuration that we used is quite compact: the longest baseline was 214.3 metres, giving a beamwidth of 15.6 arcsec.

The observations were performed in three runs during March 2002. The total observing time was 48 hours: 24 hours on March 20-21, 10 hours on March 21-22 and 14 hours on March 27-28. We used the "mosaic observing mode" because this allowed us to organize the observing sequence to minimize the slew time between the sources. The 258 sources were split in 36 clusters of sources. Clusters were observed four times each to produce a good spread in hour angles.

Many of these sources had already been targeted with the ATCA as part of a search for potential 22 GHz calibrators. The 22 GHz total intensity measurements with ATCA of the full sample were completed in January 2001. These measurements were used to determine the integration time for each target source to ensure a detection at $\geq 5\sigma$ for source polarizations $\geq 1\%$. Nevertheless, because of limited observing time, we set an upper limit of 30 minutes per source. This means that for 43 sources with 22 GHz flux density ≤ 0.192 Jy, the detection threshold is $\geq 1\%$. Because of technical problems during the runs, 8 sources were not successfully observed.

4.3 Data reduction

The radio source 1934−638 was used as the primary flux density calibrator, while phase and gain calibrators were chosen from the ATCA calibrator list. The instrumental polarization was calibrated using measurements of Jupiter, which we assumed to be unpolarized.

Unfortunately the atmospheric phase stability during the observations was poor, so it was not possible to image the sources. Instead we decided to use non-imaging model-fitting techniques. To measure calibrators sufficiently frequently to correct for phase instability

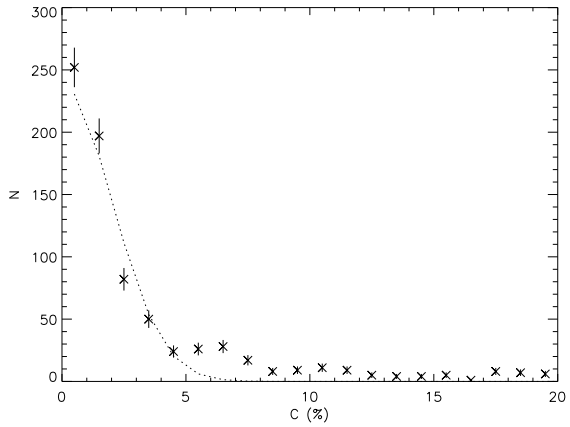

Figure 4.1: Distribution of the confusion parameter C. A semi–Gaussian fit is also shown (dotted line). The fitted standard deviation is σ=2.03.

would have been quite expensive in time: this would have reduced significantly the number of sources that we could observe in the scheduled time.

The data were reduced in the MIRIAD software package (Sault et al., 1995) to derive source flux densities in all the Stokes parameters (I,Q,U,V). In particular we used the MIRIAD task CALRED to determine the flux densities. In processing the visibilities, CALRED assumes a point source model, and produces a flux density estimate for each Stokes parameter for each scan. Along with the flux density and its error, the task computes out the theoretical rms noise, and a confusion parameter, C. The confusion parameter is an estimate of the fraction of the flux density that fails to conform to a point-source model.

A high value of C means that the source is poorly modelled as a point and that the determination of its flux density is poor. On the other hand, even in the case of truly point sources (where the value of C should be 0), noise results in a spread of the estimated value of C. For normal error distribution, C is approximately described by a semi-Gaussian distribution (negative values of C are not allowed). The observed distribution of C (Fig. 4.1) shows a strong excess over the best-fit Gaussian curve where $C \geq 5\%$: we believe that this is a result of source extension. Consequently we have chosen to exclude all the scans with $C \geq 5\%$. This resulted in the rejection of 53 sources.

For the remaining 197 sources we computed the linearly polarized flux for each scan

Table 4.1: Source number statistics for the polarization observations. The fractions in brackets are the percentages of flat and steep spectrum sources.

	All	Flat		Steep	
detections	170	114	(80%)	56	(49%)
upper limits	27	12	(8%)	15	(13%)
rejected	53	13	(9%)	40	(35%)
not observed	8	4	(3%)	4	(3%)
total	258	143		115	

i, $F_{p,i} = \sqrt{Q_i^2 + U_i^2}$ and the associated error $\sigma_{F,i} = \sigma_{Q,i} = \sigma_{U,i}$ ($\sigma_{Q,U}$ being the rms noise on the Stokes parameter Q or U). For all the sources the polarized flux, F_p, and its error, σ_F, were obtained by using a weighted mean over all the scans:

$$F_p = \sigma_F^2 \sum_i \frac{F_{p,i}}{\sigma_{F,i}^2} \tag{4.1}$$

$$\frac{1}{\sigma_F^2} = \sum_i \frac{1}{\sigma_{F,i}^2} \tag{4.2}$$

For 170 sources the polarized flux was detected with a signal-to-(theoretical)noise ratio ≥ 5. We considered such values as reliable. An upper limit of 5 $\times$ the theoretical noise was assigned to the other 27 sources. In all cases, the total intensity, I (again derived as the weighted mean of the scan total intensities), was measured with very high S/N ratio. The observations did not determine the polarization position angle: the geometry on the ATCA 12mm receivers was not calibrated sufficiently well to give reliable position angle information.

In the following analysis we subdivide the sample into flat and steep-spectrum sources. Following the classification of Stickel et al. (1994), we define as flat the sources with spectral index between 2.7 and 5 GHz $\alpha_{2.7}^5 < 0.5$ ($S_\nu \propto \nu^{-\alpha}$). Sources with $\alpha_{2.7}^5 > 0.5$ are considered steep. In table 4.1 we list the number (and the corresponding fraction of the total) of detected sources for the flat and steep-spectrum sub-samples. For both classes we also list the upper limits and the rejected sources ($C > 5\%$). While the final flat-spectrum source sample is almost complete (88%), only 49% of the steep-spectrum sources have reliable detections.

The total intensities and polarized fluxes for steep and flat-spectrum sources are listed in Tables 4.5 and 4.6, respectively. Also listed are the linear fractional polarization

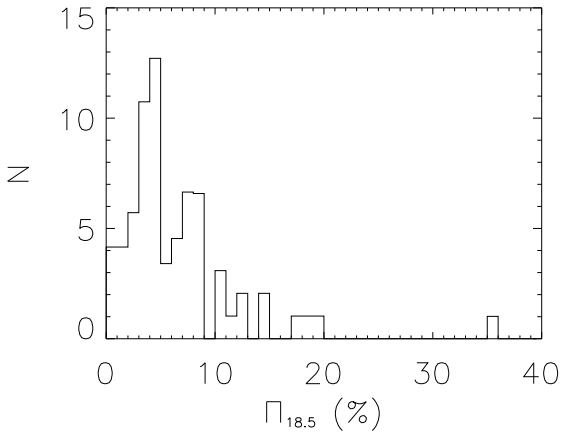

Figure 4.2: Distribution of the fractional polarization at 18.5 GHz for the steep-spectrum sources.

$\Pi_{18.5} = F_p/I$, the spectral indices between 1.4 and 5 GHz ($\alpha_{1.4}^{5}$) and 5 and 18.5 GHz ($\alpha_{5}^{18.5}$) and the 5 GHz luminosity. Source types and redshifts are from Stickel et al. (1994).

4.4 Polarization properties of sources

4.4.1 Steep-spectrum sources

As expected, most of the rejected sources (40 out of 53 with $C > 5\%$) are steep-spectrum. This is because steep-spectrum sources are more likely extended than flat-spectrum sources. This means that the following analysis is based on an incomplete sample, which can be strongly biased against extended sources (see Table 4.1). Additionally only upper limits can be given for 15 out of 71 (∼21%) of the steep-spectrum sources. Nevertheless some points are worth noticing. In Fig. 4.2 we show the parent distribution of $\Pi_{18.5}$ for the steep-spectrum sample. This was obtained by using the Kaplan–Meier estimator implemented in the routine KMESTM in the software package ASURV Rev 1.2 (Isobe & Feigelson 1990). This includes upper limits by using the survival analysis methods presented in Feigelson & Nelson (1985) and Isobe et al. (1986). The median of the distribution is $\simeq 4.8\%$ and the mean is $\simeq 6.5 \pm 0.7\%$. If we divide the sample into quasars (21 sources) and radio galaxies (50 sources) we find median values of 4.4% and 6.1%, and mean values of 5.1±0.6% and 7.0±0.9% respectively. The Peto & Prentice generalized

Table 4.2: Test for correlations between $\Pi_{18.5}$ and other properties of the steep-spectrum sources. N is the number of sources, Z is the generalized Kendall's correlation coefficient and P is the probability that a correlation is not present.

Correlation	N	Z	P
$\Pi_{18.5} - \alpha_5^{18.5}$	71	3.526	0.0004
$\Pi_{18.5} - \alpha_{1.4}^{5}$	37	2.747	0.006
$\Pi_{18.5} - z$	49	1.283	0.1996
$\Pi_{18.5} - \log L_{5\mathrm{GHz}}$	27	0.764	0.445
$\Pi_{18.5} - \Pi_{1.4}$	37	0.526	0.5992

Wilcoxon two-sample test yields a probability of 21.7% that the distributions of QSOs and radio galaxies are drawn from the same parent population.

These values are somewhat lower than those found by Klein et al. (2003) at 10.6 GHz and by Pentericci et al. (2000) at 8.4 GHz for their sample of high-redshift radio galaxies observed at high angular resolution (typical polarizations of 10–20%). Nevertheless we point out that both the high spatial resolution of the Pentericci et al. sample and the selection criterion used by Klein et al. may introduce a bias toward high fractional polarization values, as stressed in the introduction to this Chapter.

We have used the NVSS public data (Condon et al. 1998) to investigate the polarization properties of our sources at 1.4 GHz. The 37 steep-spectrum sources detected by the NVSS in the overlapping region, have a median 1.4 GHz fractional polarization of $\simeq 0.4\%$, comparable to the residual instrumental polarization (0.3%). To obtain a more reliable estimate of the 1.4 GHz polarization, we included the steep-spectrum Kühr sources in the Northern sky. This selected 184 objects in total. We find $\Pi_{1.4,\mathrm{median}} \simeq 1.1\%$. The Peto & Prentice two-sample test rules out at a very high confidence level ($\mathrm{P} < 10^{-5}$) the hypothesis that the distributions at 1.4 and 18.5 GHz are drawn from the same parent population.

The origin of this frequency dependence is not well understood. The multi-frequency polarization measurements by Klein et al. (2003), quoted by Mesa et al. (2002), indicate an increase by a factor of $\simeq 3$ of the fractional polarization of steep-spectrum sources between 1.4 and 10.4 GHz. This is attributed to Faraday depolarization in uniform slabs with effective rotation measure $RM \simeq 260\,\mathrm{rad\,m^{-2}}$. However, an increase of the fractional polarization with frequency, as expected in the case of a Faraday screen at the

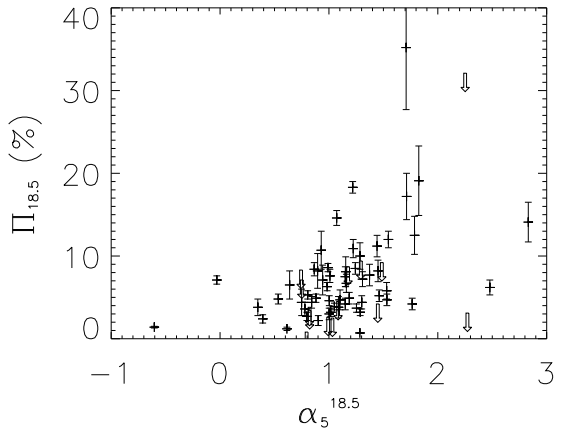

Figure 4.3: $\Pi_{18.5}$ vs $\alpha_5^{18.5}$ for the steep-spectrum sample. $\Pi_{18.5}$ upper limits are represented by downward arrows.

source, translates in a positive correlation with redshift. For example, in the presence of a Faraday screen located at redshift z, the observed rotation measure is related to the intrinsic value by $RM_{\rm obs} = RM_{\rm intr}(1+z)^{-2}$. However no significant correlation is found in our data between $\Pi_{18.5}$ and z (see Table 4.2). This may be consistent with the findings by Pentericci et al. (2000) that the fraction of powerful radio galaxies with extreme Faraday rotation measures ($RM > 1000\,{\rm rad\,m^{-2}}$) increases steeply with redshift. This suggests that their average environment becomes increasingly dense with increasing z. The larger mean fractional polarization measured at 18.5 GHz may imply that Faraday depolarization is negligible at high frequencies. Polarization measurements at intermediate frequencies are necessary to assess this.

Table 4.2 also shows the results of our investigation of possible correlations of $\Pi_{18.5}$ with other source properties. There are indications of a correlation with the spectral indices $\alpha_{1.4}^{5}$ and (more significantly) $\alpha_5^{18.5}$: steeper sources seem to have stronger $\Pi_{18.5}$ (Fig. 4.3). The fact that sources with the highest $\Pi_{18.5}$ and the steepest $\alpha_5^{18.5}$ are generally at low redshift may suggest that they are resolved and we are actually seeing highly polarized portions of them, such as radio lobes. We note, however, that any correlation should be taken with caution due to the incompleteness of the steep-spectrum source sample. The fractional polarization at 18.5 and 1.4 GHz are uncorrelated. We do not see any correlation between fractional polarization and other source properties.

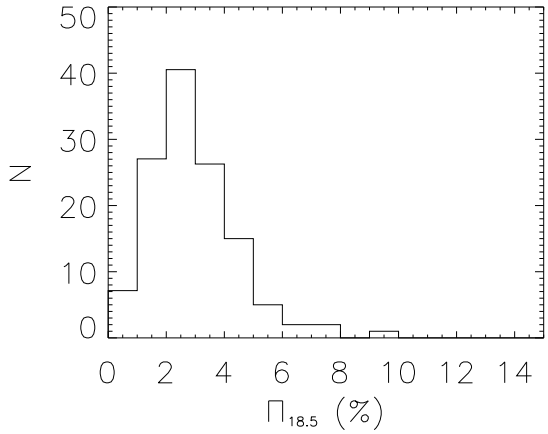

Figure 4.4: Distribution of the fractional polarization at 18.5 GHz for the flat-spectrum sample.

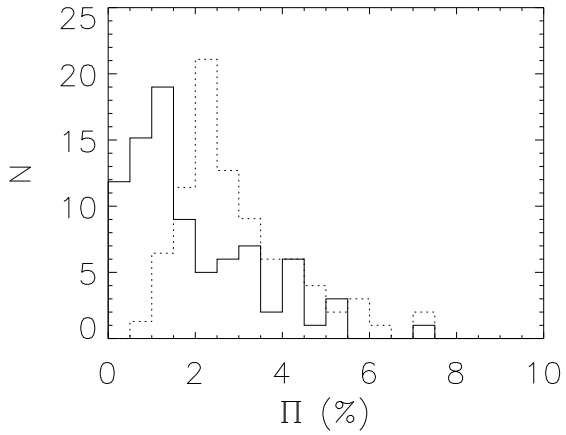

Figure 4.5: Linear fractional polarization distribution at 1.4 GHz (solid line) and 18.5 GHz (dotted line) for the 86 flat-spectrum southern Kühr sources in the NVSS survey.

4.4.2 Flat-spectrum sources

We used the Kaplan-Meyer estimator to derive the fractional polarization distribution of the 126 flat-spectrum sources in our final sample (114 detections and 12 upper limits). The result is shown in Fig. 4.4: the median value is 2.7% and the mean value is 2.9±0.1%. This is about a factor of 2 lower than that found for the steep-spectrum sources.

We used the NVSS catalog (Condon et al. 1998) to determine the fractional polarization at 1.4 GHz, $\Pi_{1.4}$: 86 flat-spectrum sources overlap with the NVSS survey. The distribution of $\Pi_{1.4}$ is shown in Fig. 4.5: it has a median value of 1.4%, comparable to the value found for steep-spectrum sources, and a factor of 2 lower than that at 18.5 GHz. This seems to be in disagreement with the results of Jones et al. (1985) and Rudnick et al. (1985), who found a constant polarization value of 2.5% in the frequency range 1.4–90 GHz.

In Table 4.3 we give the median fractional polarization for different classes of objects in the flat-spectrum sample (QSOs, BL Lacs and radio galaxies). In the last column of the table, we give the median fractional polarization at 1.4 GHz that was computed by including the northern ($\delta > 0$) Kühr sources with NVSS detection. Adding the latter sources increases the total number of flat-spectrum sources with 1.4 GHz polarization data from 86 to 238: the number of QSOs increases from 74 to 175, that of BL Lacs from 5 to 34, and that of galaxies from 5 to 25. We do not find any significant indication of differences in the 18.5 GHz polarization properties of the various sub-populations. However the very small number of BL Lacs and radio galaxies means that this comparison is not very meaningful. The comparison at 1.4 GHz is more significant: the Peto & Prentice generalized Wilcoxon two-sample test yields probabilities of $\simeq 1\%$ and of 0.001% that the fractional polarization distributions of QSOs are drawn from the same parent population as BL Lacs and radio galaxies, respectively.

Unlike the steep-spectrum sources, we do not see an increase in the fractional polarization between 1.4 and 18.5 GHz. As illustrated in Fig. 4.6, sources that are weakly polarized at 1.4 GHz show a stronger fractional polarization at 18.5 GHz. This could be suggestive of differential Faraday depolarization effects. Nevertheless, we do not see an increase of the fractional polarization with redshift, as might be expected in the case of Faraday depolarization inside the source. It should be remembered that the emission at different frequencies comes from different regions in the source, and that

Table 4.3: Median fractional polarization of flat-spectrum sources. Columns 2 and 5 give the number and the median fractional polarization at 18.5 GHz of the different classes of sources in our sample. In parentheses are the number of such sources in the NVSS area (column 3), and their median fractional polarization at 18.5 GHz (column 6) and at 1.4 GHz (column 7). Columns 4 and 8 give the total number of Kühr flat-spectrum sources of the different classes in the NVSS catalog, and their median fractional polarization at 1.4 GHz.

Type	N			$\Pi_{18.5}$ (%)		$\Pi_{1.4}$ (%)	
QSO	108	(74)	175	2.7	(2.6)	(1.4)	1.4
BL Lac	8	(5)	34	3.0	(2.9)	(1.2)	2.2
GAL	8	(5)	25	2.4	(2.5)	(1.8)	0.3

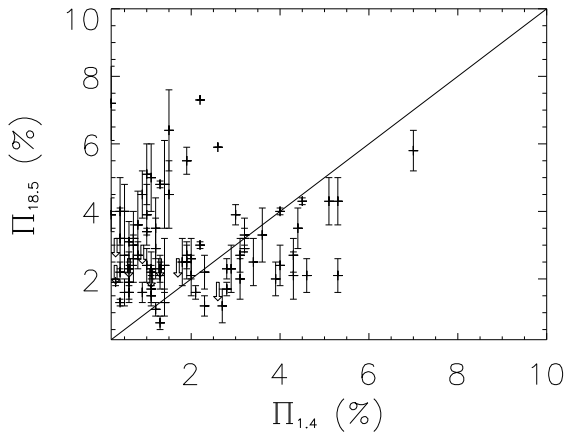

Figure 4.6: $\Pi_{18.5}$ vs $\Pi_{1.4}$ for the flat-spectrum sample. $\Pi_{18.5}$ upper limits are represented by downward arrows.

these regions may have intrinsically different polarization properties. On the other end, sources with $\Pi_{1.4} \gtrsim 2\%$ tend to have $\Pi_{1.4} \gtrsim \Pi_{18.5}$, which may be the result of the decreased contribution, at high-frequency, of the more polarized, steep-spectrum, diffuse component.

To get further hints on mechanisms that determine the polarization properties of sources, we used the generalized Kendall's rank correlation coefficient Z to look for possible correlations between $\Pi_{18.5}$, $\Pi_{1.4}$ and other properties of our flat-spectrum radio sources, such as: the low-frequency spectral index (between 1.4 GHz and 5 GHz), the high-frequency spectral index (between 5 and 18.5 GHz), the monochromatic luminosity at 5 GHz. The values of the probability P that *no* correlation is present are given for both the

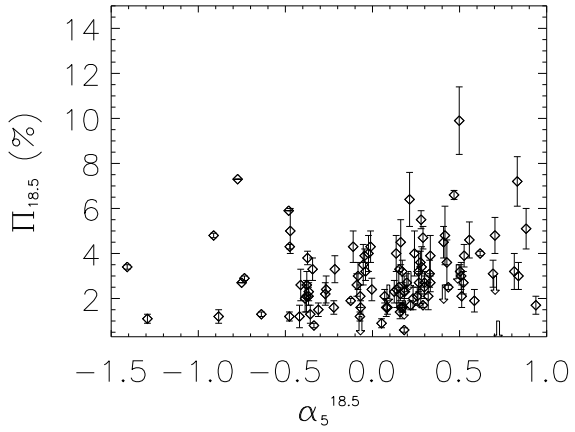

Figure 4.7: $\Pi_{18.5}$ vs $\alpha_5^{18.5}$ for the 108 flat-spectrum QSOs. $\Pi_{18.5}$ upper limits are indicated by downward arrows.

whole flat-spectrum sample and the flat-spectrum QSOs only in Table 4.4. At variance with what found for the steep-spectrum sample, there is no evidence of a correlation between $\Pi_{18.5}$ and $\alpha_5^{18.5}$ (see Fig. 4.7).

4.5 Discussion and conclusions

We have performed high-frequency observations of a large, complete sample of bright extragalactic radio sources: 250 of the 258 sources in the southern sky ($\delta < 0°$) of the 5 GHz Kühr et al. (1981) sample were observed with the ATCA at 18.5 GHz. This sample is complete to $S_{5\mathrm{GHz}} \geq 1$ Jy. The polarized flux has been measured to better than 5σ for 170 sources (114 flat-spectrum and 56 steep-spectrum) and upper limits have been set for additional 27 sources (12 flat-spectrum and 15 steep-spectrum). This represents 88% of the flat-spectrum sources and 62% of the steep-spectrum sources in the southern Kühr sample. 53 sources were not considered in our analysis, as they appear to be extended (i.e. our point-source model fitting technique showed a significant fraction of non-point-like emission). Most of the extended sources are steep-spectrum. Consequently our conclusions about this class of objects may be biased against extended sources.

The median fractional polarization at 18.5 GHz for steep and flat-spectrum sources was found to be $\simeq 4.8\%$ and $\simeq 2.7\%$, respectively. The distributions are both skewed, with tails towards high values, up to a maximum of $\simeq 20\%$ and $\simeq 10\%$, respectively.

Table 4.4: Test for correlations between the fractional polarization at 18.5 and 1.4 GHz and other properties of the flat-spectrum sources (whole sample and QSO sub-sample only). Z is the generalized Kendall's correlation coefficient and P is the probability that a correlation is not present.

Correlation	Z		P	
	All	QSO	All	QSO
$\Pi_{18.5} - \alpha_{1.4}^{5}$	0.47	0.23	0.48	0.63
$\Pi_{18.5} - \alpha_{5}^{18.5}$	1.83	2.29	0.07	0.02
$\Pi_{18.5} - z$	0.23	0.09	0.82	0.93
$\Pi_{18.5} - L_{5\mathrm{GHz}}$	0.91	0.56	0.36	0.58
$\Pi_{18.5} - \Pi_{1.4}$	0.95	0.24	0.34	0.81
$\Pi_{1.4} - \alpha_{1.4}^{5}$	0.89	0.89	0.38	0.37
$\Pi_{1.4} - \alpha_{5}^{18.5}$	1.90	1.47	0.05	0.14
$\Pi_{1.4} - z$	1.85	1.53	0.06	0.13
$\Pi_{1.4} - L_{5\mathrm{GHz}}$	1.75	1.58	0.08	0.11

That steep-spectrum sources generally display higher fractional polarization than flat-spectrum sources could be explained either in terms of different intrinsic polarization properties of the two classes of objects, or in terms of different internal depolarization effects (flat sources, usually dominated by their core emission, could be more heavily depolarized). An alternative to depolarization by internal Faraday rotation is also offered by gradients in an external Faraday screen that are not resolved by our observations. However, these two depolarizing mechanisms cannot be distinguished given polarization measurements at only two frequencies. Moreover, spectral indices and polarization levels of low-redshift steep-spectrum radio sources with high polarization degrees ($\Pi_{18.5} > 10\%$) could be overestimated due to resolution effect. Magnetic fields are more ordered on small angular scales, thus increasing polarization degrees on those scales.

We used the NVSS survey data to derive the fractional polarization at 1.4 GHz for the Kühr all-sky sample. We find very similar median values for both the steep and the flat sources (1.1% and 1.4%, respectively). This means a factor of $\sim$4 ($\sim$2) increase from 1.4 to 18.5 GHz for the steep (flat) spectrum sources. It is unclear whether such an increase can be attributed to a decreased internal Faraday depolarization. In this case we would expect the fractional polarization to be correlated with redshift. However such a correlation is not found either for the steep or for the flat spectrum sources. For steep-spectrum sources, any redshift dependence could be counteracted by a steep increase

of the intrinsic Faraday rotation measures with redshift, reflecting an increase of the environmental density (Pentericci et al. 2000). For the flat-spectrum sample, on the other hand, it is more likely that the increase in polarization is because the radio emission at different frequencies comes from different core components, that may have intrinsically different polarization properties.

We do not see any significant correlation between $\Pi_{18.5}$ and other source properties, such as the low-frequency spectral index and the luminosity at 5 GHz. A possible weak (3σ) correlation between $\Pi_{18.5}$ and the high-frequency spectral index, $\alpha_5^{18.5}$, is apparent in the steep-spectrum sample only.

An important application of these results is the estimate of the contamination of CMB polarization maps by extragalactic radio sources (Mesa et al. 2002), shown in Fig. 4.8. Based on the multi-frequency radio polarimetry by Klein et al. (2003), Mesa et al. (2002) estimated an average increase by a factor of 3 of the fractional polarization of steep-spectrum sources from 1.4 GHz to higher frequencies. Our data suggest an increase by a larger factor (~ 4), although caution is needed because of the strong incompleteness of the steep-spectrum sample. On the other hand, it is worth noticing that steep-spectrum sources provide a minor contribution to polarization fluctuations at frequencies ($\gtrsim 30\,\mathrm{GHz}$) where CMB measurements are carried out. For flat-spectrum sources, Mesa et al. (2002) considered two possibilities: that the fractional polarization remains, on average, constant from 1.4 GHz to high frequencies (as found by Rudnick et al. 1985), or increases by a factor of 3 (as found by Nartallo et al. 1998). Our results are intermediate (an increase of a factor of ~ 2). This suggests a contamination of CMB polarization maps which is likely to be within the ranges considered by Mesa et al. (2002).

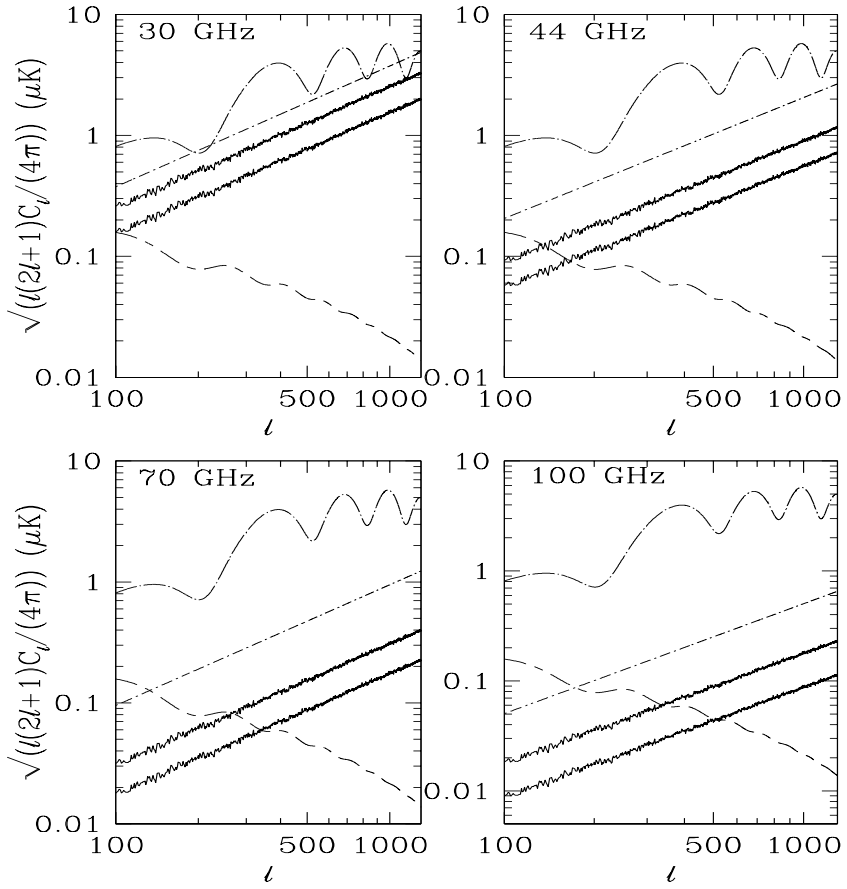

Figure 4.8: Power spectrum of polarization fluctuations due to extragalactic radio sources (irregular lines; E- and B-modes are indistinguishable) at PLANCK-LFI frequencies: 30 GHz (upper left-hand panel), 44 GHz (upper right-hand panel), 70 GHz (lower right-hand panel), and 100 GHz (lower right-hand panel). The lower irregular lines correspond to the case of a frequency-independent polarization degree for flat- and inverted spectrum sources, while the upper ones correspond to a factor of 3 increase of the mean polarization degree at Planck frequencies, compared to NVSS measurements. In both cases the mean polarization degree of steep-spectrum sources measured by the NVSS survey has been corrected upwards by a factor of 3. The dot-dashed straight line shows the preliminary estimate by De Zotti et al. (1999b). Also shown, for comparison, are the CMB E- (dot-dashed curve) and B-mode (long-short dashes) power spectra for a flat CDM cosmological model with $\Omega_\Lambda = 0.7$, $\Omega_{\rm darkmatter} = 0.25$, $\Omega_{\rm baryon} = 0.05$, $H_0 = 70\,{\rm km\,s^{-1}\,Mpc^{-1}}$, and a tensor contribution to the temperature quadrupole equal to 30% of that of scalar perturbations. The CMB power spectra were computed with CMBFAST (Seljak & Zaldarriaga 1996). (After Mesa et al. 2002)

Table 4.5: Summary of observed and derived quantities of the steep spectrum sample: (1) source name (B1950); (2) observation dates (1=March 20−21, 2= March 22, 3=March 27−28); (3) redshift; (4) source type; (5)–(6) 18.5 GHz total intensity and its error in mJy; (7)–(8) 18.5 GHz polarized flux and its error in mJy; (9)–(10) 18.5 GHz fractional polarization (%) and its error (%); (11) spectral index between 1.4 and 5 GHz; (12) spectral index between 5 and 18.5 GHz; (13) logarithm of the 5 GHz luminosity in W Hz^{-1}; (14) 1.4 GHz NVSS fractional polarization (%).

(1) name	(2) dates	(3) z	(4) type	(5) I	(6) σ_I	(7) $F_{\rm p}$	(8) $\sigma_{\rm F}$	(9) $\Pi_{18.5}$	(10) σ_Π	(11) $\alpha_{1.4}^{5}$	(12) $\alpha_{5}^{18.5}$	(13) $\log L_5$	(14) $\Pi_{1.4}$
0003−003	2,3	1.037	QSO	525.0	14.0	<43.5	8.7	<8.3	1.7	0.81	0.74	27.86	0.66
0008−421	1	...	EF	181.6	0.6	9.4	1.2	5.2	0.7	...	1.46	...	...
0022−423	1	...	QSO	339.9	0.6	10.9	1.4	3.2	0.4	...	1.28	...	...
0023−263	3	0.322	GAL	1143.7	5.5	55.8	6.2	4.9	0.5	0.69	0.88	27.20	0.11
0035−024	2,3	0.220	GAL	651.0	14.0	<29.0	5.8	<4.5	0.9	0.65	1.08	26.73	0.20
0039−445	1	...	GAL	218.6	0.7	15.7	2.0	7.2	0.9	...	1.30	...	...
0042−357	1	...	NO ID	269.9	0.7	20.6	2.1	7.6	0.8	0.73	1.00	...	1.31
0045−255	2	0.001	GAL	638.4	2.9	<16.6	3.3	<2.6	0.5	0.19	0.99	21.84	<0.10
0105−163	2,3	0.400	GAL	114.0	2.0	14.2	2.6	12.5	2.3	0.99	1.78	26.95	0.45
0114−211	2,3	...	EF	280.5	1.7	18.9	3.1	6.7	1.1	0.91	1.16	...	0.10
0117−155	2,3	0.565	GAL	325.0	2.0	35.5	3.7	10.9	1.1	0.90	1.22	27.39	0.68
0123−016	2,3	0.018	GAL	170.0	6.0	32.4	7.1	19.1	4.2	...	1.82	...	...
0131−367	1	...	GAL	54.9	0.6	7.8	1.3	14.1	2.4	...	2.83	...	...
0159−117	2,3	0.669	QSO	690.0	5.0	33.1	4.4	4.8	0.6	0.53	0.53	27.40	3.52
0201−440	1	...	QSO?	256.0	1.4	37.3	2.4	14.6	0.9	...	1.07	...	...
0235−197	2	0.620	GAL	154.1	1.0	26.5	4.3	17.2	2.8	0.91	1.71	27.43	2.93
0237−233	2	2.224	QSO	915.8	3.5	42.0	5.9	4.6	0.6	0.47	1.00	28.78	0.83
0252−712	1	...	GAL	316.6	0.9	11.7	1.7	3.7	0.5	...	1.25	...	...
0407−658	1	...	QSO?	462.0	2.2	21.7	3.0	4.7	0.7	...	1.53	...	...
0409−752	1	...	GAL	984.0	4.8	73.3	11.7	7.5	1.2	...	1.15	...	...
0413−210	2	0.807	QSO	856.1	2.3	20.4	4.2	2.4	0.5	0.52	0.39	27.57	1.15
0518−458	1	...	GAL	791.0	5.0	<24.5	4.9	<3.1	0.6	...	2.27	...	...
0602−319	1	0.452	QSO	416.0	1.4	18.1	2.8	4.4	0.7	0.67	0.84	27.03	1.00
0604−203	2	0.164	GAL	172.5	1.4	13.3	2.3	7.7	1.3	0.81	1.37	26.07	0.40
0614−349	1	0.329	GAL	494.1	1.7	17.8	4.0	3.6	0.8	0.58	0.77	26.78	<0.08
0806−103	2	0.107	GAL	388.0	3.0	18.4	4.7	4.7	1.2	0.40	1.10	25.87	4.10
0834−196	2	...	GAL?	410.0	1.4	12.3	2.8	3.0	0.7	0.89	1.00	...	0.16
0842−754	1	...	QSO	305.0	5.0	<26.5	5.3	<8.7	1.7	...	1.17	...	...
0858−279	2	2.152	QSO	1477.0	1.6	105.5	6.7	7.1	0.5	0.02	−0.03	28.15	<0.15
0915−118	2	0.055	GAL	1851.4	3.3	222.4	18.8	12.0	1.0	0.84	1.54	26.23	0.04
0941−080	2	...	GAL	371.5	2.1	<12.7	2.5	<3.4	0.7	0.72	0.82	...	0.09
1015−314	1	...	GAL	451.3	1.6	37.8	3.4	8.4	0.8	0.79	0.86	...	0.08
1017−426	1	...	QSO	249.9	0.7	21.2	1.8	8.5	0.7	...	1.24	...	...
1143−483	1	...	GAL	419.7	1.9	<15.8	3.2	<3.8	0.8	...	0.82	...	...
1151−348	1	0.258	QSO	996.9	1.8	27.0	5.0	2.7	0.5	0.61	0.79	26.89	<0.04
1221−423	1	...	GAL	359.5	1.2	18.9	1.9	5.3	0.5	...	0.80	...	...
1229−021	2,3	1.045	QSO	679.7	2.1	26.2	6.9	3.8	1.0	0.33	0.34	27.60	0.58
1239−044	2,3	0.480	GAL	186.0	3.0	<17.5	3.5	<9.4	1.9	1.01	1.29	27.05	0.45
1245−197	2	1.275	QSO	767.7	1.6	16.9	4.3	2.2	0.6	0.56	0.90	28.22	0.33
1246−410	1	...	GAL	209.1	0.9	23.4	2.7	11.2	1.3	...	1.44	...	...

Table 4.5: *continued*

(1) name	(2) dates	(3) z	(4) type	(5) I	(6) σ_I	(7) $F_{\rm p}$	(8) $\sigma_{\rm F}$	(9) $\Pi_{18.5}$	(10) σ_Π	(11) $\alpha_{1.4}^{5}$	(12) $\alpha_{5}^{18.5}$	(13) $\log L_5$	(14) $\Pi_{1.4}$
1306−095	2,3	0.464	GAL?	841.0	3.0	54.5	13.9	6.5	1.7	0.61	0.63	27.24	0.28
1308−220	2	...	EF	215.8	1.3	21.6	3.4	10.0	1.6	0.99	1.28	...	0.34
1318−434	1	...	GAL	523.4	1.5	<12.9	2.6	<2.5	0.5	...	1.03	...	...
1320−446	1	...	QSO	283.1	0.6	8.9	1.3	3.2	0.5	...	1.01	...	...
1322−428	1	...	GAL	6609.9	6.9	93.0	3.5	1.4	0.1	...	−0.60	...	...
1331−098	2,3	0.081	GAL	70.0	4.0	<22.5	4.5	<32.1	6.5	...	2.25	...	...
1333−337	1	0.013	GAL	269.7	1.7	16.8	2.3	6.2	0.9	...	2.47	...	...
1335−061	2,3	0.625	QSO	146.0	3.0	<13.5	2.7	<9.2	1.9	0.83	1.48	27.27	2.24
1355−416	1	...	QSO	194.5	1.7	11.3	1.9	5.8	1.0	...	1.53	...	...
1524−136	2,3	1.687	QSO	461.4	3.7	20.5	7.6	4.4	1.6	0.66	0.74	28.19	0.22
1637−771	1	...	GAL	430.8	1.7	<18.0	3.6	<4.2	0.8	...	1.44	...	...
1733−565	1	...	GAL	342.5	1.7	14.3	2.4	4.2	0.7	...	1.76	...	...
1740−517	1	...	GAL?	1361.8	1.6	16.5	3.1	1.2	0.2	...	0.61	...	...
1814−637	1	...	GAL	1584.3	2.2	<13.0	2.6	<0.8	0.2	...	0.79	...	...
1829−718	1	...	NO ID	258.3	0.5	10.0	1.2	3.9	0.4	...	1.05	...	...
1934−638	1,2,3	...	GAL	1166.3	0.3	8.6	0.5	0.7	0.0	...	1.28	...	...
1938−155	3	0.452	GAL	495.1	7.2	39.9	9.0	8.1	1.8	0.86	1.15	27.32	3.32
2008−068	3	...	GAL	399.7	6.2	28.5	7.0	7.1	1.8	0.50	0.94	...	0.28
2032−350	1	...	GAL?	468.0	2.0	17.9	6.0	3.8	1.3	0.84	1.08	...	5.75
2044−027	3	0.942	QSO	382.0	6.0	<27.0	5.4	<7.1	1.4	0.63	0.75	27.58	0.35
2053−201	3	0.156	GAL	109.0	7.0	38.4	8.1	35.2	7.5	0.77	1.70	26.01	<0.14
2135−209	3	0.635	GAL	479.9	7.1	39.4	10.0	8.2	2.1	0.69	0.89	27.43	<0.06
2140−816	1	...	NO ID	149.8	1.4	12.3	1.9	8.2	1.3	...	1.451	...	...
2149−287	3	...	NO ID	403.6	8.1	43.3	9.4	10.7	2.3	0.585	0.929	...	2.67
2150−520	1	...	QSO?	268.9	0.6	11.2	1.8	4.2	0.7	...	1.150	...	...
2226−411	1	...	QSO	295.2	0.8	25.4	1.5	8.6	0.5	...	0.991	...	...
2250−412	1	...	GAL	281.3	0.7	13.7	2.0	4.9	0.7	...	1.187	...	...
2252−530	1	...	GAL?	279.2	0.6	17.5	1.3	6.3	0.5	...	0.983	...	...
2317−277	2,3	...	GAL	67.0	2.0	<32.0	6.4	<47.8	9.6	0.398	2.267	...	16.20
2323−407	1	...	GAL	221.5	0.8	40.5	1.5	18.3	0.7	...	1.218	...	...
2331−417	1	...	GAL	290.0	1.4	12.8	2.3	4.4	0.8	...	1.301	...	...

Table 4.6: Summary of observed and derived quantities for flat-spectrum sources. Same columns as in Table 4.5.

(1) name	(2) dates	(3) z	(4) type	(5) I	(6) σ_I	(7) $F_{\rm p}$	(8) $\sigma_{\rm F}$	(9) $\Pi_{18.5}$	(10) σ_Π	(11) $\alpha_{1.4}^{5}$	(12) $\alpha_{5}^{18.5}$	(13) $\log L_5$	(14) $\Pi_{1.4}$
0003−066	2,3	0.347	QSO	2561.3	11.9	29.8	13.4	1.2	0.5	0.25	−0.41	26.82	2.7
0047−579	1	1.797	QSO	1643.0	2.8	77.5	7.8	4.7	0.5	...	0.29	...	...
0048−097	2,3	...	QSO	1397.1	4.9	37.2	7.7	2.7	0.5	−0.69	0.26	...	3.1
0056−572	1	...	QSO	580.1	3.1	<20.1	4.0	<3.5	0.7	...	0.48	...	...
0112−017	2,3	1.381	QSO	777.6	5.4	30.5	6.9	3.9	0.9	−0.08	0.33	27.72	1.0
0113−118	2,3	0.672	QSO	1430.1	2.9	28.4	7.6	2.0	0.5	−0.06	0.23	27.41	3.9
0122−003	2,3	1.070	GAL	1721.5	3.4	60.0	10.7	3.5	0.6	0.17	−0.25	27.63	4.4
0130−171	2,3	1.022	QSO	1614.4	8.4	36.7	6.8	2.3	0.4	−0.14	−0.36	27.41	1.3
0131−522	1	...	QSO	794.5	1.8	24.7	4.5	3.1	0.6	...	0.32	...	...
0138−097	2,3	0.501	QSO	922.8	3.0	59.4	11.3	6.4	1.2	−0.48	0.21	...	1.5
0202−172	2	1.740	QSO	1087.3	4.8	<20.3	4.1	<1.9	0.4	−0.09	0.18	27.93	2.6
0208−512	1	1.003	BLL	2913.7	7.1	99.2	9.9	3.4	0.3	...	0.09	...	...
0238−084	2,3	0.005	QSO	1012.5	8.2	<24.4	4.9	<2.4	0.5	−0.35	0.26	...	0.3
0302−623	1	...	QSO	1870.5	2.4	61.8	10.9	3.3	0.6	...	−0.21	...	...
0308−611	1	...	QSO	1215.5	1.0	18.9	4.1	1.6	0.3	...	0.08	...	...
0332−403	1	1.445	QSO	1786.4	1.9	63.9	9.1	3.6	0.5	...	0.27	...	...
0336−019	2,3	0.852	QSO	4485.9	7.8	147.1	21.7	3.3	0.5	−0.13	−0.34	27.74	3.2
0400−319	1	...	GAL	885.6	3.2	22.0	5.8	2.5	0.7	−0.34	0.13	...	1.8
0402−362	1	1.417	QSO	3180.9	3.0	42.2	4.1	1.3	0.1	−0.14	−0.63	27.78	0.4
0403−132	2	0.571	QSO	2292.2	3.0	36.6	5.6	1.6	0.2	0.30	0.17	27.53	2.1
0405−385	1	1.285	QSO	1636.5	2.9	24.9	5.7	1.5	0.3	−0.18	−0.31	27.59	1.1
0405−123	2	0.574	BLL	1430.6	3.3	23.8	5.8	1.7	0.4	0.31	0.24	27.37	1.1
0414−189	2	1.536	QSO	913.0	2.8	25.1	4.4	2.7	0.5	−0.06	0.29	27.85	0.5
0420−014	2	0.915	QSO	7912.8	13.0	85.5	12.5	1.1	0.2	0.49	−1.29	27.67	1.2
0426−380	1	1.030	BLL	1056.3	2.2	61.5	6.2	5.8	0.6	−0.36	0.07	...	7.0
0434−188	2	2.702	QSO	423.9	2.1	13.7	3.6	3.2	0.8	−0.42	0.81	27.98	0.7
0437−454	1	...	QSO	1127.2	1.4	36.5	5.1	3.2	0.5	...	0.17	...	...
0438−436	1	2.852	QSO	3926.9	3.0	97.3	2.4	2.5	0.1	...	0.43	...	...
0440−003	2	0.844	QSO	1214.8	3.4	22.6	6.4	1.9	0.5	−0.30	0.58	27.65	0.6
0454−810	1	0.444	QSO	1574.3	3.5	40.7	7.3	2.6	0.5	...	−0.09	...	...
0451−282	2	2.559	QSO	1746.6	1.6	46.9	7.8	2.7	0.4	0.09	0.19	28.50	0.8
0454−463	1	0.858	QSO	3599.6	2.3	27.8	3.8	0.8	0.1	...	−0.33	...	...
0454−234	2	1.003	QSO	5389.8	4.9	157.5	4.3	2.9	0.1	−0.13	−0.73	27.71	3.2
0458−020	2	2.286	QSO	1568.7	3.5	24.5	6.8	1.6	0.4	0.20	0.07	28.37	0.5
0506−612	1	1.093	BLL	2436.4	2.0	50.2	9.5	2.1	0.4	...	−0.26	...	...
0511−220	2	1.296	QSO	768.5	2.2	34.2	5.7	4.5	0.7	−0.55	0.40	27.54	0.9
0514−459	1	0.194	QSO	886.8	2.1	35.9	7.1	4.0	0.8	...	0.13	...	...
0524−460	1	1.479	QSO	523.9	2.6	15.9	3.3	3.0	0.6	...	0.50	...	...
0528−250	2	2.765	QSO	469.3	2.7	14.4	2.7	3.1	0.6	0.00	0.69	28.21	0.6
0537−441	1	0.896	QSO	10682.9	3.9	290.8	2.7	2.7	0.0	...	−0.75	...	...
0537−286	2	3.119	QSO	865.7	3.0	20.1	3.9	2.3	0.5	−0.13	0.12	28.16	0.6
0539−057	2	0.839	QSO	782.7	2.8	21.0	4.1	2.7	0.5	−0.44	0.52	27.38	4.3
0605−085	2	0.872	BLL	1958.8	3.2	58.6	2.8	3.0	0.1	−0.47	0.44	27.75	2.2
0606−223	2	1.926	QSO	949.1	1.8	23.6	4.6	2.5	0.5	−0.56	0.29	27.79	1.9

Table 4.6: *continued*

(1) name	(2) dates	(3) z	(4) type	(5) I	(6) σ_I	(7) $F_{\rm p}$	(8) $\sigma_{\rm F}$	(9) $\Pi_{18.5}$	(10) σ_Π	(11) $\alpha_{1.4}^{5}$	(12) $\alpha_{5}^{18.5}$	(13) $\log L_5$	(14) $\Pi_{1.4}$
0607−157	2	0.324	QSO	5999.5	7.5	287.2	5.1	4.8	0.1	0.32	−0.91	26.86	1.3
0637−752	1	0.654	QSO	4777.8	4.4	156.8	3.0	3.3	0.1	...	0.15	...	...
0642−349	1	2.165	QSO	321.5	2.1	16.5	3.0	5.1	0.9	−0.27	0.88	27.86	1.0
0743−006	2	0.994	QSO	1615.1	3.7	35.1	5.1	2.2	0.3	−0.86	0.16	27.47	0.4
0805−077	2	1.837	QSO	1659.5	2.0	21.0	6.2	1.3	0.4	0.33	−0.35	28.04	1.4
0834−201	2	2.752	QSO	4383.0	5.8	81.7	3.9	1.9	0.1	−0.49	−0.12	28.43	0.3
0859−140	2	1.339	QSO	1190.3	1.5	38.4	3.5	3.2	0.3	0.18	0.50	28.08	3.2
0919−260	2	2.300	QSO	1442.5	2.1	23.0	4.7	1.6	0.3	−0.01	−0.06	28.14	0.9
1032−199	2	2.198	QSO	1260.3	2.4	26.7	6.5	2.1	0.5	−0.18	−0.07	27.97	5.3
1045−188	2	0.595	QSO	1625.2	2.1	36.4	7.7	2.2	0.5	0.01	−0.27	27.10	2.3
1057−797	1	...	QSO	2638.0	1.9	100.1	8.4	3.8	0.3	...	−0.37	...	...
1104−445	1	1.598	QSO	2273.0	2.4	27.7	3.5	1.2	0.2	...	−0.07	...	...
1116−462	1	0.713	BLL	963.8	2.3	39.8	1.3	4.1	0.1	...	0.25	...	...
1127−145	2	1.187	QSO	2926.2	2.2	116.3	2.7	4.0	0.1	−0.12	0.61	28.34	4.0
1143−245	2	1.950	QSO	691.3	3.3	<17.7	3.5	<2.6	0.5	0.15	0.40	28.06	1.7
1144−379	1	1.048	QSO	4431.6	5.8	323.7	2.2	7.3	0.0	0.08	−0.77	...	2.2
1145−071	2	1.342	QSO	809.9	1.7	22.2	3.6	2.7	0.4	−0.41	0.33	27.60	1.9
1148−001	2	1.982	QSO	972.2	1.0	20.6	4.6	2.1	0.5	0.29	0.51	28.35	4.6
1202−262	2	0.789	NO ID	509.3	1.5	<11.5	2.3	<2.3	0.5	0.36	0.54	27.37	1.1
1213−172	2	...	GAL	1897.1	2.5	41.3	3.9	2.2	0.2	0.09	−0.19	...	1.1
1237−101	2,3	0.753	QSO	1032.6	5.4	23.6	7.6	2.3	0.7	0.11	0.18	27.37	2.9
1243−072	2,3	1.286	QSO	712.1	1.0	24.5	6.7	3.4	0.9	...	0.28	...	...
1244−255	2	0.633	GAL	1848.1	3.1	60.6	14.4	3.3	0.8	−0.12	−0.23	27.20	3.6
1253−055	1,2,3	0.536	QSO	28043.5	12.3	1648.5	1.7	5.9	0.0	−0.33	−0.48	28.07	2.6
1255−316	1	1.924	QSO	2000.6	3.5	86.9	13.7	4.3	0.7	−0.32	−0.11	27.99	5.3
1302−102	2,3	0.286	QSO	827.0	2.0	26.4	7.4	3.2	0.9	−0.39	0.26	26.48	0.4
1313−333	1	1.210	BLL	1457.6	3.0	33.2	8.0	2.3	0.5	−0.04	−0.05	27.69	1.1
1334−127	2,3	0.539	QSO	7107.4	6.8	88.4	23.0	1.2	0.3	0.14	−0.88	27.34	2.3
1352−104	2,3	0.332	QSO	1659.4	2.0	35.1	10.9	2.1	0.7	−0.21	−0.37	26.56	4.3
1354−152	2	1.890	QSO	999.8	1.3	21.4	6.0	2.1	0.6	−0.63	0.32	27.78	2.0
1406−076	2,3	1.494	QSO	1792.3	4.9	35.2	11.3	2.0	0.6	−0.35	−0.38	27.62	3.1
1424−418	1	1.522	QSO	2923.3	2.1	25.6	4.5	0.9	0.2	...	0.05	...	...
1451−375	1	0.314	QSO	2004.8	3.1	78.1	5.8	3.9	0.3	−0.54	−0.04	26.75	3.0
1504−166	3	0.876	QSO	1498.6	10.0	<47.3	9.5	<3.2	0.6	0.24	0.21	27.70	0.3
1508−055	2,3	1.191	BLL	1272.2	6.2	37.3	11.9	2.9	0.9	0.30	0.49	28.05	1.2
1510−089	2,3	0.361	QSO	2527.6	5.7	63.1	18.9	2.5	0.7	−0.10	0.15	27.12	3.4
1514−241	3	0.049	QSO	2030.1	11.4	86.9	13.4	4.3	0.7	0.01	−0.01	...	5.1
1519−273	3	...	QSO	1632.3	8.8	90.4	6.8	5.5	0.4	−0.59	0.27	...	1.9
1541−828	1	...	GAL	589.7	1.8	15.0	3.1	2.5	0.5	...	0.69	...	...
1549−790	1	0.149	QSO	1429.2	2.1	<14.8	3.0	<1.0	0.2	...	0.72	...	...
1555+001	2,3	1.770	QSO	891.5	3.8	<26.3	5.3	<3.0	0.6	−0.55	0.70	27.95	0.9
1610−771	1	1.710	QSO	2674.3	3.0	46.1	2.0	1.7	0.1	...	0.29	...	...
1619−680	1	1.354	GAL	724.7	1.4	<14.7	2.9	<2.0	0.4	...	0.72	...	...
1622−253	3	...	QSO	2144.1	19.4	86.7	16.8	4.0	0.8	0.15	−0.02	...	0.5
1718−649	1	0.015	QSO	3003.2	2.7	18.7	4.4	0.6	0.1	...	0.18	...	...

Table 4.6: *continued*

(1) name	(2) dates	(3) z	(4) type	(5) I	(6) σ_I	(7) $F_{\rm p}$	(8) $\sigma_{\rm F}$	(9) $\Pi_{18.5}$	(10) σ_Π	(11) $\alpha_{1.4}^{5}$	(12) $\alpha_{5}^{18.5}$	(13) $\log L_5$	(14) $\Pi_{1.4}$
1741−038	3	1.057	QSO	4921.9	21.8	77.2	13.6	1.6	0.3	−0.75	−0.22	27.81	0.6
1815−553	1	...	QSO	1097.2	2.2	15.4	3.4	1.4	0.3	...	0.15	...	...
1831−711	1	1.356	QSO	2221.1	2.1	27.1	4.3	1.2	0.2	...	−0.47	...	...
1903−802	1	0.500	QSO	614.9	2.0	18.5	3.5	3.0	0.6	...	0.83	...	...
1933−400	1	0.966	QSO	1162.7	1.5	26.9	3.3	2.3	0.3	−0.30	0.18	27.49	2.8
1936−155	3	1.657	QSO	966.6	8.1	34.7	9.4	3.6	1.0	−0.80	0.42	27.69	0.8
1936−623	1	...	QSO	531.4	1.4	24.4	4.0	4.6	0.8	...	0.55	...	...
1954−388	1	0.626	GAL	3810.4	1.8	26.5	6.0	0.7	0.2	−0.25	−0.47	27.34	1.3
1958−179	3	0.650	QSO	1337.7	6.0	39.7	8.7	3.0	0.6	−0.61	−0.08	27.06	0.7
2000−330	1	3.777	EF	514.7	1.9	<13.3	2.7	<2.6	0.5	−0.74	0.61	27.91	<0.6
2005−489	1	0.071	QSO	1345.5	1.3	<15.9	3.2	<1.2	0.2	...	−0.06	...	...
2008−159	3	1.180	QSO	2245.9	7.5	46.7	9.3	2.1	0.4	−0.73	−0.36	27.45	1.3
2052−474	1	1.491	QSO	739.1	1.5	12.3	2.8	1.7	0.4	...	0.93	...	...
2106−413	1	1.055	QSO	1895.0	2.8	29.7	4.5	1.6	0.2	...	0.16	...	...
2126−158	3	3.266	QSO	933.5	10.9	36.9	9.5	4.0	1.0	−0.60	0.24	27.98	<0.4
2128−123	3	0.501	QSO	3390.8	16.8	86.6	21.7	2.6	0.6	−0.12	−0.37	27.20	2.0
2131−021	3	0.557	QSO	2272.8	17.9	79.7	20.0	3.5	0.9	−0.17	−0.05	...	1.2
2142−758	1	1.139	QSO	687.9	2.2	68.4	10.5	9.9	1.5	...	0.49	...	...
2155−152	3	0.672	QSO	2505.5	17.1	60.5	14.7	2.4	0.6	0.42	−0.26	27.48	4.0
2203−188	2,3	0.619	QSO	2200.0	11.6	85.8	11.5	3.9	0.5	0.29	0.52	27.78	0.2
2204−540	1,3	1.206	QSO	1306.6	2.2	86.1	2.0	6.6	0.2	...	0.46	...	...
2206−237	2,3	0.087	QSO	340.6	2.5	24.6	3.8	7.2	1.1	0.53	0.83	...	0.2
2210−257	2,3	1.833	QSO	609.1	15.2	29.3	7.6	4.8	1.3	0.11	0.41	27.94	1.4
2216−038	3	0.901	QSO	2571.6	13.5	66.9	17.5	2.6	0.7	0.30	−0.41	27.62	0.7
2223−052	3	1.404	QSO	8394.5	10.8	359.7	10.8	4.3	0.1	0.39	−0.47	28.49	4.5
2227−088	3	1.561	QSO	1570.5	8.1	<40.2	8.0	<2.6	0.5	−0.47	0.09	27.81	1.3
2243−123	3	0.630	QSO	2043.7	9.8	48.8	16.4	2.4	0.8	−0.20	0.13	27.43	1.4
2255−282	2,3	0.926	QSO	11226.5	20.3	379.2	6.7	3.4	0.1	−0.27	−1.40	27.55	1.0
2311−452	1,3	2.884	QSO	585.6	1.6	28.1	4.5	4.8	0.8	...	0.70	...	...
2326−477	1,3	1.306	GAL	1571.0	2.8	23.1	3.6	1.5	0.2	...	0.30	...	...
2329−162	2,3	1.155	QSO	1964.4	8.1	99.2	19.7	5.0	1.0	0.18	−0.47	27.63	1.1
2331−240	2,3	0.048	QSO	1095.7	3.5	25.8	5.8	2.4	0.5	−0.26	−0.00	...	1.0
2333−528	1,3	...	QSO	1113.9	0.9	23.3	3.3	2.1	0.3	...	0.07	...	...
2345−167	2,3	0.576	QSO	2747.7	5.1	46.8	5.4	1.7	0.2	−0.25	0.21	27.53	2.8
2353−686	1,3	1.716	QSO	785.4	0.9	16.4	3.4	2.1	0.4	...	0.25	...	...
2354−117	3	0.960	QSO	1197.1	7.2	54.0	12.3	4.5	1.0	0.16	0.16	27.62	1.5
2355−534	1,3	1.006	QSO	1602.1	2.7	51.9	6.9	3.2	0.4	...	−0.04	...	...

Chapter 5

Analysis of Kühr flat-spectrum quasars

5.1 Introduction

During the high-frequency radio observations accomplished at the Australia Telescope Compact Array (ATCA) in March 2002, described in Chapter 4 (see also Ricci et al. 2004a), we obtained low-resolution (HPBW=15.6 arcsec) reliable flux density measurements in total intensity and linear polarization of 198 out of the 258 sources present in the southern part of the 1 Jy sample (Kühr et al. 1981; Stickel et al. 1994). The linear polarization data were analysed in Chapter 4 (Ricci et al. 2004a), whereas the total intensity 18.5 GHz flux density measurements are used here to compute the high-frequency (18.5 GHz) radio luminosity function of the flat-spectrum quasars.

No previous study of the flat-spectrum quasar luminosity function at such a high radio frequency is reported in literature. This is due to the lack of complete samples of objects for which high-frequency flux density and redshift measurements are available. As the Kühr sample is selected at low frequency (5 GHz) and we aim at obtaining the luminosity function (LF) at 18.5 GHz, we relied on the bivariate technique to compute the LF of flat-spectrum radio quasars (FSRQs). In other wavelength bands the bivariate approach was used by Loveday (2000) to compute the K-band luminosity function of nearby field galaxies. It was implemented based on the Sondré & Lahav (1993) extension of the stepwise maximum likelihood (SWML) method developed by Efstathiou et al. (1988). This technique is suited when any good a priori parametric model of the bivariate LF is known and enough objects are present in each redshift bin. In this study we decided not

to implement this method because of the sample smallness per redshift bin.

In § 5.2 of this Chapter we describe how we selected the FSRQ sub-sample and how we estimated the sample incompleteness in redshift and high-frequency flux density. As no 5 GHz LF of the Kühr sample FSRQs was reported in literature and the 5 GHz LF is the basis to build the high-frequency bivariate LF, in § 5.3 we describe its computation in four redshift bins and the comparison with the 5 GHz model LF for FSRQs by De Zotti et al. (2004) (hereafter GDZ04), presented in Chapter 2. In § 5.4 we checked the GDZ04 5 GHz model LF against the observables (redshift distribution and differential source counts) of Kühr FSRQ sub-sample to verify its reliability. In § 5.5 we worked out the space density of Kühr sample FSRQs and compared it to the theoretical space density obtained integrating the GDZ04 model LF. This was done again to test the model predictions and study the evolution properties of FSRQs. Finally the bivariate distribution matrix approach, chosen to compute the 18.5 GHz LF of Kühr sample FSRQs, is described in § 5.6 and tested against the high-frequency bivariate LF obtained by convolving the 5 GHz GDZ04 model LF with the $\alpha_5^{18.5}$ spectral index distribution of Kühr sample FSRQs.

In the computations of this Chapter, we adopted a flat Λ cosmology with $\Omega_\Lambda = 0.7$ and $H_0 = 70$ km s^{-1} Mpc^{-1}.

5.2 Sample selection

To select the flat-spectrum quasars among the 1 Jy sample objects we used the optical and radio spectrum classification provided by Stickel et al. (1994) in their Table 1 (optical data) and 2 (radio data). The morphological type (column 4) "QSO" in their Table 1 was used to classify Kühr radio sources as quasars, while the spectral label FS in column 8 of their Table 2 was preferred to 2.7-5 GHz spectral index to classify sources as flat-spectrum. This criterion was chosen because the labelling "FS" takes the overall radio source spectral shape into account, whereas 2.7-5 GHz spectral indices only rely on non-coeval two-frequency flux density measurements. At the end of this preliminary selection we ended up with a sample of 214 flat-spectrum radio quasars (FSRQs).

As our primary aim is to determine radio luminosity functions, we also needed to obtain as much redshift information as possible. The redshift incompleteness of the 1 Jy sample, as reported in Stickel et al. (1994) is very low. Of all the 214 FSRQs, only 16 redshifts are missing ($\simeq 7.5\%$). A search on the NASA-IPAC Extragalactic Database (NED) yielded 8

Table 5.1: Flux density distribution of Kühr FSRQs. $N_{\rm bin}$ is the number of sources with measured redshift. $N_{\rm tot}$ is the total number of sources.

$\log S_{5,\rm min}$	$\log S_{5,\rm max}$	$\rm N_{bin}$	$\rm N_{tot}$	$\rm N_{bin}/N_{tot}$
0.00	0.20	115	122	0.94
0.20	0.40	56	57	0.98
0.40	0.60	20	20	1.00
0.60	0.80	7	7	1.00
0.80	1.00	3	3	1.00
1.00	1.20	3	3	1.00
1.20	1.40	1	1	1.00
1.40	1.60	0	0	–
1.60	1.80	1	1	1.00

more redshifts. Redshift completeness histograms as a function of low-frequency (5GHz) flux density and optical magnitude are presented in Table 5.1 and Table 5.2, respectively.

Of the 114 FSRQs observed with ATCA, 11 do not have reliable 18.5 GHz flux density measurements (confusion parameter $C > 5\%$; see Ricci et al. 2004a and Chapter 4). The statistics of 18.5 GHz flux density incompleteness as a function of 5GHz flux density is shown in Table 5.3.

Data on the position, 5 GHz flux density, spectral index, magnitude, redshift for all the flat-spectrum quasars, and ATCA 18.5 GHz flux density measurements for the southern sub-sample are also provided in Table 5.4.

5.3 Low-frequency luminosity function of Kühr FSRQs

The first step to construct the high-frequency *bivariate* luminosity function is to compute the low-frequency (5GHz) LF for the Kühr FSRQ sub-sample taking the redshift incompleteness into account.

For all the 206 quasars of the FSRQ sample having redshift information we computed the 5 GHz luminosity according to the formula:

$$L_5 = \frac{4\pi d_L^2 S_5}{(1+z)^{1-\alpha}} \tag{5.1}$$

where $\rm L_5$ is the 5 GHz luminosity, $(1+z)^{1-\alpha}$ is the K-correction term for a power-law radio spectrum $\rm S_\nu \propto \nu^{-\alpha}$ and d_L is the luminosity distance. When computing d_L we used

Table 5.2: Apparent magnitude distribution of Kühr FSRQs. N_{bin} is the number of sources with measured redshift. N_{tot} is the total source number.

mag_{min}	mag_{max}	N_{bin}	N_{tot}	N_{bin}/N_{tot}
14.0	14.5	0	0	–
14.5	15.0	1	1	1.00
15.0	15.5	1	1	1.00
15.5	16.0	3	3	1.00
16.0	16.5	11	11	1.00
16.5	17.0	21	21	1.00
17.0	17.5	27	27	1.00
17.5	18.0	22	22	1.00
18.0	18.5	35	36	0.97
18.5	19.0	34	36	0.94
19.0	19.5	23	24	0.96
19.5	20.0	10	10	1.00
20.0	20.5	8	8	1.00
20.5	21.0	3	4	0.75
21.0	21.5	4	5	0.80
21.5	22.0	1	3	0.33
22.0	22.5	0	0	–
22.5	23.0	1	1	1.00

Table 5.3: Fraction of Kühr FSRQs with confusion parameter $C < 5\%$ (reliable 18.5GHz flux density) in ATCA observations. N_{bin} is the number of sources with $C < 5\%$. N_z is the number of sources with $C < 5\%$ and measured redshift.

$\log S_{5,min}$	$\log S_{5,max}$	N_z	N_{bin}	N_{tot}	N_{bin}/N_{tot}
0.0	0.2	53	59	64	0.92
0.2	0.4	31	33	36	0.92
0.4	0.6	13	13	13	1.00
0.6	0.8	3	3	3	1.00
0.8	1.0	2	2	2	1.00
1.0	1.2	1	1	1	1.00

both the Λ cosmology (H_0=70 km s^{-1} Mpc^{-1}; Ω_M=0.3; Ω_Λ=0.7) formula:

$$d_L = \frac{c(1+z)}{H_0} \int_0^z \frac{dz'}{\sqrt{(1+z')^2(1+\Omega_M z') - z'(2+z')\Omega_\Lambda}} \tag{5.2}$$

and the Einstein-de Sitter cosmology (H_0=50 km sec^{-1} Mpc^{-1}; q_0=0.5) formula:

$$d_L = \frac{c}{H_0 q_0^2} \left[z q_0 + (q_0 - 1)(-1 + \sqrt{2 q_0 z + 1})\right]. \tag{5.3}$$

In choosing the $\alpha^5_{2.7}$ value to be used for the K-correction computation we tried three different possibilities:

(i) the individual $\alpha^5_{2.7}$ values tabulated by Stickel et al. (1994) in their Table 2;

(ii) $\alpha^5_{2.7} = 0$ for all the sources;

(iii) the median value of the spectral index distribution $\alpha^5_{2.7,\mathrm{med}} = -0.14$ ($S_\nu \propto \nu^{-\alpha}$).

The last solution was chosen as our baseline.

The $1/V_{\mathrm{max}}$ method (Schmidt 1968) was then used to work out a non-parametric 5 GHz luminosity function in four redshift bins ($0.4 < z \leq 0.8$; $0.8 < z \leq 1.2$; $1.2 < z \leq 2$; $2 < z \leq 3$) according to the formula:

$$\Phi(L_5, z) = \sum_{L_i \in [L_5 - \Delta L/2, L_5 + \Delta L/2]} \frac{w_i^z}{V_{\mathrm{max,i}}} \tag{5.4}$$

where w_i^z is the redshift incompleteness weight worked out for each source as the inverse of the fraction of objects having measured redshift in 5 GHz flux density logarithmic bins as shown in Table 5.1 and $V_{\mathrm{max,i}}$ is the accessible volume (Avni & Bahcall 1980) of the *ith* source in the L_5 luminosity bin computed according to the formula:

$$V_{\mathrm{max,i}} = \int_{z_{\mathrm{min}}}^{z_{\mathrm{max}}} dz \, \frac{dV}{dz} \tag{5.5}$$

where the volume element dV/dz is for Λ cosmology:

$$\frac{dV}{dz} = \frac{c}{H_0} \, d_M^2 \, \left[(1+z)^2 \, (1 + \Omega_M \, z) - z(2+z)\Omega_\Lambda\right]^{-1/2} \, \Omega_{\mathrm{eff}} \tag{5.6}$$

being d_M the proper motion distance (Carroll et al. 1992):

$$d_M = \frac{c}{H_0} \int_0^z \left[(1+z')^2(1 + \Omega_M \, z') - z'(2+z')\Omega_\Lambda\right]^{-1/2} dz' \tag{5.7}$$

and for EdS cosmology

$$\frac{dV}{dz} = \frac{c}{H_0} \, \Omega_{\mathrm{eff}} \, \frac{d_L^2(z; H_0, q_0)}{(1+z)^3 (1 + 2 \, q_0 \, z)^{1/2}} \tag{5.8}$$

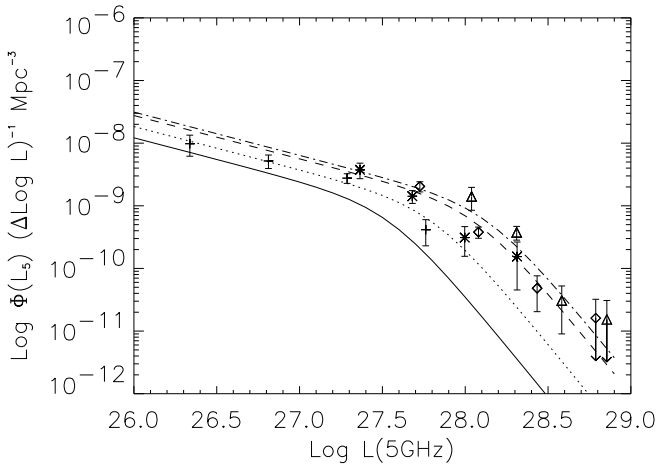

Figure 5.1: 5 GHz radio luminosity function of Kühr sample FSRQs for different redshift bins compared with GDZ04 model LF.

In equation 5.5 $z_{\rm min}$ is equal to the lower bound of the source redshift bin and $z_{\rm max}$=min($z_{\rm up}$,$z_{\rm inv}$), being $z_{\rm up}$ the upper bound of the source redshift bin and $z_{\rm inv}$ the redshift a source would have if its flux density were $S_{\rm lim}$=1 Jy.

In equations 5.6 and 5.8 the term $\Omega_{\rm eff}$ is the survey effective area, being 9.81 sr in the 1 Jy sample. In general survey effective area is dependent on flux density ($\Omega_{\rm eff}$(S)), but in the 1 Jy sample case $\Omega_{\rm eff}$ is considered to be independent on S down to the survey limiting flux density $S_{\rm lim}$=1 Jy.

The 5 GHz RLF of the 1 Jy FSRQ sample in the aforesaid redshift bins is shown in Fig. 5.1 compared with the GDZ04 model LF of the FSRQs computed in the same redshift bins of the former LF.

The symbol and line codings are as follows: crosses with error bars (1Jy FSRQ) and solid line (GDZ04) for the $0.4 < z \leq 0.8$ bin; stars with error bars (1Jy FSRQ) and dotted line (GDZ04) for the $0.8 < z \leq 1.2$ bin; diamonds with error bars (1Jy FSRQ) and dashed line (GDZ04) for the $1.2 < z \leq 2$ bin and triangles with error bars (1Jy FSRQ) and dot-dashed line (GDZ04) for the $2 < z \leq 3$ bin. The model LF was evaluated at the redshift bin centres.

The comparison in Fig. 5.1 is for illustration only, as the difference between the LF averaged over the redshift distribution (data points) and the LF at the bin centre (lines) is larger when the evolution is stronger.

5.4 Redshift distributions and source counts

As a consistency check for the low-frequency (5 GHz) luminosity function we tested how the GDZ04 model LF reproduces our observables (redshift distribution and differential source counts of the 1 Jy catalogue FSRQs).

We work out the theoretical redshift distribution using the formula:

$$N_{\mathrm{z_i}} = \Omega_{\mathrm{eff}} \int_{z_i}^{z_i+\Delta z} dz \, \frac{dV}{dz} \int_{\mathrm{L_{5,min}(\alpha,S_{lim},z)}}^{\mathrm{L_{5,max}}} dL_5 \; \Phi(L_5, z) \tag{5.9}$$

where $N_{\mathrm{z_i}}$ is the theoretical source number in the *ith* redshift bin $[z_i, z_i + \Delta z]$, being Δz the redshift binsize; dV/dz is the volume element defined in eqns. 5.6 and 5.8; $\mathrm{L_{5,max}}$ and $\mathrm{L_{5,min}}$ are the maximum and minimum luminosities allowed for in that redshift bin, the former being fixed to a finite value for computational reasons and the latter being given by equation 5.1 having $\mathrm{S_{lim}}$ instead of $\mathrm{S_5}$. Finally $\Phi(L_5, z)$ is the GDZ04 model LF of the FSRQs. The comparison between theoretical and observed redshift distribution is shown in Fig. 2.10 of Chapter 2. The values of the model LF parameters are reported in Table 2.1 of Chapter 2.

The fit seems to marginally under-reproduce the source numbers in the intermediate redshift bins (around $z \simeq 2$), but appears to be acceptable in the lowest bins and very good above $z \simeq 2$.

To compute the differential source counts of the 1 Jy FSRQ sample we used the formula:

$$n(S) = \frac{N_{\mathrm{obs}}}{\Omega_{\mathrm{eff}} \; \ln 10 \; S \; \Delta \log S} \tag{5.10}$$

where N_{obs} is source number in the flux density bin centred on S and having binsize $\Delta \log S$. In this formula Ω_{eff} units are steradians.

For the theoretical differential source counts we utilized the following expression:

$$n(S_i) = \int_{z_l}^{z_h} dz \, \frac{dV}{dz} \, \frac{L_5(S_i, z)}{S_i} \, \Phi(L_5(S_i, z), z) \tag{5.11}$$

where $n(S_i)$ is the theoretical differential count per unit area and unit flux at the flux density S_i, dV/dz is the volume element, $L_5(S_i, z)$ the 5GHz luminosity as a function of flux density S_i and redshift, Φ is the GDZ04 model LF and the integration extrema are $z_l = z(S_i, L_{\mathrm{min}})$, i.e. the redshift corresponding to the minimum luminosity L_{min} at a given flux density S_i and z_h=min$[z_{\mathrm{max}}, z(S_i, L_{\mathrm{max}})]$, i.e. the minimum redshift value between quasar formation redshift $\mathrm{z_{max}}$ and the redshift a source would have if it had

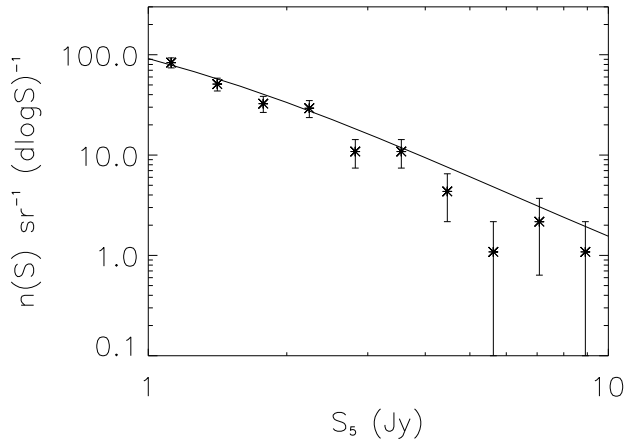

Figure 5.2: Observed differential counts (asterisks with error bars) of Kühr sample FSRQs compared with theoretical counts obtained integrating the GDZ04 model LF.

the maximum luminosity $L_{\rm max}$ for a given flux density S_i. In the actual computation the minimum luminosity was chosen to be $L_{\rm min} = 10^{23}$ W Hz^{-1}, the maximum luminosity $L_{\rm max} = 10^{29}$ W Hz^{-1}, the quasar formation redshift $z_{\rm max} = 6$ and flux density binsize in the observed counts $\log \Delta S = 0.18$.

The resulting source counts are compared in Fig. 5.2. The reduced χ^2 was $\chi^2_{\rm red} = 2.26$ and the theoretical integrated source number with limiting flux density $S_{\rm lim} > 1$ Jy are $N_{\rm th}(S_{\rm lim}) = 231.92$ against 214 objects actually observed. Theoretical and observed counts appear to be in good agreement in the faint flux density bins, whereas in the bins brighter than ~ 3 Jy the model counts appear to overestimate the observed counts. The model and observed counts appear to be well reproduced by a single power law.

5.5 5-GHz space density of Kühr FSRQs

As the 1 Jy FSRQs span a large redshift range (from z$\simeq$0.4 to z$\simeq$4) it is also worth computing the source space density above a given 5 GHz luminosity threshold and compare it with previous results (e.g. Hook et al. 1998). Such redshift range also overlaps with the region ($2 \lesssim z \lesssim 4$) in which a drop-off in QSO space density as a function of redshift has been reported in previous observational works (Warren et al. 1994; Schmidt et al. 1995; Shaver et al. 1996; Hook et al. 1998) and already modelled by Dunlop & Peacock (1990).

In order to compare the space density $\rho(z)$ in various redshift bins, we applied an overall

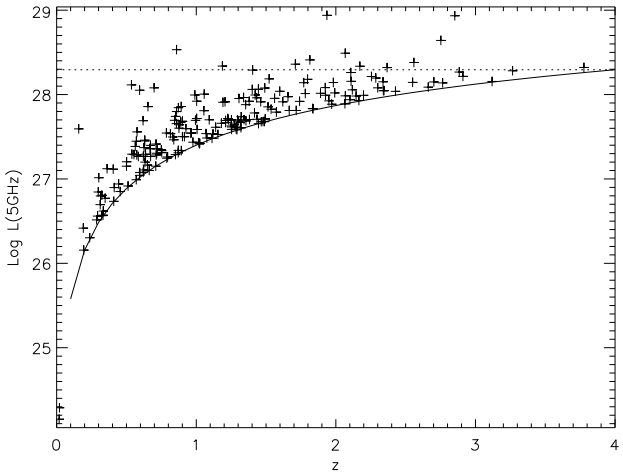

Figure 5.3: 5 GHz luminosity vs. redshift scatter plot of Kühr sample flat-spectrum quasars. The solid curve represents the limiting luminosity as a function of redshift for $S_{\rm lim} = 1$ Jy. The dotted line represents the luminosity cut corresponding to the maximum redshift in the Kühr sample. Only objects having their luminosity above that threshold were used in the space density computation.

luminosity threshold shown in the 5 GHz luminosity vs. redshift scatter plot (Fig. 5.3), so that only the objects having a 5 GHz luminosity L_5 above the limiting luminosity $L_{5,\rm lim}$ are used in the space density computation. The limiting luminosity $L_{5,\rm lim}$ represents the luminosity an object located at a redshift $z = 4$ would have if its flux density were equal to the 5 GHz limiting flux density $S_{\rm lim}$=1 Jy.

We worked out the 1 Jy FSRQ sample space density in four redshift bins spanning all the sample redshift range again using the $1/{\rm V_{max}}$ approach.

The 1 Jy FSRQ sample space density is presented in Fig. 5.4 where it is also compared with the space density obtained by integrating the GDZ04 model LF. The theoretical predictions seem to be in reasonale agreement with the data apart from the $2 < z \leq 3$ redshift bin where the GDZ04 model slightly overestimates the space density. The predicted density evolution as a funciton of redshift is basically confirmed by the data.

An important issue arising from the analysis of the Parkes flat-spectrum quasar sample in Hook et al. (1998) is the luminosity binned space density computation. They argue that the space density peak redshift increases with increasing luminosity. We test whether the same behaviour is also apparent in the 1 Jy FSRQ data. We sampled the 1 Jy FSRQ high-luminosity tail in three bins so as to have a statistically meaningful number of objects

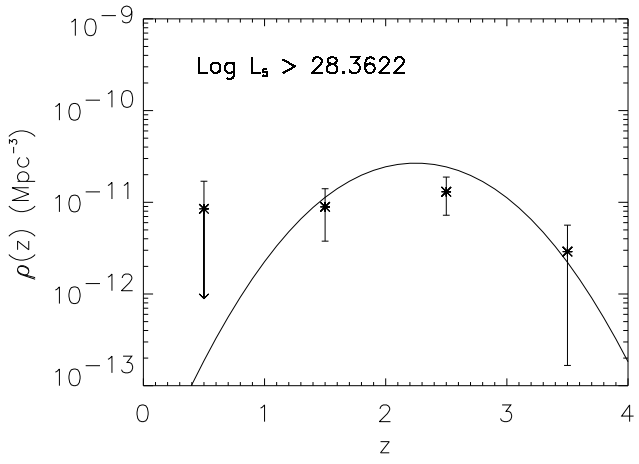

Figure 5.4: Space density of Kühr sample FSRQs having a 5 GHz luminosity above the threshold (stars with error-bars) in different redshift bins. The solid line is the space density derived integrating the GDZ04 model LF above the threshold 5 GHz luminosity.

in each luminosity bin. The binning we used is indicated by the dotted lines in the 5 GHz luminosity vs. redshift scatter plot in Fig. 5.5. The luminosity binned space density of the 1 Jy FSRQ is presented in Fig. 5.6. A positive trend of the peak redshift with luminosity is not clearly visible in that plot, probably because of the small number of objects present in the sampled redshift bins.

5.6 18.5-GHz bivariate LF of Kühr FSRQs

As the direct transformation matrix approach underestimates derived luminosity functions at the faint end of the luminosity bins in case of small source samples, we also computed the 18.5 GHz LF following a method that does not depend on sample size to evaluate the 18.5 GHz LF incompleteness in the faintest 18.5 GHz luminosity bins.

First of all, following the direct matrix-element bivariate approach, we work out the 5 GHz luminosity function for the objects in the $0.8 < z < 1.2$ redshift bin based on the $1/V_{max}$ method. Then we construct the 4×4 transformation matrix $n_{i,j}$ in bins of 5 GHz luminosity log L_5 (columns) and in bins of 18.5 GHz luminosity log $L_{18.5}$ (lines). In each matrix element we put the corresponding number of objects choosing between the 103 sources having a reliable measurement of 18.5 GHz flux density and a measured redshift, taking the 18.5 GHz flux density incompleteness into account through the weights w_i^S.

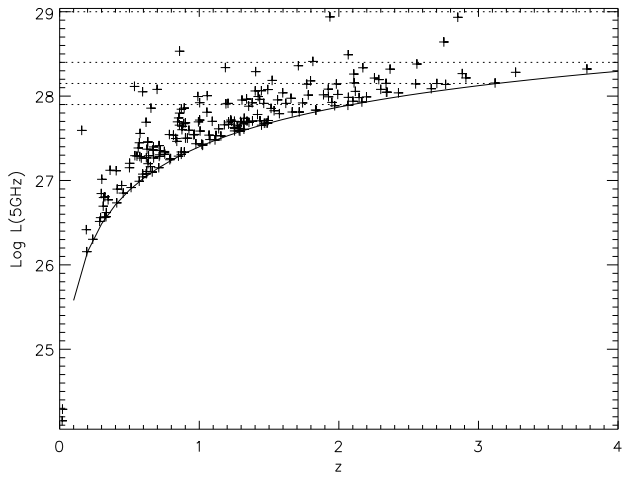

Figure 5.5: 5 GHz luminosity vs. redshift scatter plot of Kühr sample flat-spectrum quasars. The solid curve represents the limiting luminosity as a function of redshift for $S_{\rm lim} = 1$ Jy. The dotted lines are the luminosity bin limits.

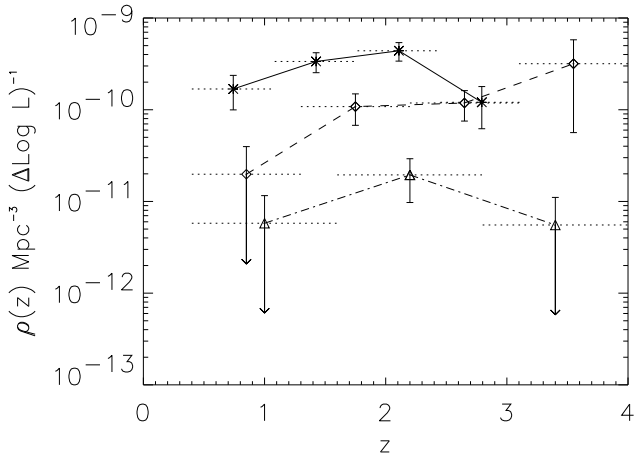

Figure 5.6: Space density at 5GHz for different 5GHz luminosity bins. The dotted lines show the redshift bin limits. The stars represent the lowest luminosity bin, the diamonds the intermediate bin and the triangles the highest.

Then we compute the statistical frequency elements $f_{i,j}$ by integrating in Log L_5 bins (along the $n_{i,j}$ matrix lines) based on the formula:

$$f_{i,j} = \frac{n_{i,j}}{\sum_j n_{i,j}} \tag{5.12}$$

For each log $L_{18.5}$ luminosity bin the 18.5 GHz luminosity function is computed using the formula:

$$\Phi_{18.5,\mathrm{i}} = \sum_j \Phi_{5,\mathrm{j}} \times f_{i,j} \tag{5.13}$$

The resulting 18.5 GHz luminosity function (crosses with error bars) is shown in Fig. 5.8.

The second method relies on the normalized spectral index distribution $\mathrm{N}(\alpha_5^{18.5})$ (Fig. 5.7) to sample the probability $p(L_{18.5}, L_5)$ that a source with given 5 GHz luminosity L_5 also has a 18.5 GHz luminosity $\mathrm{L}_{18.5}$. All these computations are valid under the hypothesis that source radio spectra follow a power law:

$$L_5 = L_{18.5} \left(\frac{18.5}{5}\right)^{\alpha} \tag{5.14}$$

where α is the $5 - 18.5$ GHz spectral index and the convention $\mathrm{L}_\nu \propto \nu^{-\alpha}$ is used.

The 18.5 GHz derived LF is then worked out based on the convolution of the 5 GHz LF with the probability $p(L_{18.5}, L_5)$:

$$\Phi(L_{18.5}) = \int_0^{+\infty} \Phi(L_5)\ p(L_{18.5}, L_5)\ dL_5 \tag{5.15}$$

where $p(L_{18.5}, L_5)$ is normalized to unity in L_5:

$$\int_0^{+\infty} p(L_{18.5}, L_5)\ dL_5 = 1 \tag{5.16}$$

and $\Phi(L_5)$ is the GDZ04 model LF evaluated at the redshift bin centre $z = 1$.

In Fig. 5.8 it is apparent that the direct transformation matrix evaluation of the bivariate distribution brings a strong incompleteness in the faint end of the 18.5 GHz LF. The derivation of the 18.5 GHz LF based on this spectral index distribution overcomes this incompleteness although it is model dependent. The comparison in Fig. 5.8 is only indicative, because the bivariate LF is averaged over the redshift distribution while the solid line refers to the redshift centre bin $z = 1$. More accurate comparison would require weighting the model LF over the same redshift interval used for the bivariate LF.

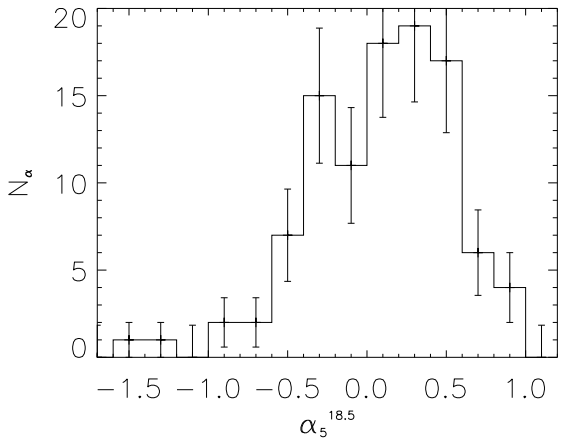

Figure 5.7: Spectral index $\alpha_5^{18.5}$ histogram with error bars of the Kühr sample FSRQs.

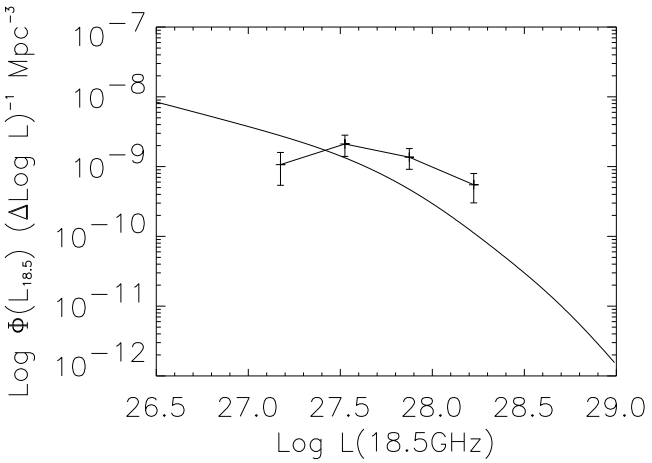

Figure 5.8: 18.5 GHz bivariate luminosity function (BLF) of the Kühr sample FSRQs (crosses with error bars), worked out in the redshift bin $0.8 < z \leq 1.2$., compared with the high-frequency LF obtained by the convolution of the 5 GHz model LF with the normalized spectral index $\alpha_5^{18.5}$ distribution (solid line). The BLF is averaged over the redshift distribution, while the solid line refers to the redshift bin centre $z = 1$. More accurate comparison would require weighting the model LF over the same redshift interval used for the bivariate LF.

5.7 Conclusions

In this Chapter we presented preliminary results on the first determination of the high-frequency (18.5 GHz) bivariate radio luminosity function of flat-spectrum radio quasars, built upon the 5 GHz luminosity function of Kühr sample FSRQs.

The low-frequency LF obtained through the $1/V_{max}$ method was compared with a new model LF (named GDZ04), whose derivation is extensively described in Chapter 2, in four redshift bins spanning the redshift range $0.4 < z \leq 3$. A reasonable agreement between theoretical predicted and experimental LFs was found, even though a better evaluation of the theoretical curves could be obtained by computing the redshift bin integrated model LF.

The observed space density of FSRQs above a threshold 5 GHz luminosity corresponding to the highest redshift measured in the Kühr FSRQ sub-sample appears to be in reasonable agreement with the GDZ04 model LF derived space density and confirms the predicted redshift evolution of flat-spectrum radio quasar population.

No clear hint of a positive trend in the peak redshift of the 5 GHz luminosity binned space density distribution with increasing 5 GHz luminosity, as reported by Hook et al. (1998) from the analysis of the Parkes quarter-Jy flat-spectrum quasar sample. Anyhow, such discrepancy could be due to the smallness of the Kühr quasar sub-sample in the higher 5 GHz luminosity redshift bins (in the $28.4 < \log\ L_5 < 29.0$ luminosity bin only six objects are present).

Finally, it is apparent from this analysis that larger complete samples of flat-spectrum quasars are needed to directly and reliably determine the high-frequency luminosity function of this population of radio sources in a wide and evolution sensitive redshift range. Even better than the high-frequency follow-up of large low-frequency surveys as is the case of PMN (Gregory et al. 1994) and GB6 (Gregory et al. 1996) would be a high-frequency ($\nu \geq 20$ GHz) blind survey, as high frequencies are known to be particularly suited to select flat-spectrum/rising-spectrum sources. The pilot study of a large area (all the southern sky) high-frequency (20 GHz) blind radio survey (AT20G) was presented in Chapter 3 of this Thesis (see also Ricci et al. 2004b).

Table 5.4: Flat-spectrum quasar sample of the Kühr catalogue: table summarizing positional, flux density, spectral index, magnitude, redshift and extension information. When three dots appear high-frequency information is not determined (northern objects or southern objects with no 18.5 GHz measurement). Extended sources (having confusion parameter $C > 5\%$) are labelled R (resolved) beside the source name, whereas southern sources without 18.5 GHz flux density measurement are labelled *.

seq.	name	RA (J2000)	Dec (J2000)	S_5	$S_{18.5}$	$\sigma_{18.5}$	$\alpha^5_{2.7}$	mag	z
–	–	–	–	Jy	mJy	mJy	–	–	–
1	0003-066	00:03:40.29	-06:40:17.3	1.48	2351.8	118.2	0.02	18.5	0.347
6	0016+731	00:16:54.20	+73:10:51.3	1.65	...	...	0.16	18.0	1.781
21	0047-579	00:47:48.20	-57:54:46.8	2.40	1647.3	82.4	0.33	18.5	1.797
25	0056-572	00:56:38.64	-57:15:22.1	1.10	579.6	29.1	0.58	18.3	0.018
26	0056-001	00:56:31.76	-00:09:18.7	1.40	...	...	-0.39	17.3	0.717
29	0106+013	01:06:04.52	+01:19:01.0	2.28	...	...	-0.08	18.4	2.107
32	0112-017	01:12:43.94	-01:42:55.2	1.20	789.0	39.9	-0.01	17.4	1.381
33	0113-118	01:13:43.22	-11:52:04.5	1.94	1419.2	71.0	0.14	18.5	0.672
39	0119+041	01:19:21.39	+04:06:43.9	1.67	...	...	0.04	19.5	0.637
40	0119+115	01:19:03.13	+11:34:08.5	1.01	...	...	0.33	19.0	0.570
41	0122-003	01:22:55.30	-00:21:33.6	1.23	1728.4	86.5	-0.02	16.7	1.070
45	0130-171	01:30:17.64	-17:10:11.2	1.00	1541.1	77.6	-0.06	18.4	1.022
46	0131-522	01:31:05.60	-52:15:26.4	1.22	796.8	39.9	0.18	20.3	0.020
49	0133+476	01:33:55.11	+47:36:12.8	3.22	...	...	0.62	17.7	0.859
51	0135-247R	01:35:17.12	-24:46:08.9	1.70	872.5	43.6	0.35	17.3	0.831
53	0146+056	01:46:45.63	+05:40:59.3	1.19	...	...	0.81	20.0	2.345
54	0149+218	01:49:31.74	+21:52:20.7	1.03	...	...	-0.20	18.0	1.320
55	0153+744	01:53:04.34	+74:28:05.7	1.52	...	...	-0.31	16.0	2.338
59	0202-172	02:02:34.48	-17:15:39.2	1.38	1076.3	54.0	-0.03	18.5	1.740
60	0202+149	02:02:07.40	+14:59:50.8	2.47	...	...	-0.43	21.3	0.405
61	0202+319	02:02:09.66	+31:58:10.3	1.03	...	...	0.27	18.2	1.466
62	0208-512	02:08:56.96	-51:15:07.8	3.31	2893.2	144.8	-0.12	16.9	1.003
64	0212+735	02:12:49.91	+73:35:40.0	2.20	...	...	-0.12	19.0	2.367
68	0221+067	02:21:50.05	+06:45:49.2	1.03	...	...	0.69	19.0	0.5114
69	0223+341	02:23:09.74	+34:08:01.6	1.29	...	...	-0.46	21.3	2.910
70	0229+131	02:29:02.52	+13:09:40.7	1.00	...	...	-0.33	17.7	2.065
71	0234+285	02:34:55.59	+28:35:11.3	1.44	...	...	-0.24	18.5	1.210
77	0248+430	02:48:18.50	+43:02:57.0	1.20	...	...	0.37	18.6	1.316
80	0256+075	02:56:46.98	+07:35:45.5	1.04	...	...	0.45	18.0	0.893
82	0302-623	03:02:48.12	-62:23:03.7	1.41	1865.9	93.3	0.18	18.0	...
85	0308-611	03:08:51.28	-61:09:58.2	1.36	1211.1	60.6	0.76	18.6	...
89	0319+121	03:19:08.15	+12:10:32.3	1.09	...	...	-0.34	19.0	2.662
92	0332-403	03:32:25.24	-40:18:24.0	2.56	1781.2	89.1	0.43	18.5	1.445

Table 4 (*continued*)

seq.	name	RA (J2000)	Dec (J2000)	S_5	$S_{18.5}$	$\sigma_{18.5}$	$\alpha^5_{2.7}$	mag	z
–	–	–	–	Jy	mJy	mJy	–	–	–
93	0332+078	03:32:12.10	+07:50:16.7	1.14	...	...	0.72	21.5	...
94	0336-019	03:36:58.95	-01:56:17.0	2.86	4061.9	203.3	0.30	18.4	0.852
99	0400+258	04:00:03.59	+25:51:46.6	1.79	...	...	0.11	18.0	2.109
100	0402-362	04:02:02.60	-36:13:11.8	1.38	3175.3	158.8	0.46	17.2	1.417
102	0403-132	04:03:13.98	-13:16:18.2	2.88	2280.7	114.1	-0.05	17.1	0.571
105	0405-385	04:05:12.02	-38:34:26.1	1.09	1638.4	82.0	0.11	18.0	1.285
106	0405-123	04:05:27.45	-12:19:32.4	1.96	1413.2	70.8	-0.30	14.8	0.574
111	0414-189	04:14:23.32	-18:58:29.5	1.35	904.0	45.3	0.22	18.5	1.536
112	0420-014	04:20:43.54	-01:27:28.8	1.46	7930.5	396.8	0.01	17.0	0.915
118	0434-188	04:34:48.94	-18:50:48.0	1.23	423.6	21.3	0.25	19.0	2.702
119	0437-454	04:37:30.67	-45:28:12.3	1.41	1124.3	56.2	0.24	20.5	...
120	0438-436	04:38:43.18	-43:38:53.2	6.94	3896.0	194.8	0.25	18.8	2.852
121	0440-003	04:40:05.29	-00:23:20.5	2.61	1215.1	60.9	-0.29	19.2	0.844
124	0451-282	04:51:15.08	-28:12:28.8	2.26	1747.2	87.4	-0.04	18.5	2.559
128	0454-810	04:54:17.96	-81:05:54.2	1.40	1564.8	78.3	0.29	19.6	0.444
129	0454-463	04:54:24.18	-46:20:38.5	2.32	3584.8	179.3	-0.03	17.4	0.858
130	0454-234	04:54:57.30	-23:29:28.3	2.06	5400.9	270.1	0.16	18.5	1.003
133	0458-020	04:58:41.35	-02:03:34.2	1.74	1570.4	78.6	-0.08	18.4	2.286
134	0500+019	05:00:45.18	+01:58:53.8	1.82	...	...	-0.39	21.2	0.58457
135	0506-612	05:06:08.36	-61:13:33.3	1.73	2455.4	122.8	-0.10	16.9	1.093
137	0511-220	05:11:41.82	-22:02:41.4	1.31	768.3	38.5	0.13	19.5	1.296
139	0514-459	05:14:19.33	-45:59:58.2	1.06	886.7	44.4	-0.32	17.5	0.194
143	0524-460	05:24:05.99	-46:00:28.0	1.02	523.8	26.4	0.14	17.3	1.479
144	0528-250	05:28:05.22	-25:05:44.7	1.16	468.4	23.6	-0.20	17.3	2.765
145	0528+134	05:28:06.76	+13:29:42.3	3.97	...	...	0.47	19.5	2.067
147	0537-286	05:37:56.93	-28:41:28.0	1.02	864.9	43.4	0.52	20.0	3.119
149	0539-057	05:39:10.99	-05:43:15.1	1.55	757.3	38.0	1.41	19.2	0.839
151	0602+673	06:02:38.89	+67:21:18.5	1.06	...	...	0.42	20.6	1.970
153	0605-085	06:05:36.05	-08:34:19.2	3.49	1930.4	96.6	0.09	18.0	0.872
155	0606-223	06:06:53.38	-22:19:46.3	1.40	951.0	47.6	0.55	20.0	1.926
156	0607-157	06:07:26.02	-15:42:02.5	1.82	5991.2	299.7	-0.01	17.0	0.324
158	0615+820	06:15:32.71	+82:03:56.5	1.00	...	...	-0.03	17.5	0.710
163	0637-752	06:37:23.39	-75:13:37.5	5.85	4779.9	239.0	0.19	15.8	0.654
164	0642-349	06:42:37.40	-34:56:32.7	1.02	322.2	16.3	0.13	18.5	2.165
165	0646-306*	06:46:19.17	-30:40:54.3	1.09	...	...	0.23	18.6	0.455
167	0707+476	07:07:02.54	+47:37:07.9	1.01	...	...	-0.13	18.2	1.292
169	0711+356	07:11:05.64	+35:39:51.9	1.52	...	...	-0.29	19.5	1.620
174	0736+017	07:36:42.55	+01:43:59.4	1.99	...	...	-0.13	16.5	0.191
175	0738+313	07:38:00.19	+31:19:02.1	2.49	...	...	0.27	16.1	0.631
178	0743-006	07:43:21.05	-00:36:55.7	1.99	1613.7	80.8	0.57	17.1	0.994
179	0745+241	07:45:35.73	+24:07:55.5	1.01	...	...	0.48	19.0	0.409

Table 4 (*continued*)

seq.	name	RA (J2000)	Dec (J2000)	S_5	$S_{18.5}$	$\sigma_{18.5}$	$\alpha^5_{2.7}$	mag	z
–	–	–	–	Jy	mJy	mJy	–	–	–
180	0748+126	07:48:05.02	+12:38:45.6	2.28	...	...	0.49	17.8	0.889
183	0804+499	08:04:58.39	+49:59:23.1	2.05	...	...	0.47	17.5	1.433
184	0805-077	08:05:50.56	-07:42:22.0	1.04	1660.5	83.1	-0.32	18.4	1.837
187	0812+367	08:12:10.71	+36:44:27.5	1.01	...	...	-0.02	18.0	1.025
194	0833+585	08:33:23.78	+58:35:30.2	1.09	...	...	1.26	18.0	2.101
195	0834-201	08:34:24.60	-20:06:30.4	3.72	4353.3	217.8	0.03	19.4	2.752
197	0836+710	08:36:21.63	+71:04:21.9	2.59	...	...	-0.32	16.5	2.172
199	0839+187	08:39:14.09	+18:46:27.3	1.20	...	...	0.02	16.4	1.272
201	0850+581	08:50:50.15	+58:08:55.7	1.39	...	...	0.75	18.0	1.322
205	0859-140	08:59:54.95	-14:03:38.8	2.30	1189.7	59.5	-0.42	16.6	1.339
206	0859+470	08:59:39.99	+47:02:56.8	1.78	...	...	-0.15	18.7	1.462
207	0906+015	09:06:35.18	+01:33:48.2	1.04	...	...	0.04	17.8	1.018
208	0906+430	09:06:17.29	+43:05:59.0	1.80	...	...	-0.38	18.5	0.668
211	0917+624	09:17:40.30	+62:28:38.5	1.00	...	...	0.08	19.5	1.446
212	0919-260	09:19:16.71	-26:05:54.5	1.32	1441.2	72.1	0.22	18.4	2.300
213	0923+392	09:23:55.32	+39:15:23.7	8.73	...	...	1.03	17.9	0.698
217	0945+408	09:45:50.11	+40:53:43.1	1.39	...	...	0.11	17.5	1.252
221	0953+254	09:53:59.74	+25:29:33.7	1.82	...	...	0.83	17.2	0.712
222	0954+556	09:54:14.36	+55:37:16.4	2.28	...	...	-0.19	17.7	0.901
229	1030+415	10:30:07.80	+41:31:34.5	1.13	...	...	0.42	18.2	1.120
232	1032-199	10:32:37.37	-19:56:02.2	1.15	1261.2	63.1	0.07	17.3	2.198
233	1034-293*	10:34:55.83	-29:18:26.8	1.51	...	...	0.35	16.5	0.312
235	1039+811	10:39:27.82	+81:10:23.5	1.14	...	...	0.38	16.5	1.254
237	1045-188	10:45:40.10	-18:53:44.1	1.14	1626.2	81.3	0.32	18.8	0.595
238	1046-409R	10:46:22.65	-40:58:07.7	1.07	413.4	20.7	-0.41	17.5	0.620
239	1049+215	10:49:07.16	+21:35:49.0	1.26	...	...	0.34	18.5	1.300
240	1055+018	10:55:55.32	+01:50:03.6	3.47	...	...	0.32	18.3	0.892
242	1057-797	10:57:49.73	-79:47:47.8	1.62	2561.3	128.1	0.58	19.3	...
243	1104-445	11:04:50.37	-44:32:52.8	2.07	2277.9	113.9	0.16	18.2	1.598
244	1116-462	11:16:06.19	-46:17:50.0	1.35	959.0	48.0	-0.35	17.0	0.713
245	1116+128	11:16:20.78	+12:51:06.7	1.41	...	...	-0.36	19.3	2.118
247	1127-145	11:27:35.68	-14:32:54.4	6.57	2925.5	146.3	0.03	16.9	1.187
248	1136-135R	11:36:38.51	-13:34:05.4	2.11	434.1	21.8	-0.42	16.2	0.554
252	1143-245	11:43:36.36	-24:30:52.7	1.18	691.5	34.8	-0.18	18.5	1.950
254	1145-071	11:45:18.30	-07:08:00.8	1.25	811.0	40.6	0.22	18.0	1.342
256	1148-001	11:48:10.12	-00:07:13.3	1.90	963.6	48.2	-0.44	17.6	1.982
257	1150+497	11:50:47.98	+49:47:50.1	1.12	...	...	-0.48	17.1	0.334
258	1150+812	11:50:23.49	+81:15:10.2	1.18	...	...	-0.09	18.5	1.250
261	1202-262	12:02:58.82	-26:17:22.6	1.04	513.7	25.8	-0.41	19.5	0.789
264	1213+350	12:13:24.81	+35:04:55.7	1.01	...	...	-0.34	20.1	0.851
266	1216+487	12:16:38.58	+48:46:35.2	1.08	...	...	0.30	18.5	1.076

Table 4 (*continued*)

seq.	name	RA (J2000)	Dec (J2000)	S_5	$S_{18.5}$	$\sigma_{18.5}$	$\alpha^5_{2.7}$	mag	z
–	–	–	–	Jy	mJy	mJy	–	–	–
269	1226+023	12:26:33.24	+02:19:43.4	42.85	...	...	0.15	12.8	0.158
272	1237-101	12:37:07.28	-10:07:00.7	1.31	1035.0	52.1	-0.25	18.1	0.753
274	1243-072	12:43:28.79	-07:14:23.5	1.03	699.6	35.0	0.44	18.0	1.286
275	1244-255	12:44:06.72	-25:31:26.9	1.36	1848.0	92.5	0.30	17.4	0.633
281	1252+119	12:52:07.71	+11:57:20.7	1.09	...	...	-0.02	16.6	0.871
282	1253-055	12:53:35.84	-05:31:07.8	14.95	27945.9	1397.4	0.30	17.8	0.536
284	1255-316	12:55:15.18	-31:39:05.1	1.73	1996.2	99.9	0.24	18.7	1.924
285	1302-102	13:02:55.85	-10:17:16.5	1.17	820.0	41.1	0.17	15.2	0.286
289	1313-333	13:13:20.05	-33:23:09.7	1.36	1457.3	72.9	0.50	20.0	1.210
298	1334-127	13:34:59.81	-12:42:09.6	2.24	7036.3	351.9	0.17	17.2	0.539
302	1352-104	13:52:06.89	-10:26:21.9	1.01	1622.7	81.2	0.40	18.4	0.332
303	1354-152	13:54:28.56	-15:12:51.4	1.52	998.0	49.9	-0.10	18.5	1.890
304	1354+195	13:54:42.10	+19:33:44.1	1.56	...	...	-0.07	16.0	0.720
308	1406-076	14:06:17.85	-07:38:15.2	1.08	1771.3	88.7	0.19	18.4	1.494
315	1424-418	14:24:46.68	-41:52:54.5	3.13	2913.1	145.7	0.28	17.7	1.522
317	1435+638	14:35:37.23	+63:49:35.8	1.24	...	...	-0.20	16.1	2.068
319	1451-375	14:51:18.28	-37:35:22.3	1.89	2022.1	101.1	0.37	16.7	0.314
322	1502+106	15:02:00.17	+10:41:17.8	2.56	...	...	0.57	18.6	0.563
324	1504-166	15:04:16.38	-16:40:59.0	1.98	1447.0	73.1	-0.16	18.5	0.876
326	1508-055	15:08:14.99	-05:31:49.5	2.43	1282.3	64.4	-0.30	17.2	1.191
328	1510-089	15:10:08.90	-08:54:47.5	3.08	2490.3	124.7	0.31	16.5	0.361
336	1532+016	15:32:20.25	+01:41:00.5	1.14	...	...	0.06	18.0	1.435
339	1546+027	15:46:58.29	+02:46:06.1	1.45	...	...	0.46	17.8	0.412
341	1548+056	15:48:06.94	+05:36:11.3	2.24	...	...	0.09	17.7	1.422
343	1550-269R	15:50:59.81	-26:55:51.1	1.17	583.5	30.4	-0.23	21.5	2.145
344	1555+001	15:55:17.69	+00:06:43.5	2.24	879.5	44.2	0.34	19.3	1.770
349	1606+106	16:06:23.40	+10:36:59.9	1.49	...	...	0.42	18.5	1.226
352	1610-771	16:10:51.48	-77:09:52.4	3.91	2653.7	132.7	0.06	19.0	1.710
353	1611+343	16:11:47.92	+34:20:19.9	2.67	...	...	0.10	17.5	1.401
354	1619-680	16:19:13.52	-68:02:16.1	1.86	717.7	35.9	0.07	18.0	1.354
355	1622-297*	16:22:57.24	-29:44:41.3	1.92	...	...	0.19	20.5	0.815
356	1622-253	16:22:44.11	-25:20:51.6	2.08	2200.2	111.7	-0.14	20.3	0.786
357	1624+416	16:24:18.27	+41:41:23.5	1.32	...	...	-0.26	22.5	2.550
358	1633+382	16:33:30.64	+38:14:10.1	4.02	...	...	0.73	18.0	1.814
361	1637+574	16:37:17.45	+57:26:15.8	1.42	...	...	0.35	17.0	0.750
364	1638+398	16:38:48.17	+39:52:30.1	1.15	...	...	0.17	16.5	1.666
366	1641+399	16:41:17.62	+39:54:10.9	10.81	...	...	0.54	16.0	0.594
367	1642+690	16:42:18.10	+69:02:13.3	1.39	...	...	-0.10	19.2	0.751
368	1648+015	16:48:31.56	+01:34:26.0	1.03	...	...	0.33	21.2	...
372	1655+077	16:55:43.95	+07:45:59.5	1.65	...	...	0.43	20.0	0.621
373	1656+053	16:56:05.62	+05:19:47.0	2.16	...	...	0.44	16.5	0.879

Table 4 (*continued*)

seq.	name	RA (J2000)	Dec (J2000)	S_5	$S_{18.5}$	$\sigma_{18.5}$	$\alpha^5_{2.7}$	mag	z
–	–	–	–	Jy	mJy	mJy	–	–	–
379	1725+044	17:25:56.33	+04:29:27.9	1.24	...	...	0.76	17.0	0.293
381	1732+389	17:32:40.49	+38:59:46.9	1.13	...	...	0.85	19.0	0.976
384	1739+522	17:39:29.02	+52:13:10.4	1.98	...	...	0.68	18.5	1.379
386	1741-038	17:41:20.63	-03:48:48.9	3.68	4873.2	244.7	0.75	18.6	1.057
389	1751+441	17:51:53.69	+44:10:17.7	1.02	...	...	0.90	19.5	0.871
390	1800+440	18:00:03.22	+44:04:18.5	1.00	...	...	0.57	16.8	0.663
394	1815-553	18:15:35.15	-55:22:37.9	1.35	1087.7	54.4	-0.02	18.9	...
399	1830+285	18:30:52.38	+28:31:17.0	1.06	...	...	-0.30	17.2	0.594
400	1831-711	18:31:41.24	-71:11:14.2	1.19	2222.4	111.1	-0.17	17.3	1.356
405	1903-802	19:03:55.98	-80:15:00.3	1.84	614.6	30.8	0.29	19.0	0.500
406	1928+738	19:28:49.38	+73:51:44.9	3.34	...	...	-0.01	15.5	0.302
409	1933-400	19:33:51.11	-40:04:46.8	1.48	1164.8	58.3	0.26	18.0	0.966
411	1936-623	19:36:52.63	-62:18:20.8	1.10	534.5	26.8	-0.16	21.5	...
412	1936-155	19:36:36.12	-15:32:40.9	1.69	968.1	49.1	0.26	19.4	1.657
417	1954-388	19:54:39.01	-38:53:13.3	2.06	3800.1	190.0	0.43	17.1	0.626
418	1954+513	19:54:22.49	+51:23:46.3	1.43	...	...	-0.01	18.5	1.230
419	1958-179	19:58:04.61	-17:57:17.1	1.20	1364.2	68.5	0.13	17.5	0.650
420	2000-330	20:00:13.01	-33:00:13.0	1.15	515.6	25.9	0.78	19.0	3.777
423	2008-159	20:08:25.92	-15:55:38.3	1.39	2268.6	113.7	1.02	17.2	1.180
429	2037-253R	20:37:10.75	-25:18:26.4	1.20	446.9	23.9	0.42	18.8	1.574
431	2052-474	20:52:50.10	-47:26:19.5	2.52	741.3	37.1	-0.11	17.8	1.491
436	2106-413	21:06:19.40	-41:22:33.6	2.35	1890.5	94.6	0.17	21.0	1.0547
437	2113+293	21:13:20.58	+29:21:06.6	1.47	...	...	0.62	19.5	1.514
439	2126-158	21:26:26.76	-15:51:50.3	1.28	931.2	47.9	0.14	17.3	3.266
440	2128-123	21:28:52.68	-12:20:20.6	2.07	3610.5	181.3	0.11	16.1	0.501
443	2134+004	21:34:05.21	+00:28:25.0	12.30	...	...	0.83	16.8	1.936
446	2136+141	21:36:37.41	+14:10:00.5	1.11	...	...	-0.10	18.5	2.427
448	2142-758	21:42:12.79	-75:50:06.1	1.32	684.8	34.3	-0.07	17.3	1.139
449	2144+092	21:44:42.48	+09:15:51.4	1.01	...	...	0.23	18.5	1.113
450	2145+067	21:45:36.09	+06:43:40.8	4.00	...	...	0.25	16.5	0.990
451	2149-306*	21:49:00.62	-30:42:00.8	1.19	...	...	-0.17	18.4	2.340
458	2155-152	21:55:23.25	-15:15:30.2	1.77	2471.7	124.8	0.15	19.4	0.672
460	2201+315	22:01:01.45	+31:31:05.8	2.32	...	...	0.24	15.6	0.298
461	2203-188	22:03:25.72	-18:50:17.0	4.38	2196.7	110.5	-0.28	18.5	0.619
462	2204-540	22:04:26.26	-54:01:15.0	2.41	1276.8	63.9	0.16	18.0	1.206
465	2210-257	22:10:14.14	-25:44:22.5	1.05	604.4	33.9	0.15	19.0	1.833
468	2216-038	22:16:16.39	-03:50:40.8	1.50	2539.9	127.7	0.48	16.4	0.901
470	2223-052	22:23:11.05	-05:12:17.4	4.51	8129.1	406.6	-0.11	18.4	1.404
473	2227-399R	22:27:45.01	-39:58:16.7	1.05	753.5	37.8	0.05	17.9	0.323
474	2227-088	22:27:02.26	-08:48:16.5	1.77	1618.0	81.3	-0.03	17.5	1.561
477	2234+282	22:34:01.74	+28:13:23.1	1.06	...	...	0.08	19.0	0.795

Table 4 (*continued*)

seq.	name	RA (J2000)	Dec (J2000)	S_5	$S_{18.5}$	$\sigma_{18.5}$	$\alpha^5_{2.7}$	mag	z
–	–	–	–	Jy	mJy	mJy	–	–	–
479	2243-123	22:43:39.80	-12:22:40.2	2.45	2183.1	109.6	-0.18	16.5	0.630
481	2245-328R	22:45:51.44	-32:51:42.5	1.85	164.4	8.3	-0.13	18.6	2.255
483	2247+140	22:47:56.71	+14:03:57.4	1.02	...	...	-0.63	16.9	0.237
485	2251+158	22:51:29.53	+15:52:54.3	17.42	...	...	0.64	16.1	0.859
488	2255-282	22:55:22.46	-28:14:25.7	1.78	...	...	0.41	16.8	0.926
490	2311-452	23:11:21.90	-45:12:10.8	1.47	577.8	29.0	-0.38	19.0	2.884
493	2318+049	23:18:12.15	+04:57:22.9	1.13	...	...	-0.11	19.0	0.623
494	2319+272	23:19:32.00	+27:16:18.9	1.07	...	...	0.20	19.0	1.253
499	2326-477	23:26:33.71	-47:46:51.8	2.33	1531.0	76.6	-0.06	16.8	1.306
500	2328+107	23:28:08.81	+10:43:45.2	1.01	...	...	-0.05	18.1	1.489
501	2329-162	23:29:02.40	-16:13:30.9	1.06	1996.1	100.1	-0.06	19.9	1.155
508	2344+092	23:44:03.77	+09:14:05.5	1.43	...	...	-0.09	16.0	0.673
509	2345-167	23:45:27.69	-16:47:52.7	3.66	2412.0	120.7	0.51	18.4	0.576
510	2351+456	23:51:49.98	+45:36:22.8	1.42	...	...	-0.05	20.6	1.992
512	2353-686	23:53:22.99	-68:36:45.8	1.10	784.7	39.3	0.26	17.0	1.716
513	2354-117	23:54:57.20	-11:42:21.1	1.48	1197.0	60.3	-0.24	18.5	0.960
514	2355-534	23:55:18.17	-53:27:56.1	1.52	1523.2	76.2	0.36	17.8	1.006

Chapter 6

Conclusions

In this Thesis we analyzed high-frequency properties of extragalactic radio sources, such as: cosmic evolution, radio spectral index, differential counts, polarization and optical morphological type. The study of these properties is important on its own, because in high-frequency selected radio surveys new and rare classes of radio sources, which can shed light on the physics of AGN in their early and late stages, emerge.

Moreover, the study of high-frequency source properties is also strongly linked to the characterization of extragalactic discrete source foreground contamination to the Cosmic Microwave Background, which dominates on the sub-degree angular scales (corresponding to the higher multipole moments l), where the extragalactic source contamination is stronger than for other foregrounds.

We now briefly review the results obtained in this Thesis.

In Chapter 2, we described the development of a new model for the time-dependent luminosity function of flat-spectrum (FSRQs and BL Lacs) and steep-spectrum (FRI and FRII) classical radio sources, taking into account the results of the recent high-frequency radio surveys: 9C survey (Waldram et al. 2003) at 15 GHz, ATCA pilot survey (Ricci et al. 2004b) at 18 GHz and WMAP spanning the frequency range $22.8 - 90$ GHz (Bennett et al. 2003b). We then used this new model, provisionally dubbed GDZ04, to predict the differential counts at two high radio frequencies (20 and 30 GHz) important for CMB studies. This work was complemented with the estimates of the differential counts of special source classes. Namely, we focused on star-forming galaxies (proto-spheroids, starburst galaxies and spirals), Sunyaev-Zel'dovich signals (SZ clusters and galaxy-scale SZ effects caused by quasar feedback and virialized gas), advection-dominated systems (ADAFs and ADIOS), extreme GPS sources (quasars and radio galaxies), and GRB radio

afterglows. The synoptic view of their separate and total predicted counts, shown in Fig. 2.17 and 2.18 of Chapter 2, in the flux density range 10 μJy $\leq$ S $\leq$ 10 Jy allowed us to say that: (i) the dominant population at bright flux densities are blazars (i.e. FSRQs and BL Lacs); (ii) below $\sim$ 100 mJy FSRQs become sub-dominant at fainter flux densities; (iii) the $20 - 30$ GHz counts are expected to flatten in the $1 - 10$ mJy range, as FRII sources largely disappear; (iv) a large fraction of sub-mJy radio sources are moderate redshift star-forming galaxies; (v) this population is overcome by proto-spheroidal galaxies below $\sim$ 100 μJy; (vi) ADAFs, extreme GPS sources and GRB afterglows are sub-dominant in every flux density regime by two order of magnitude or more; (vii) the SZ signals on galactic scales can be a major contributor to the counts, together with proto-spheroids, at the faintest flux densities explored. The wide range spanned in flux density is justified by the fact that the faintest flux densities will be observed by next-generation millimetre arrays such as ALMA, whereas the brightest end is well constrained by the WMAP discrete source catalog.

In the pilot study, described in Chapter 3, for the first all–sky radio survey at short wavelengths, we have observed 1216 deg^2 of the southern sky at 18 GHz (16 mm) using a novel wide–band (3.4 GHz bandwidth) analogue correlator on one baseline of the Australia Telescope Compact Array (ATCA). We scanned a region of sky between declination -71° and -59° with an rms noise level of 15 mJy. Follow–up radio imaging of candidate sources above a 4σ detection limit of 60 mJy resulted in 221 confirmed detections, for which we measured accurate positions and flux densities. For extragalactic sources, the survey was roughly 70% complete at a flux density of 126 mJy and 95% complete above 300 mJy. Almost half the detected sources lie within a few degrees of the Galactic plane, but there are 123 sources with $|b| > 5^\circ$ which we assumed to be extragalactic. We performed the differential counts for extragalactic sources in the range 0.1 Jy $\leq S_{18\mathrm{GHz}} \leq$ 3 Jy, which were well fitted by a power-law relation of the form $n(S) = 57\,(S/\mathrm{Jy})^{-2.2\pm0.2}\,\mathrm{Jy}^{-1}\,\mathrm{sr}^{-1}$, in good agreement with the 15 GHz counts published by Taylor et al. (2001) and Waldram et al. (2003). Over 70% of the extragalactic sources have a flat radio spectrum ($\alpha^{18}_{0.843} > -0.5$, $S_\nu \propto \nu^\alpha$), and 29% have inverted radio spectra ($\alpha^{18}_{0.843} > 0$), thus confirming that a high-frequency selected blind radio survey is very efficient in isolating flat- and rising-spectrum sources. 51% of the extragalactic sources are identified with stellar objects (candidate QSOs), 22% with galaxies and only 27% with faint optical objects or blank fields. The

reliability of the optical IDs was checked against chance superposition of a radio source and a foreground star or galaxy. We estimated that the fraction of spurious IDs is $\sim 17\%$. The chance coincidence corrected optical ID rate (73%) resulted to be much higher than what found for weak low-frequency samples by Windhorst et al. (1984) and McMahon et al. (2002), but comparable to the one found by Snellen et al. (2002) for a sample of flat-spectrum sources selected at 6 cm and limiting flux density (200 mJy) similar to ours. This indicates that in high-frequency blind radio surveys we tend to select more nearby objects having brighter magnitudes and easier to identify. A spectroscopic follow-up of the 18 GHz pilot survey extragalactic source sample is ongoing at the Siding Spring Observatory (NSW, Australia).

In order to study the polarization properties of high-frequency radio sources, in Chapter 4 we described the observations of 250 of the 258 southern sources in the complete 5-GHz 1-Jy sample by Kühr et al. (1981) using the Australia Telescope Compact Array (ATCA) at 18.5 GHz. In the analysis we subdivided the sample into flat and steep spectrum sources using the classification of Stickel et al. (1994), where spectral indices were measured between 2.7 and 5 GHz. The polarized flux was measured with a $S/N > 5$ for 170 sources (114 flat-spectrum and 56 steep-spectrum). We were able to set upper limits for additional 27 sources (12 flat-spectrum and 15 steep-spectrum). The median fractional polarization at 18.5 GHz for the flat-spectrum sub-sample was $\Pi_{18.5} \simeq 2.7\%$, which is about a factor of 2 higher than at 1.4 GHz ($\Pi_{1.4} \simeq 1.4\%$, based on NVSS data). For flat-spectrum sources we found a weak correlation between $\Pi_{18.5}$ and the high-frequency ($5 - 18.5$ GHz) spectral index. We found no evidence of significant correlations of the fractional polarization with other source properties. The median value of $\Pi_{18.5}$ for the steep spectrum sources was $\simeq 4.8\%$, but our sample might be biased against extended sources. We found some correlation between $\Pi_{18.5}$ and both the low-frequency (1.4–5 GHz) and the high-frequency ($5 - 18.5$ GHz) spectral indices. An important application of this work is the estimation of the contamination of CMB polarization maps by extragalactic radio sources. Our results indicate that such contamination is within the range explored by Mesa et al. (2002).

As a by-product of the ATCA observing campaign of the high-frequency polarization properties of Kühr sample southern sources, in Chapter 5 we focused on the 18.5 GHz total intensity measurements to study the evolution properties of the flat-spectrum radio

quasars. We worked out, using the $1/V_{max}$ method, the 5 GHz luminosity function of Kühr FSRQs and obtained, through a transformation matrix bivariate approach, the 18.5 GHz luminosity function in the redshift bin $0.8 < z \leq 1.2$. We note that this is the first determination of a radio luminosity function for this class of objects at high radio frequencies. As the direct transformation matrix bivariate approach underestimates the source density in the fainter high-frequency luminosity bins resulting in a flattening of the luminosity function, we utilized the 5 GHz model luminosity function of FSRQs described in Chapter 2 to correct it for incompleteness, as a reasonable agreement was found between the model and experimental LFs in the redshift bin used to compute the high-frequency bivariate LF. We also studied the FSRQ space density and compared it with the one obtained by integrating the 5 GHz De Zotti et al. (2004b) model LF. A clear indication of evolution as a function of redshift was present. On the contrary, the positive trend in the peak redshift of the 5 GHz luminosity binned space density at increasing 5 GHz luminosity, reported by Hook et al. (1998) from the analysis of the Parkes quarter-Jy FSRQ sample, was not found in our analysis of the Kühr FSRQs. We suspect that the small number statistics in the our luminosity binned space density determination worked against the detection of this feature, together with the much higher limiting flux density ($S_{lim} = 1$ Jy) of the Kühr sample with respect to the one of the Parkes quarter-Jy sample.

As a final remark, the work done in this Thesis constitutes only the first step towards a thorough characterization of high-frequency source properties which include long-scale (about one year) and short scale (less than one day) variability, a radio luminosity function obtained from a high-frequency selected source sample, Rotation Measure and intrinsic magnetic field orientation study. These achievements are one of the main goals of the ongoing ATCA 20 GHz (AT20G) sky survey, whose plan is to cover all the southern sky (2×10^4 deg^2) down to a limiting flux density of 40 mJy. The survey, taking advantage of an improved and more powerful version of the wide-band correlator, whose operation is described in Chapter 3, (three baselines and 8-GHz bandwidth) associated to a faster antenna elevation slewing speed (15° min^{-1} instead of 10° min^{-1}), aims at detecting about a radio source per square degree down to the aforesaid limiting flux density. In October 2003 the first observing run of the AT20G survey, having an effective frequency of 22 GHz, covered 1800 deg^2 in the same sky strip ($-70° < \delta < -60°$) of the pilot study, making it the largest radio survey performed at such a high frequency and low limiting flux density.

In the multi-frequency ($5 - 22$ GHz) almost simultaneous (November 2003) follow-up at the ATCA in a 5-antenna T-shaped array configuration, we were able to confirm ~ 350 S/N > 5 detections including ~ 180 extragalactic sources above a limiting flux density of 60 mJy. Simultaneous radio spectra in the frequency range spanned by the follow-up will be very useful, during the data analysis, to single out candidate High Frequency Peakers in the extragalactic sample. Polarization measurements at 5, 8.4, 17, 19, 21 and 23 GHz will allow us to study the Faraday Rotation Measure, depolarization and intrinsic magnetic field orientation of a complete sample of radio sources selected at high frequency. We aim at completing the southern survey before the launch of the Planck satellite in 2007, so that we can provide the Planck science team with a complete and large enough extragalactic radio source catalog to be used as a template for source detection/removal from CMB all-sky maps produced by the Planck Low Frequency Instrument.

Bibliography

[1] Aghanim, N., Balland, C. & Silk, J., 2000, A&A, 357, 1

[2] Aizu, K., Inuoe, M., Tabara, H., Kato, T., 1990, IAU Symp. 140: *Galactic and Intergalactic Magnetic Fields*, p. 472

[3] Allen, S.W., Schmidt, R.W., & Fabian, A.C. 2002, MNRAS, 334, L11

[4] Aller, M.F., Aller, H.D., Hughes, P.A., 1992, ApJ, 399, 16

[5] Aller, M.F., Aller, H.D., Hughes, P.A., & Latimer, G.E. 1999, ApJ, 512, 601

[6] Auriemma, C., Perola, G.C., Ekers, R.D., Fanti, R., Lari, C., Jaffe, W.J., Ulrich, M.H., 1977, A&A, 57, 41

[7] Avni, Y., & Bahcall, J.N., 1980, ApJ, 235, 694

[8] Baganoff, F.K., Maeda, Y., Morris, M., Bautz, M.W., Brandt, W.N., et al., 2003, 591, 891

[9] Barbosa, D., Bartlett, J.G., Blanchard, A., & Oukbir, J. 1996, A&A, 314, 13

[10] Bartlett, J.G., & Amram, P., 1998, in *Fundamental Parameters in Cosmology*, proc. Rencontres de Moriond, astro-ph/9804330

[11] Begelman, M.C., 1996, in *Cygnus A: Study of a Radio galaxy*, eds., C. Carilli & D. Harris, Cambridge University Press, p. 209

[12] Bennett, C.L., Bay, M., Halpern, M., Hinshaw, G., Jackson, C., et al., 2003a, ApJ, 583, 1

[13] Bennett, C.L., Hill, R.S., Hinshaw, G., Nolta, M.R., Odegard, N., et al., 2003b, ApJS, 148, 97

[14] Benoît, et al., 2003, (astro-ph/0306222)

[15] Bernard, J.-Ph., Meny, C., Dupac, X., et al. 2003, paper presented at the Planck WG7 meeting, Jodrell Bank

[16] Bicknell, G.V., Dopita, M.A., O'Dea, C.P.O., 1997, ApJ, 485, 112

[17] Birkinshaw, M., 1999, *Physics Report*, 310, 97

[18] Blain, A.W., Kneib, J.-P., Ivison, R.J., & Smail, I., 1999, ApJ, 512, L87

[19] Blandford, R.D., & Begelman, M.C., 1999, MNRAS, 303, L1

[20] Bond, J.R., Contaldi, C. & Pogosyan, D., 2003, Royal Society of London Transactions Series A, vol. 361, p. 2435

[21] Bond, J.R., Contaldi, C.R., Pen, U.L., et al. 2002, ApJ, submitted (astro-ph/0205386)

[22] Bondi, H., 1952, MNRAS, 112, 195

[23] Brandie, G.W., Bridle, A.H., 1974, AJ, 79, 903

[24] Brandie, G.W., Bridle, A.H., Kesteven, M.J.L., 1974, Nature, 252, 212

[25] Brinkmann, W., Siebert, J., & Boller, Th., 1994, A&A, 281, 355

[26] Bryan, G.L., & Norman, M.L., 1998, ApJ, 495, 80

[27] Carroll, S.M., Press, W.H., & Turner, E.L., 1992, Annu. Rev. Astron. Astrophys., 30, 499

[28] Chapman, S.C., Scott, D., Borys. C., & Fahlman, G.G., 2002, MNRAS, 330, 92

[29] Chapman, S.C., Barger, A.J., Cowie, L.L., et al. 2003, ApJ, 585, 57

[30] Christiansen, W.N., & Warburton, J.A., 1955, Obs., 75, 9

[31] Ciardi, B., & Loeb, A. 2000, ApJ, 540, 687

[32] Colafrancesco, S., Mazzotta, P., Rephaeli, Y., & Vittorio, N. 1997, ApJ, 479, 1

[33] Coles, S., Lacey, C.G., Baugh, C.M., Carlton, M., Frenk, C.S., 2000, MNRAS, 319, 168

[34] Condon, J.J. 1992, ARA&A, 30, 575

[35] Condon, J.J., Cotton, W.D., Greisen, E.W., Yin, Q.F., Perley, R.A., Taylor, G.B., & Broderick, J.J. 1998, AJ, 115, 1693

[36] Crawford, T., Marr, J., Partridge, R.B., Strauss, M.A., 1996, ApJ, 460, 225

[37] Dallacasa, D., Stanghellini, C., Centonza, M., & Fanti, R. 2000, A&A, 363, 887

[38] Dawson, K.S., Holzapfel, W.L., Carlstrom, J.E., Joy, M., LaRoque, S.J. et al., 2002, ApJ, 581, 86

[39] de Bernardis, P., Ade P.A.R., Bock, J.J., Bond, J.R., Borrill, J., et al., 2000, Nature, 404, 955

[40] Dennison, B., Simonetti, J.H., & Topasna, G.A., 1998, PASA, 15, 147

[41] Devriendt, J.E.G, & Guiderdoni, B., 2000, A&A, 363, 851

[42] De Zotti, G., Franceschini, A., Toffolatti, L., Mazzei, P., Danese, L., 1996, ApL&C, 35, 289

[43] De Zotti, G., Toffolatti, L., Argüeso Gómez, F., Davies, R.D., Mazzotta, P., Partridge, R.B., Smoot, G.F., Vittorio, N., 1999a, in proc. "3K Cosmology", L. Maiani, F. Melchiorri, & N. Vittorio eds., AIP Conf. Proc., 476, 204

[44] De Zotti, G., Gruppioni, C., Ciliegi, P., Burigana, C., Danese, L., 1999b, NewA, 4, 481

[45] De Zotti, G., Granato, G.L., Silva, L., Maino, D., Danese, L., 2000, A&A, 354, 467

[46] De Zotti, G., Burigana, C., Cavaliere, A., Danese, L., Granato, G.L., Lapi, A., Platania, P., Silva, L. 2004a, in proc. int. symp. "Plasmas in the Laboratory and in the Universe: new insights and new challenges", eds. G. Bertin, D. Farina & R. Pozzoli, AIP conf. proc., 703, 375

[47] De Zotti, G., Ricci, R., Mesa, D., Silva, L., Mazzotta, P., 2004b, in preparation

[48] Dickinson, C., Davies, R.D., &, Davis, R.J., 2003, MNRAS, 341, 369

[49] Di Matteo, T., Fabian, A.C., Rees, M.J., Carilli, C.L., Ivison, R.J., 1999, MNRAS, 305, 492

[50] Di Matteo, T., Quataert, E., Allen, S.W., Narayan, R., Fabian, A.C., 2000, MNRAS, 311, 507

[51] Di Matteo, T., Carilli, C.L., Fabian, A.C., 2001, ApJ, 547, 731

[52] Doroshkevich, A.G., Zel'dovich, Y.B., Sunyaev, R.A., 1978, *Soviet Astronomy*, 22, 523

[53] Draine, B.T., & Lazarian, A., 1998, ApJ, 494, L19

[54] Draine, B.T., & Lazarian, A., 1999, ApJ, 512, 740

[55] Dunlop, J.S. & Peacock, J.A. 1990, MNRAS, 247, 19

[56] Dupac, X., Giard, M., Bernard, J.-P., Lamarre, J.-M., Mény, C., et al., 2001, ApJ, 553, 604

[57] Dupac, X., Giard, M., Bernard, J.-P., Boudet, N., Lamarre, J.-M., et al., 2002, A&A, 392, 691

[58] Dupac, X., Bernard, J.-P., Boudet, N., et al. 2003, A&A, 404, L11

[59] Edge, A.C., & Stewart, G.C., 1991, MNRAS, 252, 414

[60] Edge, A., et al., 1996, in proc. *2nd workshop on GPS & CSS Radio Sources*, eds., I. Snellen, R.T. Schilizzi, H.J.A. Röttgering, M.N. Bremer, p. 43

[61] Edge, A.C., Pooley, G.G., Jones, M., Grainge, K., Saunders, R., 1998, in proc. IAU Coll. 164: *Radio Emission from Galactic and Extragalactic Compact Sources*, eds., J.A. Zensus, G.B. Taylor, & J.M. Wrobel, ASP Conf. Ser., 144, 187

[62] Efstathiou, G., Ellis, R.S., & Peterson, B.A., 1988, MNRAS, 232, 431

[63] Eke, V.R., Navarro, J.F., Frenk, C.S. 1998, ApJ, 503, 569

[64] Ettori, S., Tozzi, P., Borgani, S., & Rosati, P. 2004, A&A, 417, 13

[65] Fabbiano, G. 1989, ARAA, 27, 87

[66] Fabbiano, G. & Juda, J. 1997, ApJ, 476, 666

[67] Fabbiano, G., Elvis, M., Markoff, S., Siemiginowska, A., Pellegrini, S., Zezas, A., Nicastro, F., Trinchieri, G. & McDowell, J. 2003, ApJ, 588, 175

[68] Fabian, A.C., & Rees, M.J., 1995, MNRAS, 277, L55

[69] Fanti, R., Fanti, C., Schilizzi, R.T., Spencer, R.E., Nan Rendong, Parma, P., van Breugel, W.J.M., Venturi, T., 1990, A&A, 231, 333

[70] Fanti, C., Fanti, R., Dallacasa, D., et al., 1995, A&A, 302, 317

[71] Fanaroff, B.L. & Riley, J.M. 1974, MNRAS, 167, 31P

[72] Feigelson, E.D., & Nelson, P.I., 1985, ApJ, 293, 192

[73] Ferrarese, L. & Merritt, D. 2000, ApJ 539, L9

[74] Finkbeiner, D.P., Davis, M., & Schlegel, D.J., 1999, ApJ, 524, 867

[75] Finkbeiner, D.P., 2003a, ApJS, 146, 407

[76] Finkbeiner, D.P., 2003b, (astro-ph/0311547)

[77] Fixen, D.J., Cheng, E.S., Gales, J.M., Mather, J.C., Shafer, R.A., et al., 1996, ApJ, 473, 576

[78] Fomalont, E.B., Kellermann, K.I., Partridge, R.B., Windhorst, R.A., & Richards, E.A. 2002, AJ, 123, 2402

[79] Fossati, G., Maraschi, L., Celotti, A., Comastri, A., Ghisellini, G., 1998, MNRAS, 299, 433

[80] Franceschini, A., Vercellone, S., Fabian, A.C., 1998, MNRAS, 297, 817

[81] Garrett, M.A. 2002, A&A, 384, L19

[82] Gaustad, J., McCullough, P.R., & van Buren, D., 1996, PASP, 108, 351

[83] Gaustad, J., McCullough, P.R., Rosing, W., Buren, D.V., 2001, PASP, 113, 1326

[84] Gautier, T.N., Boulanger, F., Perault, M., & Puget, J.-L., 1992, AJ, 103, 1313

[85] Gavazzi, G., Cocito, A., & Vettolani, G. 1986, ApJ, 305, L15

[86] Ge, J., & Owen, F.N., 1994, AJ, 108, 1523

[87] Gebhardt, K., Bender, R., Bower, G., Dressler, A., Faber, S.M., 2000, ApJ Letters, 539, L13

[88] Gehrels, N. 1986, ApJ, 303, 336

[89] Ghisellini, G., Celotti, A., Fossati, G., Maraschi, L., Comastri, A., 1998, MNRAS, 301, 451

[90] Ginzburg, V.L., & Syrovatskii, S.I., 1964, *Origin of Cosmic Rays*, New York, Pergamon Press

[91] Goldstein, J.H., Ade, P.A.R., Bock, J.J., et al., 2003, ApJ, 599, 773

[92] Gnedin, N.Y., & Jaffe, A.H. 2001, ApJ, 551, 3

[93] Graham, A. W., Erwin, P., Caon, N., & Trujillo, I. 2001, ApJ, 563, L11

[94] Grainge, K. & Edge, A., 1998, in "Fundamental Parameters in Cosmology", eds., J. Trân Thanh Vân, et al., ed. Frontiéres, p. 151

[95] Grainge, K., Carreira, P., Cleary, K., et al. 2003, MNRAS, 341, L23

[96] Granato, G.L., Silva, L., Monaco, P., Panuzzo, P., Salucci, P., De Zotti, G., Danese, L., 2001, MNRAS, 324, 757

[97] Granato, G.L., De Zotti, G., Silva, L., Bressan, A., & Danese, L. 2004, ApJ, 600, 580

[98] Green, D.A., & Scheuer, P.A.G., 1992, MNRAS, 258, 833

[99] Gregory, P.C., & Condon, J.J. 1991, ApJS, 75, 1011

[100] Gregory, P.C., Vavasour, J.D., Scott, W.K., Condon, J.J., 1994, ApJS, 90, 173

[101] Gregory, P.C., Scott, W.K., Douglas, K., & Condon, J.J. 1996, ApJS, 103, 427

[102] Gruppioni, C., Oliver, S., & Serjeant, S. 2001, Ap&SS, 276, 791

[103] Guerra, E.J., Myers, S.T., Partridge, R.B., Cabanela, J.E., 2002, BAAS, 33, 1496

[104] Haffner, L.M., Reynolds, R.J., Tufte, S.L., Madsen, G.J., Jaening, K., Percival, J.W. 2003, ApJS, 149, 405

[105] Hambly, N.C. et al., 2001, MNRAS, 326, 1279

[106] Haslam, C.G.T., Klein, U., Salter, C.J., Stoffel, H., Wilson, W.E., et al., 1981, A&A, 100, 209

[107] Helou, G., Soifer, B.T., & Rowan-Robinson, M. 1985, ApJ, 298, L7

[108] Ho, L. C., Feigelson, E. D., Townsley, L. K., Sambruna, R. M., Garmire, Go. P., Brandt, W. N., Filippenko, A. V., Griffiths, R. E., Ptak, A. F., & Sargent, W. L. W. 2001, ApJ 549, L51

[109] Hobson, M.P., Barreiro, R.B., Toffolatti, L., Lasenby, A.N., Sanz, J.L., et al., 1999, MNRAS, 306, 232

[110] Holder, G.P. 2002, ApJ, 580, 36

[111] Hook, I.M., Shaver, P.A., & McMahon, R.G., 1998, in *The Young Universe*, ASP Conf. series, S. D'Odorico, A. Fontana, E. Giallongo, eds., Vol. 146, p. 17

[112] Hu, W., & White, M., 1997, *New Astronomy*, 2, 323

[113] Hu, W., & Dodelson, 2002, ARA&A, 40, 171

[114] Hu, W., Hedman, M.M., & Zaldarriaga, M., 2003, Phs Rev D, 67, d3004

[115] Ikebe, Y., Reiprich, T.H., Böhringer, H., Tanaka, Y., & Kitayama, T. 2002, A&A, 383, 773

[116] Ikeuchi, S., 1981, PASJ, 33, 211

[117] Inoue, M., Tabara, H., Kato, T., Aizu, K., 1995, PASJ, 47, 725

[118] Isobe, T., & Feigelson, E.D., 1990, Bull. Amer. Astro. Society, 22, 917

[119] Isobe, T., Feigelson, E.D., & Nelson, P.I., 1986, ApJ, 306, 490

[120] Jackson, C.A. & Wall, J.V. 2001, in "Particles and Fields in Radio Galaxies", ASP Conf. Proc. 250, R.A. Laing and K.M. Blundell eds., p. 400

[121] Jackson, C.A., Wall, J.V., Shaver, P.A., Kellermann, K.I., Hook, I.M., & Hawkins, M.R.S. 2002, A&A, 386, 97

[122] Jarrett, T.H., Chester, T., Cutri, R., et al., 2000, AJ, 119, 2498

[123] Jauncey, D.L., Savage, A., Morabito, D.D., Preston, R.A., Nicolson, G.D., Tzioumis, A.K., 1989, AJ, 98, 54

[124] Jauncey, D.L., Bignall, H.E., Lovell, J.E.J., Kedziora-Chudczer, L., Tzioumis, A.K., Macquart, J.-P., Rickett, B. J., 2003a, in Radio Astronomy at the Fringe, J.A. Zensus, M.H. Cohen & E. Ros eds., ASP Conf. Proc., Vol. 300, p. 199

[125] Jauncey, D.L., King, E.A., Bignall, H.E., Lovell, J.E.J., Kedziora-Chudczer, L., et al., 2003b, PASA, 20, 151

[126] Jones, T.W., Rudnick, L., Fiedler, R.L., Aller, H.D., Aller, M.F., Hodge, P.E., 1985, ApJ, 290, 627

[127] Jones, P.A., McAdam, W.B., 1992, ApJS, 80, 137

[128] Kamionkowski, M., Spergel, D.N., Sugiyama, N., 1994, ApJ Lett., 426, L57

[129] Kamionkowski, M., Kosowsky, A., Stebbins, A., 1997, Phys. Rev., D55, 7368

[130] Katgert, P., Katgert-Merkelijn, J.K., Le Poole, R.S., van der Laan, H., 1973, A&A, 23, 171

[131] Kato, T., Tabara, H., Inoue, M., Fukue, J., 1987, Nature, 329, 223

[132] Kedziora-Chudczer, L., Rickett, B.J., Bignall, H.E., Jauncey, D.L., Lovell, J.E.J., Tzioumis, A.K., & Macquart, J.P., 2003, in Radio Astronomy at the Fringe, J.A. Zensus, M.H. Cohen & E. Ros eds., ASP Conf. Proc., Vol. 300, p. 211

[133] Klein, U., Mack, K.-H., Gregorini, L., & Vigotti, M., 2003, A&A, 406, 579

[134] Koekemoer, A.M., & Bicknell, G.V., 1998, ApJ, 497, 662

[135] Kogut A., Banday, A.J., Bennett, C.L., Górski, K.M., Hinshaw, G., Reich, W.T., 1996, ApJ, 460, 1

[136] Kogut, A., Spergel, D.N., Barnes, C., Bennett, C.L., Halpern, M., et al., 2003, ApJS, 148, 161

[137] Kompaneets, A.S., 1957, *Sov. Phys. JEPT*, 4, 730

[138] Kormendy, J., & Gebhardt, K., 2001, in proc. 20th Texas Symp. on relativistic astrophysics, p. 363

[139] Kovac, J.M., Leitch, E.M., Pryke, C., Carlstrom, J.E., Halverson, N.W., Holzapfel, W.L., 2002, Nature, 420, 772

[140] Krichbaum, T.P., Kraus, A., Fuhrmann, L., Cimó, G., Witzel, A., 2002, PASA, 19, 14

[141] Kühr, H., Witzel, A., Pauliny-Toth, I.I.K., & Nauber, U. 1981, A&AS, 45, 367

[142] Lapi, A., Cavaliere, A. & De Zotti, G., 2003, ApJ, 597, 93

[143] Lasenby, A.N., 1996, in *Microwave Background Anisotropies*, proc. XVI Moriond Astrophysics Meeting, eds. F.R. Bouchet, R. Gispert, B. Guiderdoni, J. Trân Thanh Vân, p. 453

[144] Lawson, K.D., Mayer, C.J., Osborne, J.L., & Parkinson, M.L., 1987, MNRAS, 225, 307

[145] Lisenfeld, U., & Völk, H.J., 2000, A&A, 354, 423

[146] Lee, A.T., Ade, P., Balbi, A., Bock, J., Borrill, J., et al., 2001, ApJ, 561, 1

[147] Leitch, E.M., Pryke, C., Halverson, Kovac, J., Davidson, G. et al., 2002, ApJ, 568, 28

[148] Loewenstein, M., Mushotzky, R. F., Angelini, L., Arnaud, K. A. & Quataert, E. 2001, ApJ Letters, 555, L21

[149] Le Roux, E., 1961, Ann. Astroph., 24, 71

[150] Lo, K.Y., Chiueh, T.H., Martin, R.N., et al., 2001, in *20th Texas Symposium on relativistic astrophysics*, eds., J. Craig Wheeler and Hugo Martel, AIP Conf. Proc., 586, 172

[151] Longair, M., 1994, *High energy astrophysics*, Cambridge, Cambridge University Press

[152] Loveday, J., 2000, MNRAS, 312, 557

[153] Lovell, J.E.J., Jauncey, D.L., Bignall, H.E., Kedziora-Chudczer, L., Macquart, J.-P., Rickett, B. J., & Tzioumis A. K., 2003, AJ, 126, 1699

[154] Ma, C., Arias, E.F., Eubanks, T.M., Fey, A.L., Gontier, A.-M., et al. 1998, AJ, 116, 516

[155] Magliocchetti, M., Moscardini, L., Panuzzo, P., Granato, G.L., De Zotti, G., Danese, G., 2001, MNRAS, 325, 1553

[156] Magorrian, J., Tremaine, S., Richstone, D., Bender, R., Bower, G., Dressler, A., Faber, S. M., Gebhardt, K., Green, R. & Grillmair, C. 1998, AJ, 115, 2285

[157] Marecki, A., Falcke, H., Niezgoda, J., Garrington, S.T., Patnaik, A.R., 1999, A&AS, 135, 273

[158] Mason, B.S., Pearson, T.J., Readhead, A.C.S., Shepherd, M.C., Sievers, J., et al., 2003, ApJ, 591, 540

[159] Mauch, T., Murphy, T., Buttery, H.J., Curran, J., Hunstead, R.W., et al., 2003, MNRAS, 342, 1117

[160] McMahon, R.G., White, R.L., Helfand, D.J., & Becker, R.J., 2002, ApJS, 143, 1

[161] Mesa, D., Baccigalupi, C., De Zotti, G., Gregorini, L., Mack, K.-H., Vigotti, M., Klein, U., 2002, A&A, 396, 463

[162] Mészáros, P., 1999, A&AS, 138, 533

[163] Miller, A.D., Caldwell, R., Devlin, M.J., Dorwart, W.B., Herbig, T., et al., 1999, ApJ Lett., 524, L1

[164] Morganti, R., Garrett, M.A., Chapman, S., Baan, W., Helou, G., Soifer, T. 2004, A&A, in press (astro-ph/0405418)

[165] Morsi, H.W., & Reich, W., 1987, A&AS, 69, 533

[166] Murgia, M., Fanti, C., Fanti, R., Gregorini, L., Klein, U., Mack, K.-H., Vigotti, M., 1999, A&A, 345, 769

[167] Narayan, R., & Yi, I., 1994, ApJ, 428, L13

[168] Nartallo, R., Gear, W.K., Murray, A.G., Robson, E.I., & Hough, J.H. 1998, MNRAS, 297, 667

[169] Natarajan, P., Sigurdsson, S. & Silk, J., 1998, MNRAS, 298, 577

[170] Natarajan, P. & Sigurdsson, S., 1999, MNRAS, 302, 288

[171] O'Dea, C.P., Baum, S.A., Stanghellini, C., Morris, G.B., Patnaik, A.R., Gopal-Krishna, 1990, A&AS, 84, 549

[172] O'Dea, C.P., Baum, S.A., Stanghellini, C., 1991, ApJ, 380, 66

[173] O'Dea, C.P., & Baum, S.A., 1997, AJ, 113, 148

[174] O'Dea, C.P., 1998, PASP, 110, 493

[175] Oh, S.P. 1999, ApJ, 527, 16

[176] Okudaira A., Tabara, H., Kato, T., & Inoue, M. 1993, PASJ, 45, 153

[177] Oster, L., 1961, Rev. Mod. Phys., 33, 525

[178] Owen, F.N. & Mufson, S.L., 1978, AJ, 82, 776

[179] Owsianik, I., & Conway, J.E., 1998, A&A, 337, 69

[180] Owsianik, I., Conway, J.E., Polatidis, A.G., 1998, A&A, 336, L37

[181] Partridge, R.B., Cabonela, J., Guerra, E., Myers, S., 2003, in "Quasar Cores and Jets", XXV IAU General Assembly, JD18

[182] Pauliny-Toth, I.I.K., Witzel, A., Preuss, E., Kühr, H., Fomalont, E.B., Davis, M.M., & Kellermann, K.I. 1978a, AJ, 83, 451

[183] Pauliny-Toth, I.I.K., Witzel, A., Preuss, E., Baldwin, J.E., & Hills, R.E. 1978b, A&AS, 34, 253

[184] Peacock, J.A., 1985, MNRAS, 217, 601

[185] Peebles, P.J.E., 1968, ApJ, 153, 1

[186] Peebles, P.J.E., & Yu, J.T., 1970, ApJ, 162, 815

[187] Peebles, P.J.E., 1980, *The Large-Scale Structure of the Universe*, (Princeton, Princeton University Press)

[188] Peebles, P.J.E. 1993, Principles of physical cosmology, Princeton University Press

[189] Pellegrini, S., Baldi, A., Fabbiano, G. & Kim, D.-W. 2003, ApJ, 597, 175

[190] Pentericci, L., Van Reeven, W., Carilli, C.L., Röttgering, H.J.A.,& Miley, G.K. 2000, A&AS, 145, 121

[191] Perley, R.A., Schwab, F.R., & Bridle, A.H., 1989, *Synthesis imaging in radio astronomy*, ASP Conf. Ser., Vol. 6

[192] Perley, R.A., 1990, IAU Symp. 140: *Galactic and Intergalactic Magnetic Fields*, p. 463

[193] Perna, R., & Di Matteo, T. 2000, ApJ, 542, 68

[194] Perrotta, F., Baccigalupi, C., Bartelmann, M., De Zotti, G., Granato, G.L., 2002, MNRAS, 329, 445

[195] Perrotta, F., Magliocchetti, M., Baccigalupi, C., Bartelmann, M., De Zotti, G., et al., 2003, MNRAS, 338, 623

[196] Pierpaoli, E., Borgani, S., Scott, D., & White, M. 2003, MNRAS, 342, 163

[197] Pierpaoli, E., Scott, D., & White, M. 2001, MNRAS, 325, 77

[198] Platania, P., Burigana, C., De Zotti, G., Lazzaro, E., Bersanelli, M., 2002, MNRAS, 337, 242

[199] Polatidis, A., Wilkinson, P.N., Xu, W., Readhead, A.C.S., Pearson, T.J., Taylor, G.B., Vermeulen, R.C., 1999, New Astr. Rev., 43, 657

[200] Press, W.H., Teukolsky, S.A., Vetterling, W.T., & Flannery, B.P. 1992, Numerical recipes in FORTRAN. The art of scientific computing, Cambridge University Press

[201] Readhead, A.C.S., Taylor, G.B., Pearson, T.J., Wilkinson, P.N., 1996, ApJ, 460, 634

[202] Rees, M.J. & Ostriker, J.P., 1977, MNRAS, 179, 541

[203] Rees, M.J., Phinney, E.S., Begelman, M.C., & Blandford, R.D. 1982, Nature, 295, 17

[204] Reich, P., & Reich, W., 1988, A&AS, 74, 7

[205] Reynolds, R.J., Haffner, L.M., & Madsen, G.J., 2002, in ASP Conf. Ser. 282, eds. M. Rosado, L. Binette, L. Arias

[206] Ribicki, G.B. & Lightman, A.P., 1979, *Radiative Processes in Astrophysics*, New York, Wiley

[207] Ricci, R., Prandoni, I., Gruppioni, C., Sault, R.J., & De Zotti, G., 2004a, A&A, 415, 549

[208] Ricci, R., Sadler, E.M., Ekers, R.D., Staveley–Smith, L., Wilson, W.E., Kesteven, M.J., Subrahmanyan, R., Walker, M.A., Jackson, C.A., & De Zotti, G. 2004b, MNRAS, accepted (astro-ph/0407130)

[209] Roy, A.L., & Norris, R.P., 1997, MNRAS, 289, 824

[210] Romani, R.W., Sowards-Emmerd, D., Greenhill, L., & Michelson P., 2004, ApJ, 610, L9

[211] Rosa-González, D., Terlevich, R., Terlevich, E., Friaça, A., Gaztañaga, E., 2004, MNRAS, 348, 669

[212] Rowan-Robinson, M., & Fabian, A.C., 1974, MNRAS, 167, 419

[213] Rudnick, L., Jones, T.W., Fiedler, R.L., Aller, H.D., Aller, M.F., et al., 1985, ApJ Suppl., 57, 693

[214] Rudy, D.J., Muhleman, D.O., Berge, G.L., et al., Icarus, 71, 159

[215] Runyan, M.C., Ade, P.A.R., Bhatia, R.S., et al., 2003, ApJS, 149, 265

[216] Ryle, M., 1962, Obs., 82, 245

[217] Saikia, D.J., & Salter, C.J. 1988, ARA&A, 26, 93

[218] Salucci, P., Szuszkiewicz, E., Monaco, P., Danese, L., 1999, MNRAS, 307, 637

[219] Sault, R.J., Teuben, P.J., & Wright, M.C.H., 1995, "A retrospective view of Miriad" in *Astronomical Data Analysis Software ans Systems*, eds. R. Shaw, H.E. Payne, & J.J.E. Haynes, ASP Conf. Series, 77, 433

[220] Saunders, W., Rowan-Robinson, M., Lawrence, A., Efstathiou, G., Kaiser, N., et al. 1990, MNRAS, 242, 318

[221] Sazhin, M.V., & Korolëv, V.A. 1985, Soviet Astronomy Letters, 11, 204

[222] Schlegel, D.J., Finkbeiner, D.P., & Davis, M., 1998, ApJ, 500, 525

[223] Schmidt, M., 1968, ApJ, 151, 393

[224] Schmidt, M., Schneider D.P., Gunn J.E., 1995, AJ, 110, 68

[225] Schwartz, P.R., 1982, ApJ, 252, 589

[226] Seljak, U., & Zaldarriaga, M., 1996, ApJ, 469, 437

[227] Seljak, U., 1997, ApJ, 482, 6

[228] Seaton, D.B., & Partridge, R.B. 2001, PASP, 113, 6

[229] Shaver, P.A., Wall, J.V., Kellermann, K.I., Jackson, C.A., Hawkins, M.R.S., 1996, Natur, 384, 439

[230] Sheth, R.K., Mo, H.J., & Tormen, G. 2001, MNRAS, 323, 1

[231] Silva, L., De Zotti, G., Granato, G.L., Maiolino, R., & Danese, L. 2004, A&A, submitted (astro-ph/0403166)

[232] Silva, L., Granato, G.L., Bressan, A., & Danese, L. 1998, ApJ, 509, 103

[233] Smail, I., Ivison, R.I., & Blain, A.W., 1997, ApJ, 490, L5

[234] Smoot, G.F., Bennett, C.L., Kogut, A., Wright, E.L., Aymon, J., et al., 1992, ApJ Lett., 396, L1

[235] Smoot, G.F., 1998, preprint (astro-ph/9801121)

[236] Snellen, I.A.G., Schilizzi, R.T., de Bruyn, A.G., et al., 1998, A&AS, 131, 435

[237] Snellen, I.A.G., Schilizzi, R.T., Bremer, M.N., Miley, G.K., de Bruyn, A.G., Röttogering, H.J.A., 1999, MNRAS, 307, 149

[238] Snellen, I.A.G., Schilizzi, R.T., Miley, G.K., de Bruyn, A.G., Bremer, M.N., Röttgering, H.J.A., 2000, MNRAS, 319, 445

[239] Snellen, I.A.G., McMahon, R.G., Dennett-Thorpe, J., Jackson, N., Mack, K.-H., Xanthopoulos, E., 2001, MNRAS, 325, 1167

[240] Snellen, I.A.G., McMahon, R.G., Hook, I.M., & Browne, I.W.A., 2002, MNRAS, 329, 700

[241] Sondré, L., & Lahav, O., 1993, MNRAS, 260, 285

[242] Stanghellini, C., O'Dea, C.P., Dallacasa, D., Baum, S.A., Fanti, R., Fanti, C., 1998, A&AS, 131, 303

[243] Stanghellini, C., O'Dea, C.P., & Murphy, D.W., 1999, A&AS, 134, 309

[244] Stanghellini, C., Dallacasa, D., O'Dea, C.P., Baum, S.A., Fanti, R., Fanti, C., 2001, A&A, 377, 377

[245] Stickel, M, Meisenheimer, K., & Kühr, H., 1994, A&A Supp. Ser., 105, 211

[246] Sunyaev, R.A., & Zel'dovich, Ya.B., 1970, *Astrophys. Sp. Sci.*, 7, 3

[247] Sunyaev, R. A., & Zeldovich, Y. B. 1972, Comm. Ap. Sp. Phys., 4, 173

[248] Tauber, J.A., 2001, in "The Extragalactic Infrared Background and its Cosmological Implications", proc. IAU Symp. 204, M. Harwit ed., p. 493

[249] Taylor, G.B., Inoue, M., Tabara, H., 1992, A&A, 264, 421

[250] Taylor, G.B., Marr, J.M., Pearson, T.J., Readhead, A.C.S., 2000, ApJ, 541, 112

[251] Taylor, A.C., Grainge, K., Jones, M.E., Pooley, G.G., Saunders, R.D.E., & Waldram, E.M. 2001, MNRAS, 327, L1

[252] Tegmark, M., & Efstathiou, 1996, MNRAS, 281, 1297

[253] Tegmark, M., & de Oliveira-Costa, A., 1998, ApJ, 500, L83

[254] Thompson, A.R., Moran, J.M., & Swenson, G.W., 1986, *Interferometry and synthesis in radio astronomy*, New York, Wiley-Interscience

[255] Thompson, A.R., 1999, in *Synthesis Imaging in Radio Astronomy II*, eds. G.B. Taylor, C.L. Carilli & R.A. Perley, ASP Conf. Ser., 180, 11

[256] Tingay, S.J., Jauncey, D.L., Reynolds, J.E., Tzioumis, A.K., King, E.A., et al., 1997, AJ, 113, 2025

[257] Tinti, S., Dallacasa, D., De Zotti, G., Stanghellini, C., Celotti, A., 2003, in *Future Directions in High Resolution Astronomy: The 10th Anniversary of the VLBA*, eds., J.D. Romney & M.J. Reid, ASP Conf. Ser., (astro-ph/0309354)

[258] Tinti, S., Dallacasa, D., De Zotti, G., Celotti, A., & Stanghellini, C. 2004, A&A, submitted

[259] Toffolatti, L., Franceschini, A., Danese, L., De Zotti, G., 1987, A&A, 184, 7

[260] Toffolatti, L., Argüeso-Gómez, F., De Zotti, G., Mazzei, P., Franceschini, A., Danese, L., Burigana, C., 1998, MNRAS, 297, 117

[261] Tornikoski, M., Lainela, M., Valtaoja, E., 2000, AJ, 120, 2278

[262] Totsuji, H., & Kihara, T., 1969, PASJ, 21, 221

[263] Tornikoski, M., Jussila, I., Johansson, P., Lainela, M., Valtaoja, E., 2001, AJ, 121, 1306

[264] Trushkin, S.A., 2003, Bull. Spec. Astrophys. Obs. N. Caucasus, 55, 90, (astro-ph/0307205)

[265] Tschager, W., Schilizzi, R.T., Röttgering, H.J.A., Snellen, I.A.G., Miley, G.K., 2000, A&A, 360, 887

[266] Tucci, M., Martínez-González, E., Toffolatti, L., González-Nuevo, J., De Zotti, G., 2003, NewAR, 47, 1135

[267] Ulich, 1981, AJ, 86, 1619

[268] Veeraraghavan, S., & Davies, R.D., 1997, in *Particle Physics and the Early Universe*, eds. Bately, R. Jones, M.E., & Green, D.A.

[269] Vielva, P., Barreiro, R.B., Hobson, M.P., Martínez-González, E., Lasenby, A.N., 2001, MNRAS, 328, 1

[270] Voelk, H.J., 1989, A&A, 218, 67

[271] Voges, W., Aschenbach, B., Boller, H., et al., 1999, A&A 349, 389

[272] Wagner, S.J. & Witzel, A., 1995, ARA&A, 33, 163

[273] Waldram, E.M., Pooley, G.G., Grainge, K.J.B., Jones, M.E., Saunders, R.D.E., Scott, P.F., & Taylor, A.C. 2003, MNRAS, 342, 915

[274] Warren, S.J., Hewett, P.C., Osmer, P.S., 1994, ApJ, 421, 412

[275] Watson, R.A. et al., 2003, MNRAS, 341, 1057

[276] Waxman, E., 1997, ApJ, 489, L33

[277] White, G.L., Batty, M.J., Bunton, J.D., Brown, D.R., Corben, J.B., 1987, MNRAS, 227, 705

[278] White, S.D.M. & Rees, M.J., 1978, MNRAS, 183, 341

[279] Wijers, R.A.M.J., & Galama, T.J., 1999, ApJ, 523, 177

[280] Windhorst, R.A., Kron, R.G., & Koo, D.C., 1984, A&AS, 58, 39

[281] Witzel, A., Pauliny-Toth, I.I.K.,Geldzahler, B.J., Kellerman, K.I., 1978, AJ, 83, 475

[282] Yi, I., & Boughn, S.P., 1998, ApJ, 499, 198

[283] Yun, M.S., & Carilli, C.L., 2002, ApJ, 568, 88

[284] Zaldarriaga, M., & Seljak, U., 1997, Phys. Rev., D55, 1830

[285] Zel'dovich, Y., Kurt, V., Sunyaev, R., 1969, Sov. Phys. JETP, 28, 146